Structural, interfacial, and spin-orbital effects in epitaxial $SrIrO_3$ thin films

By

Trevor Jeffrey Anderson

A dissertation submitted in partial fulfillment of

the requirements for the degree of

Doctor of Philosophy

(Materials Science)

at the

UNIVERSITY OF WISCONSIN-MADISON

2017

Date of final oral examination: June 20th, 2017

The disseration is approved by the following members of the Final Oral Committee:

Chang-Beom Eom, Professor, Materials Science and Engineering

Mark Rzchowski, Professor, Physics

Robert McDermott, Professor, Physics

Xudong Wang, Professor, Materials Science and Engineering

Tomas Tybell, Professor, Electronics and Telecommunications

© Trevor Jeffrey Anderson 2017

All Rights Reserved

For my mother and father, and for Karen

Abstract

Perovskite ABO_3 materials exhibit a plethora of emergent phenomena such as piezoelectricity, colossal magnetoresistance, high-T_c superconductivity, and 2-dimensional electron gases. In these materials, the B-site transition metal element assumes an orbital configuration that creates a strongly correlated electronic state. Traditionally, the study of perovskite ABO_3 materials has been dominated by B-site elements from the 3*d* row in the periodic table. However, the incorporation of heavy transition metal elements such as iridium from the 5*d* row adds the flavor of strong spin-orbital coupling to the strong electron-electron correlations present in these materials. The interplay between these competing flavors suggests that such material systems are good candidates for the study of such phenomena as spin liquids, topological states, and spin-to-charge current conversion. The epitaxial layering of materials like $AIrO_3$ (A = metal) iridates with the more-commonly studied 3*d* perovskites and also elemental and alloyed metals can thus create new interfaces with exciting behavior that is applicable to next-generation devices.

Among these 5*d* perovskite candidates are the Ruddlesden-Popper phases $Sr_{n+1}Ir_nO_{3n+1}$. The $n = \infty$ case of perovskite $SrIrO_3$ has garnered significant attention due to theory predictions and observations that it hosts topologically-protected states, spontaneous ferromagnetism, and various interfacial magnetic coupling. However, $SrIrO_3$ is a polymorph that assumes a non-perovskite monoclinic structure in ambient conditions, whereas the orthorhombic perovskite phase is only stable in extreme conditions. Furthermore, bulk perovskite $SrIrO_3$ synthesis to date has yielded polycrystalline samples, complicating the study of intrinsic material properties, which means stabilizing epitaxial thin films is critical. This thesis will discuss a coordinated effort of material synthesis, structural, electronic/magnetic characterization, and theoretical computation to design,

grow, and evaluate the structural and physical behavior of epitaxial 5*d* $SrIrO_3$ with various other ABO_3 perovskites and also the alloyed ferromagnetic metal, $Ni_{0.8}Fe_{0.2}$ (Permalloy). The results presented in this thesis demonstrate the flexibility of $SrIrO_3$ as a candidate for both fundamental materials science and also the study and manipulation of electron spin for next-generation spintronics applications.

First, the synthesis of $SrIrO_3$ thin films by pulsed laser deposition (PLD) along the more-straightforward cubic (001) direction will be discussed, along with its subsequent epitaxial film layering and domain structure on $SrTiO_3$ and rare-earth $AScO_3$ (A = metal) scandate substrates. Multi-domain epitaxial $SrIrO_3$ was found to be favorable on cubic $SrTiO_3$ substrates, whereas growth on the structurally-similar scandate substrates shows evidence of single-domain symmetries.

Next, perovskite $SrIrO_3$ growth along the (111) direction is presented: the first successful synthesis of perovskite $SrIrO_3$ on the (111) surface to date. Recent theory studies predict the existence of exotic band topologies in (111)-oriented $SrIrO_3$ bilayers. However, perovskite $SrIrO_3$ growth along the (111) direction is unreported to date, as the monoclinic phase is more stable on (111) perovskite substrates. Our success was achieved by synthesizing the $SrIrO_3$ in thin honeycomb-like layers sandwiched between $SrIrO_3$ to impose perovskite structural boundary conditions. The epitaxial layering and symmetry was confirmed using transmission electron microscopy (TEM) and x-ray diffraction. Our results open up an avenue to study the intrinsic band structure of honeycomb $SrIrO_3$ bilayers to see if the predicted band topologies arise.

The precise control of interfacial atomic arrangement in ABO_3 perovskites is paramount, particularly in cases where the subsequent electronic properties of the material exhibit geometrical preferences along polar crystallographic directions that feature inevitably complex surface reconstructions. Thus, we used $SrIrO_3/SrTiO_3$ heterostructures as a model system to compare the B-site interfacial structure of perovskites along the 4-/4+ polar (111) and the completely non-polar (001) directions. The heterostuctures were first examined using scanning transmission electron microscopy (STEM) and then with x-ray crystal truncation rods that were analyzed using the Coherent Bragg Rod Analysis (COBRA) method. Our results reveal the preference of B-site intermixing

across the polar interface due to the unstable initial (111) $SrTiO_3$ substrate surface prior to growth. This finding suggests that the intermixing may mitigate epitaxy along the heavily-reconstructed (111) perovskite surface and also could allow geometrically selective interfacial doping of the strongly-correlated B-site *d*-shell electronic state.

In the final part of the thesis, I will investigate the Permalloy/$SrIrO_3$ interface, which we have shown can efficiently convert charge current to spin current via the spin Hall effect (SHE). This spin-current was found to exert large spin-orbit torque on magnetization in adjacent $Ni_{0.81}Fe_{0.19}$ layers. Furthermore, both the spin Hall conductivity in $SrIrO_3$ and the torque in Permalloy show a crystallographic dependence along different directions of the $SrIrO_3$ orthorhombic unit cell. We have also demonstrated that the magnitude of the torque can be modulated by a structural change in $SrIrO_3$ as a result of film thickness, which tunes the $SrIrO_3$ band structure from whence the strong SHE arises. Our results thus demonstrate that the torque originates from the intrinsic crystal structure of $SrIrO_3$. This efficient and tunable spin-manipulation of an adjacent ferromagnetic layer illustrates that $SrIrO_3$ is a promising candidate for next-generation spintronics.

Acknowledgements

A PhD thesis bears the name of a sole author. However, in the modern world of interdisciplinary scholarship, purely ”independent” research with a single name attached to a scientific finding is rare. Many names and faces are encountered along the journey, some whose names appear on the publications, and others whose contributions are not acknowledged in print, but nonetheless critical. This page contains both such individuals.

I'd first like to thank my advisor, Prof. Chang-Beom Eom for his intellectual mentoring and financial support, without which, my dissertation work would not be possible. I especially appreciate his kindness and patience during the inevitable struggles, frustrations, and delays that accompany doctoral work. Under his tutelage, I was very fortunate to have the guidance from a true pioneer in perovskite research.

I'd also like to thank my thesis committee team of Professors Mark Rzchowski (UW-Madison, Dept. of Physics), Robert McDermott (UW-Madison Dept. of Physics), Xudong Wang (UW-Madison, Dept. of Materials Science and Engineering), and Thomas Tybell (Norwegian University of Science and Technology, Dept. of Electronics and Telecommunications). These men guided me through my research, giving me constructive feedback along the way that I am grateful for.

My research would never have gotten off the ground without the help of my lab colleagues in the Oxide Lab. Drs. Sangwoo Ryu and Jacob Podkaminer gave me my first exposure to and training in oxide film growth and characterization. Next, I must thank Dr. Tianxiang Nan, who brought in a fresh perspective on my research topic and opened up a new avenue for $SrIrO_3$ study. Drs. David Harris, Yanjun Ma, and Hyungwoo Lee also generously gave their time to offer me advice on my research. Every name and face in the Oxide Lab contributed to my work at some

point along the way.

Next, my colleagues and collaborators, who are among the best in the world at what they do. I'd especially like to thank Prof. Mark Rzchowski of UW-Madison Physics and his graduate students, Neil Campbell and Julian Irwin. I probably would not have published anything without Dr. Hua Zhou at Argonne National Laboratory, who has given me guidance and high-quality data for virtually every topic covered in this thesis. Next, Prof. Xiaoqing Pan at UM-Ann Arbor/UC-Irvine (both for putting in a good word for me to Prof Chang-Beom Eom when I was an undergraduate student at Michigan and for his subsequent collaboration on my graduate research at UW-Madison), Dr. Lin Xie of UC-Irvine and Nanjing University, Prof. Dan Ralph and Jonathan Gibbons at Cornell University, Prof. Yong Baek Kim and Dr. Kyusung Hwang at the University of Toronto. Dr. Ryan Jacobs at UW-Madison also provided many fruitful discussions related to my research.

The long grind of graduate school was pleasantly interrupted by the company of friends to enjoy non-research activities such as team trivia, dinner nights, concerts/festivals, scotch and wine tastings, and watching football, baseball, basketball, and hockey. Acknowledgments go to Tomas, Jacob, Camilo, Ryan, Bobby, Gareth, Erik, Alyssa, Nick, Matt, Jack, Nate, Jerry, Caitlin, Shane, Katelyn, Neil, Samantha, Lori, Kevin Drew, David, Lauren, Tianxiang, Lu, Chenyu, and the many people in the UW-Madison MSE and Physics departments. This list is by no means complete, as many others who I do not have room to name must also be acknowledged. You all know who you are.

Lastly, I'd like to thank my parents, Terry Downs and Norman Anderson, and my girlfriend, Karen Gaske. My parents personally undertook responsibility for my K-12 education, through hands-on homeschooling and also by keeping a large library in the house for independent study and reference. More than I can adequately put into words, they worked harder at their jobs and in the home to provide a space for their children that was conducive to free and open inquiry. Karen, whom I met in my 3rd year of graduate school, has shown me nothing short of tireless and selfless devotion while I labored on research and its subsequent documentation. Without the presence of these 3 individuals in my life, the achievement of this doctoral degree would be much less meaningful for me. This work is therefore dedicated to them.

Preface

”The interface is the device.” So said Herbert Kroemer in his 1998 Nobel lecture. A man who wore many hats, Kroemer won his Nobel prize in physics ”for developing semiconductor heterostructures used in high-speed- and opto-electronics.” More specifically, Kroemer has pioneered the the use of molecular beam epitaxy, developing new materials and synthesis methods before their utilization in existing technologies. Thus, Kroemer understands the importance of material discovery as a means to create new technologies with superior performance. With conventional devices beginning to reach the quantum limits of the component materials, the limiting step in the development of new technologies is often the realization of increasingly complex materials that can only be realized with emerging synthesis and characterization methods: a critical research thrust in condensed matter science today.

What new materials are expected to be at the forefront of this thrust? A recent *Nature Materials* editorial, ”The interface is still the device,” highlights promising transition-metal oxide materials as a means realize new electronic states of matter through artificial synthesis methods[1]. In addition to being the most abundant material class in the earth’s crust, oxide materials like ABO_3 perovskites feature a flexible elemental tolerance, allowing the design and creation of many pure-phase and doped structures within the same material family. While generally thought of as conventional insulators, oxides actually range from electrically insulating to superconducting. As such, these materials show an often surprising variety of interesting electronic properties including piezoelectricity, high-T_C superconductivity, 2-dimensional electron gases, colossal magnetoresistance, and exotic conduction. These observations often take place in thin film heterostructures, which makes and selection and control of the interfacial structure paramount for creating a functional material.

Thus, it would seem the interface is indeed "still the device," and newer non-conventional oxide materials may play an important role in creating new interfaces with emergent phenomena and functionality. However, before any new-age devices can be developed with these materials, a careful fundamental understanding of their structural and physical properties must be obtained. The purpose of this thesis is to investigate such a material: the polymorph $SrIrO_3$ in its perovskite form. Although $SrIrO_3$ assumes a non-perovskite crystal structure in ambient conditions, a perovskite phase exists at high pressures and temperatures that only exists as a single-crystal when synthesized as a thin film. Therefore, thin film studies on perovskite $SrIrO_3$ are critical to unlock the properties therein.

Chapter 1 of this thesis provides an introduction to the diverse class of perovskite ABO_3 materials and thin films, discusing the relationship between their structural and physical properties. In particular, the flavoring of strongly-correlated electrons and heavier atoms with strong spin-orbit coupling will be addressed. Finally, Ruddlesden-Popper $Sr_{n+1}Ir_nO_{3n+1}$ will be introduced to motivate $SrIrO_3$ and the crystal structure and electronic properties of this exciting, relatively new material and the challenges and questions pertaining to its electronic structure.

Chapter 2 gives an overview of the major ABO_3 synthesis and characterization techniques used in this thesis, along with data from the growth of $SrIrO_3$ films on pseudocubic (001) substrates. Basic principles and models of epitaxy and thin film growth will be presented, along with discussions on thin film growth, pulsed laser deposition, reflection high energy electron diffraction (RHEED), and x-ray diffraction. When applicable, data from the $SrIrO_3$ film growth will be presented and analyzed to give concrete, real-application examples of these various techniques. The growth of $SrTiO_3$ on $SrTiO_3$ will also be discussed in detail, along with the resulting domain structure determined from RHEED and x-ray diffraction. Growth of $SrIrO_3$ on other perovskites substrates will also be introduced to lesser degree.

Chapter 3 discusses the epitaxial stablization of ultra-thin (111)-oriented $SrIrO_3$ thin films on $SrTiO_3$, first report of $SrIrO_3$ synthesis along the (111) direction. By growing the films thin on the order of 1 nm and imposing perovskite $SrTiO_3$ boundary conditions at both $SrIrO_3$ surfaces, the perovskite phase was stabilized: the first report of perovskite $SrIrO_3$ along the (111) direction.

This work was previously published in *Applied Physics Letters* [*Appl. Phys. Lett.* **108**, 151604 (2016)].

Chapter 4 of this chapter discusses the interfacial configuration of polar (111) and non-polar (001) $SrIrO_3/SrTiO_3$ heterostructures using the Coherent Bragg Rod Analysis (COBRA) method. In this COBRA study, it was found that the heterostructure B-site atoms (Ti and Ir) preferably intermix on the (111) substrate surface due the initial substrate surface prior to growth that results from unstable polar surface and its treatment. The intermixing is thus interpreted as a means to stabilize epitaxial growth in the polar (111) direction. During the writing of this thesis, the results of this work were being prepared for submission to *APL Materials*.

Chapter 5 discusses our work done on $Ni_{0.81}Fe_{0.19}$(Py)/$SrIrO_3$. Here we demonstrate a large spin Hall effect in $SrIrO_3$, which induces a vertical spin current that exerts spin-torque on the overlaid ferromagnet, Permalloy. The magnitude of this torque shows a crystallographic directional dependence, which is believed to originate from the band structure of the orthorhombic $SrIrO_3$. The spin-torque can also be modulated by subtle changes to the $SrIrO_3$ symmetry that result from thickness effects and strain from the growth of $SrIrO_3$ different substrates. During the writing of this thesis, the results of this work were being prepared for submission to *Nature Physics*.

Chapter 6 summarizes the main findings in this thesis and discusses possible future work therein. Also presented is a general outlook for the material system of $SrIrO_3$, discussing the challenges of its synthesis and potential avenues for further study.

Appendix A discusses the data obtained from RHEED on the mixed domain structure of $SrIrO_3$ on $SrIrO_3$(001) for different film thickness and a comparison between the mixed-domain structure on $SrTiO_3$ and the single-crystal domain orientation on the structurally similar scandate substrates $DyScO_3$, $GdScO_3$, and $NdScO_3$. Appendix B summarizes some experimental details and data from the STEM and COBRA work from Chapters 3 and 4. Appendix C presents experimental information and supplements for the work presented in Chapter 5, including the analysis methods for the spin-orbit torque ferromagnetic resonance. Finally, Appendix D presents supplementary information for theoretical calculations in Chapter 5.

Contents

Abstract **ii**

Acknowledgements **v**

Preface **vi**

Contents **ix**

List of Figures **xiv**

List of Tables **xxvii**

1 Introduction **1**

1.1 ABO_3 perovskites 1

1.2 Correlated *d*-orbital electrons 6

1.3 Strong spin-orbit coupling in 5*d* perovskites 8

1.4 Ruddlesden-Popper $Sr_{n+1}Ir_nO_{3n+1}$ iridates 11

1.5 Metastable-phase perovskite $SrIrO_3$ 13

1.6 Conclusions 15

2 Synthesis and characterization of ABO_3 thin films **17**

2.1 Epitaxy 17

2.2 ABO_3 perovskite substrates 19

2.3 Pulsed laser deposition 21

2.4 Reflection high energy electron diffraction 24
2.5 Synthesis and surface of $SrIrO_3$ thin films 27
2.5.1 PLD synthesis of $SrIrO_3$ on pseudocubic (001) substrates 27
2.5.2 Surface characterization: atomic force microscopy 28
2.6 X-ray diffraction (XRD) 29
2.6.1 Basic principles of XRD 29
2.6.2 X-ray diffraction of thin films 31
2.6.3 4-Circle x-ray diffraction 32
2.6.4 Surface-normal layering of $SrIrO_3$ on $SrTiO_3$ 35
2.7 Symmetry of $SrIrO_3$ thin films from XRD 35
2.7.1 Glazer notation of perovskite tilt systems 35
2.7.2 Symmetry and domain structure of $SrIrO_3$ on $SrTiO_3$ 38
2.7.3 Growth of $SrIrO_3$ on assorted ABO_3 perovskite substrates 42
2.8 Electronic transport of $SrIrO_3$ on (001) $SrTiO_3$ 43
2.9 Conclusions 44

3 Metastable honeycomb $SrTiO_3$/$SrIrO_3$ heterostructures 45
3.1 $SrIrO_3$ and the (111) perovskite interface 45
3.2 Synthesis and surface of $SrTiO_3$/$SrIrO_3$ heterostructures 47
3.3 Epitaxial arrangement and symmetry from STEM/XRD 49
3.4 Conclusions 53

4 Interfacial B-site atomic configuration in polar (111) and non-polar (001) $SrIrO_3$/$SrTiO_3$ heterostructures 54
4.1 Polar perovskite (111) surfaces and interfaces 54
4.2 $SrIrO_3$/$SrTiO_3$ heterostructure synthesis 56
4.3 TEM and COBRA experiments 57
4.4 Conclusions 64

5 Large spin-orbit torque in $Ni_{0.81}Fe_{0.19}/SrIrO_3$ heterostructures **66**

5.1 Spin-current magnetic random access memory (MRAM) 66

5.1.1 Spin-current coupling with ferromagnets 68

5.2 Spin current generation via the spin Hall effect 69

5.2.1 Spin Hall effects in various material systems 72

5.3 Large intrinsic spin Hall effect in $SrIrO_3$ 73

5.3.1 Synthesis of $AlO_x/Py/SrIrO_3/SrTiO_3(001)$ heterostructures 74

5.3.2 ST-FMR results of spin-orbit torque in $Py/SrIrO_3$ 76

5.3.3 Tuning of spin-torque by crystal structure of $SrIrO_3$ films 80

5.3.4 Experimental configuration SHC for bulk and thin film slab 85

5.4 Conclusions 87

6 Conclusions and outlook **89**

6.1 Novelty of $SrIrO_3$ thin films 89

6.2 Structure of $SrIrO_3$ thin films on $(001)_{pc}$ perovskites 89

6.3 Polar (111) $SrIrO_3$ interfaces 91

6.4 Large intrinsic spin-orbit torque in $Ni_{0.81}Fe_{0.19}/SrIrO_3$ heterostructures 92

6.5 Final Thoughts 93

Appendix A: Experimental supplement for Chapter 2 **94**

A.1 AFM of $SrIrO_3$ Grown on Perovskite Substrates 95

A.2 RHEED studies of $SrIrO_3$ on ABO_3 substrates 97

Appendix B: Experimental supplement for Chapters 3 and 4 **100**

B.1 Supplement to Chapter 3 100

B.1.1 Transmission electron microscopy 100

B.1.2 Synchrotron XRD and COBRA methods 100

B.2 Supplement to Chapter 4 100

B.2.1 Transmission electron microscopy 100

B.2.2 Synchrotron XRD and COBRA methods 101

Appendix C: Experimental supplement for chapter 5 **103**

C.1 Lab source x-ray diffraction 104

C.2 Transmission electron microscopy 105

C.3 Synchrotron x-ray thin film diffraction 106

C.4 Setup for ST-FMR measurements 106

C.4.1 ST-FMR line shape analysis and frequency dependent spin torque ratio . . 107

C.4.2 ST-FMR dc-tuned analysis and thickness dependent spin torque ratio . . . 111

C.4.3 Transmission of spin current in Py/$SrIrO_3$ 112

C.4.4 Measurements on *ex-situ* Py/$SrIrO_3$, Py, and Pt/Py controls samples 113

C.5 $SrIrO_3$ and AlO_x/Py/$SrIrO_3$ Transport Properties 115

Appendix D: Theoretical supplement for chapter 5 **116**

D.1 Bulk spin Hall conductivity in $SrIrO_3$ 117

D.1.1 Tight-binding model 117

D.1.2 Origin of the large $SrIrO_3$ bulk SHC and its directional dependence 118

D.1.3 Lattice symmetry in the $[110]_o$ slab geometry 120

Bibliography **122**

List of Figures

1.1 Simple cubic ABO_3 perovskite, with the A atom on the corner unit cell site, B atom in the center, and oxygen atoms on the faces. 2

1.2 Periodic table showing elementally compatible perovskite constituents. Reproduced and adapted from Schlom *et al.*, 2008, with permission from the Journal of the American Ceramic Society. 3

1.3 (a) Simple cubic $SrTiO_3$ structure showing no distortions of the TiO_6 (b) orthorhombic $SrRuO_3$ structure showing RuO_6 tilts and rotations. 4

1.4 Pseudocubic lattice parameters of the most common ABO_3 perovskite and related oxide substrates. Reproduced from Langenberg, *et al.* 2016 with permission from APL Materials. 5

1.5 *d*-shell degeneracy lifted as a result of *d-p* orbital coupling between transition-metals and oxygen in perovskites. Reproduced and adapted from Tokura and and Nagaosa 2000 with permission from Science. 7

1.6 Simple cartoon of relativistic electron spin-orbit coupling with the host atom. . . . 8

1.7 Schematic showing the possible physical phenomena that can occur at interfaces with the presence of strong spin-orbit interactions (inner circles), which can lead to effects relevant to spintronics applications (outer circle). Reproduced from Soumyanarayanan, *et al.* 2016 with permission from the Nature Publishing Group. 10

1.8 (a) General Ruddlesden-Popper phase $A_{n+1}B_nO_{3n+1}$ layered perovskites showing increasing BO_6 stacking with n (b) *d*-orbital splitting in iridates with strong spin-orbit coupling showing the creation of the 3/2 and 1/2 effective momentum bands. 12

1.9 Bulk structures of (a) ambient monoclinic and (b) high temperature/pressure orthorhombic $SrIrO_3$. 14

2.1 (a), (b), (c) 3 basic growth modes of thin films, Wolmer-Weber, Stranski-Krastanov, and Frank van der Merwe, respectively (d), (e) Epitaxial strain of thin films in the case of in-plane compressive and tensile strain, respectively. 18

2.2 Surfaces of (a) (001) $SrTiO_3$ (b) (111) $SrTiO_3$ showing preservation step-terrace formation from chemical and thermal treatment. 20

2.3 (a) "Main" PLD chamber (b) "Hybrid" PLD/sputtering chamber. Both chambers are equipped with loadlock chambers and *in situ* RHEED setups. 21

2.4 (a) Freshly-sanded $SrIrO_3$ PLD target before ablation (b) Same $SrIrO_3$ target after ablation showing circular ablation tracks 23

2.5 (a) RHEED diffraction geometry showing a typical RHEED pattern on a phosphorous screen (b) RHEED oscillations and the surface coverage at points of interest (c) $SrTiO_3$substrate (1,0) RHEED pattern. (a) and (b) reprinted with permission from TU-Braunschweig. 25

2.6 Specular diffraction intensity of a 20 uc thick $SrIrO_3$film with RHEED images of the substrate (left inset) and $SrIrO_3$film at the end of the growth (right inset). . . . 28

2.7 Surfaces of (a) TiO_2-terminated (001) $SrTiO_3$ substrate (b) 10 nm $SrIrO_3$thin film showing preservation of the underlying substrate step-terrace surface (c) 35 nm $SrIrO_3$thin film showing 3D island surface with "wedding cake" features. 29

2.8 (a) Real space depiction of Bragg diffraction showing integer path difference for adjacent incident and ecxident x-ray beams, which leads to Bragg's law (b) Reciprocal space depiction of diffraction showing the Laue condition met on the surface the Ewald sphere. 30

2.9 4-circle XRD geometry. 33

2.10 (a) Out-of-plane x-diffraction scans of a 35 nm $SrIrO_3$ thin film on $SrTiO_3$ showing single-phase epitaxial $SrIrO_3$ (b) Region around the (002) $SrTiO_3$ substrate peak, showing sharp Kiesig fringing in the $SrIrO_3$, indicating high quality interface with $SrIrO_3$ (c) Rocking curve around $(002)_{pc}$ $SrIrO_3$ peak indicating good alignment of planes and overall crystalline quality. 36

2.11 (a) Orthorhombic arrangement of a typical orthorhombic perovskite on a cubic substrate (e.g., $SrTiO_3$) with the $[110]_o$ direction aligned along $[001]_c$, $[001]_o$ direction aligned along $[010]_c$, and $[1\bar{1}0]_o$ direction aligned along $[100]_c$, resulting in a distorted orthorhombic (monoclinic-like) symmetry (b) reciprocal space mappings around the $\{103\}$ $SrTiO_3$ family of peaks indicating coherence with the underlying substrate and a peak splitting along $[1\bar{1}0]_o$ due to compressive strain where γ does not equal 90°. 39

2.12 (a) H-scan reciprocal space mapping around the $(\frac{1}{2}02)_{pc}$ and $(002)_{pc}$ reflections (b) K-scan reciprocal space mapping around the $(0\frac{1}{2}2)_{pc}$ and $(002)_{pc}$ reflections. The presence of these half-order $SrIrO_3$ peaks in orthogonal in-plane directions implies a mixed domain $SrIrO_3$ structure with about 90% preferential $[001]_o$ domain alignment along $[010]_c$ of $SrTiO_3$. 41

2.13 (a) Out-of-plane x-diffraction scans of $SrIrO_3$ thin films on 5 different perovskite substrates (b) rocking curve scans of the films grown in (a). Both plots indicate high quality single-crystal $SrIrO_3$ films on each substrate. 43

2.14 Resistivity vs. temperature of a 10 nm $SrIrO_3$thin film on $SrTiO_3$compared to known bulk orthorhombic studies (Longo *et al.*, 1974 and Zhao *et al.*, 2008). . . . 44

3.1 Schematics of (a) monoclinic $SrIrO_3$ (b) High pressure/high temperature perovskite $SrIrO_3$ (c) perovskite ABO_3 (d) Perovskite ABO_3(111) planar geometry with buckled hexagonal symmetry (e) planar stacking of the (111) cubic perovskite layering with AO_3 and B planar repeating units, i.e., a (111) bilayer. 46

3.2 (a) In situ high pressure RHEED intensity oscillation spectrum of the specular spot during the growth of a bare 3 bilayer $SrIrO_3$ film with RHEED diffraction patterns of the substrates before growth (left inset) and $SrIrO_3$ surface at the end of the growth (right inset). The intensity oscillations and streaky RHEED image patterns of the diffraction spots indicate layer-by-layer growth. (b) $SrTiO_3$ growth with RHEED image of the $SrIrO_3$ film before $SrTiO_3$ growth (left inset) and $SrTiO_3$ surface at the end of the growth (right inset). (c) AFM image of the bare $SrIrO_3$ film in (a) showing an atomically smooth film surface with cross-sectional profile (white line) indicating single bilayer step-terrace heights. (d) AFM image of a similarly ultra-thin $SrIrO_3$ film capped with a 5 bilayer $SrTiO_3$ film with cross-sectional profile (white line) showing preservation of the atomically flat surface and single bilayer step-terrace height. 48

3.3 (a), (b) Filtered cross-sectional STEM HAADF images of a 3 bilayer $SrIrO_3$ film capped with a 5 bilayer $SrTiO_3$ along the [1-10] zone axis, suggesting a perovskite epitaxial layering with the bright iridium (highest Z) atoms confined to the 3 bilayer $SrIrO_3$ film region and B-site column (c) FFT of the image in (a) implying structural coherence of the $SrTiO_3/SrIrO_3$ heterostructure with the underlying $SrTiO_3$ substrate. 50

3.4 (a) $\{11L\}$ and $\{21L\}$ CTR families that would exhibit 3-fold in-plane symmetry in pseudo-cubic crystal structures, shown in a reciprocal lattice HK grid. (b), (d) CTR intensities of $\{11L\}$ and $\{21L\}$, respectively, of the $SrTiO_3/SrIrO_3$ heterostructure with the 3 CTRs in each family superimposed. (c), (e) Magnified regions of the CTR intensity at reciprocal space points near the substrate Bragg peaks of (b) and (d), respectively. As can be seen in (c) and (e), there is no intensity deviation within either CTR family at each reciprocal space point, thus showing that our total heterostructure has the same in-plane symmetry as the $SrTiO_3$ substrate. . . . 51

4.1 (a), (b) Planar layering for (111) and (001) $SrIrO_3/SrTiO_3$ heterostructures, respectively. 55

4.2 (a), (b) RHEED intensity of the specular diffraction spot for the (111) and (001) $SrIrO_3/SrTiO_3$ heterostructures, respectively, showing layer-by-layer growth except in the case of the (111) $SrTiO_3$ capping film. The RHEED pattern insets in both plots show from left to right the $SrTiO_3$ substrate surface, final $SrIrO_3$ surface, and final $SrTiO_3$ capping layer surface (c), (d) AFM images of the heterostructures in (a) and (b) showing atomically-smooth surfaces. 56

4.3 (a), (b) Filtered cross-sectional STEM-HAADF images of $SrIrO_3/SrTiO_3$ heterostructures for the (111) and (001) samples, respectively (c), (d) Averaged integrated line intensities along the B-site column in the (111) and (001) heterostructures, respectively. 58

4.4 (a), (b) Specular crystal truncation rod scans of the (111) and (001) samples, respectively, showing discernable midzone features and good agreement with the COBRA calculated CTRs. (c), (d) Layer-by-layer electron densities as a function of distance normal to the surface of the (111) and (001) $SrIrO_3/SrTiO_3$ heterostructures, respectively. The origin on the x-axis denotes the position of the $SrIrO_3$ film/$SrTiO_3$ substrate. interface. 60

4.5 (a), (b) COBRA-extracted electron numbers as a function of planar layering for (111) and (001) $SrIrO_3/SrTiO_3$ heterostructures, respectively (c), (d) enlarged area of (a) and (b) close to the origin. As can be seen in (c), there is a pronounced monotonic increase in the electron number of the substrate B-planes approaching the interface with the $SrIrO_3$ film. This feature is not observed in the BO_2 planes of the (001) $SrTiO_3$ substrate in (d). The origin on the x-axis denotes the position of the $SrIrO_3$ film/$SrTiO_3$ substrate interface. It should be noted that the decrease in electron number of the top $SrTiO_3$ layers is due to incomplete coverage in these layers. 61

4.6 (a), (b) COBRA-resolved planar electron densities of like-treated (111) and (001) $SrTiO_3$ substrates, respectively, at a growth condition of 550°C and 10^{-3} mbar oxygen partial pressure. The top 4 bilayers near the surface of the (111) substrate show significant charge depletion, which is likely a result of the diverging polar potential at the surface and the surface treatment prior to growth. Such depletion is not observed in the (001) substrate, where only the top 2 atomic layers are significantly depleted (c) Poisson model illustrating the resultant potential along the (111) substrate surface that arises to compensate the diverging potential along the nominal (111) layering. The net charge in the top 4 bilayers of the (111) $SrTiO_3$ substrate to screen the diverging potential is $+2e$, or about +0.5 *e*/layer. 63

5.1 (a) MRAM bit circuit utilizing a magnetic tunnel junction Reproduced and adapted from Åkerman 2005 with permission from Science. 67

5.2 (a) Magnetic torque on a ferromagnetic layer induced by a spin-current. The electron is transmitted or reflected depending on the relative orientation of the electron-spin and the ferromagnetic moment (b) Magnetization dynamics induced by spin-currents as described by the Landau-Lifshitz-Gilbert-Slonczewski equation. Reproduced and adapted from Brataas *et. al* 2012 with permission from Nature Publishing Group. 69

5.3 (a) Ordinary Hall effect (b) analogous spin Hall effect (c) Extrinsic spin Hall effect where spins split at defect with strong-spin orbit coupling (d) Intrinsic spin Hall effect from Berry curvature band structure 71

5.4 (a) Calculated bulk $SrIrO_3$ spin Hall conductivity (SHC) as a function of Fermi energy ϵ_F. Left inset: Orthorhombic perovskite crystal structure of bulk $SrIrO_3$, where *a*, *b*, and *c* correspond to the $[100]_o$, $[010]_o$, and $[001]_o$ directions (subscript o for orthorhombic notation), respectively. Right inset: Momentum-resolved SHC $\Omega(k)$ in the Brillouin zone for the case $\epsilon_F = 0$ (b) Electron energy band structure of the bulk system on the XURS plane of the Brillouin zone. The red arcs at the bottom represent the momentum-resolved SHC, which is the net Berry curvature summed over occupied electron levels below a given Fermi level (green) (c) Electron band structure along the path U-R-S-U-X-S, where the gray boxes highlight the nearly degenerate energy bands responsible for the large bulk SHC (d) Schematic illustrations of the lattice symmetry of $SrIrO_3$ when grown on cubic non-tilted $SrTiO_3$ where a partial suppression of the IrO_6 octahedral tilt exists up to a certain thickness before a tilted octahedral pattern is established in thicker films. 74

5.5 (a) Atomic force microscopy images of a treated (001) $SrTiO_3$ substrate (b) subsequently deposited heterostructure of AlO_x(1 nm)/Py(3 nm)/$SrIrO_3$(8 nm) showing near preservation of the atomically smooth $SrTiO_3$ substrate surface. 75

5.6 (a) Scanning transmission electron microscope image of Py/$SrIrO_3$ heterostructure on (001) $SrIrO_3$ substrate. The image contrast is approximately proportional to the atomic number Z, where brighter colors represent heavier elements. Subscripts c and o denote the cubic and orthorhombic notation, respectively. (a, (c), Expanded image of the top Py/$SrIrO_3$ interface [shown in (b)], and the bottom $SrIrO_3$/$SrTiO_3$ interface [shown in (c)], showing the high quality $SrIrO_3$ film with atomically-sharp interfaces. The stacking of the atomic constituents are highlighted in the blown-up images by the superimposed filled dots of different colors (Sr in green, Ir in yellow and Ti in blue). 76

5.7 (a) Schematic of the Py/$SrIrO_3$ bilayer on $SrTiO_3$(001) and the current-induced torque geometries. Incoming charge current (J_c) generates a spin current (J_s) along the out-of-plane $[110]_o$ direction of the $SrIrO_3$ film ($[001]_c$ of the $SrTiO_3$ substrate) (b) ST-FMR spectrum (fitted to a Lorentzian function, solid line) for a 3.5 nm Py/8 nm (20 uc) $SrIrO_3$ sample with microwave current applied along the $[010]_c$ axis. The dashed lines represent the fits of the symmetric and antisymmetric components. The external magnetic field is oriented at an angle $\phi = -45^\circ$ with respect to the current axis. The applied microwave frequency and power are 5.5 GHz and 12 dBm. The V_{mix} across the device bar is acquired by a dc voltage meter (c) Symmetric and antisymmetric resonance components as a function of the external magnetic field angle ϕ, which are fitted to $\sin(2\phi)cos\phi$ (d) In-plane crystallographic orientation (current applied along from $[100]_c$ to $[010]_c$) dependence of the measured spin-torque ratio. The external magnetic field angle is fixed at $\phi = 45^\circ$. The solid line shows the fit to $\sin(\psi + \psi_0)$. 77

5.8 (a), (b) Resonance linewidth and effective magnetic damping as a function of dc current density in $SrIrO_3$ for Py/$SrIrO_3$ [shown in (a)] and for Py/$SrRuO_3$ [shown in (b)] with both positive and negative external magnetic field. The solid lines represent linear fitting (c) Current-induced modulation of Py effective damping as a function of external magnetic field angle for the Py/$SrIrO_3$ sample. The solid line shows the fit to $\sin\phi$. The Py/$SrRuO_3$ data points are taken at $\phi = 45^\circ$ and -135°. . 79

5.9 (a), (b), (c), (d) The change of resonance linewidth as the functions of applied current and the corresponding current density in $SrIrO_3$ for the 3.5 nm Py/$SrIrO_3$ with the $SrIrO_3$ thicknesses of 8 uc (a), 12 uc (b), 16 uc (c), and 20 uc (d). The solid lines represent linear fitting. All measurements were taken with the external magnetic field applied at $\phi = -135°$. The microwave power is 12 dBm and the frequency is 5.5 GHz. (e) $SrIrO_3$ thickness dependent of spin orbit ratio $\theta_{\|}$ determined by the dc biased ST-FMR measurements. (f) $SrIrO_3$ thickness dependent of Gilbert damping parameter α determined by ST-FMR and broadband FMR measurements. The dashed curve represents the fit to the diffusive spin-pumping model. 81

5.10 (a) Epitaxial arrangement of orthorhombic $SrIrO_3$ on cubic $SrTiO_3$ (b) Integrated reciprocal space mappings around the $\{103\}$ $SrTiO_3$ substrate reflection of 8, 12, 16, and 20 uc $SrIrO_3$ films on $SrIrO_3$(001) substrates. The separation of the $(103)_{pc}$ and $(\text{-}103)_{pc}$ film peak positions, which indicate an out-of-plane tilt of the $SrIrO_3$ film relative to the substrate due to the coherent epitaxial strain, is shown to decrease to zero from 20 uc to 8 uc, indicating a partial suppression of the IrO_6 orthorhombic tilt to a near tetragonal-like structure (c) Intensity of orthorhombic $(221)_o$ $SrIrO_3$ peak, which decreases from 20 to 8 uc (d) Intensity comparison of the $SrIrO_3$ $(103)_{pc}$ and $(221)_o$ peak intensities as a function of film thickness. 83

5.11 (a) Thickness dependent orthorhombicity factor, defined as a/b, of $SrIrO_3$. The dashed line represents a trend for the $SrIrO_3$ crystalline symmetry transition (b) SHC $\sigma_{\|}$ of Py/$SrIrO_3$ bilayer (with Py thickness fixed at 3.5 nm) as a function of $SrIrO_3$ thickness (c) Schematic illustrations of the $SrIrO_3$ lattice symmetry change originating from the IrO_6 octahedral distortion that is partially suppressed up to 12 unit cells when grown on $SrTiO_3$. 85

5.12 Calculated SHC in $SrIrO_3$ film slab (red) and the bulk (blue) for the experimental configuration (where the spin current is along the $[110]_o$ direction). In the film slab system, significant enhancement of SHC is observed compared to the bulk system. 86

A.1 AFM images of $SrIrO_3$ films grown on (a) $NdGaO_3$ (b) $(LaAlO_3)_{0.3}$-$(Sr_2AlTaO_6)_{0.7}$ (LSAT) (c) $SrTiO_3$ (d) $DyScO_3$ and (e) $GdScO_3$. The RHEED pattern taken at the end of the growth (at growth temperature and pressure) of each film is shown in the insets. 96

A.2 (a), (b), (c) RHEED patterns of $SrIrO_3$ films on $SrTiO_3$(001) substrates as a function of thickness for 4, 8, and 40 uc, respectively. The substrate and $SrIrO_3$ patterns for each thickness are shown at the growth temperature and partial O_2 pressure in the first 2 rows, and the $SrIrO_3$ films at room temperature and partial O_2 pressure are shown in the bottom row. As can be seen, the $SrIrO_3$ films are cubic at the growth temperature, but the 8 and 40 uc samples show extra peaks in between the pseudocubic diffraction peaks, indicating orthorhombic [001] domains along that direction. The 4 uc $SrIrO_3$ film is cubic in-plane, indicating a purely tetragonal symmetry is established at this thickness. 98

A.3 RHEED patterns of 20 uc $SrIrO_3$ films on (a) $SrTiO_3$(001) (b) $DyScO_3$(110) (c) $GdScO_3$(110) (d) $NdScO_3$(110) substrates. The substrate and $SrIrO_3$ patterns for each substrate are shown at the growth temperature and partial O_2 pressure in the first 2 rows, and the $SrIrO_3$ films at room temperature and partial O_2 pressure are shown in the bottom row. As can be seen in (a), the $SrIrO_3$ films show orthorhombic [001] domains along both in-plane directions (white arrows). Inspection of the $SrIrO_3$ RHEED patterns on the 3 scandates in (b), (c), (d) suggests the symmetry of the underlying orthorhombic substrates is preserved at room temperature. . . . 99

B.1 (a), (b) Integrated HAADF-STEM Sr column intensities for the (111) and (001) $SrIrO_3$/$SrTiO_3$heterostructures, respectively. The decrease in Sr intensity in the surface layers of the (111) $SrTiO_3$ is consistent with the COBRA resolved SrO_3^{-4} planar configuration shown in Figures 4.5 and 4.6. The increase of the background intensity in the SrIrO3 films in (a) and (b) is likely due to $SrIrO_3$ film degradation from the TEM prep. The decrease in electron number of the top $SrTiO_3$ layers in the (111) sample is due to incomplete coverage in these layers. 101

B.2 (a), (b) d-spacing as a function of distance normal to the surface of the (111) and (001) $SrTiO_3$/$SrIrO_3$/$SrTiO_3$ heterostructures, respectively. The origin on the x-axis denotes the position of the $SrIrO_3$ film/$SrTiO_3$ substrate interface. 102

B.3 (a), (b) Specular crystal truncation rod scans of the (111) and (001) $SrTiO_3$ substrates at 550 °C and 10^{-3} mbar, respectively, showing discernable midzone features and good agreement with the COBRA calculated CTRs. 103

C.1 Epitaxial structure and coherence of $SrIrO_3$ thin films from x-ray diffraction. a, $2\theta-\omega$ x-ray scan of 30 uc (12 nm) $SrIrO_3$ thin film on $SrTiO_3$(001) substrate showing single-phase $SrIrO_3$ with thickness oscillations indicating a smooth surface and sharp interface with the substrate. (b) ϕ-scan of the $SrIrO_3$ film showing its equivalent pseudocubic epitaxial arrangement with the underlying $SrTiO_3$ substrate. (c) reciprocal space mapping around the $(\bar{1}03)$ $SrTiO_3$ substrate peak confirming the fully coherent in-plane lattice of the $SrIrO_3$ film on the $SrTiO_3$ substrate. 105

C.2 Calculation of spin-Hall angle with ST-FMR lineshape and the calibration of microwave current. (a) Microwave power dependence of the symmetric and anti-symmetric components of the mixed voltage V_{mix} for a 3.5 nm Py/ 20 uc $SrIrO_3$ bilayer sample (20 μm 40 μm) at f = 5.5 GHz and $\phi = -135^{\circ}$ (b) Resistance R of the same device as a function of the external magnetic field angle ϕ. ΔR is fitted to $cos(2\phi)$ for extracting $dR/d\phi$. (c) Applied microwave power (red) and dc current (blue) induced device resistance change due to the Joule heating effect (d) Frequency dependent spin torque ratio of a 20 uc $SrIrO_3$ sample determined from ST-FMR line shape (red) and dc-tuned (blue) analysis. 109

C.3 Spin-torque ferromagnetic resonance (ST-FMR) in 3.5 nm Py/ 20 uc $SrIrO_3$ bilayer at different frequency f. (a) ST-FMR spectral for Py/$SrIrO_3$ sample at various f (4.5-6.5 GHz) and with the external magnetic field H_{ext} angle of 45° and -135°. Inset shows an optical image of the device layout and ST-FMR measurement circuit. b, Dependence of the frequency f on the resonance magnetic field HFMR. The data is fitted to the Kittel equation, which gives an effective magnetization of 0.85 T. (c) Frequency f dependence of the resonance linewidth W. The solid curve shows the fit to a linear function, which gives a Gilbert damping coefficient of 0.011. 110

C.4 ST-FMR measurements on an *ex-situ* Py deposition and a bare Py control sample (a) ST-FMR spectral for an in-situ (red) and an *ex-situ* (blue) deposited sample. The microwave power is fixed at 12 dBm at a frequency of f = 6 GHz. The external magnetic field Hext is oriented at an angle $\phi = 45^\circ$ with respect to the current axis (b) ST-FMR spectrum of a bare 10 nm Py control sample taken at $\phi = 45^\circ$ and f = 5.5 GHz. The microwave power is fixed at 12 dBm. 113

C.5 ST-FMR measurements on a Pt/Py control sample. (a) ST-FMR spectral for the 4 nm Pt/ 4 nm Py/$SrTiO_3$ sample with different applied I_{dc} at $\phi = -135^\circ$. The microwave power is fixed at 12 dBm and the frequency at 5.5 GHz. (b) The zoom-in view of the resonance peak shown in (a) (c) Resonance linewidth and effective magnetic damping as the functions of applied current and the corresponding current density in Pt for the Pt/Py. The solid lines represent linear fitting. (d) Spin torque ratio and the spin Hall conductivity of the Pt/Py bilayer measured at various microwave frequencies. 114

C.6 Transport and dc current faction of $SrIrO_3$ thin films. (a) Temperature dependence of the resistivity of the 20 uc $SrIrO_3$/$SrTiO_3$ sample with the current applied along both $SrTiO_3$ $[100]_c$ and $[010]_c$ directions. (b) $SrIrO_3$ room temperature resistivity and the current fraction of the 3.5 nm Py/$SrIrO_3$/$SrTiO_3$ with various $SrIrO_3$ thicknesses. 115

D.1 Momentum-resolved spin Hall conductivity $\Omega^a_{cb}(\mathbf{k})$ of the bulk system. As Fermi level arises, the distribution of $\Omega^a_{cb}(\mathbf{k})$ changes in accordance with the shape of fermi surface on the XURS plane of the Brillouin zone. 119

D.2 Directional dependence of the bulk spin Hall conductivity $\sigma^\rho_{\mu\nu}$. Depending on the configuration represented by ρ (spin polarization axis), μ (spin current direction), ν (charge current direction), the system shows a different pattern of spin Hall response. 119

D.3 n-glide and a $[110]_o$ slab of $SrIrO_3$. The yellow arrow and pink plane represent the translation vector $\frac{a+c}{2}$ and reflection plane (perpendicular to the b axis) composing the n-glide. 121

List of Tables

1.1 Goldschmidt tolerance factors for Perovskites. 3

1.2 Lattice parameters and symmetries of bulk $SrIrO_3$ polymorphs. 14

2.1 Lattices of assorted perovskite substrates and their lattice mismatch with $SrIrO_3$. . . 42

D.1 Non-symmorphic symmetries in bulk $SrIrO_3$. (*) denotes symmetries broken in the $[110]_o$ film slab. 120

Chapter 1

Introduction

1.1 ABO_3 perovskites

Progress in the design and synthesis of artificial oxide heterostructures, particularly ABO_3 perovskites (Figure 1.1 using VESTA[2]), has led to the realization of metastable material properties, particularly at the interfaces of these heterostructures[3–5]. The richness of the observed phenomena in these perovskites, such as high Tc superconductivity, ferroelectricity, and 2-dimensional electron gases are due to the strong crystal field effects, electron-electron interactions, and electron-phonon coupling contributions to the electronic band structure[6], making these materials much more complicated than conventional electronic materials. As I will discuss later in this chapter, oxides with heavier transition metal ingredients are a current hot topic due to the strong spin-orbit coupling present in their band structure. Such materials like perovskite $SrIrO_3$ have thus attracted attention after predictions that they may be prime material candidates for the creation and study of interesting, yet-undiscovered phases of matter.

Perovskites derive their name from the mineral $CaTiO_3$, which was first discovered in 1839 near the Ural mountains by Gustav Rose and is named after the Russian mineralogist Lev Alekseevich Perovski (1792-1856). The perovskite structure was first quantitatively proposed by Goldschmidt in 1926[7] and then experimentally confirmed for the case of $BaTiO_3$ by Megaw in 1946[8], the latter of which opened up the field of perovskite piezoelectrics. Next, in 1950, colossal magnetore-

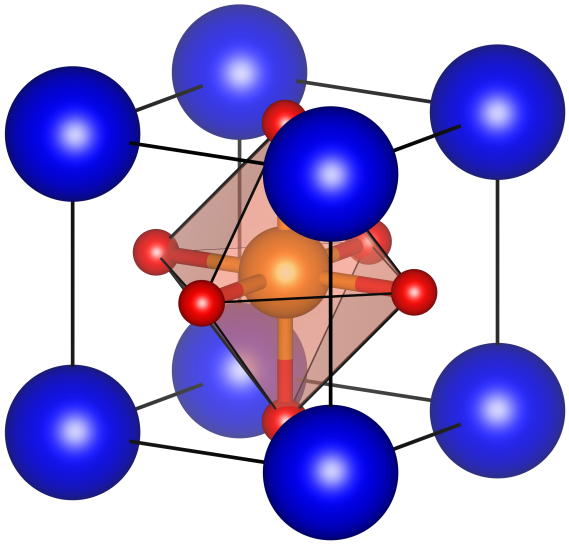


Figure 1.1: Simple cubic ABO_3 perovskite, with the A atom on the corner unit cell site, B atom in the center, and oxygen atoms on the faces.

sistance was found in manganate perovskites[9], and from there, giant magnetoresistance[10] in the 1960s. The next major discovery came in the 1980s and 1990s when high-T_C superconductivity was discovered in doped CuO_2-based layered perovskites[11,12]. The early 2000s brought about the surprise findings in metastable thin films of a 2-dimensional electron gas between the band insulators $LaAlO_3$ and $SrTiO_3$[13] and large multiferroic behavior[14]. More recently, perovskites that are metallic while simultaneously exhibiting electrically polar behavior were predicted and discovered[15–17]. As many of these recent findings arise in thin films, an important outlook in the perovskite community is increasingly tending towards the realization of diverse and metastable structures and properties that do not exist in conventional bulk materials.

While the strict perovksite crystal structure is ABX_3, where X can take H, O, F, S, Cl, Se, and Br atoms, the majority of perovskite compounds are oxide-based. As can be seen in Figure 1.2, there are scores of possible known stable perovskite materials because of large flexibility of elements that can occupy the A and B cation sites[3]. The stability of of these elements in the perovskite structure can be quantified by the Goldschmidt tolerance factor[7], which is given by:

$$t = \frac{r_A + r_O}{\sqrt{2}(r_B + r_O)} \tag{1.1}$$

Table 1.1: Goldschmidt tolerance factors for Perovskites.

Tolerance Factor	Cation Size	Likely Symmetry
>1	(1) A cation too big (2) B cation too small	Hexagonal
0.9-1	Ideal A and B cation size	Cubic
0.71-0.9	A cations are too small for B cation site	Tetragonal, Orthorhombic, or Rhombohedral
0.71<	A and B cations have similar radii	Various structures

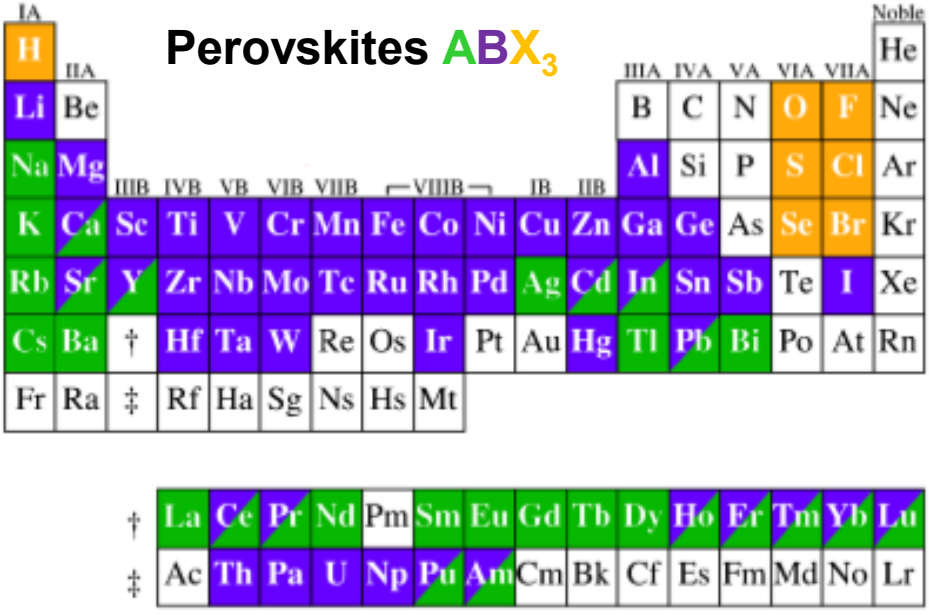


Figure 1.2: Periodic table showing elementally compatible perovskite constituents. Reproduced and adapted from Schlom *et al.*, 2008, with permission from the Journal of the American Ceramic Society.

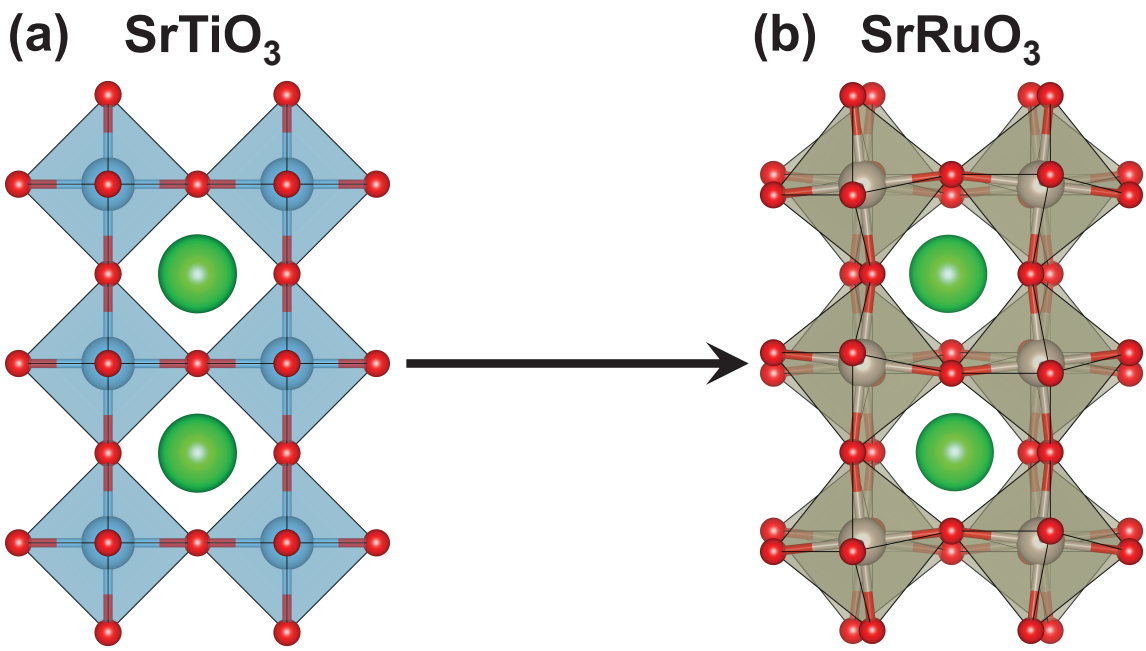


Figure 1.3: (a) Simple cubic $SrTiO_3$ structure showing no distortions of the TiO_6 (b) orthorhombic $SrRuO_3$ structure showing RuO_6 tilts and rotations.

Here, r_A, r_A, and r_O are the radii of the A, B, and O atoms, respectively. Thus, the tolerance factor t is determined from the size of the individual components of the perovskite. Furthermore, once the stability is established, the value of the tolerance factor determines the symmetry of the perovskite. For example, the $SrTiO_3$ crystal in Figure 1.3(a) exhibits a simple cubic symmetry like the perovskite depicted in Figure 1.1 due to the optimal relative sizes of the Sr and Ti atoms. This perovskite has a tolerance factor of 1. Non-unity tolerance factors generally denote lower-symmetry crystal structures, such as tetragonal, orthorhombic, rhombohedral, etc. General trends for this tolerance factor are summarized in Table 1.1. Perhaps the simplest example of a lower-symmetry perovskite would be to replace the Ti atom in $SrTiO_3$ for Ru, which yields $SrRuO_3$: an orthorhombic perovskite, where the unit cell is doubled along the c-axis [Figure 1.3(b)]. This unit cell doubling is due to the atoms exerting coulombic forces that cause the nominally non-rigid BO_6 octahedra to tilt and rotate along certain axes of the unit cell. This distortion can be classified using the notation developed by Glazer that describes the nature of the tilts and rotations along the orthogonal directions of the crystal[18]. As one could imagine, these structural distortions impact the orbital configuration of the material by changing equilibrium bond-lengths and angles, which

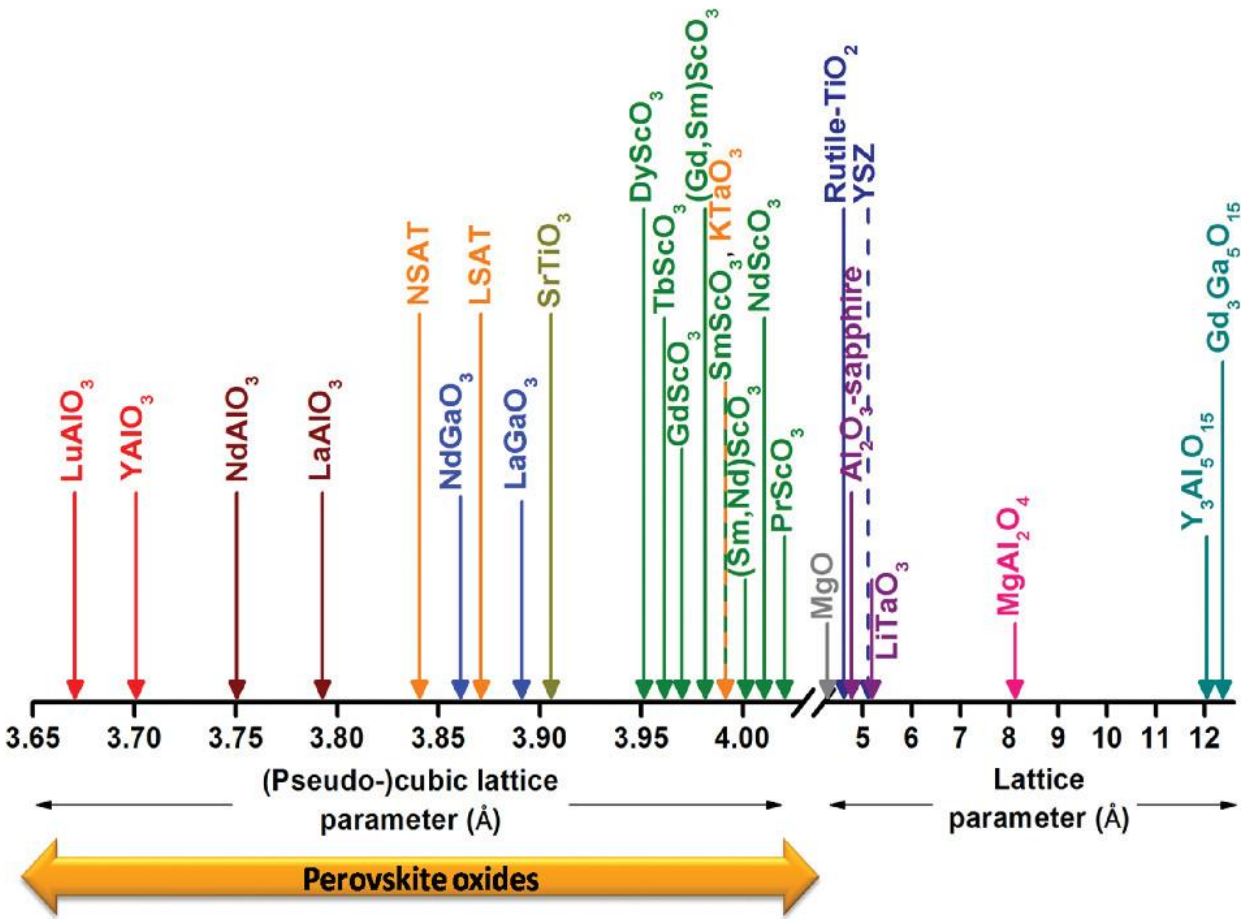


Figure 1.4: Pseudocubic lattice parameters of the most common ABO_3 perovskite and related oxide substrates. Reproduced from Langenberg, *et al.* 2016 with permission from APL Materials.

affects orbital overlap between atomic constituents. These distortions are particularly important in instances when the material is under epitaxial strain, which can further alter this octahedral configuration and, therefore, the electronic structure[19]. However, since the typical distorted perovskite still shows close to simple cubic symmetry, particularly in the case of epitaxial thin films, I will often refer to the pseudocubic lattice of these lower symmetry ABO_3 perovskites[20]. A more detailed discussion of octahedral tilt systems and pseudocubic film arrangement on perovskite substrates will be presented in the next chapter when I discuss structural studies of orthorhombic $SrIrO_3$ on cubic $SrTiO_3$ substrates.

Given their diverse elemental compatibility, the perovskites are quite structurally similar, taking lattice parameters and chemistry that allow broad possibilities to incorporate different per-

ovskites into interfaces. A sampling of the lattice parameters of common perovskites is shown in Figure 1.4. The similar structural preference of these materials increases the likelihood of achieving high-quality single-crystal interfaces through thin film epitaxy, a critical baseline for studying intrinsic material properties without the influence of extrinsic effects such as point defects, grain-boundaries, and chemical intermixing between layers. This opens up countless possibilities to create a host of different interfaces to create and manipulate the previously-mentioned phenomena predicted and observed in perovskites. Additionally, many of these substrates such as $LaAlO_3$, $(LaAlO_3)_{0.3}$-$(Sr_2AlTaO_6)_{0.7}$ (LSAT), $NdGaO_3$, $SrTiO_3$, $DyScO_3$, $GdScO_3$, and $NdScO_3$ have become increasingly easier to purchase commercially, which is critical for the long-term feasibility of perovskites to be competitive with conventional electronics materials like Si and GaAs. On this point, it has also been demonstrated that $SrTiO_3$, the most commonly-used perovskite substrate, can be epitaxially stabilized on silicon[21], subsequently allowing the potential incorporation of perovskites and their rich physical properties on the commercially-dominant substrates[22].

1.2 Correlated *d*-orbital electrons

The significant elemental compatibility of perovskites also allows enormous flexibility to engineer the *d*-shell electron filling of the B-site atom (usually a transition-metal), which couples with the 2*p* bands from oxygen atoms on the unit cell face to form an BO_6 octahedra (shown back in Figure 1.1). Historically, the study of ABO_3 perovskites has mainly focused on materials with 3*d* B-site transition-metals. Such perovskites include the titanates, cuprates, mangenates, and cobaltates. In conventional semiconductor band theory, these electron correlations are ignored, which is a reasonable approximation for semiconductors due to the absence of valence *d*-bands. However, with the introduction of *d*-electrons to materials like ABO_3 perovskites, bands become localized or charge can be transfered between bands as a result of the prevously-discussed crystal field splitting, creating a hybridized band structure not predicted by semiconductor band-theory that results in phenomena such as high-T_c superconductivity, metal-insulator transitions, ferrelectricity, ferromagnetism, and various multiferroic behavior in ABO_3 perovskites[6]. As the *d*-shells become larger with the introduction of even heavier metals, the narrow bandwidth typical of the 3*d* perovskites

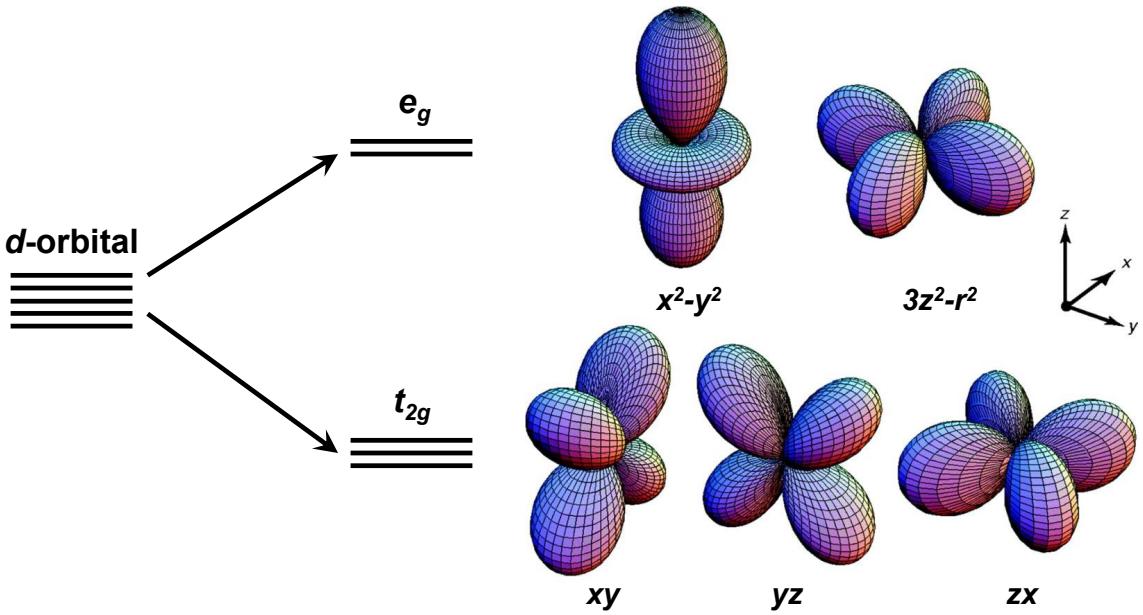


Figure 1.5: *d*-shell degeneracy lifted as a result of *d*-*p* orbital coupling between transition-metals and oxygen in perovskites. Reproduced and adapted from Tokura and and Nagaosa 2000 with permission from Science.

broadens as a result of weaker electron correlations, and the materials generally become more metallic. The canonical example of this is the 4*d* perovksite $SrRuO_3$, which is most commonly used as an electrode due to its metallic behavior and high-quality epitaxy on $SrTiO_3$.

From an electronic orbital viewpoint, the transition-metals as free atoms exhibit a *d*-band orbital degeneracy comprised of x^2-y^2, $3z^2$-r^2, *xy*, *yz*, and *zx* orbitals for a maximum electron occupancy of 10. Because the and $3z^2$-r^2 orbitals point directly at their nearest orbital neighbors, the 2*p* bands from the oxygen atoms on the faces of the unit cell [Figure 1.1], the electrons in these orbitals experience a greater coulombic repulsion. Thus, this resultant crystal field separates these bands from their previously degenerate *xy*, *yz*, and *zx* orbitals, which are not directly on axis with any of their nearest neighbors[23]. The resulting band-splitting forms two bands, the e_g comprised of the former two orbitals, and the t_{2g}, comprised of the latter three, as shown in Figure 1.5. As more flavors such as strain, symmetry, structure distortion, chemical doping, and spin-orbit coupling are added, these bands can be modified further. In general, the coupling between these *d*-bands of the transition-metal and the *p*-bands of the oxygen provides vast freedom to manipulate electron spin ordering, orbital configuration, and charge-transfer between atoms and interfaces. The proposed

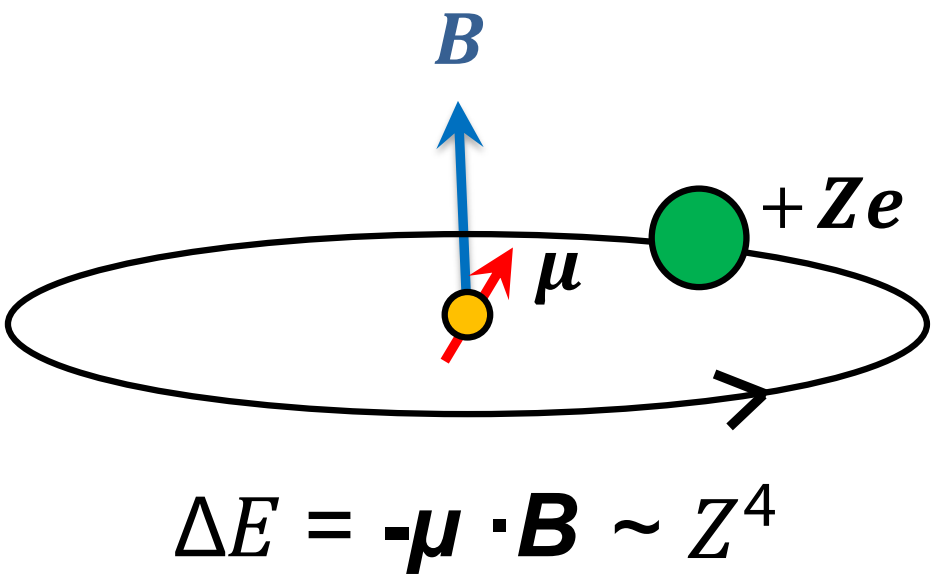


Figure 1.6: Simple cartoon of relativistic electron spin-orbit coupling with the host atom.

band splitting in $SrIrO_3$ will be discussed later in this chapter.

1.3 Strong spin-orbit coupling in 5*d* perovskites

More recently, there has been a push to synthesize ABO_3 perovskites that contain 5*d* transition metals to add the flavor of strong spin-orbit coupling. This contrasts their 3*d* and 4*d* cousins, where this spin-orbit interaction is relatively weak. Spin-orbit coupling can be naively described by considering the schematic in Figure 1.6. If a single electron orbits a charged nucleus of atomic number *Z*, its spin μ feels a magnetic field *B* that arises from the orbiting charge of the atom. This magnetic perturbation from the host atom can shift the electron's energy state, depending on the orientation of the electron's spin. The magnitude of the shift can be derived by considering the electron frame of reference using relativistic quantum mechanics to be proportional to Z^4. Thus, electrons from heavier elements experience a larger magnetic field, and hence a greater spin-orbit coupling. This energy shift implies that electrons in these heavy *d* orbitals experience a lifting of orbital degeneracy, which can lock spin and orbital momentum in a particular orbital. Thus, spin-orbit coupling could be thought of as an intrinsic Zeemann effect. Spin-orbit coupling is particularly important in heavy 5*d* ABO_3 perovskites, as the spin-orbit interaction in on the

same energy scale as the electron correlations, which further modifies the already correlated band structure. The nature of these modifications is still a matter of debate, particularly the interplay between the strong-spin orbit interactions and the electron correlations.

Moreover, the existence of these stronger spin-orbit interactions at interfaces and reduced dimensions can unlock Rashba splitting, topologically-protected surface states, and Dzyaloshinskii-Moriya interactions[24,25]. These dimensional physical effects can then allow efficient charge-to-spin conversion, stabilize graphene-like Dirac band structures, and create complicated chiral spin textures and interactions [Figure 1.7]. Of particular interest to this work is the creation of strong spin-torques, which can result from interfacial Rashba-Edelstein effect or the spin Hall effect. The latter of the two cases and the subsequent spin-current interaction with magnetic moment of adjacent ferromagnets will be further discussed in Chapter 5.

While the majority of mature commercial electronics ignore the parameter of electron spin, unlocking spin as a degree of freedom can allow the manipulation of electronic devices with spin or vice-versa, eliminating the need for an externally-applied field. Furthermore, another great advantage related to spin control and manipulation lies in the trend towards the small dimensions of modern devices, which continue to shrink in accordance with Moore's Law. These device sizes are approaching quantum material limits, which induce the very size effects at which electron-spin interactions become significant. The incorporation of materials with these spin-related phenomena into next-generation devices has the potential to promote important advances in relatively immature technologies such as Magneto-resistive Random Access Memory (MRAM), spin logic, and spin batteries, which are all subsets of the general field of spintronics[26]. The grand challenge of achieving the advanced engineering of electronic spin states is identifying the promising material candidates and obtaining a high-quality material with excellent performance by selective control of the interfacial structure and its resulting properties.

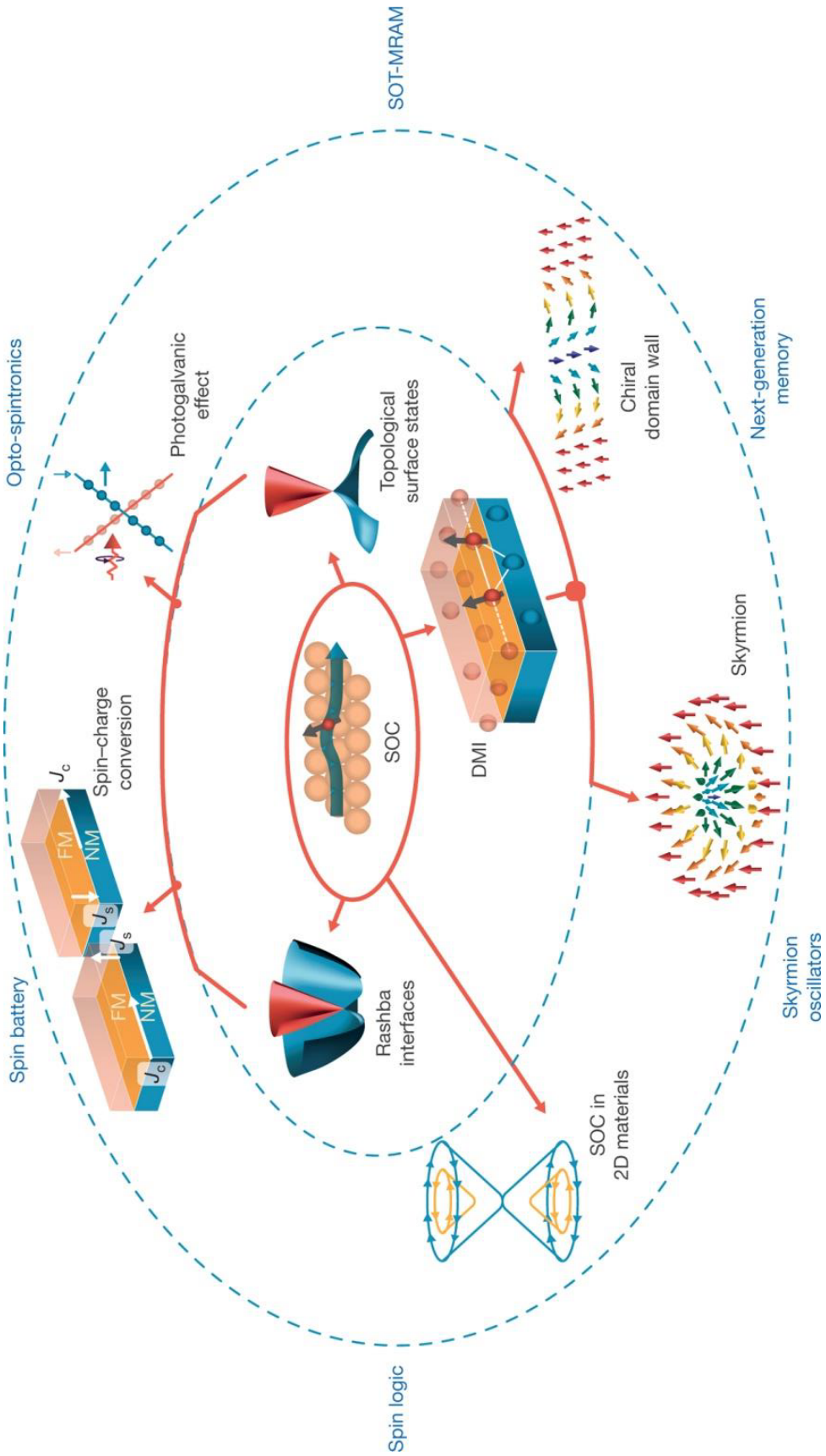


Figure 1.7: Schematic showing the possible physical phenomena that can occur at interfaces with the presence of strong spin-orbit interactions (inner circles), which can lead to effects relevant to spintronics applications (outer circle). Reproduced from Soumyanarayanan, *et al.* 2016 with permission from the Nature Publishing Group.

1.4 Ruddlesden-Popper $Sr_{n+1}Ir_nO_{3n+1}$ iridates

Along this motif of creating interfaces with stronger spin-orbit coupling, iridates of pyrochlore $A_2Ir_2O_7$, honeycomb A_2IrO_3, and Ruddlesden-Popper $Sr_{n+1}Ir_nO_{3n+1}$ phases have been proposed as ideal material systems for the study of spin liquids, topological states, and spin-orbit coupled Mott insulators due to the diverse and material-dependent interplay[27] between crystal structure, electron correlations, and strong spin-orbit coupling. Of particular interest to this work are the Ruddlesden-Popper (RP) iridates of $Sr_{n+1}Ir_nO_{3n+1}$ [28–31] (n = integer), which show a dramatic change in electronic behavior from Mott-insulating in Sr_2IrO_4, to barely insulating in $Sr_3Ir_2O_7$, and finally to metallic in the $n = \infty$ case of perovskite $SrIrO_3$, which is metallic. This change is believed to be a result of the the progressively widening orbital bandwith as the IrO_2 networking increases with n[28,32,33]. This is shown in Figure 1.8(a), where the RP-phase structure is presented. For simplicity, non-distorted RP-phase structures are depicted. As can be seen, the $A_{n+1}B_nO_{3n+1}$ family consists of 2D layered ABO_3 networks that are offset from the adjacent network by $(\frac{1}{2}, \frac{1}{2}, \frac{1}{2})$ with a SrO layer separating each offset network. Increasing n from 1 to 2 doubles the BO_6 stacking within the unit cell. It is thus evident that the stacking of BO_6 octahedra within a given network increases with n until $n = \infty$ when the simple perovskite structure is globally established, and the BO_6 stacking is infinite in all directions. The widening bandwidth from this increasing BO_6 stacking in the $Sr_{n+1}Ir_nO_{3n+1}$ family is the previously-mentioned t_{2g} d-orbital structure, which is illustrated in Figure 1.8(b). As with 3d perovskites (Figure 1.5), the d-band degeneracy in 5d perovskites is lifted due to the crystal field interactions from the BO_6 octahedra. However, in addition to the crystal field splitting, the presence of strong spin-orbit coupling in the RP-iridates is believed to further lift the degeneracy of the t_{2g} orbitals into effective angular momentum bands, $J_{3/2}$ and $J_{1/2}$. Thus, within the same family of material, drastically different electronic properties can be engineered by changing the perovskite structural layering.

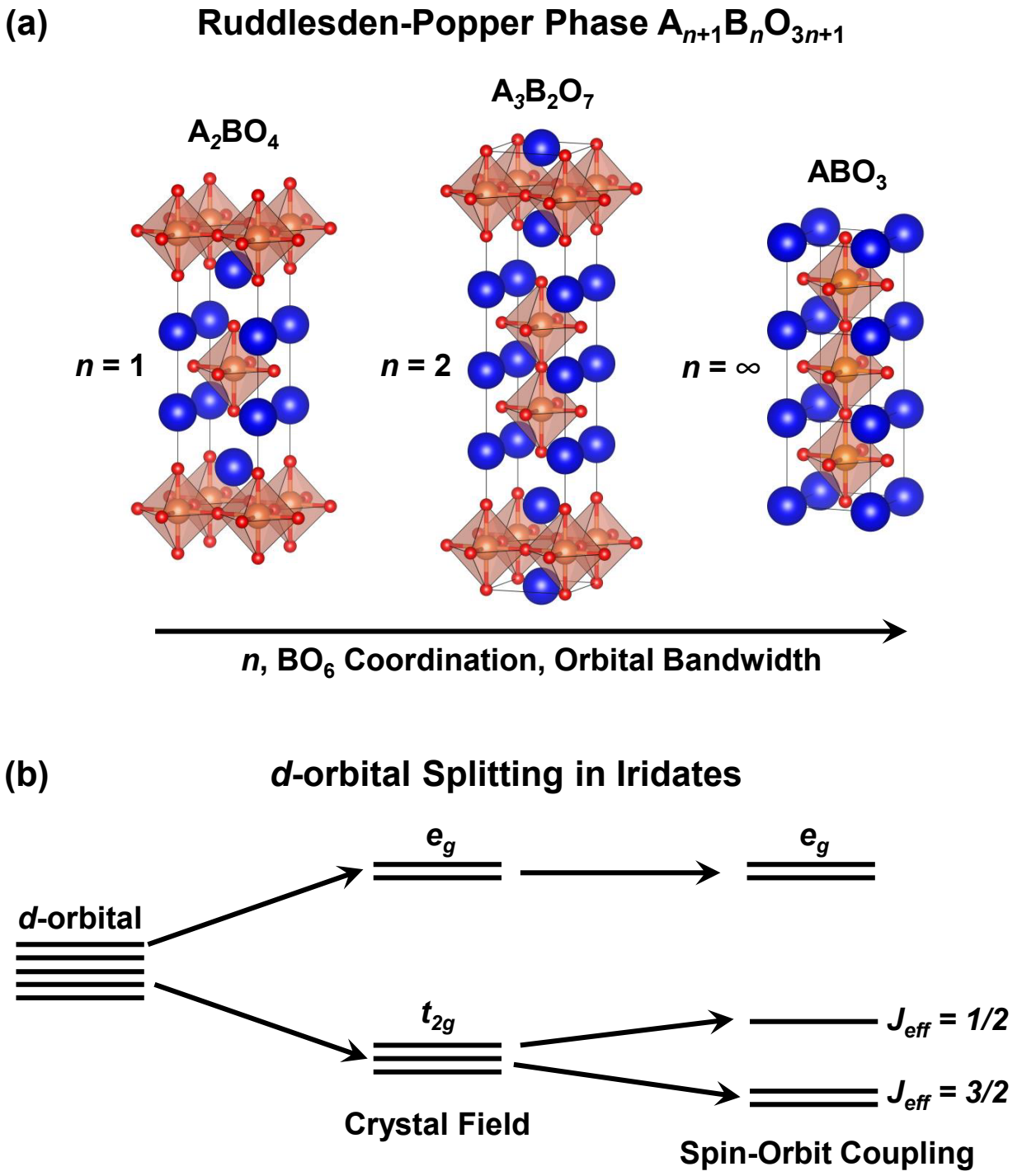


Figure 1.8: (a) General Ruddlesden-Popper phase $A_{n+1}B_nO_{3n+1}$ layered perovskites showing increasing BO_6 stacking with n (b) d-orbital splitting in iridates with strong spin-orbit coupling showing the creation of the 3/2 and 1/2 effective momentum bands.

1.5 Metastable-phase perovskite $SrIrO_3$

Of these RP-phase Sr-Ir perovskites, the $n = \infty$ case of $SrIrO_3$ has attracted significant attention due to theory predictions that it exhibits topologically-protected states[34–36] and a non-zero Chern number[31]. Apart from these band topology predictions, $SrIrO_3$ has also been shown to be a promising material for oxygen catalysis[37] and thermoelectrics[38]. However, the equilibrium crystal structure of $SrIrO_3$ presents a challenge to the study of intrinsic single-crystal properties. In bulk[39], $SrIrO_3$ assumes a monoclinic structure of space group *C2/c* (a = 5.604 Å, b = 9.62 Å, c = 14.17 Å, = 93.65°) that is energetically favorable at room temperature and atmospheric pressure. However, a perovskite orthorhombic structure (a = 5.60 Å, b = 5.58 Å, c = 7.89 Å) of space group Pbnm is stable at high temperature and pressure. It is helpful to redefine this orthorhombic unit cell as a pseudocubic cell[20] with a lattice parameter of 3.95 Å that is close to those of conventional perovskites like $SrTiO_3$(3.905 Å). This similar structural relationship prompted epitaxial synthesis of $SrIrO_3$ on perovskite (001)-oriented single-crystal substrates such as LSAT, $SrTiO_3$, $DyScO_3$, $GdScO_3$, and $NdScO_3$ in single-layer films[40–43], and superlattices[44] by molecular beam epitaxy (MBE), pulsed laser deposition (PLD), and sputtering. These thin films studies of $SrIrO_3$ are critical, since bulk synthesis has yielded polycrystalline samples[38,39,45–47], which adds contributions to the material behavior from extrinsic sources such as grain boundaries and point defects that are difficult to decouple from the true intrinsic behavior. Thus, thin films are generally recognized as the gateway to truly intrinsic perovskite $SrIrO_3$ study.

Bulk $SrIrO_3$ is characterized as a metal, with the polycrystalline bulk studies reporting resistivity values on the order of 1-10 mΩ-cm, which places it between good conductors and typical semiconductors. Positive magnetoresistance with decreasing temperature was reported by three of these studies, and the current thinking is that bulk $SrIrO_3$ is paramagnetic at lower temperatures with the possible existence of a Dirac semimetallic state[45,47]. However, since the bulk samples are polycrystalline and thus likely contain extrinsic contributions from grain-boundaries and crystallographic texturing, little is known about the completely intrinsic bulk transport properties of $SrIrO_3$. A number of studies have used thin films to examine the transport characteristics. While the $SrIrO_3$

Table 1.2: Lattice parameters and symmetries of bulk $SrIrO_3$ polymorphs.

Crystal Symmetry	Space Group	Lattice Parameters (Å)	b (Å)	c (Å)	
Monoclinic	*C2/c*	5.604	9.62	14.17	$\alpha = \gamma = 90°, \beta = 93.26°$
Orthorhombic	*Pbmn*	5.58	5.60	7.89	$\alpha = \beta = \gamma = 90°$

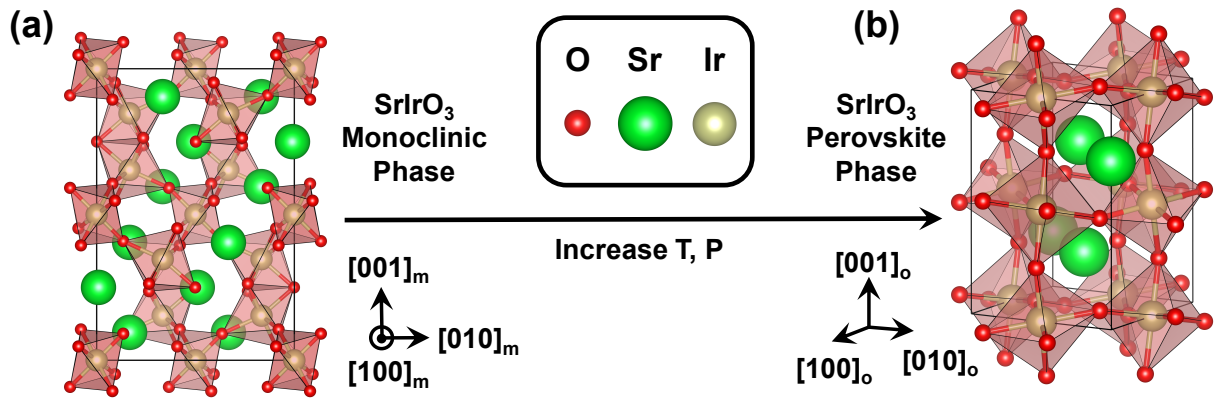


Figure 1.9: Bulk structures of (a) ambient monoclinic and (b) high temperature/pressure orthorhombic $SrIrO_3$.

thin films are also nominally metallic like the bulk, metal-insulator transitions have been reported as a result of disorder[48,49] and and strain[41,50,51].

Since the transport properties of bulk and thin film $SrIrO_3$ show variation, it should be no surprise that the band structure is also controversial. While the previously-discussed dimensionality-controlled bandwidth of the $Sr_{n+1}Ir_nO_{3n+1}$ family has traditionally been accepted as the explanation behind the metal-insulator transition with decreasing n, it has been shown by angular resolved photoemission spectroscopy (ARPES) that $SrIrO_3$ films on (001) LSAT substrates show narrow than expected bands[42], which are narrower than those reported for Sr_2IrO_4[28]. Thus, the simple J_{eff} band structure picture of $SrIrO_3$ may not fully explain the whole story of strained $SrIrO_3$, as it has been shown that these bands can overlap[52].

Moreover, while prediction of creating of topologically-protected states remains the grand thrust in the community regarding $SrIrO_3$, it has been shown both directly by ARPES[52] and indirectly by structurally-refined *ab initio* calculations[53], however, that the Dirac nodes in are actually

lifted by strain when epitaxially stabilized on perovskite substrates, suppressing the topological state. From the previously-discussed bulk work, it may be that the topological states may require an as-of-yet unreported bulk single-crystal synthesis, given the apparent sensitivity of the $SrIrO_3$ band structure to epitaxial strain. As evidenced by theory work, the interaction of electron correlations with the spin-orbit coupling may be more complicated than originally thought[54–56]. The added complication of strain in epitaxial thin films to this interplay thus presents a challenge to fully these complicated 5*d* perovskites. However, since bulk $SrIrO_3$ exhibits a Dirac semimetal character, effort on the topological insulator front continues.

While bare film or bilayer heterostructures have been the focus of the $SrIrO_3$ transport and band structure studies, the majority of superlattice work with $SrIrO_3$ has been used to investigate magnetic coupling at interfaces with other perovskites. While bulk $SrIrO_3$ is nominally paramagnetic[45], when layered as an ultra-thin film with other ABO_3 materials, $SrIrO_3$ has been reported to have a canted magnetic moment when interfaced with $SrTiO_3$ layers[44,57] that can tune the electronic structure, used to change the magnetic easy axis of an overlaid ferromagnetic $La_{2/3}Sr_{1/3}MnO_3$ from $[110]_{pc}$ to $[001]_{pc}$[58], exhibited interfacial charge transfer with $SrMnO_3$ that produces magnetism[59,60], and also an observation of the topological Hall effect at the interface between $SrIrO_3$ and $SrRuO_3$[61]. Thus, it has been shown that $SrIrO_3$ can be used to engineer magnetic functionality in superlattices while itself seemingly lacking any concrete magnetic ordering.

1.6 Conclusions

To conclude this chapter, I have discussed the flexibility, both chemical and structural, of ABO_3 perovskites. This class of materials hosts a variety of behavior due the strongly correlated electronic state that depends on the delicate interplay between crystal structure, electron-electron interactions, and, in the case of perovskites with heavier atomic constituents, spin-orbit coupling. The latter of these becomes particularly relevant at interfaces or in reduced dimensions, which can unlock further manipulation of the electron spin. Finally, we have motivated the study of the perovskite $SrIrO_3$ and discussed its structural and physical properties, the difficulty of its single-crystal bulk synthesis, and need for high-quality single-crystal thin films for the study of intrinsic material

behavior. In the next chapter, I will discuss the methods used to synthesize and characterize the $SrIrO_3$ films in this thesis and the growth behavior and domain structure therein.

Chapter 2

Synthesis and characterization of ABO_3 thin films

2.1 Epitaxy

Epitaxy is a Greek word with roots meaning "being on or supported upon" (*epi*) and "in an orderly manner" (*taxis*)[62]. In the scope of thin film deposition it can be understood as single-domain crystalline arrangement of an overlayed material (film) on an underlying single-crystal template (substrate). Since the development of molecular beam epitaxy as a means to synthesis single-crystal semiconductor heterostructures, the importance of epitaxial film growth has become paramount in the processing of solid state microelectronics. This section will give a very brief introduction to thin film growth, but a more detailed discussion that I draw on heavily here can be found elsewhere[63].

As a basic starting point, thin film growth can described by thermodynamics: in particular, the relative free energy change required to form the film layer on the initial surface of the substrate. In this model, there are 3 growth modes, shown in Figure 2.1. If the film wetting on itself rather than on the substrate lowers the free energy of the surface, the film atoms tend to coalesce in islands, and completely 3D island growth ensues (Wolmer-Weber), shown in Figure 2.1(a). On the other hand, if the free energy is lowered when the film wets on the substrate, 2D layer-by-layer growth

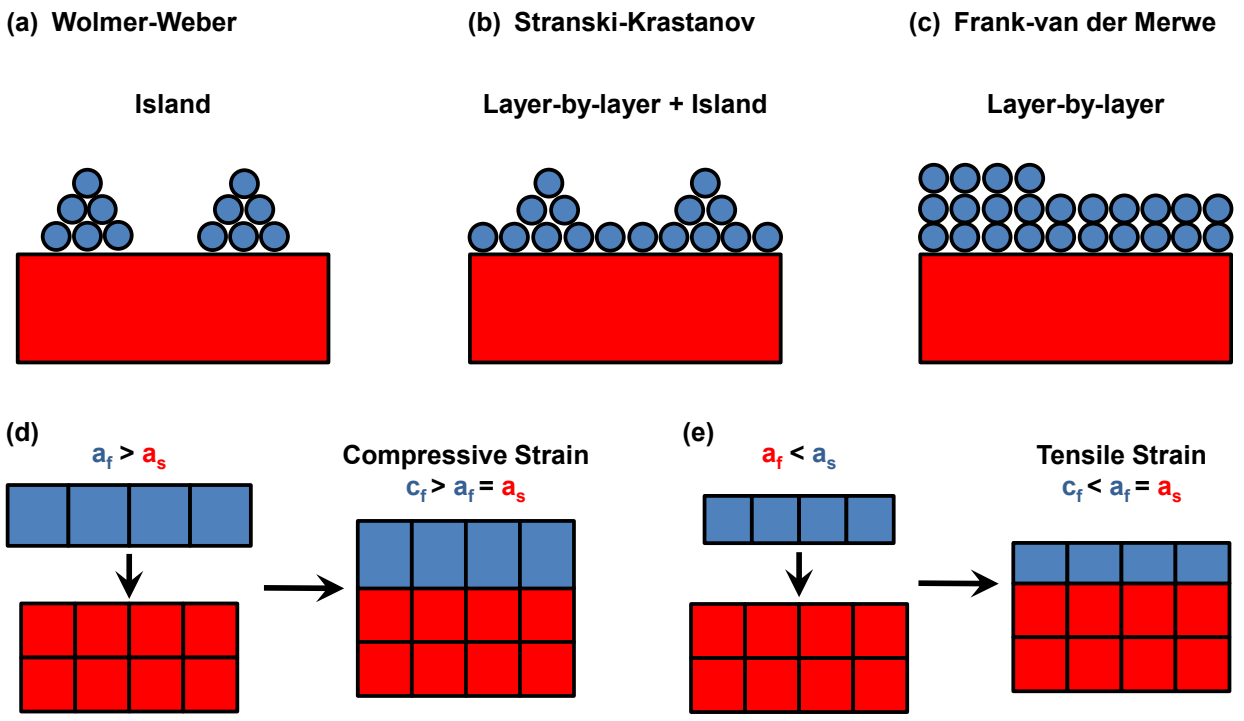


Figure 2.1: (a), (b), (c) 3 basic growth modes of thin films, Wolmer-Weber, Stranski-Krastanov, and Frank van der Merwe, respectively (d), (e) Epitaxial strain of thin films in the case of in-plane compressive and tensile strain, respectively.

is preferable (Frank-van der Merwe), shown in Figure 2.1(c), where single atomic layers nucleate out on the surface to form a complete layer. The intermediate case between these two extremes is layer-by-layer film growth for the initial atomic layers followed by 3D island nucleation on top of the preliminary 2D layers (Stranski-Krastanov), shown in Figure 2.1(b).

In reality, however, thin film epitaxy is a non-equilibrium process due to the dependence on the deposition of adatom flux and absorption, chemical bonding, surface diffusion and nucleation, and interfacial interdiffusion. Therefore, thermodynamics is ultimately insufficient to fully describe the mechanisms of thin film growth in most synthesis methods. Thus, a kinetics approach must also be considered to account for dynamic behavior of deposited species[64]. Because the surface of each substrate will be cut along a finite miscut angle (see the next section), adatom diffusion on the sample surface will particularly influence the growth mode, as these atoms will tend to diffuse across the terraced steps that result from the miscut. These atoms will tend to diffuse to the step edge and the resulting 2D growth mode will be referred to as ”step-flow” mode. The preference of

a 2D film to grow step-flow over layer-by-layer will depend on the length of the steps (dependent on the miscut angle) and the diffusion length of the surface adatoms. Therefore, regardless of the model, the chemistry and surface of the substrate is expected to strongly influence the initial epitaxy.

Epitaxy in which the film and substrate materials are identical is referred to as *homoepitaxy*, and *heteroepitaxy* when they are not. In the case of heteroepitaxy, epitaxial strain becomes an important consideration for both the synthesis of the film and its subsequent properties. The amount of strain can be defined as a percentage:

$$f = \frac{a_s - a_f}{a_s} \times 100 \tag{2.1}$$

Here, a_f and a_f are the lattice constants of the film and substrate, respectively. If the film lattice constant is larger than than the film as shown in Figure 2.1 (d), the film is strained compressively in-plane, decreasing the in-plane lattice constant to be commensurate with the substrate. As a consequence, the out-of-plane lattice constant will then elongate. Alternatively, if the film lattice constant is smaller, the opposite scenario occurs, which is depicted in Figure 2.1 (e). It should be noted that volume will not necessarily be conserved, depending on the elastic modulus of the film material. As the film thickness increases, the energy from the epitaxial strain will cause misfit dislocations and surface roughening in the film. Eventually, at some critical thickness (material dependent), the lattice will typically relax, returning to its bulk unit cell volume.

2.2 ABO_3 perovskite substrates

Given the sensitivity of initial film deposition on the substrate, careful consideration of the substrate surface is critical. As will be further discussed in Chapters 3 and 4, the pseudocubic (abbreviated henceforth as ”pc”) planar layering of ABO_3 perovskites in the [001] direction consists of alternating AO and BO_2 layers (or AO_3 and B in the case of the [111] direction). Typically, as-received substrates from commercial vendors exhibit a mixed surface termination of these A and B cation planes that is a result of an unavoidable miscut angle between the mechanical blade and the targeted crystal direction. It is hopefully no surprise to the reader that single atomic termination is an important pre-requisite for the growth of atomically smooth epitaxial thin films. In case of $SrRuO_3$

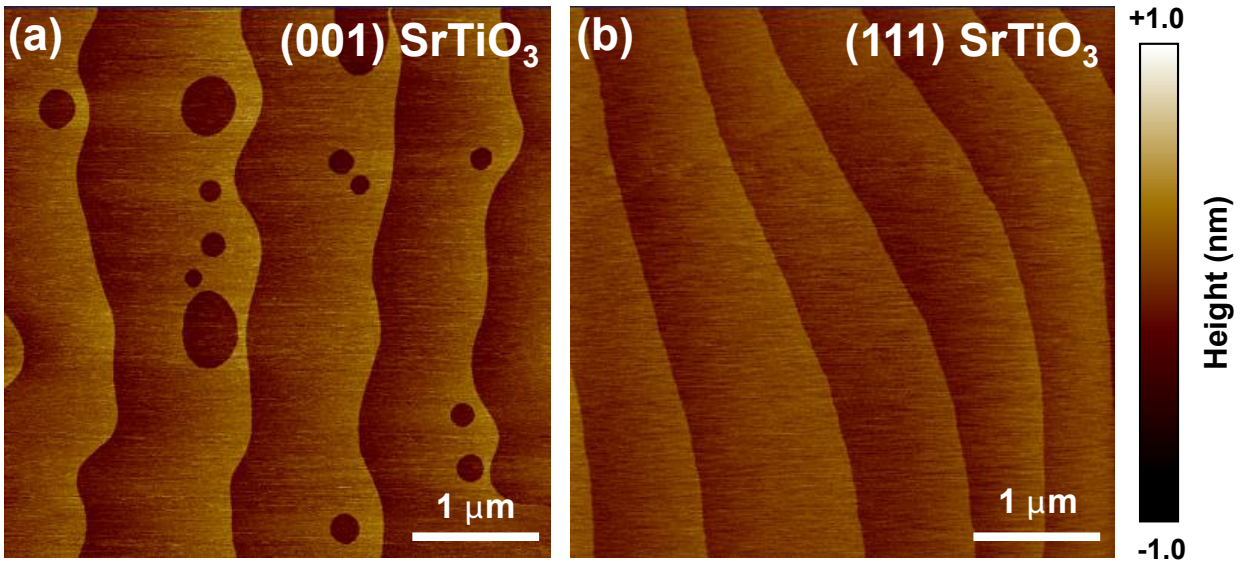


Figure 2.2: Surfaces of (a) (001) $SrTiO_3$ (b) (111) $SrTiO_3$ showing preservation step-terrace formation from chemical and thermal treatment.

films alone, it has been shown that controlled engineering of the substrate surface termination can produce a variety of different $SrRuO_3$ surfaces, including a smooth 2D film[65], self-assembled nanostripes[66], and nanodots[67]. Thus, the controlled, reproducible chemical and thermal treatment of the as-received substrate surface is a critical preliminary step for achieving high-quality epitaxy in ABO_3 perovskite thin films.

Among the commercially common ABO_3 perovskite substrates, the treatments of $SrTiO_3$[68–72], $NdGaO_3$ and $LaAlO_3$[71] are the most mature, yielding 100% (or close to 100%) single-termination. Less established is the preparation of single-termination $(LaAlO_3)_{0.3}$-$(Sr_2AlTaO_6)_{0.7}$ (LSAT), which remains challenging[67,73], likely due to its relatively complicated elemental composition compared to non-composite ABO_3 perovskite substrates. Most recently, there has been a push to achieve single-termination on rare-earth scandate (e.g., $DyScO_3$, $GdScO_3$, etc) surfaces[74], but these reports are rare, and $SrTiO_3$ thus remains the substrate of choice in the ABO_3 perovskite synthesis community.

Based on these earlier studies, the (001) and (111) $SrTiO_3$ substrates in this work were chemically and thermally treated using a combination of buffered hydrofluoric (BHF) acid solution etching and thermal annealed at 900-1000 °C in an O_2-rich atmostphere to obtain a TiO_2-terminated

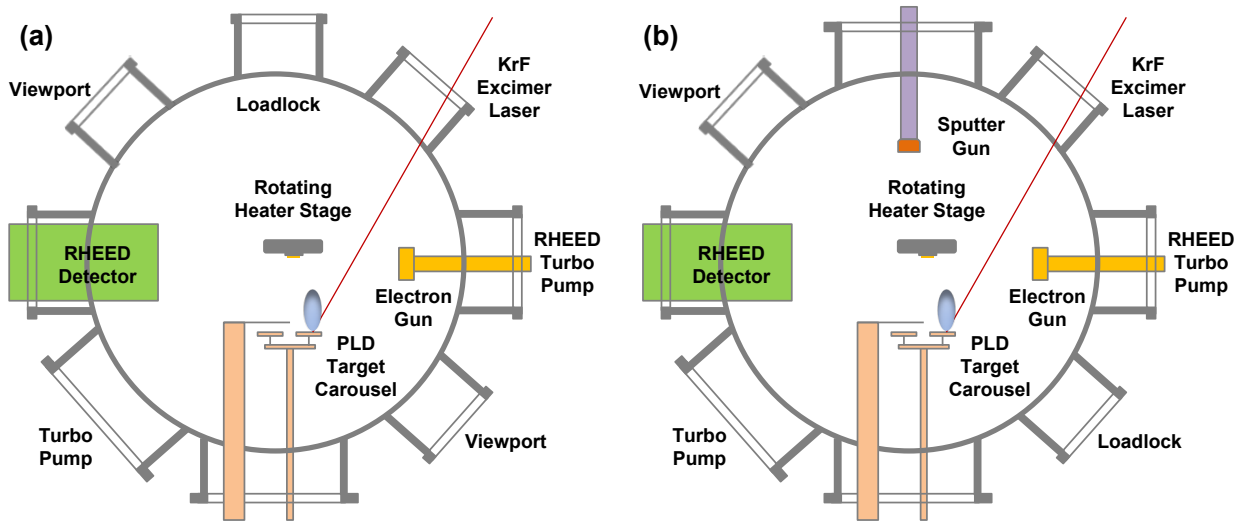


Figure 2.3: (a) "Main" PLD chamber (b) "Hybrid" PLD/sputtering chamber. Both chambers are equipped with loadlock chambers and *in situ* RHEED setups.

surface. The $SrTiO_3$ substrates were first placed in H_2O for 30 minutes to ensure the SrO surface layers formed SrOH, which was then etched away in a 60-second BHF immersion. The substrates were then placed in a tube furnace and annealed for 6 hours in the previously mentioned temperature/pressure environment. Despite the initial BHF immersion, an additional 60-second BHF treatment was used in some cases, depending on the quality of the $SrTiO_3$ crystals. The substrates were then examined using atomic force microscopy. The atomically smooth surface of both (001) and (111) $SrTiO_3$ are shown in Figure 2.2 using atomic force microscopy (AFM). The step-terrace structure that arises from the miscut angle of the substrate is clearly evident in both images, with the step heights of a single unit cell, corresponding to roughly 4 Å for (001) substrates and 2 Å for (111). Similarly smooth surfaces of orthorhombic (110)-oriented $NdGaO_3$, $DyScO_3$, $GdScO_3$, and $NdScO_3$ were obtained by thermal annealing at 1000-1100 °C for several hours. Due to the previously-reported complicated surface treatment of $(LaAlO_3)_{0.3}$-$(Sr_2AlTaO_6)_{0.7}$ (LSAT) substrates, these crystals were not treated before $SrIrO_3$ synthesis.

2.3 Pulsed laser deposition

Pulsed laser deposition (PLD) provides a relatively inexpensive approach for fundamental thin film research. A schematic of the two chambers used for this thesis work are shown in Figure 2.3. The

pulsed laser beam (KrF excimer laser, 248 nm) enters the chamber and ablates the PLD target, resulting in the generation of a plasma plume that leads to deposition of the atomic components at the substrate surface. To avoid concentrated excessive thermal heating of the target as well as maintain a stoichiometric material transfer, the target must be rotated. The surface of the target, as a result of this rotation, exhibits a circular ring known as the ablation track. This is shown in Figure 2.4(b) in the case of the $SrIrO_3$ target used for the work in this thesis. Assuming optimized growth conditions, it yields nearly perfect stoichiometric a transfer from target to substrate surface.

Typical lasers for PLD are KrF excimers (248 nm), ArF (193 nm), and XeCl (308 nm)[75]. While the technique of PLD itself is relatively simple, the science behind the plasma formation and subsequent behavior are complicated, and beyond the scope of this thesis. The general process parameters that must be considered to optimize the growth of a thin film include laser fluence, laser energy, laser spot size on the target, laser plume size, chamber partial pressure, chamber total pressure, substrate temperature, and substrate-to-target working distance. In between the discrete laser pulses, relaxation of the adatoms on the substrate surface occurs as these ablated species diffuse and nucleate. Due to the large kinetic energy from the ablation process, PLD can achieve very smooth surfaces if the growth parameters are tuned properly. Like most synthesis techniques in thin film science, many of the process parameters are coupled, so a careful systematic experimental design must be utilized when exploring new materials to ensure ideal synthesis. One downside to PLD is its lack of scalability due the small size of the ablation plume, making it unattractive for industrial applications when compared with more scalable deposition techniques such as chemical vapor deposition and sputtering. However, for research purposes, it is invaluable for the synthesis of atomically precise surfaces and interfaces at a relatively inexpensive cost and implementation simplicity when compared to techniques such as molecular beam epitaxy (MBE) and chemical vapor deposition (CVD).

Thus, the ABO_3 materials studied in this thesis were synthesized using pulsed laser deposition (PLD). For reasons discussed later in this chapter, the $SrIrO_3$ target was periodically resurfaced with ultra-fine sandpaper to recover the surface shown in Figure 2.4(a). The substrate was mounted to the resistive heater with a silver paste/alcohol solvent solution to provide a good thermal contact

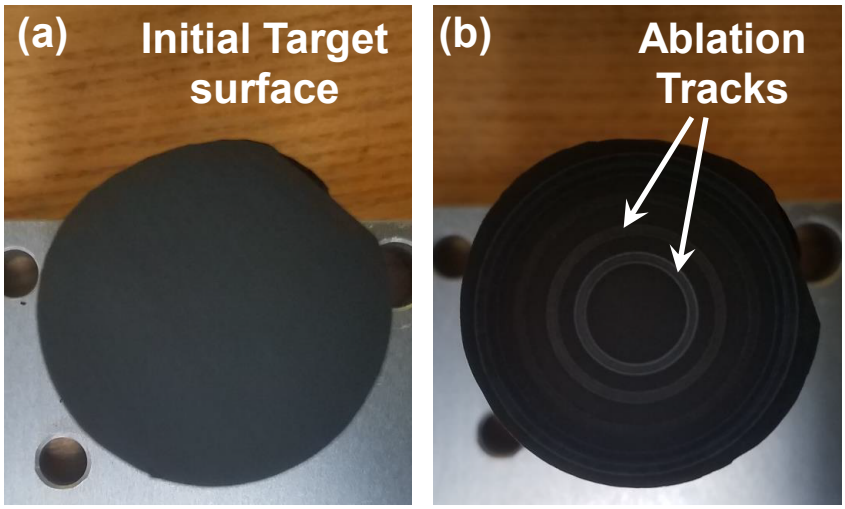


Figure 2.4: (a) Freshly-sanded $SrIrO_3$ PLD target before ablation (b) Same $SrIrO_3$ target after ablation showing circular ablation tracks

between the heater plate and the substrate. Since the heating of the substrate relies on thermal conductivity, this step is critical for maintaining substrate temperature uniformity, especially given that perovskite single crystals exhibit much smaller thermal conductivity than typical substrates such as silicon[76]. The $SrTiO_3$/$SrIrO_3$ heterostructures discussed in Chapter 3 were fabricated in the "main" PLD chamber depicted in Figure 2.3(a). The heterostructures in which metal deposition on top of the oxide films was required were synthesized in the "Hybrid" PLD/Sputtering chamber, where a sputter gun was inserted into the chamber to allow metal capping of the $SrIrO_3$ without breaking vacuum. This allowed preservation of the as-grown surfaces to allow a clean interface between $SrIrO_3$ and the capping metals since the sample was not exposed to the ambient in between the deposition of subsequent layers. This *in situ* PLD/sputtering approach had important consequences for our $SrIrO_3$ spin-torque generation work, which will be discussed in Chapter 5.

Both chambers utilized an *in situ* reflection high energy electron diffraction source/detector setup to provide real-time analysis of the sample surface during the deposition. The RHEED source/detector geometry is shown in Figure 2.3. Simultaneous to ablation of the target and subsequent deposition on the substrate surface, a focused electron beam is fired to be incident on the substrate surface and the resulting diffracted beam is detected on the phosphorous screen, resulting in RHEED patterns. The intensity of these spots is thus monitored to give real time analysis of the

surface of the film/substrate, as I will discuss next.

2.4 Reflection high energy electron diffraction

After the first observation of electron diffraction in 1928[77], electron beam guns and detector screens were then incorporated with molecular beam epitaxy in the 1960s 1970s to provide *in situ* surface characterization of semiconductor thin films. RHEED is sensitive to only the surface and a few underlying layers, which makes it a powerful tool to study such surface characteristics as morphology, defects, global surface reconstructions, structural domains, lattice symmetry, thin film growth mode, and growth rate. While the application of RHEED in this thesis utilizes a basic understanding of the technique, a much more thorough discussion of RHEED that I rely on for this section can be found elsewhere[78].

While oxide PLD synthesis initially utilized RHEED at low pressures, which detrimentally induced oxygen vacancies into the films, the technique of RHEED became invaluable after its relatively recent incorporation with in situ high pressure RHEED[79], which allowed real time characterization of oxide thin film surfaces grown by PLD at high oxygen partial pressures. Previously, the chemically sensitive nature of the RHEED gun tungsten filament meant RHEED techniques were limited to lower working pressure deposition environments, which hindered synthesis of high-quality oxide thin films, which generally are grown at higher partial pressures for reasons just mentioned. The original RHEED with PLD setup utilized a 2-stage vacuum pump system that kept the tungsten filament protected at a sufficiently low pressure while simultaneously allowing the main chamber to be operated at the relatively higher O_2 partial pressures needed for high-quality PLD-synthesized oxides. This setup has become widely utilized in the community, and a similar approach was used for this thesis.

The basic working principle of RHEED is shown Figure 2.5(a). Here, we see the direct RHEED beam incident on a sample, where it is reflected off the surface. The outgoing reflected beam along with the diffracted beam from substrate surface are detected on a screen along with the Laue spots along the Ewald sphere. Because RHEED is surface sensitive (in-plane reflections), the sample must be rotated along its azumuthal axis to access the crystallographic planes that produce the

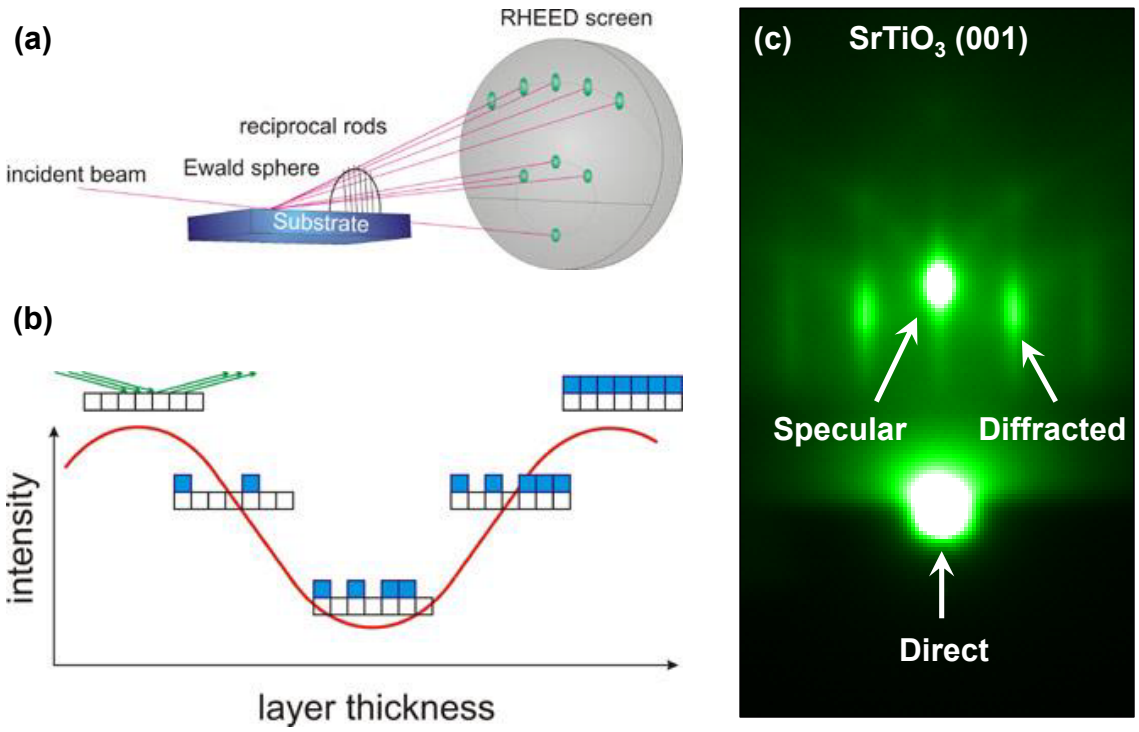


Figure 2.5: (a) RHEED diffraction geometry showing a typical RHEED pattern on a phospherous screen (b) RHEED oscillations and the surface coverage at points of interest (c) $SrTiO_3$substrate (1,0) RHEED pattern. (a) and (b) reprinted with permission from TU-Braunschweig.

pattern. Since RHEED utilizes diffraction, the RHEED pattern is a reciprocal space mapping of the in-plane crystal lattice of the sample surface. Therefore, diffraction spots normal to the surface are represented by rods as dictated by 2D diffraction. Unsurprisingly, the relative spacing of these spots gives information about the d-spacing of the atomic planes. In this particular example, the RHEED pattern reveals a single-crystal material with a smooth surface. For amorphous surfaces, the RHEED screen will detect a diffuse background and will not detect any diffraction spots. For polycrystalline films, an ring-like intensity analogous to x-ray powder diffraction will be the result. If the sample features a 3D surface that still exhibits good crystalline quality, a grid-like pattern is produced on the detector screen. By far the most relevant application of RHEED pertains to smooth, layer-by-layer epitaxy, which I will focus on in this work.

To further illustrate the concept of RHEED as it applies to this thesis, a RHEED pattern of an (001) $SrTiO_3$ substrate is shown in Figure 2.5(c). The specular spot in the RHEED pattern characterizes the smoothness and coverage of the surface, whereas the diffracted spots yield struc-

tural information from the underlying layers. If the incident RHEED beam is aligned to the (100) plane of the cubic $SrTiO_3$ substrate, the specular spot is defined as the (0,0) peak. It thus follows that the specular diffraction spots here denote the ($\bar{1}$,0) and (1,0) spots in this particular example. The kikuchi line streaks trailing outward from the diffraction spots originate from the dynamical diffraction contribution to the RHEED diffraction model. Such lines are an indication of the high quality crystalline lattice of the substrate.

When the growth mode of the film in question is the previously discussed layer-by-layer mode, oscillations the RHEED intensity spots are observed. The immediate consequences of these oscillations can be most easily conceived of using the schematic in Figure 2.5(b). Here we see the intensity is maximum at the start of the growth when the diffracted electrons remain completely in-phase with each other due to the atomically flat nature of the substrate surface. As adatoms arrive at the surface, they form islands (with a height of a single atomic layer) that nucleate out, causing the diffracted electrons to become out of phase with each other. This results in destructive interference, leading to a decrease in spot intensity on the detector screen. Once the islands nucleate out to cover 50% of the original surface, the intensity reaches its minimum and from there, recovers until reaching its maxiumum once the adatoms have nucleated to form a complete layer. It then follows from this argument that a decrease in spot intensity is a result of surface roughening from increased island nucleation before a layer is completed. Another powerful tool of RHEED oscillations is unit-cell resolution control of the film thickness, as RHEED oscillations can be tallied to calculated film thickness assuming the spacing of the film lattice is known. It must be stressed, however, that the RHEED oscillation period is sensitive to both the surface and also the incident beam energy[80], so film thicknesses measured by RHEED should always be verified with other methods such as ellipsometry and x-ray reflectivity.

2.5 Synthesis and surface of $SrIrO_3$ thin films

2.5.1 PLD synthesis of $SrIrO_3$ on pseudocubic (001) substrates

The ceramic $SrIrO_3$ target used in this work was commercially synthesized using spark plasma sintering[81] of stoichiometric mixtures of $SrCO_3$ and IrO_2 raw powders. The first attempt synthesize $SrIrO_3$ targets used stoichiometric mixings of these powder that were ball-milled and sintered in a laboratory tube furnace. However, it became apparent based on discussion with other groups that spark-plasma sintering produced dense $SrIrO_3$ targets. This finding was later reported in literature[82], and we obtained a commercial target accordingly.

During the deposition, the target-to-substrate distance ranged from 55-60 mm. The laser fluence was varied from 1-2 J/cm^2. The substrate temperature varied from 550 to 600 °C, depending on the substrate orientation (see individual studies in the subsequent chapters). The initial optimization process yielded films that were deposited at 2.5 mJ/cm^2 at 550 °C. However, it was later discovered from x-ray measurements that these films were off-stoichiometry, and the laser energy fluence was further varied along with temperature. Close to stoichiometric films (see Figure) on (001)-oriented $SrTiO_3$with a fluence of 1-1.5 J/cm^2, a substrate temperature of 600 °C, and an oxygen partial pressure of 75 mTorr. The target was resurfaced with sandpaper after each film growth to avoid Ir-enrichment of the target, as reported elsewhere[83,84]. It should be noted that the optimum laser fluence window was consistent with other reports studying the effect of laser fluence on ABO_3 thin film stoichiometry[85–87].

As stated, the subsequent layers of the films were monitored *in situ* using reflection high energy electron diffraction (RHEED). The thickness obtained from RHEED was confirmed independently using x-ray reflectivity. In Figure 2.6, the intensity of the specular intensity spot is plotted, showing layer-by-layer growth of $SrIrO_3$ on $SrTiO_3$. The RHEED image (right inset) shows no sign of secondary phases and preserves the diffraction pattern of the underlying $SrTiO_3$substrate (left inset), indicating a smooth surface and good crystalline quality. The step-flow growth mode was not observed in the initial layers of growth, even at high temperatures (750 °C). However, constant RHEED intensities with no oscillations were typical after the initial 30 or 40 uc atomic layers

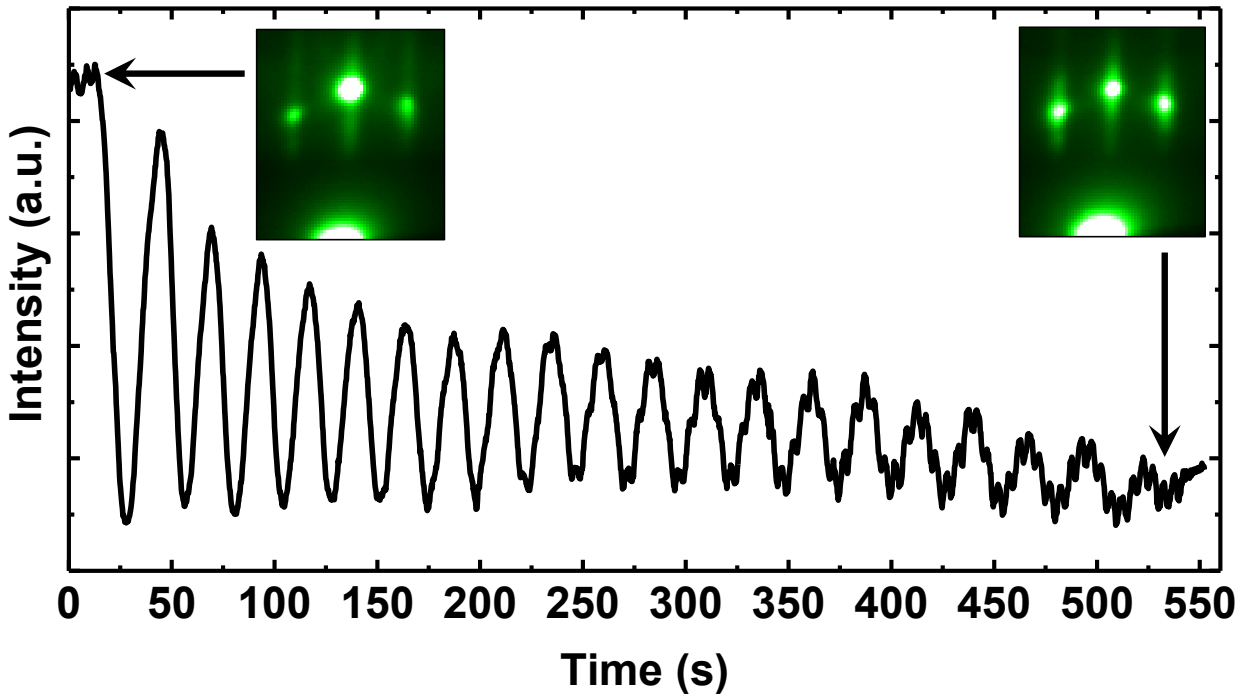


Figure 2.6: Specular diffraction intensity of a 20 uc thick $SrIrO_3$film with RHEED images of the substrate (left inset) and $SrIrO_3$film at the end of the growth (right inset).

of $SrIrO_3$, indicating that a steady-state roughness is achieved. The periods of the RHEED oscillations became longer as the film thickness increased, which is consistent with other studies[84]. This slower growth rate is attributed to the increased metalization of the target as a result of the previously-mentioned Ir-enrichment, which would hinder absorption of the laser beam by the target (metals tend to reflect the laser beam more so than ABO_3 oxides).

2.5.2 Surface characterization: atomic force microscopy

The surfaces of both the treated substrates and the various heterostructures were examined using atomic force microscopy (AFM). In Figure 2.7(b), we see that a 10 nm $SrIrO_3$ thin film shown in nearly preserves the terraced surface of the underlying $SrTiO_3$ substrate in Figure 2.7 (a), indicating a smooth 2D surface, as observed with the *in situ* RHEED during the growth. As the film thickness increases, the surface roughens to form smooth islands with unit cell height, shown in Figure 2.7 (c). This surface structure is sometimes known as the ”wedding cake.” As will be shown in the next section, the 35 nm $SrIrO_3$ remained fully strained by the substrate despite the increasing 3D

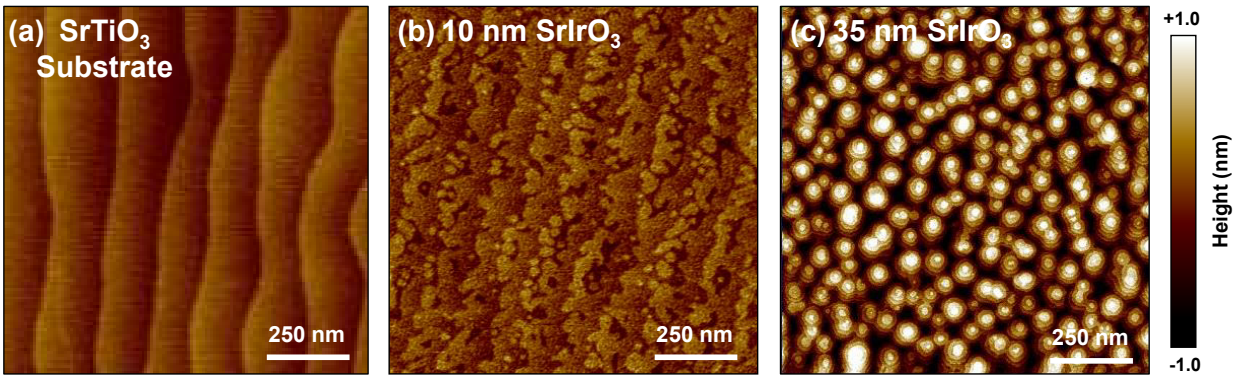


Figure 2.7: Surfaces of (a) TiO_2-terminated (001) $SrTiO_3$ substrate (b) 10 nm $SrIrO_3$thin film showing preservation of the underlying substrate step-terrace surface (c) 35 nm $SrIrO_3$thin film showing 3D island surface with "wedding cake" features.

nature of the surface. It has recently been reported that this periodic long range "wedding cake" surface morphology in perovskites is a result of stress fields from the misfit strain[88]. Nonetheless, the pseudocubic $SrIrO_3$ remains fully coherent with the substrate despite the observed surface roughening, as we will discuss next.

2.6 X-ray diffraction (XRD)

2.6.1 Basic principles of XRD

X-ray diffraction (XRD) is a widely used technique to characterize the structural, chemical, and electronic properties of materials because the wavelength of the x-rays are on the order of typical atomic radii, which ensures maximum interaction of the x-rays with the atomic constituents. The principles of x-ray diffraction are similar to those of RHEED discussed earlier. The main difference lies in the fact that x-ray diffraction can probe 3D materials, whereas RHEED is surface sensitive. While the concepts of x-ray diffraction are quite quantitative, I will provide a simple description relevant to the work in this thesis. Comprehensive discussions on the theory and applications of x-ray diffraction can be found elsewhere[89,90].

X-ray diffraction provides a reciprocal space view of the structural characteristics of the film and substrate. Diffraction from a single-crystal will only occur at certain points in reciprocal space as defined by the structure factor. This is a physical form factor that depends on the atomic

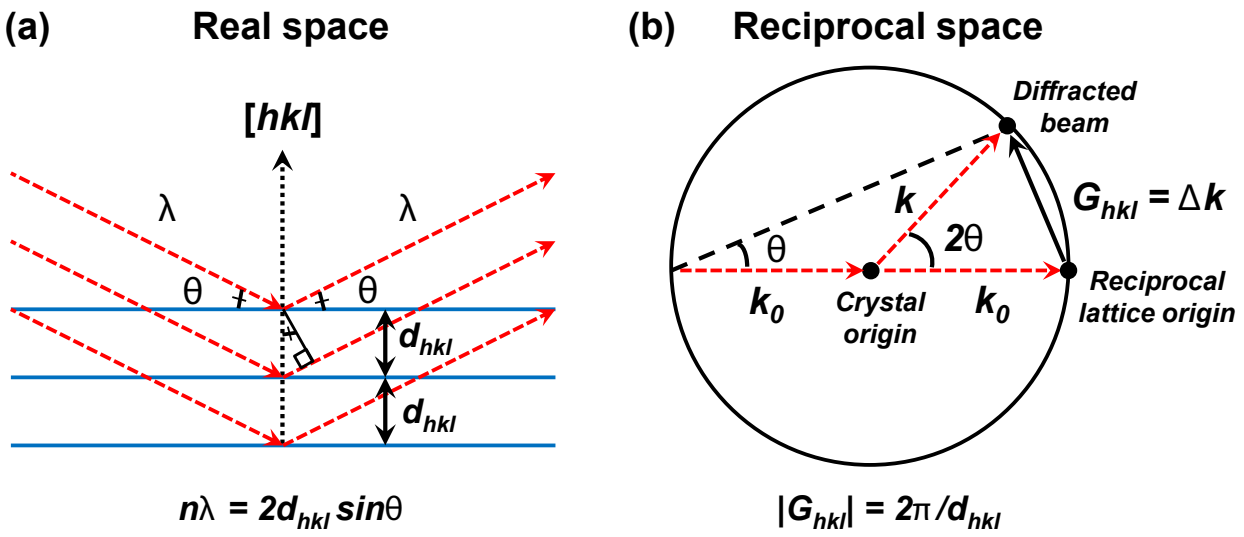


Figure 2.8: (a) Real space depiction of Bragg diffraction showing integer path difference for adjacent incident and ecxident x-ray beams, which leads to Bragg's law (b) Reciprocal space depiction of diffraction showing the Laue condition met on the surface the Ewald sphere.

constituents of the crystal, which scatter x-rays differently depending on the atom. The most important contributions to the structure factor are from the electron densities of the atoms located at distinct reciprocal space points within the material. In the case of real materials, a reciprocal lattice point generally represents an atomic plane in real space. When the structure factor of a particular plane or family of planes $\{hkl\}$ is zero, this indicates no diffraction intensity from that plane. The implication of this is that certain crystal structures will have *forbidden peaks* based on their crystalline symmetry and positions of the atoms within the unit cell. For example, in the case of body-centered lattices, the addition of $(h + k + l)$ must produce an even integer, otherwise the structure factor is zero and no intensity is produced. Another common example is that of face-centered lattices, where h, k, and l must be unmixed (either all odd or all even integers) or else the structure factor similarly vanishes. In general, the presence (or lack) of certain x-ray diffraction peaks, as I will describe later for the particular case of $SrIrO_3$, is a powerful tool for determining film symmetry.

The diffraction condition in real space and reciprocal space is depicted in Figure 2.8. In real space [Figure 2.8(a)], x-rays of a certain wavelength λ are incident on the a material with planar spacing d_{hkl} at an incidence angle θ. When the path length difference between incident x-rays is an

integer wavelength, constructive interference occurs and the out-going x-rays produce an intensity. This path difference can be shown to be $2d_{hkl}\sin\theta$ by drawing a triangle as shown in the figure. It thus follows that half-wavelength path differences result in destructive interference and no intensity is produced. From this geometric analysis of the real space x-ray diffraction, Bragg's law can be derived, which is denoted by

$$n\lambda = 2d_{hkl}\sin\theta \tag{2.2}$$

In this simplest case, x-ray diffraction can be considered as a *kinematic* process. In many cases *dynamical* diffraction must be considered as the a finite number of x-rays depicted in Figure 2.8(a) will backscatter off of crystal planes and interfaces instead of immediately leaving the sample.

In Figure 2.8(b), the reciprocal space picture of x-ray diffraction is shown. An x-ray wave vector $\boldsymbol{k_0} = 2\pi/\lambda$ is incident on a crystal at an angle θ and an excident x-ray $\boldsymbol{k}$ scatters off the crystal at an angle 2θ. The difference between these wave vectors, $\Delta\boldsymbol{k}$, determines if diffraction occurs. First, we consider a reciprocal lattice vector $\boldsymbol{G_{hkl}}$, which is the reciprocal space equivalent of d_{hkl}. If $\boldsymbol{G_{hkl}} = \Delta\boldsymbol{k}$ at some coupled θ-2θ angle, the Laue condition occurs, which is the reciprocal space equivalent of Bragg's law. Since this diffraction model is elastic, it occurs only when the the magnitudes of $\boldsymbol{k_0}$ and $\boldsymbol{k}$ are equal. The implication of this is that any diffraction points must lie on the surface of the sphere, known as the Ewald sphere. The radius of the Ewald sphere is equal to the wave vector of the x-rays, or $2\pi/\lambda$. Since x-ray diffracton data must be related back to real space information, it is helpful to relate $\boldsymbol{G_{hkl}}$ back to d_{hkl}. It can therefore be shown that $|\mathbf{G_{hkl}}| = 2\pi/d_{hkl}$.

2.6.2 X-ray diffraction of thin films

As has been mentioned, x-rays are quite sensitive to defects, strain and relaxation, chemical composition, density, and dimensionality features, which make it a very attractive method to study the structure and properties of thin films. While x-ray diffractometers are a relatively expensive initial investment, their relative efficiency to produce the degree of accurate macrostructural information they provide is a huge advantage. Another benefit of x-ray diffraction is that it is non-destructive, unlike other structural analysis techniques such as transmission electron microscopy.

Possibly the most important application of x-ray diffraction in the case of thin films is determining the film lattice parameter, which provides insight into the crystalline quality of the thin film. Since x-ray diffraction represents reciprocal space, d_{hkl} scales inversely as 2θ. Thus, relatively *large* real-space d-spacings appear at relatively *small* 2θ. In heteroepitaxy, the peaks from the film(s) and substrate will be shifted relative to each other in 2θ. The position of diffraction peaks is also affected by the degree of strain on the film, its composition, and any crystallographic tilt in the film relative to the substrate. It should come as no surprise that perfect homoepitaxy results in no peak shift (or any evidence of a film peak) in relationship to the substrate, as such a shift would indicate a structural deviation in the thin film from the bulk.

Additionally, the relative peak widths give information on the thickness of the film/substrate. Whereas diffraction from an infinite (3D) crystal will take the form of a δ-function, the peak of a thin film of relatively finite thickness will broaden in reciprocal space. In the case of a sharp interface between film and substrate, the dynamical nature of diffracted x-rays interacting with the interface and film surface will result in fringing on either side of the film peak. Such fringes are known as Kiessig fringes, and the thickness of the film can be estimated using the Sherrer formula or fit to Bragg's law or other models. Analytically fitting low angle fringes from x-ray reflectivity is particularly effective for determining thin film thicknesses and densities.

2.6.3 4-Circle x-ray diffraction

4-circle x-ray diffractometry is powerful tool to characterize single-crystal materials due to the geometric degrees of freedom to rotate the sample to access allowed diffraction peaks. A typical stage geometry is depicted in Figure 2.9. In the setup used for this thesis work, the x-ray source tube is stationary, whereas the sample and detector can be rotated by ω and 2θ, respectively. Here, as can be seen from the figure, ω is identical to the previously-discussed θ angle. The sample stage also has azimuthal (ϕ) and polar (χ) degrees of freedom so that planes that are not normal to the sample surface can be accessed.

The lab-source x-ray techniques in this thesis include 2θ-ω (θ-2θ) scans to examine the epitaxial arrangement and phase of the films, rocking curve ω scans to determine the crystalline quality

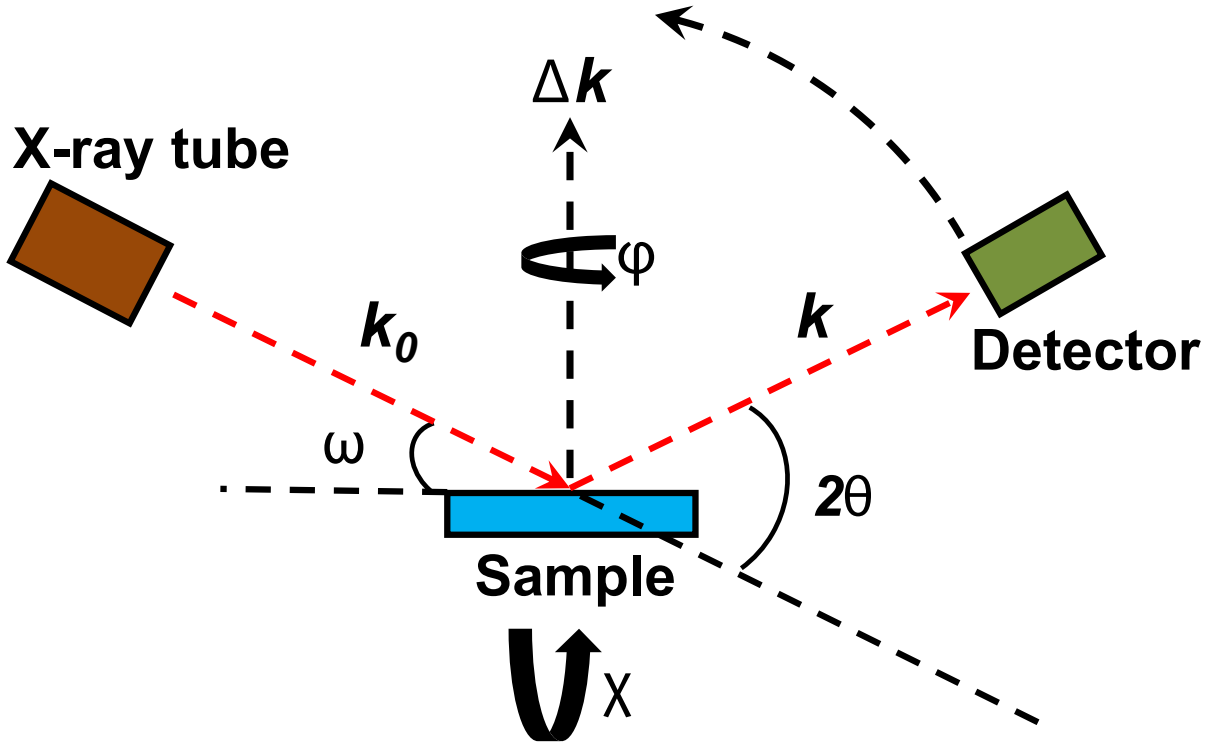


Figure 2.9: 4-circle XRD geometry.

and mosaic spread, x-ray reflectivity to determine the film thicknesses and densities, and reciprocal space mappings to determine the coherency and epitaxial arrangement of the films. These measurements were conducted on a Bruker D8 Discover equipped with a point detector. Reciprocal space mappings (RSM) of the materials presented here were obtained on the same diffractometer, but with a line detector. The phase and stoichiometry of the $SrIrO_3$ ceramic target was checked using powder diffraction on a Bruker D8 Discover equipped with a 2D detector.

During a 2θ-ω scan, the sample (ω) and detector (2θ) are aligned to the Bragg diffraction plane of interest (usually selected by considering the structure factor to maximize the intensity). The sample and detector are then incremented in coupled unison to scan reciprocal space normal to the direction of the alignment. In the case of high-quality single-crystalline thin films, only one family of planes are observed in such a scan, whereas peaks from multiple planes are observed if the sample is polycrystalline or textured. In the case of amorphous films, no diffraction peaks are measured as a large diffuse background is the result.

A special case of a a low-angle type of 2θ-ω scan, is x-ray reflectivity, in which the sample and detector are aligned to the reflected surface. In this scan, the beam is reflected until a critical 2θ angle that depends on the film density is reached, after which the beam enters the sample and intensity fringing is measured. The spacing and relative intensity of these fringes gives information on the thickness and surface/interfacial roughening of the film. This information is extracted by fitting models to the data. In this work, XRR plots were fit using the Bruker DIFFRAC.suite Leptos software.

A rocking curve scan fixes the detector (2θ) at a film peak and rotates ω around and through the peak. As ω is rotated, the Bragg condition is met, depending on the cystalline quality of the material. This scan is especially useful for determining the crystalline quality and also the relative degree of planar mis-orientation within the film, known as *mosaic spread.* High-quality epitaxial thin films will exhibit sharp rocking curve peaks with narrow rocking curve full-width at half maxima (FWHM) and thus very little mosaic spread. A large background in a thin film rocking curve scan can indicate the presence of diffuse scattering that is a result of defects and dislocations within the material.

For determining in-plane symmetry, both point and line detectors can be used. However, due to the mechanical limitations of the goiniometer, in-plane information is obtained from diffraction peaks that carry both an in-plane and out-of-plane component. Thus, to access peaks where sample peaks that are not normal to the surface are scanned, ϕ and χ must be adjusted according to the Ewald sphere. Alternatively, reciprocal space mappings, as their name suggests, provide more than a point in reciprocal space. While ϕ scans with point detectors can be used to determine sample symmetry and epitaxial layering and even reciprocal space mappings, use of a line or 2D detector can speed up the time needed to acquire the same information.

Reciprocal space mappings provide an intensity contour map preserving in-plane and out-of-plane information. In this thesis, RSM scans were taken using a line detector, where ω is parked at discreet angles and diffraction intensity is measured by the detector. Each of these scans provides not only the reciprocal space point in which diffraction occurs, but also slices of reciprocal space around the diffraction points due to the use of the line detector. By taking many of these scans and

acquiring a series of the slices, the reciprocal space of the film and substrate peaks is mapped out as a coordinate of the out-of-plane component (often denoted by L) and the in-plane component (denoted by H or K). RSM scans are particularly useful for measuring the epitaxial layering and symmetry of films on substrates, unit-cell volume, and strain-relaxation.

2.6.4 Surface-normal layering of $SrIrO_3$ on $SrTiO_3$

A 35 nm $SrIrO_3$ film on (001) $SrIrO_3$ is shown in Figure 2.10. Figure 2.10(a) the surface normal x-ray 2θ-ω diffraction pattern around the (001) and (002) $SrTiO_3$ peaks is shown, indicating a a single-crystal $SrIrO_3$ thin film orientation without the presence of other textures or chemical phases. In Figure 2.10(b) a zoom-in around the $(002)_{pc}$ peak shows clear Kiessig thickness oscillations, indicating a relatively smooth surface and sharp interface with the underlying $SrTiO_3$ substrate. Finally, the rocking curve around the film $(002)_{pc}$ film shows a full width at half maximum (FWHM) of 0.02° [Figure 2.10(c)], which is on the same order of magnitude as the underlying $SrTiO_3$ substrate, indicating very little planar mosaic spread within the film. Thus, from the out-of-plane x-ray diffraction experiments, we determined that our films were high quality single-crystal material with similar epitaxial arrangement with the underlying $SrTiO_3$ substrate.

2.7 Symmetry of $SrIrO_3$ thin films from XRD

2.7.1 Glazer notation of perovskite tilt systems

As briefly mentioned in the introduction, the perovskite unit cell symmetries are generally determined by the relative size of the constituent cation radii, which determine the Goldschmidt tolerance factor[7]. Nearly half a century after Goldschmidt's work, these symmetries were further categorized by Glazer[18], who described the different symmetries by their characteristic octahedral rotations along the 3 principle axes of the pseudocubic perovskite unit cell, where the axes are $[100]_{pc}$, $[010]_{pc}$, and $[001]_{pc}$. The relationship of these pseudocubic axes to the global crystal structure depends on the symmetry of the perovskite material in question. In the case of orthorhombic *Pbnm* (No. 62) oxides such as $SrRuO_3$ (which has lattice parameters of a_o = 5.567 Å, c_o = 5.530

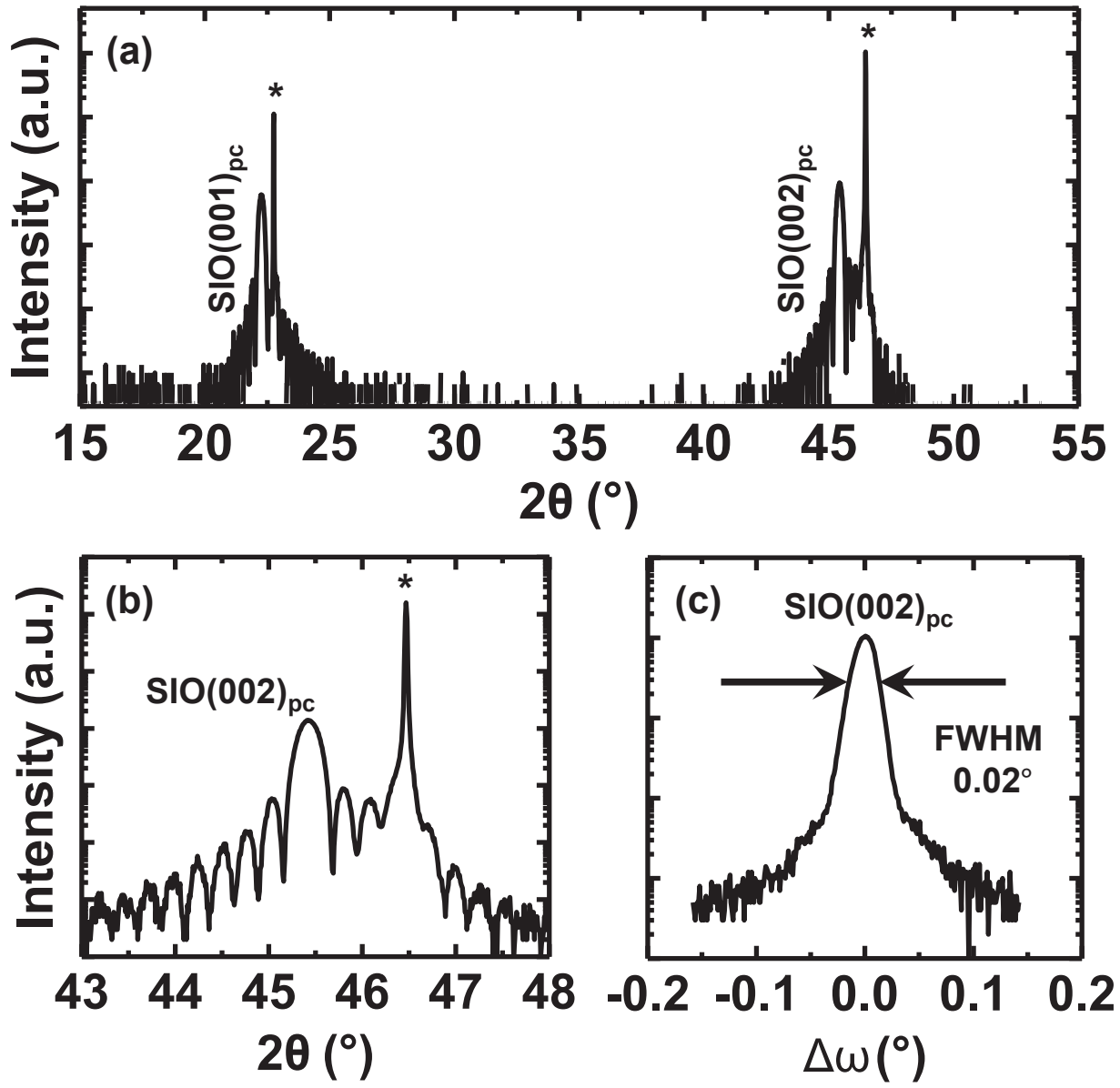


Figure 2.10: (a) Out-of-plane x-diffraction scans of a 35 nm $SrIrO_3$ thin film on $SrTiO_3$ showing single-phase epitaxial $SrIrO_3$ (b) Region around the (002) $SrTiO_3$ substrate peak, showing sharp Kiesig fringing in the $SrIrO_3$, indicating high quality interface with $SrIrO_3$ (c) Rocking curve around $(002)_{pc}$ $SrIrO_3$ peak indicating good alignment of planes and overall crystalline quality.

Å, and a_o = 7.845 Å), the relationship goes as follows:

$$a_{\mathrm{pc}} = \frac{\sqrt{{a_{\mathrm{o}}}^2 + {b_{\mathrm{o}}}^2}}{2} \approx \frac{c_{\mathrm{o}}}{2} \tag{2.3}$$

Thus, $SrRuO_3$ has a pseudocubic lattice parameter of approximately 3.923 Å. As mentioned in the introduction, I will define orthorhombic $SrIrO_3$ in the same *Pbmn* (No. 62) space group to allow easier comparison with $SrRuO_3$. Thus, by an identical analysis from the equation, the pseudocubic lattice parameter $SrIrO_3$ is approximately 3.95 Å.

From the Glazer notation, the octahedral tilt system can be described by considering the rotations along each pseudocubic axis. For example, $SrRuO_3$ has a tilt system of $a^-a^-a^+$. The letters here denote the magnitude of the rotation, whereas the exponent describes nature of the rotation. The - sign indicates that the octahedra along this axis are rotated out of phase with their coaxial neighbors, whereas a + sign indicates that the neighbors are in phase. In the case of no rotation, the 0 sign is used. Thus, in the case of $SrTiO_3$, which is perfect cubic with no rotations in any directions, the tilt system is $a^0a^0a^0$. Recall that these two octahedral tilt systems were presented in back in Figure 1.3. A quick examination of the depicted $[100]_{\mathrm{pc}}$ zone-axis view of the $SrTiO_3$ unit cell confirms this Glazer notation since the octahedra do not rotate along any of the 3 axes, and therefore, no tilt is observed. In the case of $SrRuO_3$, the coordinates must be converted from the orthorhombic to the pseudocubic. In Figure 1.3, the zone axis of the $SrRuO_3$ is $[110]_{\mathrm{o}}$, which as previously defined refers to the $[100]_{\mathrm{pc}}$ axis. As can be seen, the coaxial octahedra neighbors are rotated out of phase with each other, hence the rotation of this axis is a^-. A similar inspection of the $[010]_{\mathrm{pc}}$ ($[1\bar{1}0]_{\mathrm{o}}$) and $[001]_{\mathrm{pc}}$ ($[001]_{\mathrm{o}}$) axes yield a^- and c^+ respectively, to complete the tilt system of $a^-c^+a^-$. It should be noted that the definition of the pseudocubic unit cell within the global perovskite crystal structure is arbitrary. Therefore, depending on how it is defined, the tilt system can be indexed differently. For example, $SrRuO_3$ can also be indexed as $a^-c^+a^-$. The difference is merely a rotation of 90°.

2.7.2 Symmetry and domain structure of $SrIrO_3$ on $SrTiO_3$

It is known that orthorhombic perovskites like $SrIrO_3$ align on the cubic substrates as shown in Figure 2.11(a). The canonical example of this is $SrRuO_3$, which is chemically and structurally similar to $SrIrO_3$. Here, the $[001]_o$ domain aligns with the $[010]_c$ direction, whereas the $[1\bar{1}0]_o$ domain is aligned to the $[100]_c$ direction[20], and $[110]_o$ is oriented out of the plane along $[001]_c$. Such epitaxial arrangement leads to a distortion of the orthorhombic unit cell due to the compressive/tensile strain along $[1\bar{1}0]_o$, which causes the orthorhombic film to assume a tilt out-plane relative to the substrate. This produces a slightly distorted monoclinic film structure with $\alpha = \beta = 90^\circ \neq \gamma$, where α, β, and γ are the angles between the principle axes of the the unit cell. By examining reciprocal space around asymmetric reflections such as $\{103\}_{pc}$, ($\{204\}_{pc}$, etc) at 90° ϕ increments, it is possible to determine the degree of tilt induced by the strain[20]. This is done by comparing the film peak position in L at each ϕ angle, as a tilted film will show deviations in the surface-normal component of the reciprocal lattice vector Q_z. This will shift the peak position in L along 2 of the ϕ-angle orientations relative to each other, whereas the other 2 peaks will exist at identical L-values. In the epitaxial arrangement described for $SrIrO_3$, the L-shifts will exist along the $[103]_{pc}$ and $[-103]_{pc}$ peaks since the in-plane direction of the strain that creates the distorted tilt lies along $[100]_{pc}$. Therefore, the $[013]_{pc}$ and $[0\text{-}13]_{pc}$ reflections should exhibit the same film peak position in L, since no tilt exists along this direction.

Thus, to determine nature of the in-plane crystal structure of the 35 nm $SrIrO_3$ film, reciprocal space mappings around the $SrTiO_3$ $\{103\}$ family of reflections were measured, shown in Figure 2.11(b). In these scans $(103)_{pc}$ and $(\bar{1}03)_{pc}$ correspond to $(240)_o$ and $(420)_o$, respectively, which means $(013)_{pc}$ and $(0\bar{1}3)_{pc}$ correspond to $(332)_o$ and $(33\bar{2})_o$, respectively. Along $SrIrO_3$ $(332)_o$ and $(33\bar{2})_o$ there is indeed no shift in L (out-of-plane) as expected since the compressive strain in this direction will merely shrink the $SrIrO_3$ unit cell. However, the L-position of both the $(240)_o$ and $(420)_o$ peaks are offset from both each other and the previously discussed orthogonal directions. As previously discussed, this is a result of the compressive strain along $[1\bar{1}0]_o$ distorting the corner of the $SrIrO_3$ unit cell, which induces a non-orthogonal angle at this corner. Thus, as

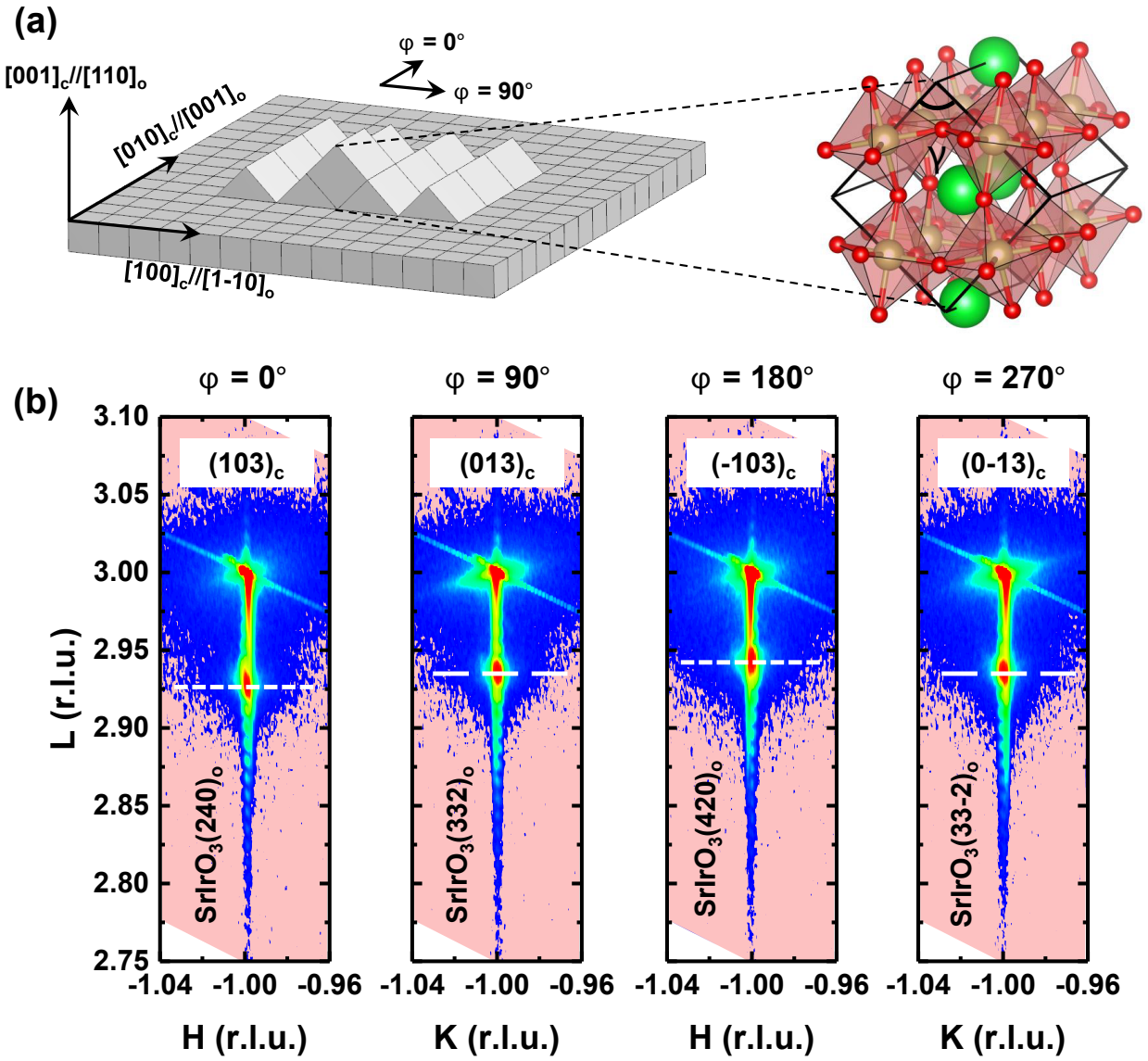


Figure 2.11: (a) Orthorhombic arrangement of a typical orthorhombic perovskite on a cubic substrate (e.g., $SrTiO_3$) with the $[110]_o$ direction aligned along $[001]_c$, $[001]_o$ direction aligned along $[010]_c$, and $[1\bar{1}0]_o$ direction aligned along $[100]_c$, resulting in a distorted orthorhombic (monoclinic-like) symmetry (b) reciprocal space mappings around the $\{103\}$ $SrTiO_3$ family of peaks indicating coherence with the underlying substrate and a peak splitting along $[1\bar{1}0]_o$ due to compressive strain where γ does not equal 90°.

expected the $SrIrO_3$ assumes a monoclinic structure that is close to orthorhombic when grown on the cubic $SrTiO_3$ substrate. Our finding here is qualitatively consistent with a recent report on the symmetry of strained $SrIrO_3$ thin films on various substrates[91]. The implications of this tilting on the electronic properties of our $SrIrO_3$ films will be further discussed in Chapter 5.

After confirming the distorted orthorhombic nature of our $SrIrO_3$ films, we then investigated their orthorhombic domain structure. This question was motivated by our RHEED work, which revealed superstructure diffraction spots along both of the orthogonal (1,0) and (0,1) directions, which is an footprint of doubling of the $SrIrO_3$ unit cell along both [001] and [010] $SrTiO_3$ directions. Such doubling occurs along the $[001]_o$ direction, which we had hypothesized only oriented along $[010]_c$. However, the observation of this superstructure pattern meant that a finite number of $[001]_o$ domains existed along both in-plane cubic directions. The implication of this mixing of domains will be discussed in greater detail in a later chapter. It was also observed from RHEED patterns that these orthorhombic domains disappear at film thicknesses below 4-5 uc, where an undistorted tetragonal symmetry is presumably established. But for the $SrIrO_3$ films thicker than 8 uc, multi-domains existed on $SrTiO_3$. Therefore, x-ray work on the 35 nm $SrIrO_3$ film on $SrTiO_3$ was undertaken to look for half-order reflections in scans of the $\{h02\}_{pc}$ family at ϕ values of 0° and 90°.

The choice of this x-ray peak was motivated by Glazer's general "recipe" for characterizing subtle structural nuances in perovskites that result from octahedral tilting, cation displacements in the unit cell, or subtle distortions of the octahedral due to strain, etc[92]. Since Glazer's nomenclature refers to the psuedocubic coordinate system, such peaks are often referred to as *half-order reflections*, as such peaks are not allowed in a cubic system. In the case of the $SrIrO_3$ tilt system, an appropriate half-order peak to look for based on Glazer's recipe is the $\{\frac{1}{2}02\}_{pc}$ family, which corresponds to the $\{221\}$ orthorhombic family. By scanning around this peak at ϕ angles 90° apart from each other, the domain structure can be examined. If the films are single-domain, only one ϕ orientation would show a $\{221\}_o$) reflection. On the other hand, if the $[001]_o$ existed along both pseudocubic axes, the mixed domain structure of our $SrIrO_3$ films on $SrTiO_3$ would be confirmed. Our approach on our diffractometer was a reciprocal space mapping around the $\{002\}$ substrate

peak where the in-plane parameter, h or k, is scanned between 0 and 1 to look for the half-order reflection.

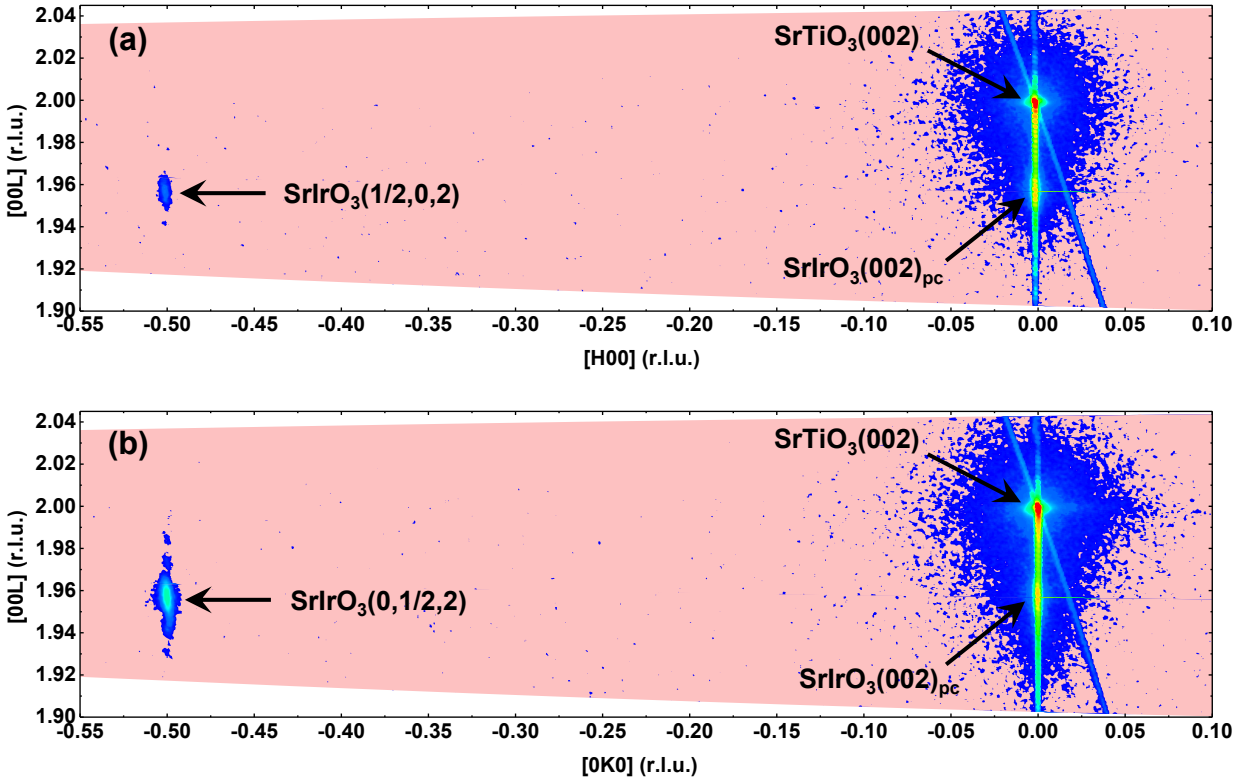


Figure 2.12: (a) H-scan reciprocal space mapping around the $(\frac{1}{2}02)_{pc}$ and $(002)_{pc}$ reflections (b) K-scan reciprocal space mapping around the $(0\frac{1}{2}2)_{pc}$ and $(002)_{pc}$ reflections. The presence of these half-order $SrIrO_3$ peaks in orthogonal in-plane directions implies a mixed domain $SrIrO_3$ structure with about 90% preferential $[001]_o$ domain alignment along $[010]_c$ of $SrTiO_3$.

In Figure 2.12, these scans around the $(h02)_{pc}$ and $(0k2)_{pc}$ peaks are shown. As can clearly be seen, These scans both show a half-order reflection from the $SrIrO_3$ film. This confirms that the $[001]_o$ axis is indeed aligned primarily along [010] of the $SrTiO_3$ substrate, but a small 10% mixture remains along [100]. Previous studies of $SrIrO_3$ films on $SrTiO_3$ [93] and LSAT[42] also report a mixed domain structure. While it is known that increasing the substrate miscut angle can result in single-domain ABO_3 films[94–97], the previously-mentioned report on the domain structure of $SrIrO_3$ on $SrTiO_3$ reported the persistence of mixed-domain microstructure even on high miscut $SrTiO_3$. If increasing the substrate miscut cannot stabilize single-domain films, it is also possible that such $SrIrO_3$ films may be stabilized on structurally similar scandate substrates such as $DyScO_3$

and $GdScO_3$. A recent report has been published where it was indeed found that $SrIrO_3$ growth on such orthorhombic substrates indeed produced single-domain films, whereas those grown on $SrTiO_3$ were multi-domain[91]. Our preliminary RHEED studies on $SrIrO_3$ grown on these scandates show evidence of single-domain films (see Appendix A), which agrees with this finding.

Table 2.1: Lattices of assorted perovskite substrates and their lattice mismatch with $SrIrO_3$.

Substrate Material	Crystal Symmetry	Lattice Parameters a (Å)	b (Å)	c (Å)	Pseudocubic a_{pc} (Å)	% Strain on $SrIrO_3$
$NdGaO_3$	Orthorhombic	5.428	5.498	7.707	3.858	-2.324
LSAT	Cubic	3.868	3.868	3.868	3.868	-2.191
$SrTiO_3$	Cubic	3.905	3.905	3.905	3.905	-1.222
$DyScO_3$	Orthorhombic	5.440	5.713	7.887	3.944	-0.212
$GdScO_3$	Orthorhombic	5.488	5.746	7.893	3.973	0.507
$NdScO_3$	Orthorhombic	5.770	5.579	7.999	4.013	1.503

2.7.3 Growth of $SrIrO_3$ on assorted ABO_3 perovskite substrates

In addition to our $SrIrO_3$ grown on $SrTiO_3$, We have also demonstrated high quality $SrIrO_3$ thin films growth on 3 other common perovskite substrates, (001) LSAT, (110)-oriented orthorhombic $DyScO_3$ and $GdScO_3$, as can be seen in Figure 2.13. Their symmetry, lattice constants (both full and pseudocubic), and the % strain they induce in $SrIrO_3$ is listed in Table 2.1[98–101]. Like with the previously-discussed $SrTiO_3$, the films all show distinct Kiessig fringes in the out-plane data [Figure 2.13(a)], again indicative of smooth surfaces and sharp interfaces with the substrates. Additionally, the FWHM values [Figure 2.13(b)] are on the same order as that of a typical perovskite substrate, so quality of the material is comparable to that of the films grown on $SrIrO_3$, which is also shown in the figure for comparison. While the $SrIrO_3$ film grown on (110) orthorhombic $NdGaO_3$ in Figure 2.13 appears to be a high-quality film, x-ray reflectivity measurements revealed

a thickness discrepancy with that measured from the Kiessig fringes, likely indicating the presence of a dead layer of poor crystalline quality. This finding is consistent with a previous report[49], and thus, $SrIrO_3$ appears to be less stable on this particular substrate. Nonetheless, the data obtained on the other 4 substrates opens the door to testing the effect of strain on the epitaxial $SrIrO_3$ films. At the time of writing this thesis, high-quality $SrIrO_3$ films on (110)-oriented $NdScO_3$ were also being pursued.

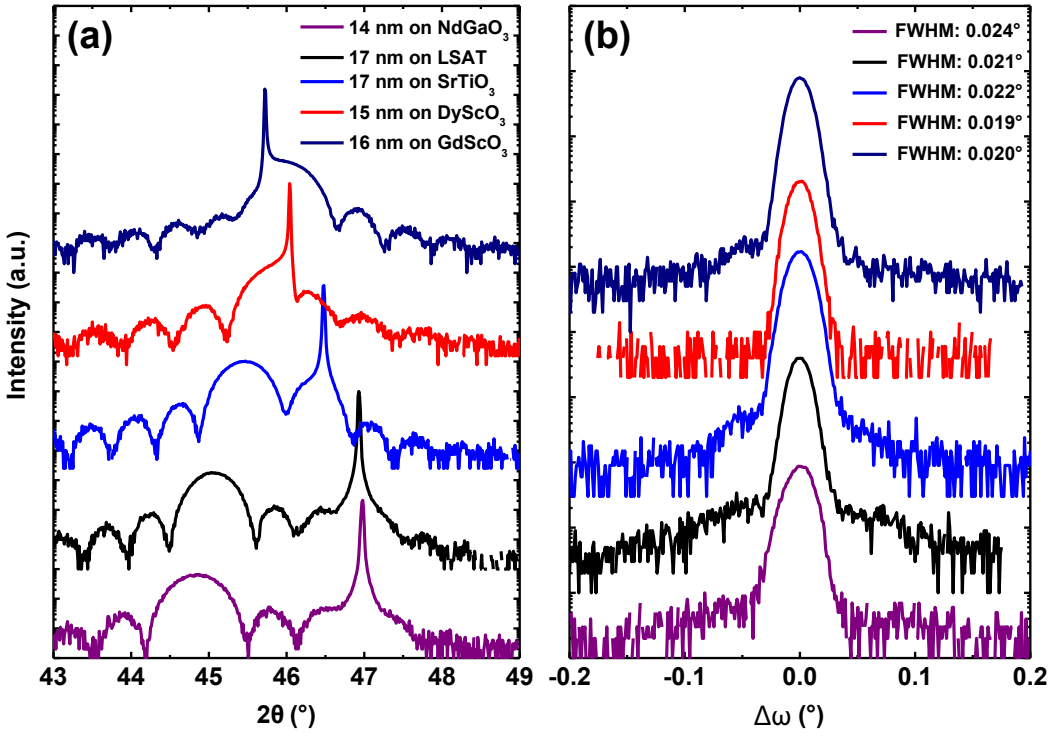


Figure 2.13: (a) Out-of-plane x-diffraction scans of $SrIrO_3$ thin films on 5 different perovskite substrates (b) rocking curve scans of the films grown in (a). Both plots indicate high quality single-crystal $SrIrO_3$ films on each substrate.

2.8 Electronic transport of $SrIrO_3$ on (001) $SrTiO_3$

Bare and capped $SrIrO_3$ were measured in a closed-cycle cryostat. Preliminary 4-point measurement on a 10 nm bare $SrIrO_3$ are presented in Figure 2.14. Here we see completely metallic transport with superior performance compared to the two known bulk $SrIrO_3$ reports, which is not surprising, given that the film is epitaxial and does not contain as many defects or grains compared to the the polycrystalline bulk samples. It should be noted that the absolute resistivity value of the

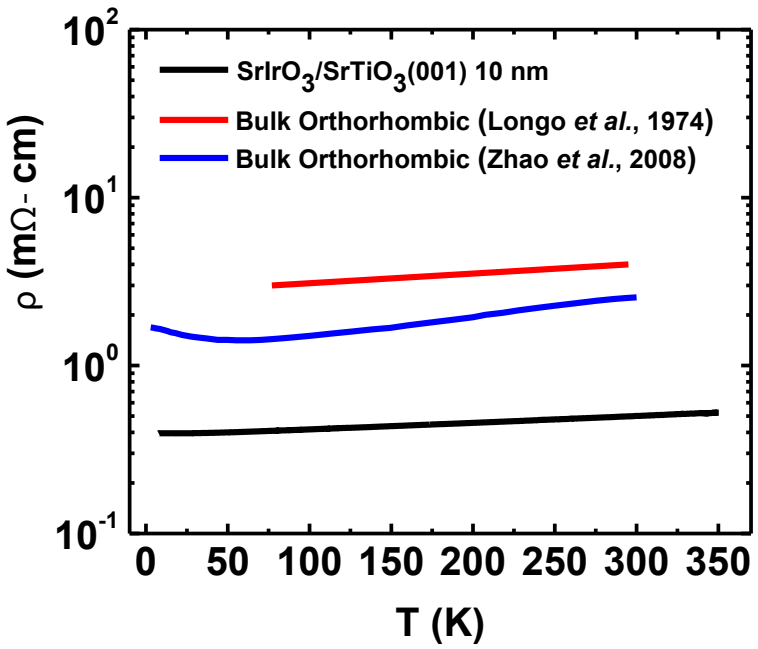


Figure 2.14: Resistivity vs. temperature of a 10 nm $SrIrO_3$thin film on $SrTiO_3$compared to known bulk orthorhombic studies (Longo *et al.*, 1974 and Zhao *et al.*, 2008).

films showed some sample to sample variation, likely due to the sensitive nature of the $SrIrO_3$ band structure, but also likely due to the previously-mentioned issues with the PLD target that have also been observed elsewhere.

2.9 Conclusions

To conclude this chaper, I have discussed basic elements of thin film epitaxy and the synthesis techniques of PLD as it pertains to ABO_3 thin films with *in situ* high-pressure RHEED. Next, the surface, structure, epitaxial arrangement of the high-quality $SrIrO_3$ films on $SrTiO_3$ substrates were discussed and presented along with the confirmation of high-quality epitaxy on additional perovskite substrates. The orthorhombic domain structure of the $SrIrO_3$ films was examined using x-ray diffraction, which revealed a mixed [001] orthorhombic domain structure along orthogonal in-plane $SrTiO_3$ substrate. Finally, the metallic transport of the $SrIrO_3$ film on $SrTiO_3$ was confirmed and compared with the previously reported bulk data. In the next chapter, I will discuss our work on the growth and structural characterization of $SrIrO_3$ thin films on the more unstable (111) ABO_3 surface.

Chapter 3

Metastable honeycomb $SrTiO_3/SrIrO_3$ heterostructures

3.1 $SrIrO_3$ and the (111) perovskite interface

As discussed in the introduction, iridates of pyrochlore $A_2Ir_2O_7$ (A = metal) and Ruddlesden-Popper $Sr_{n+1}Ir_nO_{3n+1}$ phases have generated considerable excitement due to a plethora of predicted and observed exotic physical properties believed to arise from the interplay between crystal field interactions, localized electron-electron correlations, and strong spin-orbit coupling[28–31,34,36,42,54,102,103]. Of particular interest here is the perovskite phase of $SrIrO_3$, which has attracted significant attention in the community due to recent theory predictions that it exhibits non-trivial band topologies when sandwiched in between (111) perovskite $SrTiO_3$ layers[31,34] Because these calculations are based on ultra-thin cubic perovskite $SrIrO_3$ rather than its previously discussed bulk monoclinic phase, fabrication of metastable phase thin films is the necessary gateway to probe these phenomena.

However, the equilibrium crystal structure of $SrIrO_3$ complicates the fabrication of (111) perovskite $SrIrO_3$ thin films. As stated in the introduction, the bulk ambient phase of $SrIrO_3$ assumes a monoclinic structure of space group *C2/c* that is energetically favorable at room temperature and atmospheric pressure (a = 5.604 Å, b = 9.62 Å, c = 14.17 Å, = 93.65°), shown in Figure

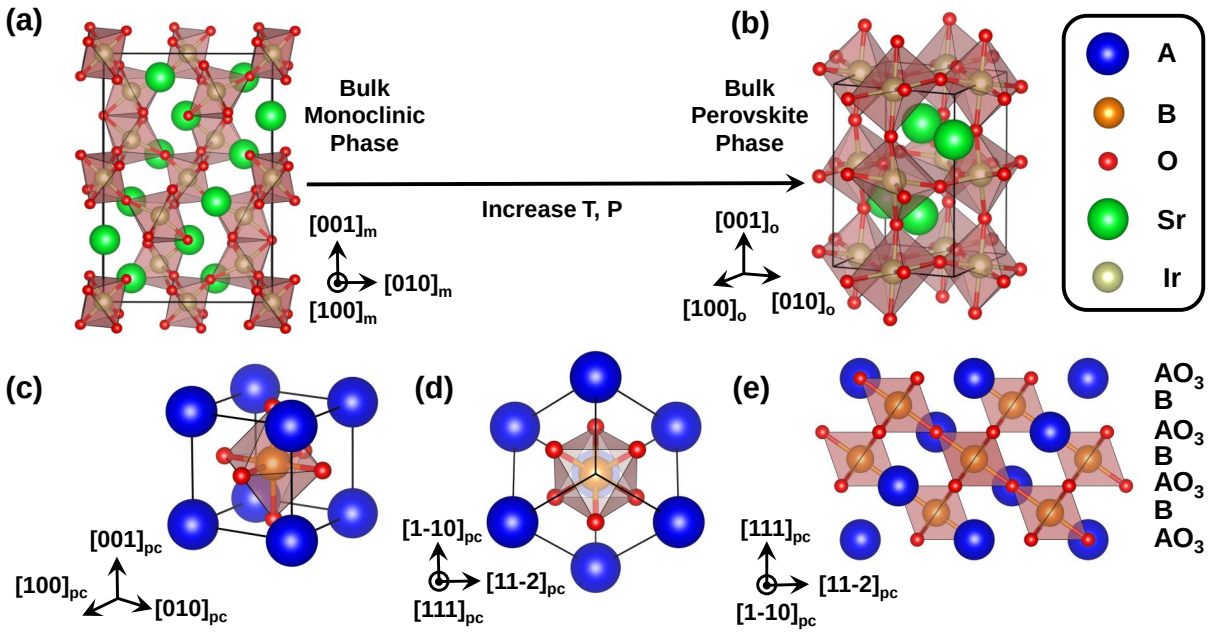


Figure 3.1: Schematics of (a) monoclinic $SrIrO_3$ (b) High pressure/high temperature perovskite $SrIrO_3$ (c) perovskite ABO_3 (d) Perovskite ABO_3(111) planar geometry with buckled hexagonal symmetry (e) planar stacking of the (111) cubic perovskite layering with AO_3 and B planar repeating units, i.e., a (111) bilayer.

3.1(a). However, a perovskite orthorhombic structure (a = 5.60 Å, b = 5.58 Å, c = 7.89 Å) of space group *Pbnm* is stable at high temperature and pressure, shown in Figure 3.1(b). A crucial distinction between these two bulk phases is that the monoclinic structure exhibits both face and corner IrO_6 octahedra sharing whereas the orthorhombic perovskite structure only exhibits corner sharing. Given this exclusive corner octahedral sharing in the orthorhombic case, it is helpful to redefine the unit cell as a pseudocubic[20] cell with a lattice parameter of 3.95 Å, which is close to those of conventional ABO_3 perovskite-structure [Figure 3.1(c)] substrates. This similar structural relationship has allowed synthesis of $SrIrO_3$ on perovskite (001)-oriented single-crystal substrates such as LSAT (3.87 Å), $SrTiO_3$ (3.90 Å), $DyScO_3$ ($\approx$ 3.94 Å), $GdScO_3$ ($\approx$ 3.96 Å), and $NdScO_3$ ($\approx$ 3.99 Å) in single-layer films[40–42,83], and superlattices[44].

However, $SrIrO_3$ growth on (111) $SrTiO_3$ has produced (001) monoclinic $SrIrO_3$[104,105]. This is possibly explained by the fact that (001) monoclinic $SrIrO_3$ is equivalent to a distorted 6H hexagonal structure[39] with in-plane hexagonal lattice parameters similar to the buckled hexagonal in-plane lattice of (111) perovskites [Figure 3.1(d)]. While the fabrication of perovskite iridate (111) films

has been demonstrated by tuning the iridate lattice constant by doping the A-site cation[105], pure perovskite (111) $SrIrO_3$ remains unreported. The (111) stacking of perovskites consists of two planes, AO_3 and B, that together constitute the (111) surface-normal repeating unit [Figure 3.1(e)], which we will hereafter refer to as a bilayer. Two of these bilayers (with spacing of 2.28 Å and 2.25 Å for perovskite $SrIrO_3$ and $SrTiO_3$, respectively) form the buckled honeycomb symmetry in (111) perovskites. Since monoclinic $SrIrO_3$ is evidently more stable on (111) perovskite substrates, any critical thickness of coherent perovskite $SrIrO_3$ on (111) $SrTiO_3$ is expected to be quite thin. Therefore, our approach was to grow ultra-thin films on the thickness order of several bilayers to ensure that our $SrIrO_3$would be perovskite phase. Finally, we capped the $SrIrO_3$ with $SrTiO_3$ to impose symmetric structural boundaries on the $SrIrO_3$ films. Our efforts to stabilize perovskite (111) $SrIrO_3$ thicker than 6-7 bilayers produced films with mixed amorphous and polycrystalline phases, so it would indeed seem that the critical thickness of single crystal perovskite $SrIrO_3$ is quite thin on (111) perovskite substrates compared to (001).

3.2 Synthesis and surface of $SrTiO_3/SrIrO_3$ heterostructures

The $SrTiO_3/SrIrO_3$ thin film heterostructures were grown using pulsed laser deposition (PLD) with a KrF 248nm excimer laser. The growth was monitored *in situ* with high-pressure reflection high energy electron diffraction (RHEED). Before deposition, the substrate surfaces were carefully treated by immersion in a buffered HF acid solution followed by annealing at 1000 °C for 6 h in a quartz tube furnace with flowing oxygen followed by a second immersion in the buffered HF. This assured that our substrates were atomically smooth with single-atom termination at the surface. The $SrIrO_3$ ceramic target used for the film growth was manufactured commercially by the spark-plasma sintering method, and the $SrTiO_3$ films were grown from a single-crystal commercial target. The $SrIrO_3$ films were grown at a substrate temperature of 550°C in an O_2 partial pressure of 10^{-1} mbar, and a target-to-substrate distance of 58 mm. The laser energy density was 1.5-2 J/cm2 and the pulse repetition rate was 3 Hz. The capping $SrTiO_3$ bilayers were deposited in the same environment as the $SrIrO_3$, with a repetition rate of 5 Hz. This was done to prevent damage to the $SrIrO_3$film quality by changing the chamber environment.

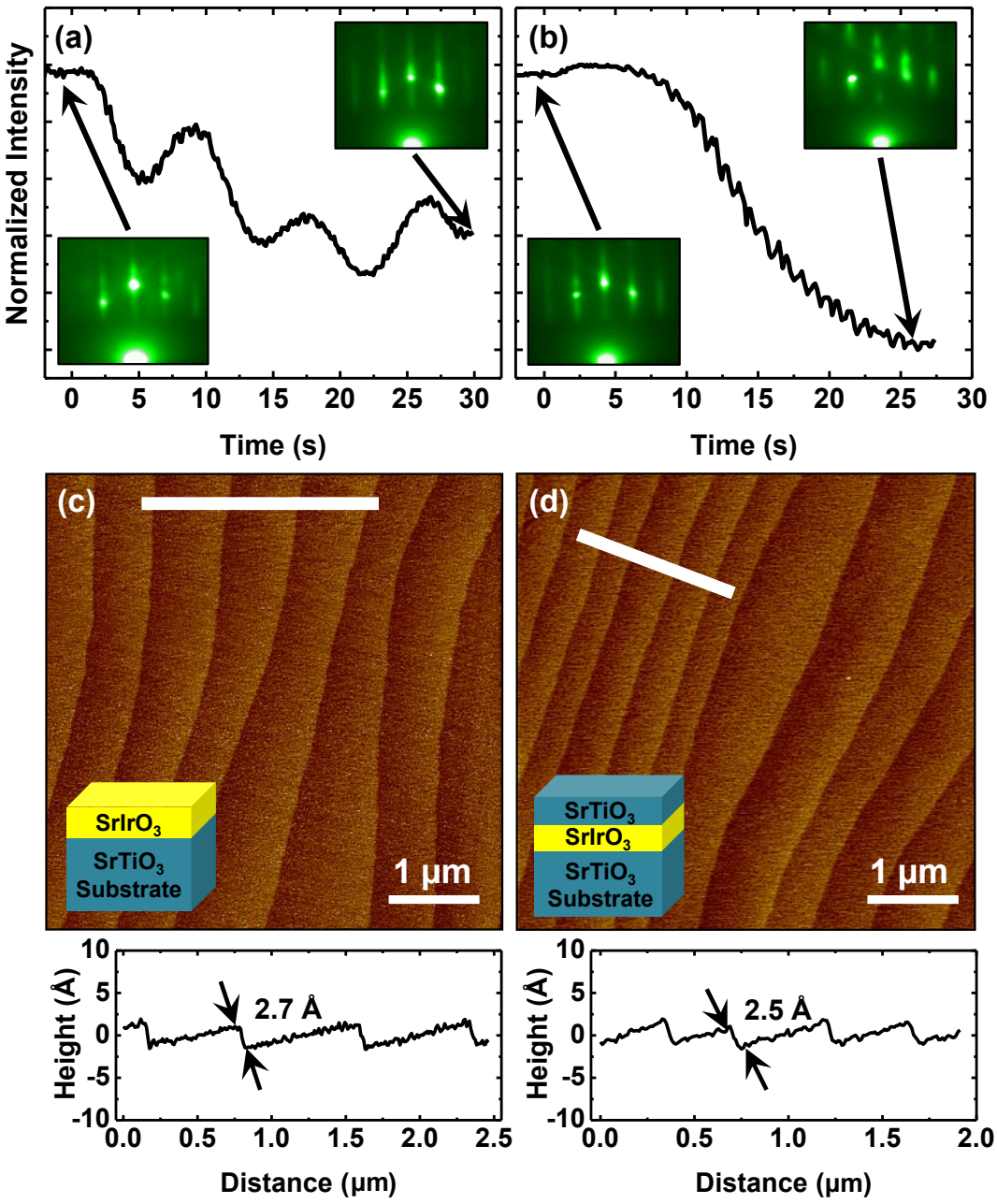


Figure 3.2: (a) In situ high pressure RHEED intensity oscillation spectrum of the specular spot during the growth of a bare 3 bilayer $SrIrO_3$ film with RHEED diffraction patterns of the substrates before growth (left inset) and $SrIrO_3$ surface at the end of the growth (right inset). The intensity oscillations and streaky RHEED image patterns of the diffraction spots indicate layer-by-layer growth. (b) $SrTiO_3$ growth with RHEED image of the $SrIrO_3$ film before $SrTiO_3$ growth (left inset) and $SrTiO_3$ surface at the end of the growth (right inset). (c) AFM image of the bare $SrIrO_3$ film in (a) showing an atomically smooth film surface with cross-sectional profile (white line) indicating single bilayer step-terrace heights. (d) AFM image of a similarly ultra-thin $SrIrO_3$ film capped with a 5 bilayer $SrTiO_3$ film with cross-sectional profile (white line) showing preservation of the atomically flat surface and single bilayer step-terrace height.

Figure 3.2 summarizes the growth of both bare $SrIrO_3$ films and $SrTiO_3$/$SrIrO_3$ heterostructures. The clear in situ RHEED specular spot intensity oscillations [Figure 3.2(a)] indicate layer-by-layer growth of our $SrIrO_3$ films. A single oscillation corresponds to one bilayer of $SrIrO_3$. Thus, the data in Figure 3.2(a) represent a 3 bilayer $SrIrO_3$ film. The RHEED image of the $SrIrO_3$ film surface in the right insets of Figure 3.2(a) exhibits streaky patterns over the substrate diffraction spots, also an indication of layer-by-layer growth. The left inset in Figure 3.2(a) shows the RHEED image of our $SrTiO_3$ substrate right before growth. The AFM surface morphology for the bare $SrIrO_3$ film in Figure 3.2(c) shows clear substrate step-terrace preservation with step heights on the order of a single perovskite bilayer spacing. As shown in Figure 3.2(b) and its insets, the $SrTiO_3$ growth does not show layer-by-layer growth on a similarly ultra-thin $SrIrO_3$ film, as no oscillations were observed and the RHEED pattern in the right inset shows spots rather than streaks, indicating a rougher capping $SrTiO_3$ surface than the underlying $SrTiO_3$ surface. This is likely attributable to the fact that we grew our $SrTiO_3$ at the same conditions as the $SrIrO_3$, which differ from those used for epitaxial $SrTiO_3$ growth. Nonetheless, the step-terrace structure from the underlying substrate and bare $SrTiO_3$ film is still preserved. Examination of the RHEED images of either film reveals no noticeable half-order peaks between the primary diffraction spots that would suggest a lower symmetry than that of the cubic $SrTiO_3$ substrate. It should also be noted that the terrace step height of the $SrTiO_3$/$SrIrO_3$ heterostructure is smaller than that of the bare $SrIrO_3$ film, which is expected given that the $SrTiO_3$ (111) bilayer spacing is smaller than that of $SrIrO_3$.

3.3 Epitaxial arrangement and symmetry from STEM/XRD

We determined the symmetry and epitaxial arrangement of the heterostructures using both scanning transmission electron microscopy (STEM) and synchrotron surface X-ray diffraction. First, STEM experiments on a 3 bilayer $SrIrO_3$ film capped with 5 bilayers of $SrTiO_3$ were performed. Figure 3.3(a) shows the filtered cross-sectional STEM high-angle annular dark field (HAADF) image of the heterostructure. The contrast of the STEM-HAADF image is approximately proportional to the atomic number Z, where brighter colors represent heavier elements. Here, we see that the brightest atoms, iridium (highest Z), are confined to the B-site columns in 3 bilayers. This indicates sharp

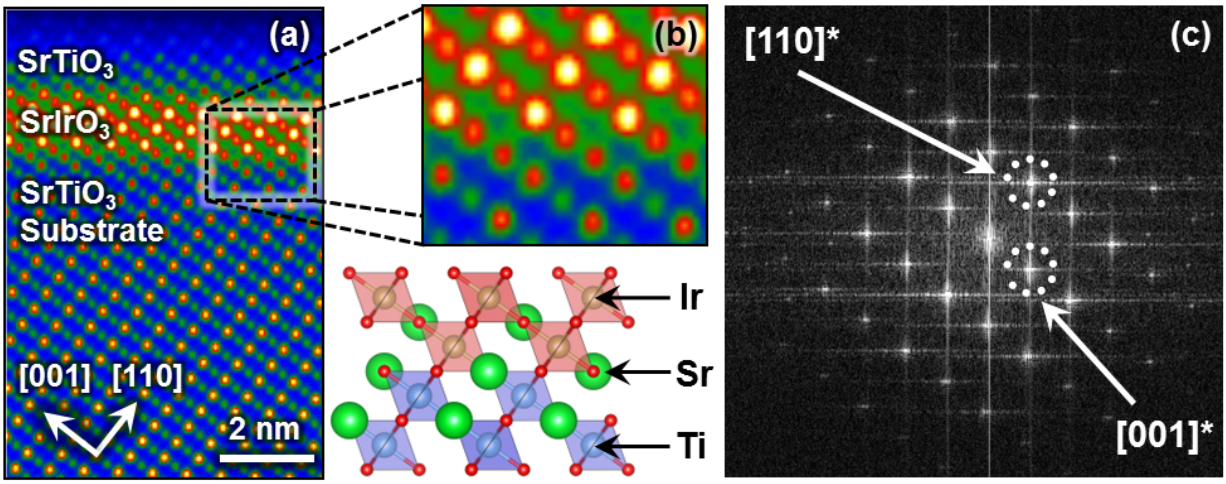


Figure 3.3: (a), (b) Filtered cross-sectional STEM HAADF images of a 3 bilayer $SrIrO_3$ film capped with a 5 bilayer $SrTiO_3$ along the [1-10] zone axis, suggesting a perovskite epitaxial layering with the bright iridium (highest Z) atoms confined to the 3 bilayer $SrIrO_3$ film region and B-site column (c) FFT of the image in (a) implying structural coherence of the $SrTiO_3$/$SrIrO_3$ heterostructure with the underlying $SrTiO_3$ substrate.

$SrIrO_3$interfaces with the $SrTiO_3$ substrate and the capping $SrTiO_3$ film. Additionally, these layers have the same stacking as those in the $SrTiO_3$ substrate, more easily seen in the magnified image and structural cartoon in Figure 3.3(b). This layering should be immediately distinguishable from the layering of monoclinic $SrIrO_3$ depicted in Figure 1(a). From this image, we extracted the FFT diffraction pattern, shown in Figure 3.3(c), which shows the symmetry of the entire filmfilmsubstrate heterostructure. The FFT shows a pattern that is characteristic of the much thicker $SrTiO_3$ substrate with no signature of additional lower-symmetry diffraction spots from the film layers. This suggests good coherence of the $SrTiO_3$/$SrIrO_3$ heterostructure with the underlying $SrTiO_3$ substrate, which would indicate equivalent in-plane symmetry for the entire 3 layers. However, given how thin our $SrIrO_3$ films were, we could not reliably confirm their symmetry solely from STEM due to the resolution limits of the FFT. Thus, from STEM, we were able to determine that our heterostructure exhibited sharp interfaces and shared the same epitaxial arrangement as the $SrTiO_3$ substrate, but more work was needed to confirm the hetero-structure symmetry.

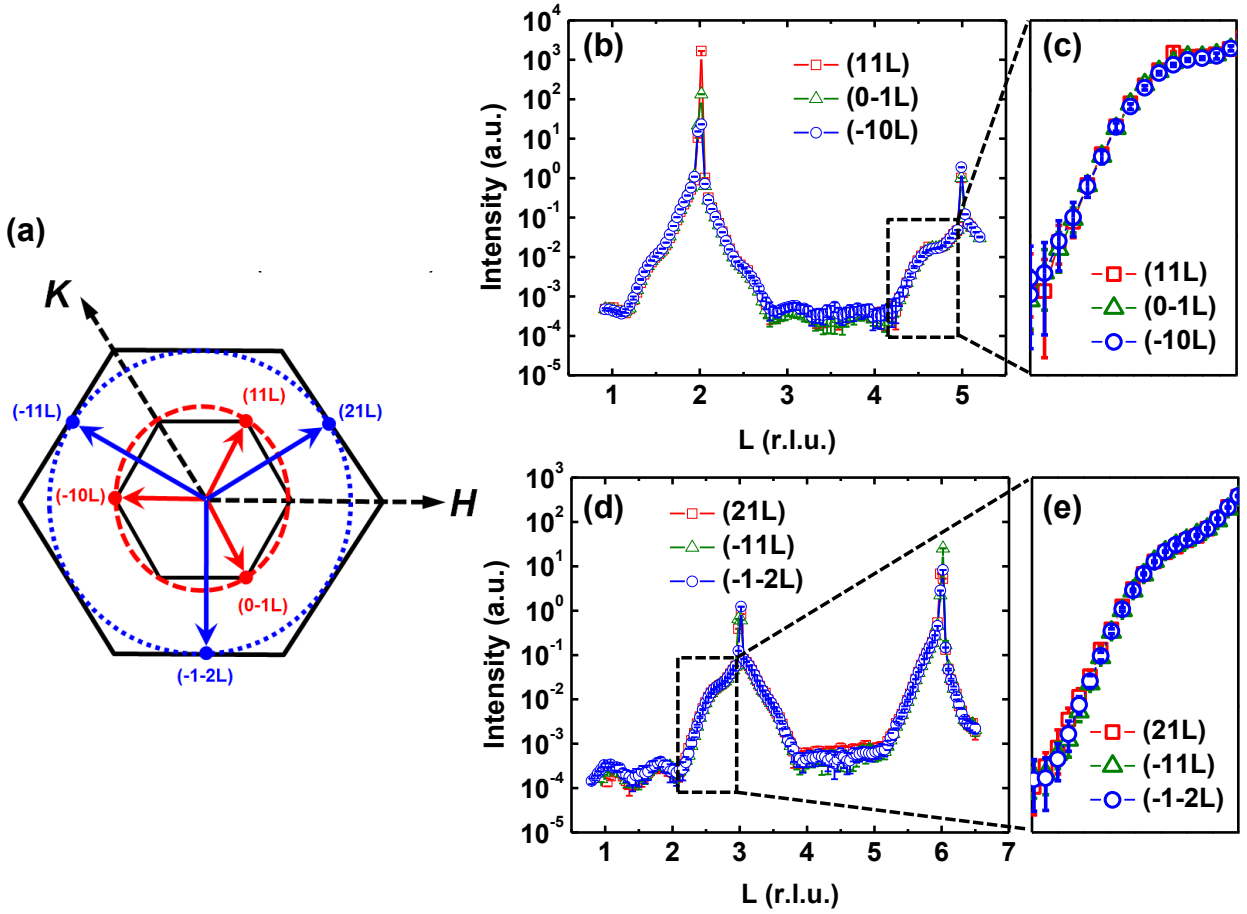


Figure 3.4: (a) {11L} and {21L} CTR families that would exhibit 3-fold in-plane symmetry in pseudo-cubic crystal structures, shown in a reciprocal lattice HK grid. (b), (d) CTR intensities of {11L} and {21L}, respectively, of the $SrTiO_3/SrIrO_3$ heterostructure with the 3 CTRs in each family superimposed. (c), (e) Magnified regions of the CTR intensity at reciprocal space points near the substrate Bragg peaks of (b) and (d), respectively. As can be seen in (c) and (e), there is no intensity deviation within either CTR family at each reciprocal space point, thus showing that our total heterostructure has the same in-plane symmetry as the $SrTiO_3$ substrate.

To unambiguously determine the film symmetry, we carried out surface X-ray diffraction measurements in the 33-ID-D beamline at the Advanced Photon Source with the samples mounted on a Kappa 4 + 2 circle diffractometer along with a Pilatus 100K 2D pixel area detector. Our approach was to start with an ansatz of 3-fold in-plane symmetry for the entire heterostructure (what we believed from our STEM work) and scan 2 sets of crystal truncation rod (CTR) families carefully chosen to exhibit in-plane 3-fold symmetry under our ansatz. From Figure 3.4(a), one CTR family, {11L}, intersects the reciprocal-space nodes of the hexagonal perovskite (111)

system, whereas the other, $\{21L\}$, intersects the nodal midpoints. If the heterostructure indeed had 3-fold symmetry in-plane, the CTR intensity features at each reciprocal space point for all 3 symmetry equivalent CTRs in the family would be identical. If not, the 3 spectra would exhibit distinct intensity differences at equivalent reciprocal space points due to diffraction points originating from a crystal structure different from that of the cubic perovskite substrate. This would indicate lattice an-isotropy in the $SrIrO_3$ layers, and hence, a different symmetry. Since these CTRs are quite sensitive to atomic layering, any deviations from the expected buckled honeycomb structure would be easily discernable from the intensity features, and any different phases present would be thus distinguishable. Thus, by choosing these 2 CTR families, the in-plane symmetry of our heterostructures would be unequivocally evident.

In Figures 3.4(b) and 3.4(b), we see the 3 symmetry equivalent CTRs superimposed on the same plot of the $\{11L\}$ and $\{21L\}$ families, respectively. Overall, the intensity spectra for the 3 rods in each family are virtually indistinguishable and, thus, indicate no structural difference along each CTR. The most deviation between equivalent CTRs (but still within experimental error) is observed in the mid-zone region halfway between the Bragg rods, but this region is more sensitive to surface atomic structure rather than the entire heterostructure and its in-plane symmetry. Of the utmost importance for our study is the CTR intensity at the reciprocal space points near the substrate Bragg peaks, which are structural indications of the overall heterostructure. From the magnified regions of these spectra [Figures 3.4(c) and 3.4(e)], we see that it is impossible to distinguish any difference between the 3 CTRs for each family near the substrate Bragg peak. Since the footprint of the $SrTiO_3$ substrate, known to have the (111) buckled honeycomb symmetry we were looking for (as previously discussed), is present in these scans, we can conclude that the $SrTiO_3/SrIrO_3$ films have that equivalent in-plane structure and layering, and no other symmetries or phases exist. Therefore, the measured spectra of these CTR families give strong constraints on the overall in-plane pseudocubic perovskite symmetry of our heterostructures.

3.4 Conclusions

In conclusion, we have demonstrated the synthesis of metastable perovskite $SrTiO_3$/$SrIrO_3$ heterostructures on (111) $SrTiO_3$ substrates using pulsed laser deposition with in situ high pressure RHEED. Our STEM and synchrotron surface X-ray diffraction results demonstrate the ability to stabilize honeycomb $SrIrO_3$ on (111) $SrTiO_3$. Now that perovskite (111) $SrIrO_3$synthesis has been confirmed, it may be interesting to examine these heterostructures with surface-sensitive angle resolved photoemission spectroscopy (ARPES) to discern if the predicted non-trivial band topologies are realized. Additionally, the role of electron correlations on the electronic properties of (111) $SrIrO_3$ bilayers has recently been predicted to be significant[56], so this can also be studied now that these metastable structures can be synthesized. Thus, our work has overcome the initial obstacle of (111) perovskite $SrIrO_3$ synthesis and serves as the groundwork to proceed with further experiments on this material system. In the next chapter, I will present a quantitative interfacial structure comparison between this polar (111) heterostructure with its non-polar analogous (001) heterostructure.

The research presented in this chapter used resources of the Advanced Photon Source, a U.S. Department of Energy (DOE) Office of Science User Facility operated for the DOE Office of Science by Argonne National Laboratory under Contract No. DE-AC02-06CH11357.

The results in this chapter were published in Applied Physics Letters and reprinted with permission from the American Physical Society[106].

Chapter 4

Interfacial B-site atomic configuration in polar (111) and non-polar (001) $SrIrO_3/SrTiO_3$ heterostructures

4.1 Polar perovskite (111) surfaces and interfaces

The precise control of interfacial atomic arrangement in ABO_3 perovskites is paramount, particularly in cases where the subsequent electronic properties of the material exhibit geometrical preferences along polar crystallographic directions that feature inevitably complex surface reconstructions. While synthesis along the (001) direction has historically received the most attention in the perovskite oxide research community, there has recently been significant theory work predicting topological insulators[34,107], flat bands with a non-zero Chern number[31], and various correlated electronic phases[56,108,109] in perovskite oxide heterostructures synthesized in the (111) direction. However, growth in the (111) perovskite direction is challenging due to the polar nature of the surface, which is prone to complicated reconstructions that are difficult to control. Nonetheless, buoyed by the previously mentioned theoretical inspiration, (111) perovskite epitaxial film synthesis has been reported to date in bilayer/trilayer architectures[17,110–115] and also superlattices[105,116–118], growth along the (111) direction has unlocked phenomena that do not exist in the (001) case, thus reveal-

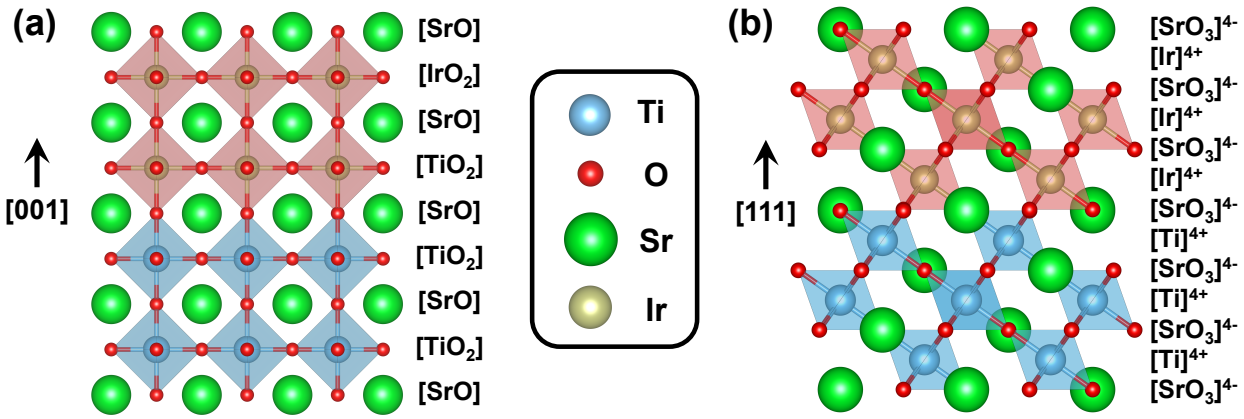


Figure 4.1: (a), (b) Planar layering for (111) and (001) $SrIrO_3/SrTiO_3$ heterostructures, respectively.

ing emergent properties that depend on crystal orientation and lattice symmetry[17,116,119]. Given these findings, careful attention must be paid to the initial growth and quality of the perovskite interfacial structure and correlate the interfacial behaviors with the observed physical phenomena.

The surface layering in (111) and (001) heterostructures for the specific case of $SrTiO_3$ on $SrTiO_3$, as a prototypic model system, is illustrated in Figure 4.1(a) and Figure 4.1(b). As can be seen, the (111) structure exhibits $AO_3$and B layering (hereafter referred to as a bilayer) which yields highly polar 4+/4- charge planes. By contrast, the (001) unit cell layering is charge neutral, and thus completely non-polar. Therefore, the polarity along the (111) creates a diverging electrical potential that must be screened by reconstructions and/or charge depletion layers, which complicate subsequent epitaxial growth of thin films. It has been demonstrated that the insertion of metallic buffer layers[112], a reduction in growth temperature[114], A-site cation mixing with the underlying substrate surface[115], and the formation of oxygen vacancies at the interface[120] can stabilize subsequent epitaxy on the (111) surface. In this study, we report that B-site intermixing with the underlying substrate is yet another effective route to mitigate epitaxial growth on polar (111) surfaces. We chose to investigate this idea in ultra-thin $SrIrO_3$ layers epitaxially grown on both (001) and (111) $SrTiO_3$ and make a quantitative comparison of the interfacial abruptness in both cases. A capping layer of $SrTiO_3$ was grown on the $SrIrO_3$ to protect these ultra-thin films from the ambient[84]. Our choice of materials eliminated the possibility of A-site cation intermixing, which would complicate the analysis of our results. Another advantage to these particular heterostruc-

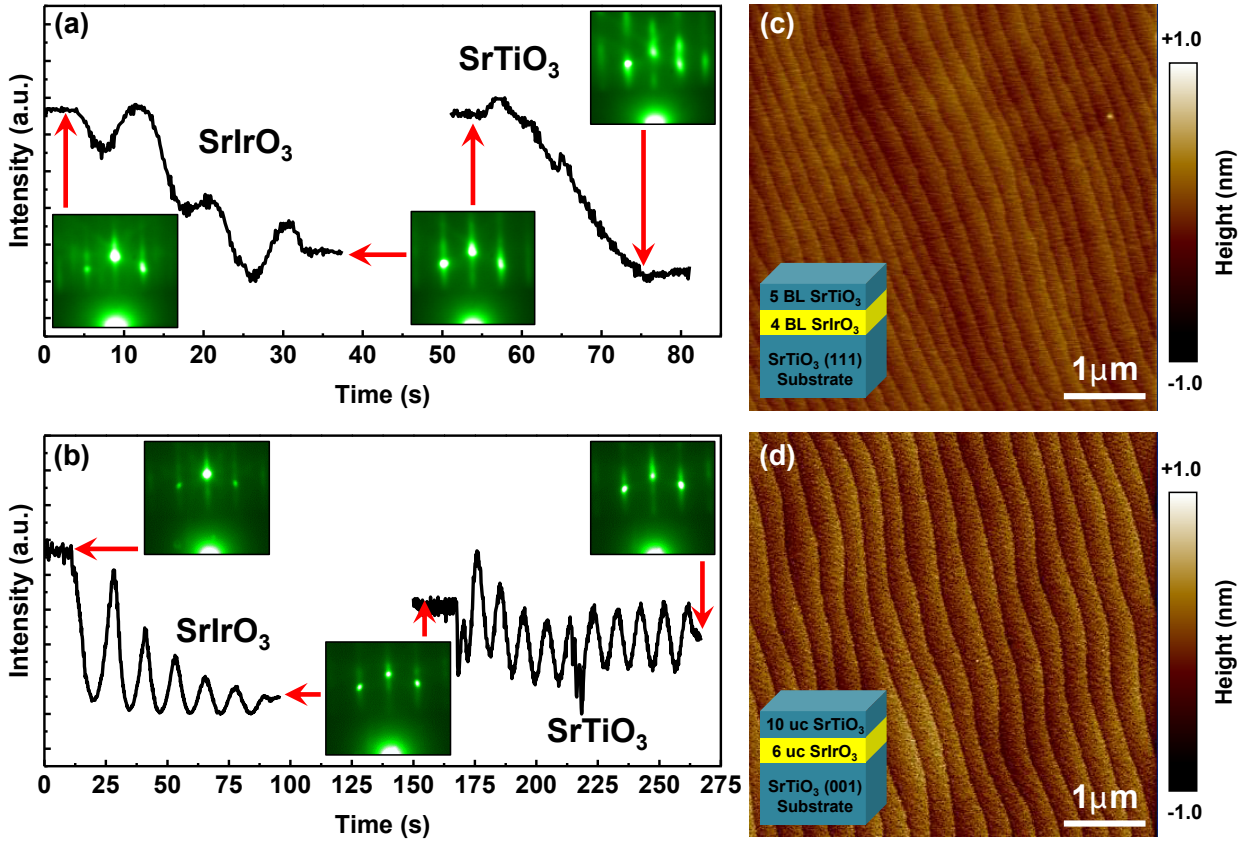


Figure 4.2: (a), (b) RHEED intensity of the specular diffraction spot for the (111) and (001) $SrIrO_3/SrTiO_3$ heterostructures, respectively, showing layer-by-layer growth except in the case of the (111) $SrTiO_3$ capping film. The RHEED pattern insets in both plots show from left to right the $SrTiO_3$ substrate surface, final $SrIrO_3$ surface, and final $SrTiO_3$ capping layer surface (c), (d) AFM images of the heterostructures in (a) and (b) showing atomically-smooth surfaces.

tures was the absence of a polar discontinuity between layers, as both materials exhibit the same degree of surface polarity in either direction. Finally, since the (001) case is completely non-polar, a direct comparison could be made between interfacial sharpness and the resulting structure of polar/polar and non-polar/non-polar interfaces.

4.2 $SrIrO_3/SrTiO_3$ heterostructure synthesis

The $SrIrO_3/SrTiO_3$ heterostructures were grown with atomic layer precision using pulsed laser deposition with in situ reflection high energy electron diffraction (RHEED). The exact growth recipe is described elsewhere in the previous chapter. The (111) samples were 4 bilayers (0.9 nm) of $SrIrO_3$ capped with 5 bilayers (1.1 nm) of $SrTiO_3$ and the (001) samples were 6 unit cells (2.4

nm) of $SrIrO_3$ capped with 10 unit cells (3.9 nm) of $SrTiO_3$. Figure 4.2(a) and 4.2(b) summarizes the growth of the (111) and (001) heterostructures. All films with the exception of the (111) $SrTiO_3$ capping film show layer-by-layer growth with the preservation of the initial substrate surface structure as indicated by the RHEED patterns at the growth temperature. Atomically smooth surfaces were confirmed by Atomic force microscopy (AFM) in Figure 4.2(c) and 4.2(d). It should be noted that the while the thickness from RHEED of the (111) $SrIrO_3$ should be between 3-4 bilayers thick by counting the RHEED oscillations in Figure 4.2(a), the following microscopy and x-ray work showed the thickness of this layer to be 4 bilayers. It has been reported that discrepancies can exist between determining thicknesses from RHEED oscillations and other thickness methods[80], so we attribute our sub-bilayer thickness discrepancy to this fact.

4.3 TEM and COBRA experiments

We first performed scanning transmission electron microscopy experiments to examine the interfaces of the (111) and (001) $SrIrO_3/SrTiO_3$ heterostructures. In Figure 4.3(a) and 4.3(b), we show the filtered cross-sectional STEM high-angle annular dark field (HAADF) image of the 2 heterostructures, where the contrast of the STEM-HAADF is proportional to the Z-number of the atomic constituents. Here we see that the (001) and (111) stacking arrangement described back in Figure 4.1 is assumed by both heterostructures, in which the brightest spots are the Ir atoms (highest Z). From these filtered images, we integrated and averaged line intensity profiles along the B-site columns (Ti and Ir) of the STEM images to examine the interfacial sharpness of each sample, shown in Figures 4.3(c) and 4.3(d). A sharp unmixed interface along these Z-sensitive columns would exhibit a sudden intensity increase across interfaces since the atomic number of Ti (22) is much lower than that of Ir (77), whereas a mixed interface would exhibit peaks with intermediate intensities between those of the baseline Ti/Ir constituent atoms. In the (111) heterostructure, shown in Figure 4.3(c), we indeed observe such intermediate intensities at both the Ti-terminated $SrTiO_3$ substrate and also at the Ir-terminated $SrIrO_3$ film, indicating Ti/Ir intermixing at both the bottom and top interfaces. The (001) sample, shown in Figure 4.3(d) shows little evidence of significant intermixing, as the intensity peaks near the interfaces do not show

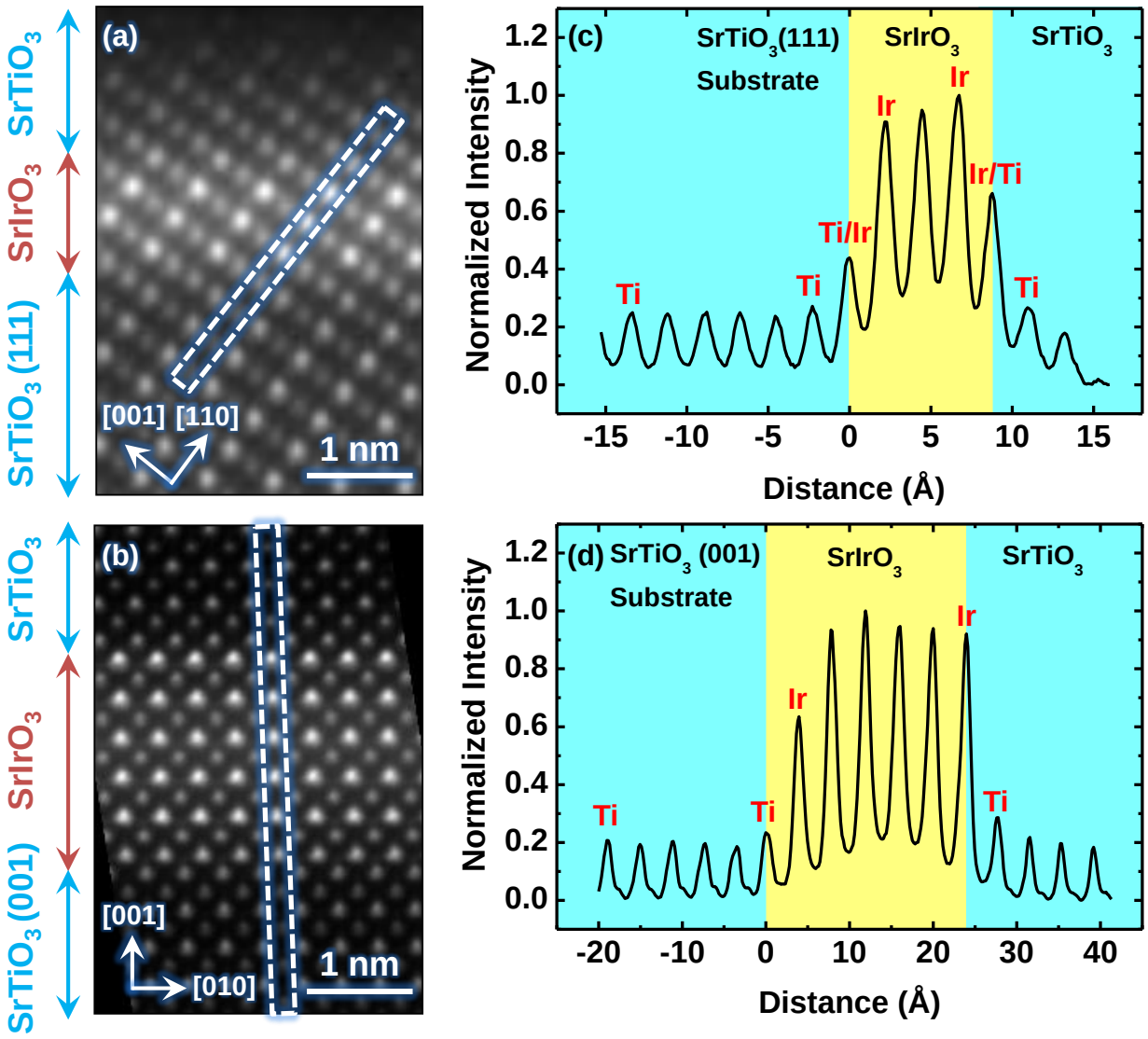


Figure 4.3: (a), (b) Filtered cross-sectional STEM-HAADF images of $SrIrO_3/SrTiO_3$ heterostructures for the (111) and (001) samples, respectively (c), (d) Averaged integrated line intensities along the B-site column in the (111) and (001) heterostructures, respectively.

such intermediate values. While it may be noted that the intensity of the first Ir peak in the (001) heterostructure is lower than that of the subsequent Ir layers, we attribute this to localized Ir vacancies in this particular region of the sample rather than global intermixing of this layer since the intensity of the adjacent Ti column in the $SrTiO_3$ substrate is quite close to the bulk baseline. An equivalent examination of the A-site columns showed very little intensity deviation in either sample within reasonable measurement error [See Appendix B, Figure B.1], which is as-expected, given that both contain the same element (Sr). Thus, from our STEM work, we concluded that any atomic intermixing was confined to the B-site at the interfaces of the (111) sample. However, quantitatively characterizing the intermixing was not performed as the $SrIrO_3$ electron energy loss spectroscopy (EELS) is challenging due to the heavy Ir constituents energy loss, which is over 2000 eV for the $M_{4,5}$ edges. Thus, a reliable quantitative analysis of the intermixing was not possible from STEM. Nonetheless, our results provided motivation to further investigate these films with qualitative techniques.

To gain this quantitative insight, we examined the layered interface of the (111) and (001) $SrIrO_3/SrTiO_3$ heterostructures with synchrotron X-ray crystal truncation rod (CTR) measurements at sector 33-ID-D at the Advanced Photon Source (Argonne National Laboratory) that were subsequently analyzed using the coherent Bragg rod analysis[121] (COBRA) method. For consistency purposes, the sample thicknesses were kept identical to those of the STEM work. The measured specular crystal truncation rod (CTR) curves for (001) and (111) oriented $SrIrO_3/SrTiO_3$ heterostructures [Figure 4.4(a) and 4.4(a)] and the COBRA calculated CTRs exhibit good agreement and show discernable features in the mid-zone regions which provide information about the surface and interfacial characteristics of the heterostructures.

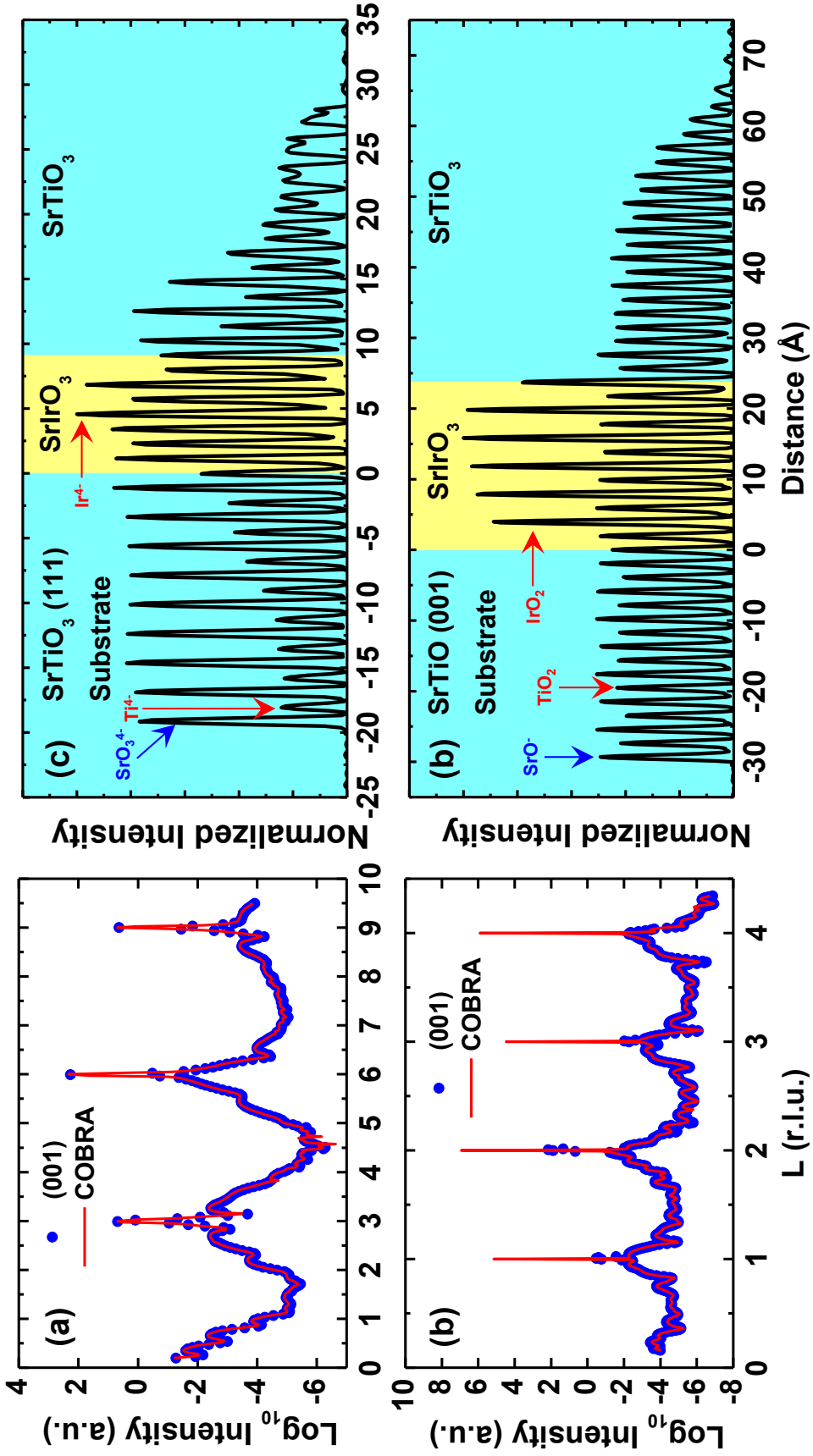


Figure 4.4: (a), (b) Specular crystal truncation rod scans of the (111) and (001) samples, respectively, showing discernable midzone features and good agreement with the COBRA calculated CTRs. (c), (d) Layer-by-layer electron densities as a function of distance normal to the surface of the (111) and (001) $SrIrO_3/SrTiO_3$ heterostructures, respectively. The origin on the x-axis denotes the position of the $SrIrO_3$ film/$SrTiO_3$ substrate. interface.

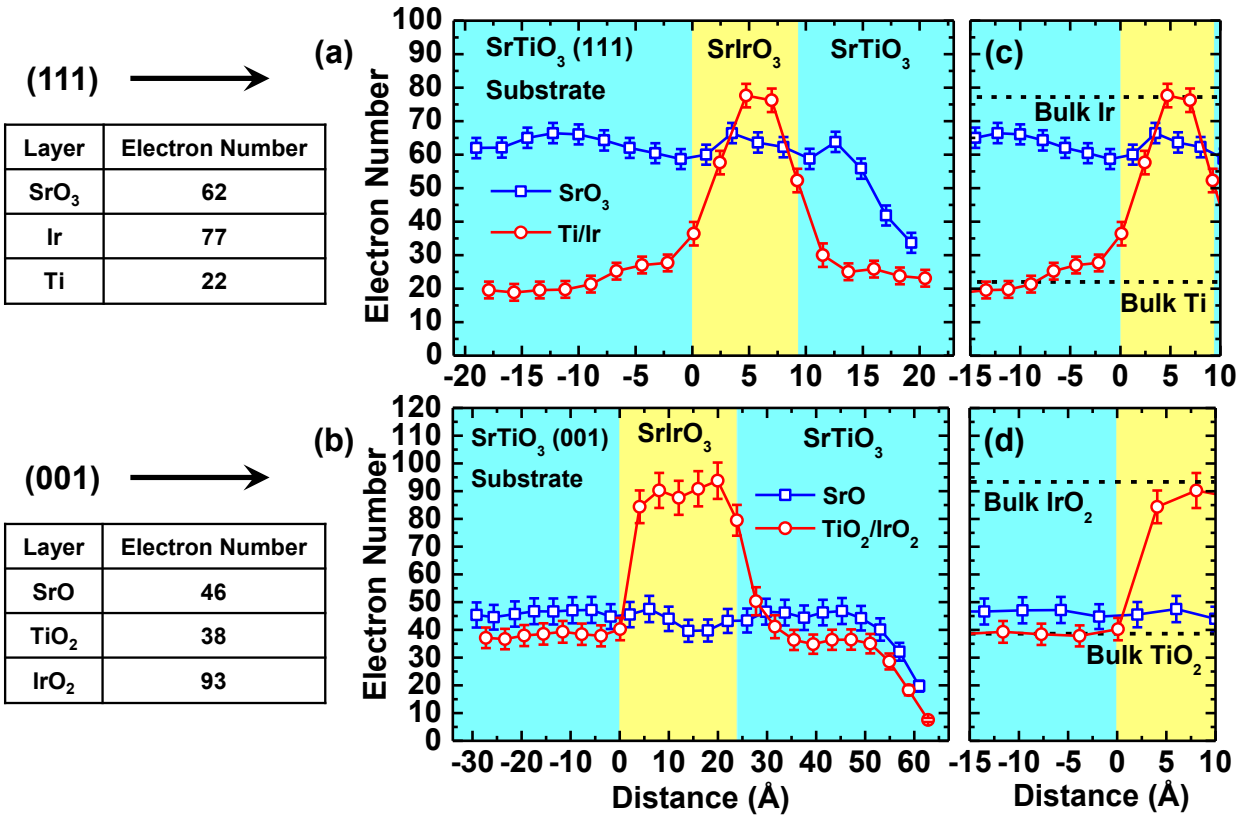


Figure 4.5: (a), (b) COBRA-extracted electron numbers as a function of planar layering for (111) and (001) $SrIrO_3/SrTiO_3$ heterostructures, respectively (c), (d) enlarged area of (a) and (b) close to the origin. As can be seen in (c), there is a pronounced monotonic increase in the electron number of the substrate B-planes approaching the interface with the $SrIrO_3$ film. This feature is not observed in the BO_2 planes of the (001) $SrTiO_3$ substrate in (d). The origin on the x-axis denotes the position of the $SrIrO_3$ film/$SrTiO_3$ substrate interface. It should be noted that the decrease in electron number of the top $SrTiO_3$ layers is due to incomplete coverage in these layers.

Using the COBRA method, we extracted the layer-by-layer electron density profile as a function of position normal to the surface of the sample [Figure 4.4(c) and 4.4(d)], and from there, the planar integrated electron numbers for each film from the CTRs, shown in Figure 4.5. In all COBRA analysis presented in this work, the origin on the x-axis denotes the position of the $SrIrO_3$ film/$SrTiO_3$ interface. As can be seen in Figure 4.5(a) and 4.5(b), the integrated electron numbers of the AO_3 and AO layers in the (111) and (001) samples do not show much deviation across the entire heterostructure, as was the case with the previously discussed STEM observations. However, inspection of the B layers near the $SrIrO_3/SrTiO_3$ (111) substrate interface in Figure 4.5(c) reveals variation from the expected values in the Ti planes (Z = 22) in the $SrTiO_3$ substrate. As with the

previous STEM data discussion, a sudden jump from Z= 22 (Ti) to Z = 77 (Ir) would be expected in the case of a sharp interface. However, a gradual increase in Z is observed 3-4 bilayers into the $SrTiO_3$ substrate moving 1-2 bilayers into the $SrIrO_3$ film. The B-site in this regime exhibits Z numbers that range between the expected values of Ti and Ir, which suggests Ti and Ir are intermixing to create this mid-level Z number between those of Ti and Ir. An analogous comparison of the BO_2 planes in the (001) sample [Figure 4.5(d)] shows no such intermixing, as a sudden change in BO_2-plane Z value from the expected 38 (TiO_2) to close to 93 (IrO_2) is observed moving across the substrate into the $SrIrO_3$ film. These results quantitatively illustrate that B-site intermixing is more pronounced in the (111) heterostructure.

It should be noted that the observed B-site cation intermixing in the (111) sample is not expected to be due to oxygen point defects or a formation of a different phase because the existence of either would presumably result in a lattice spacing change in these layers, which was not observed in either sample geometry [See Appendix B, Figure B.2]. Furthermore, while it could be suggested that intermixing is favorable since Ir and Ti assume the same valence state (4+) in these heterostructures and also that their ionic radii are similar[122], this would not explain why intermixing would be only preferable in the (111) direction and not also the (001). We thus conclude that the gradual Z value increase in the substrate near the (111) $SrIrO_3$ film is explained by intermixing of Ir and Ti at the interface.

The mechanism we propose to explain these observations lies in the interplay between the difference in surface polarity of the two directions and the reconstructed surface of treated $SrTiO_3$ prior to the the growth of $SrIrO_3$. Both the (111) and (001) $SrTiO_3$ substrates for this work were etched in buffered hydrofluoric (BHF) acid following by thermal annealing[68,70,72] and a 2nd BHF etch to ensure removal of all SrO_x from the surface. However, it is known that such treatments of (001) and (111) $SrTiO_3$ substrates exhibit exhibit TiO_x-surfaces[115,123–126]. Thus, it is expected that B-site intermixing during subsequent film growth would be likely as these layers are exposed on the surface. To confirm this, we examined the initial surface prior to growth, analogous COBRA experiments on (111) and (001) $SrTiO_3$ substrates were performed. To get an accurate picture of the substrate surfaces directly prior to growth, the COBRA CTRs were measured in a vacuum chamber

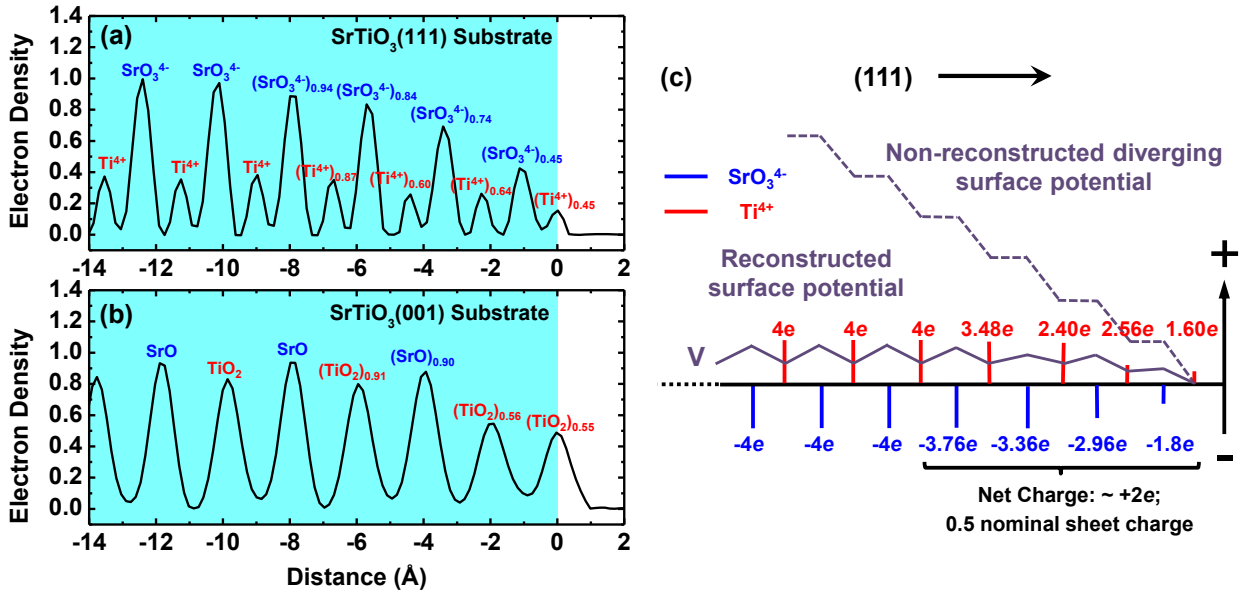


Figure 4.6: (a), (b) COBRA-resolved planar electron densities of like-treated (111) and (001) $SrTiO_3$ substrates, respectively, at a growth condition of 550°C and 10^{-3} mbar oxygen partial pressure. The top 4 bilayers near the surface of the (111) substrate show significant charge depletion, which is likely a result of the diverging polar potential at the surface and the surface treatment prior to growth. Such depletion is not observed in the (001) substrate, where only the top 2 atomic layers are significantly depleted (c) Poisson model illustrating the resultant potential along the (111) substrate surface that arises to compensate the diverging potential along the nominal (111) layering. The net charge in the top 4 bilayers of the (111) $SrTiO_3$ substrate to screen the diverging potential is +2*e*, or about +0.5 *e*/layer.

at 550 °C and 10^{-3} mbar oxygen partial pressure. In Figure 4.6(a) and 4.6(b), the COBRA-extracted electron densities are shown for (111) and (001) $SrTiO_3$, respectively. As can be seen, the densities in the (111) substrate show a significant charge reduction in the top 4 bilayers. This finding matches our film COBRA data quite well, as the B-site intermixing that was observed exists 4 bilayers into the $SrTiO_3$ (111) substrate. From the layer-by-layer electron densities in the (111), we construct the resultant electrical potential in Figure 4.6(c) based on a simple Poisson model to suggest how the (111) diverging potential is resolved. The (001) substrate, by comparison, shows comparatively little change in SrO/TiO_2 composition until the top 2 layers, where a double layer of TiO_x likely forms, which is consistent with previous studies reporting various (*n x n*) surface reconstructions on variously-treated $SrTiO_3$ substrates[123–126]. To this end, the (001) and (111) substrate RHEED images prior to growth show superstructure features between the specular and diffracted spots

[left insets of Figure 4.2(a) and 4.2(b)] that are not preserved in the RHEED pattern of the $SrIrO_3$ film. This suggests that the initial surface structure of the $SrTiO_3$ substrates may not propagate to the $SrIrO_3$ surface and may instead remains at the interface, resulting in atomic intermixing with the deposited film. Such intermixing is more pronounced at the (111) interface due to its more-depleted surface from its polarity and the treatment prior to growth. Thus, we argue that these incomplete layers are resolved by B-site intermixing, which mitigates epitaxy on this polar (111) surface much more so than on (001), where the depleted layering is confined to the layers adjacent to the interface.

4.4 Conclusions

In conclusion, we have observed B-site intermixing at the polar/polar $SrIrO_3$/$SrTiO_3$ (111) interface that is not observed in the non-polar/non-polar (001) interface. Our results were qualitatively examined using scanning transmission electron microscopy and quantitatively confirmed using surface x-ray diffraction experiments analyzed by the coherent Bragg rod analysis method. Further COBRA experiments on identically treated substrates at the growth environment shows that the $SrTiO_3$ (111) substrates show charge layering that is significantly depleted compared to the (001) substrates. This depletion must be resolved before epitaxy can be stable, and thus intermixing of the B-site is interpreted as a mechanism to achieve this. This work illustrates an important geometric implication relevant to the design of (111) artificial perovskite interfaces on substrates that require surface modification before growth. Furthermore, if such observed atomic intermixing can be precisely controlled, interfacially-doped (111) interfaces could be designed to create desirable interfacial B-site alloy properties from the strongly-correlated d-band electrons that dictate the electronic structure in this class of materials. In the next chapter, I will return to the (001) $SrIrO_3$ interface and present work done on the creation of strong spin-orbit torques in $Ni_{0.2}Fe_{0.8}$/$SrIrO_3$ heterostructures.

The research presented in this chapter used resources of the Advanced Photon Source, a U.S. Department of Energy (DOE) Office of Science User Facility operated for the DOE Office of

Science by Argonne National Laboratory under Contract No. DE-AC02-06CH11357.

Chapter 5

Large spin-orbit torque in $Ni_{0.81}Fe_{0.19}/SrIrO_3$ heterostructures

5.1 Spin-current magnetic random access memory (MRAM)

Although the concept of magnetic storage was initially conceived in the 1940s, the surfaced in the 1980s with the discovery of spin magnetization in metals[127] and giant magnetoresitance (GMR)[128,129]. The ideal of magnetic storage as "universal" memory subsequently took off in 1990s with the development of magnetoresistive random access memory (MRAM)[130]. Unlike more conventional random access memory (RAM) such as static, dynamic, and flash, MRAM information is not stored as electric charge or current, but in magnetic moments. Such memory storage is referred to as *non-volatile*, as the written state is retained even after the power to the device has been shut off. As such, non-volatile memory has the potential to consume far less power than volatile memory architectures. Furthermore, the read-and-write speeds can be very fast and the lifetime of devices is robust, making the commercialization of MRAM desirable[131].

The typical form of MRAM storage utilizes tunneling magnetoresistance (TMR) in a magnetic tunnel junction (MTJ), as shown in Figure 5.1. The MTJ consists of two magnetic layers and a tunneling barrier. One magnetic layer is kept fixed, whereas the other is allowed to be switched as the means to write the memory bit. The relative ferromagnetic orientations of this free layer

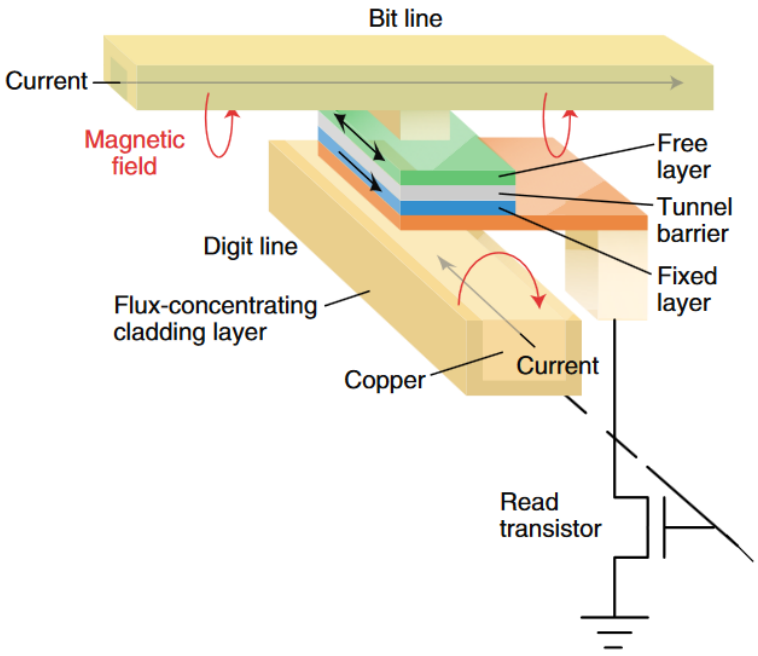


Figure 5.1: (a) MRAM bit circuit utilizing a magnetic tunnel junction Reproduced and adapted from Åkerman 2005 with permission from Science.

and the fixed layer determine the resistance of the junction where the ”on” state (magnetizations aligned) is lower resistance than the ”off” state (magnetizations not aligned). The magnetization direction within the ferromagnets can be thus thought of as a logic bit, where 0 and 1 binary states may be assigned to ”up” or ”down” orientations, for example. The relative orientation of the ferromagnetic layers determines whether electrons can tunnel across the barrier. The subsequent tunneling current is then passes through the circuit and its resistance is read out as memory by the transistor.

More recently, so-called spin-currents have been proposed as a superior way to read and write the switchable magnetic layer. This approach uses spin of the electrons within the ferromagnet itself rather than externally applied magnetic fields. The first major advantage to using spin-currents over external field bit writing is that a comparable performance of the device requires less current, which means the devices consume lower power and are more thermally stable. Another attractive feature of these architectures is that they exhibit magnetization dynamics that do not occur by analogous effects generated by an externally-applied field, which adds functionality. Furthermore, these spin-currents can exist in many various material heterostructures and subsequent device ge-

ometries[132]. The complicated nature of the physical interaction of the spins with the ferromagnets, known as a spin-transfer torque, is discussed next.

5.1.1 Spin-current coupling with ferromagnets

Since spin-current is strongly coupled to angular momentum, it should be no surprise that spin-currents can be transfered across interfaces to couple with adjacent ferromagnetic layers. As previously mentioned, this is known as a spin-transfer torque[132,133]. The spin-magnet coupling is depicted in Figure 5.2(a). The spin of an electron is passed to an material with a ferromagnetic moment, where the electron is reflected or transmitted depending on the relative orientation of its spin and the ferromagnetic moment of the adjacent material. Either of these two outcomes causes a reorientation of the electron spin that exerts a torque on the ferromagnetic moment due to conservation of angular momentum. The torque can lie within the plane of the electron spin direction (known as a "spin-transfer" torque) or perpendicular to that plane (known as a "field-like" torque). The differentiation of these torque will be relevant to the results presented later in this chapter.

The dynamics of the spin-transfer torque and its subsequent analysis from techniques like Spin-torque-ferromagnetic resonance (ST-FMR) is explained using the Landau-Lifshitz-Gilbert-Slonczewski equation[134]. A qualitative picture is given in Figure 5.2(b). Here, the magnetic moment m (in a ferromagnetic material) is subjected to a spin-transfer torque (from an adjacent material). If an external magnetic field $\mathbf{H_{eff}}$ is applied to the system, the magnetic moment of the ferromagnet will begin to precess around the applied field ($\mathbf{m} \times \mathbf{H_{eff}}$). As a result of this field, a torque from magnetic damping arises that reduces the magnitude of the precession. When a charge current is applied to the system, the spin-transfer torque is either parallel or anti-parallel to the damping torque, depending on the orientation of the applied current. As previously stated, depending on the orientation of the electron spin direction, a "spin-transfer" torque or a "field-like" torque results. In an actual experiment to detect such torque, the parameters extracted from the measurement can be fitted to the Landau-Lifshitz-Gilbert-Slonczewski equation, and the magnitude of the observed torque can be calculated from this analysis (see Appendix C for a detailed explanation).

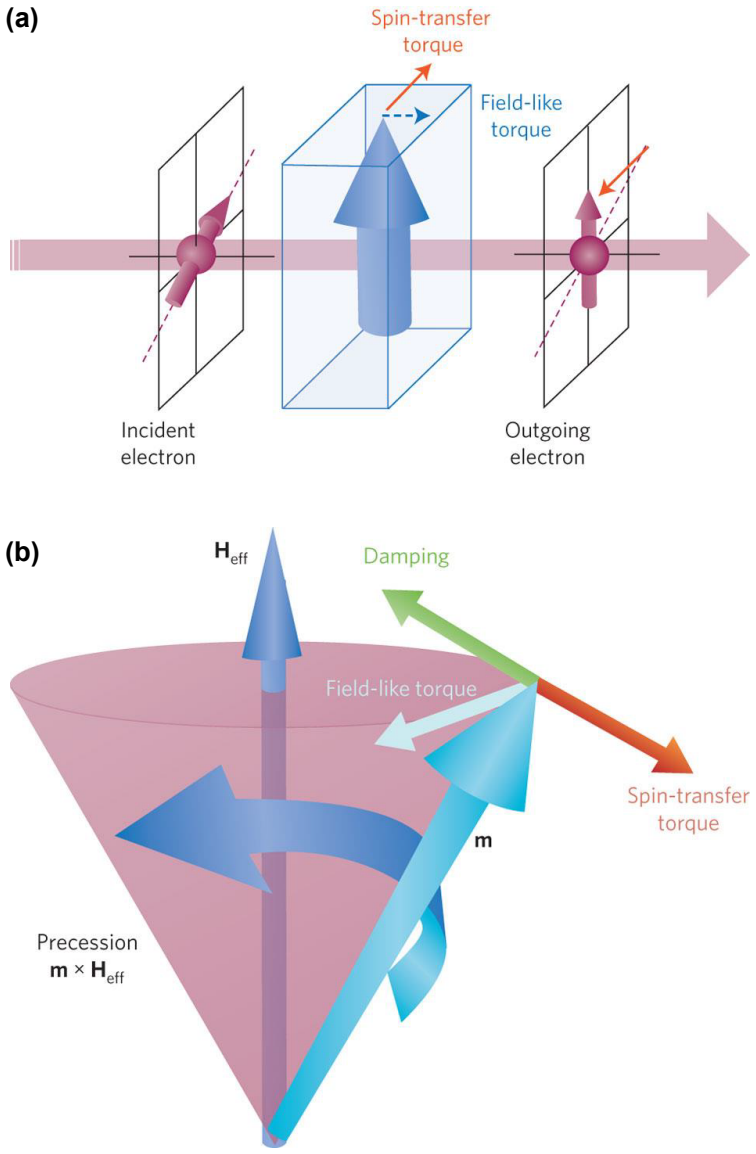


Figure 5.2: (a) Magnetic torque on a ferromagnetic layer induced by a spin-current. The electron is transmitted or reflected depending on the relative orientation of the electron-spin and the ferromagnetic moment (b) Magnetization dynamics induced by spin-currents as described by the Landau-Lifshitz-Gilbert-Slonczewski equation. Reproduced and adapted from Brataas *et. al* 2012 with permission from Nature Publishing Group.

5.2 Spin current generation via the spin Hall effect

The spin Hall effect (SHE) was first proposed by Dyakonov and Perel in 1971[135] and then experimentally observed in 1984[136], although the term itself was not coined until 1999[137]. However, it wasn't until the early 2000s that the first predictions of its proposed efficient generation of spin cur-

rents in semiconductors appeared[138,139], This was then experimentally observed shortly thereafter in $In_{1-x}Ga_xAs$ at 30 K[140]. Discovery of the SHE in metals at 4.2 K followed soon afterwards[141]. A reversal SHE at room temperature was measured in the heavy metal platinum[142], and then spin currents from the SHE in Pt was observed to exert a spin-torque on ferromagnetic $Ni_{0.81}Fe_{0.19}$[143]. After these initial findings, magnetic switching[144,145] and nano-oscillations[146,147] on overlaid ferromagnets, and also the movement of magnetic domain walls[148,149] have all been demonstrated by the spin Hall effect. Thus, the SHE shows great promise to efficiently generate the needed spin-current and also exhibits the necessary performance and integration with other materials for the previously-discussed device applications.

Most simply, the SHE can be thought of as the spin-analogous version of the ordinary Hall effect, shown in Figure 5.3(a), Here, an applied voltage V_x drives current $\boldsymbol{J_x}$ through a material and an magnetic field B_z out of the page is applied which exerts a Lorentz force on the current $\boldsymbol{J_x}$ in still another perpendicular direction, which deflects the electrons to sample edge, where they accumulate. From this accumulation, an electrical potential is established as positive charges accumulate on the opposite side of the material. At some finite time, the system reaches steady state in the *y*-direction, as enough electrons are deflected to the sample edge so that the electronic potential $\boldsymbol{V_y}$ completely cancels the Lorentz force in that direction from the magnetic field, after which, electrons flow freely once again in the direction of the applied voltage.

A schematic of the SHE is shown in Figure 5.3(b). Like in classical Hall effect, a charge current $\boldsymbol{J_x}$ driven through the material. However, instead of charge separation at the edge of the material in the y-direction, spins are separated, with one side exclusively populated with spin "up" electrons, and the other side exclusively spin "down." This separation of spins creates a "spin current" $\boldsymbol{J_s}$, which is defined as originating on "spin down" electrons and terminating on the "spin up" side. The degree of charge-to-spin current conversion efficiency is quantified by the spin Hall ratio, $\theta_{\mathrm{H}} = \dfrac{|\boldsymbol{J_s}|}{|\boldsymbol{J_x}|}$, the ratio of the two currents. While the ordinary Hall effect requires an externally-applied magnetic field to separate charge, the spin Hall effect does not require such a field to polarize spin, although the separation of spins can be manipulated or suppressed by applying magnetic fields[150]. The necessary ingredient of the spin Hall effect is strong spin-orbit

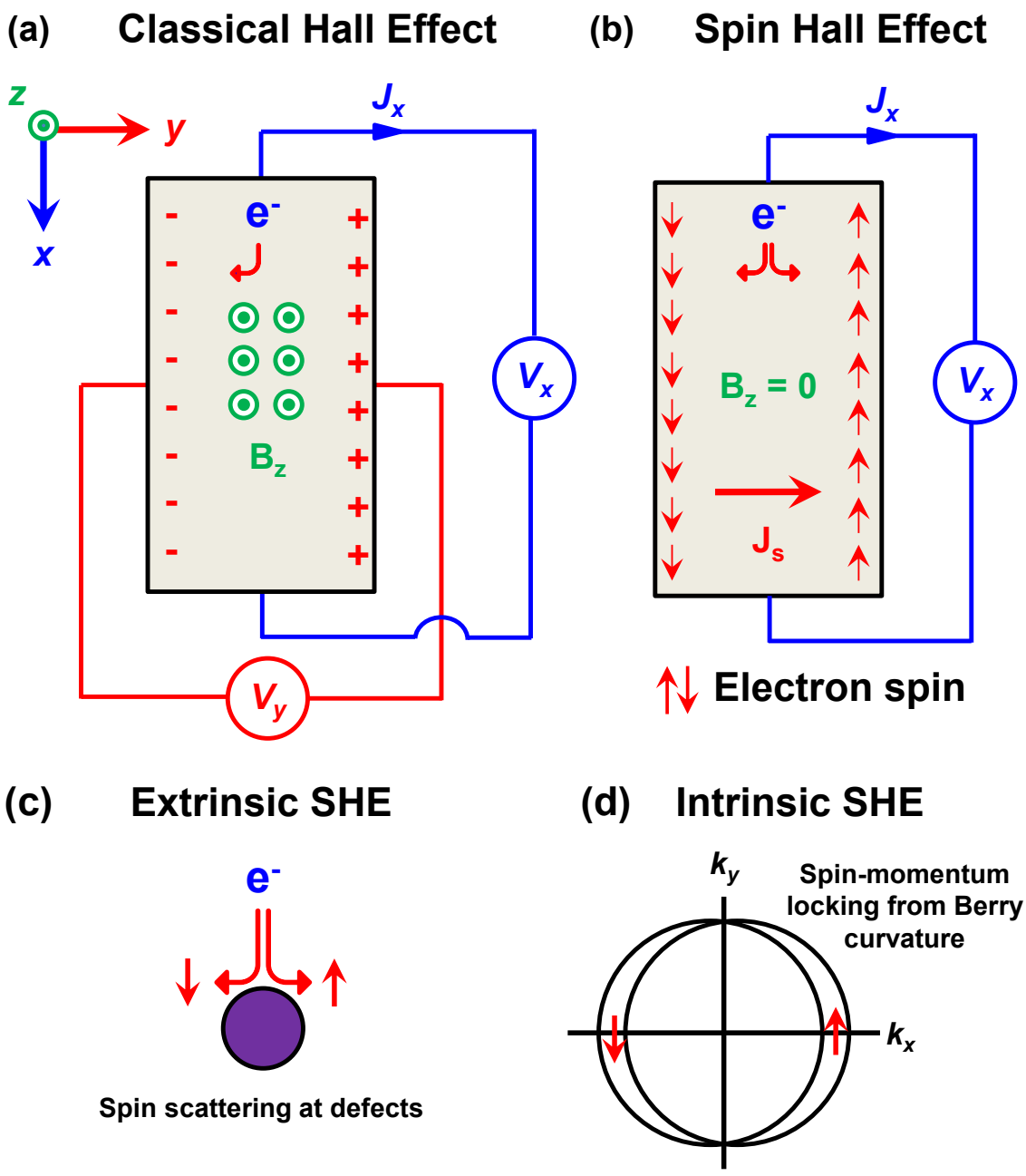


Figure 5.3: (a) Ordinary Hall effect (b) analogous spin Hall effect (c) Extrinsic spin Hall effect where spins split at defect with strong-spin orbit coupling (d) Intrinsic spin Hall effect from Berry curvature band structure

coupling[151]. The spin Hall effect can be a result of strong spin-orbit coupling from a defect, as shown in Figure 5.3(c), or a consequence of the Berry phase curvature[151,152], which is an intrinsic material property due to the band structure [Figure 5.3(d)]. It is this latter case that pertains to the results presented in this chapter.

5.2.1 Spin Hall effects in various material systems

Based on the previous motivation, it can be expected that current-induced spin-torque originating from intrinsic spin-orbit effects offers an energy efficient scheme for the electrical manipulation of magnetic devices. The key challenge in spin-transfer torque MRAM remains, however, reducing the write current to scale device sizes down for commercial-level performance requirements[153]. On this front, a 3-terminal device utilizing spin-torque switching via the SHE generated in non-magnetic materials has been proposed and demonstrated as an alternative to passing current through a conventional 2-terminal tunnel junction to switch the ferromagnetic free layer[145]. Such an approach avoids the issue of coupled read/write paths in conventional magnetic tunnel junctions. The key challenge to realizing these new devices is careful design of new materials with the desired functionality and their subsequent synthesis and incorporation into layered heterostructures.

The experimental work on the intrinsic SHE has mainly focused on heavy metals[154] and epitaxial semiconductors[140]. The first discovery in semiconductors was observed at 30 K and the spin Hall ratio for these materials are typically less than 0.005[151]. The heavy metal systems like Mo, Pd, Pt, and Au typically exhibit higher spin Hall ratios of ≈ 0.1[151] at room temperature due the presence of much stronger spin-orbit coupling in these materials. Furthermore, oxidization of these heavy metals has recently been shown to allow enhancement of the spin Hall ratio, as β-phase W[155] can increase the heavy metal SHE efficiency to 0.5. The highest efficiency (2-3.5) for spin-transfer torque has been achieved using topological insulators to generate interfacial spin-current[156,157]. However, since the topic of this chapter is spin-transfer torque generated from the spin Hall effect, we will restrict our comparison of the results that follow on $SrIrO_3$ to heavy metals and semiconductors. Based on the β-phase work, incorporating heavy metals in oxides is thus a promising avenue to engineer efficient spin-current via the spin Hall effect.

Along this line of thought, 5*d* perovskite oxide materials like $SrIrO_3$ are an attractive candidate for generating a strong room temperature spin Hall effect because they combine the strong spin-orbit coupling that exists in heavy metals along with layered single-crystal epitaxy that is possible with semiconductors that lack the elemental composition to provide strong spin-orbit coupling. Along this 5*d* oxide motif, the inverse SHE has been reported in amorphous and polycrystalline films of 5*d* IrO_2 [158]. Here, it is proposed that synthesizing an epitaxial perovskite $SrIrO_3$ film retains the necessary 5*d* electronic structure needed to generate a large SHE while simultaneously reducing the extrinsic contributions to the SHE in a cleaner material that lacks significant defects and grain boundaries. A large charge-to-spin conversion (large spin Hall ratio θ_H) could thus result solely due to intrinsic origins. Recently, there are reports of interfacial Rashba-generated spin transport in the canonical perovskite oxide single-crystal 2-dimentional electron gas interface between $LaAlO_3$ and $SrTiO_3$ [159–161]. Although $LaAlO_3$/STO is not a 5*d* system, these studies nonetheless demonstrate the emergence of perovskite oxides as a promising material candidate for efficient spin-current generation via the spin Hall effect.

5.3 Large intrinsic spin Hall effect in $SrIrO_3$

Here, we first motivate our work by theoretical calculations that show a large intrinsic spin Hall effect in the $SrIrO_3$ 3D bulk semimetal. As shown in Figure 5.4(a), a large spin Hall conductivity (SHC) is obtained from the linear response theory for the bulk orthorhombic perovskite structure. The spin Hall effect arises due to the Berry curvature in the bulk electronic band structure, with mainly contribution originating from the nearly degenerate energy bands shown in Figure 5.4(b) and 5.4(c). Such characteristic band structure occurs as a combined effect of spin-orbit coupling and the IrO_6 octahedral tilting configuration in the bulk system. Generally speaking, precise control of the octahedral tilting in transition-metal perovskites can allow fine-tuning of the electronic band structure [19]. Moreover, it is known that such tilting can be partially suppressed up to a certain thickness due to the structural imprint of non-tilted cubic substrates such as $SrTiO_3$ [Figure 5.4(d)] [162]. Experimentally, we observed a large change in the spin-torque efficiency that directly correlates to this structural transition, demonstrating the ability to control the magnitude of the spin

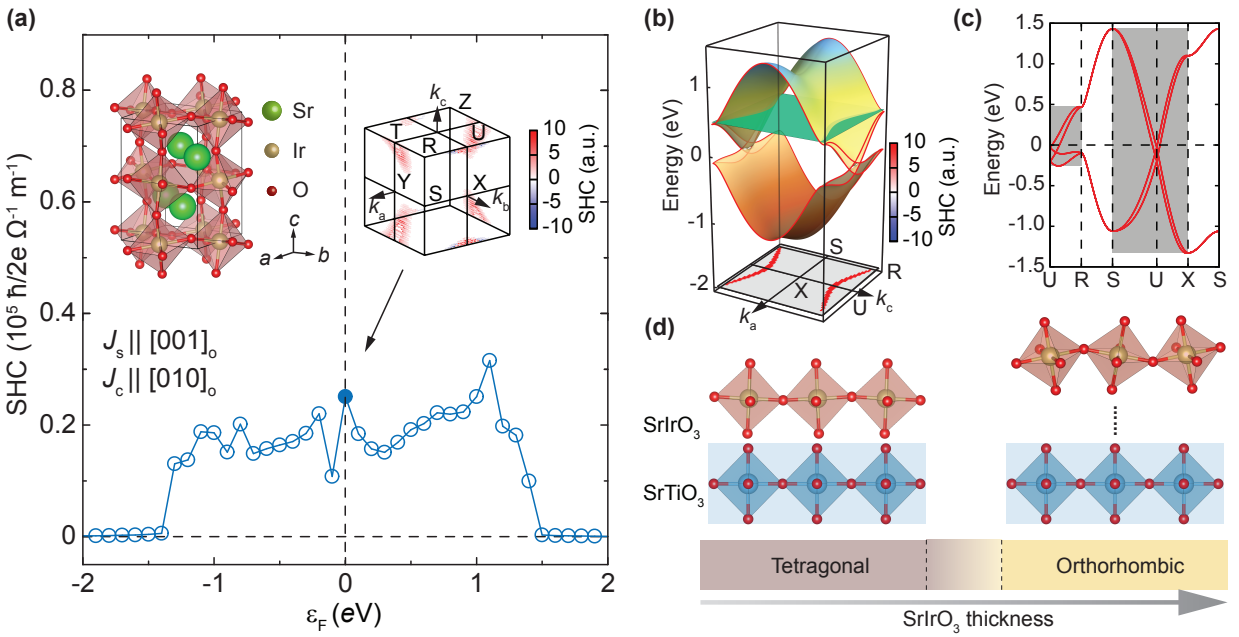


Figure 5.4: (a) Calculated bulk $SrIrO_3$ spin Hall conductivity (SHC) as a function of Fermi energy ϵ_F. Left inset: Orthorhombic perovskite crystal structure of bulk $SrIrO_3$, where a, b, and c correspond to the $[100]_o$, $[010]_o$, and $[001]_o$ directions (subscript o for orthorhombic notation), respectively. Right inset: Momentum-resolved SHC $\Omega(k)$ in the Brillouin zone for the case $\epsilon_F = 0$ (b) Electron energy band structure of the bulk system on the XURS plane of the Brillouin zone. The red arcs at the bottom represent the momentum-resolved SHC, which is the net Berry curvature summed over occupied electron levels below a given Fermi level (green) (c) Electron band structure along the path U-R-S-U-X-S, where the gray boxes highlight the nearly degenerate energy bands responsible for the large bulk SHC (d) Schematic illustrations of the lattice symmetry of $SrIrO_3$ when grown on cubic non-tilted $SrTiO_3$ where a partial suppression of the IrO_6 octahedral tilt exists up to a certain thickness before a tilted octahedral pattern is established in thicker films.

Hall effect by crystalline symmetry.

5.3.1 Synthesis of AlO_x/Py/$SrIrO_3$/$SrTiO_3$(001) heterostructures

$SrIrO_3$ films were epitaxially synthesized on (001) $SrIrO_3$ substrates using pulsed laser deposition (PLD). During the growth, layer-by-layer deposition was observed by *in situ* reflection high energy electron diffraction (RHEED). Before the growth, the (001) $SrTiO_3$ substrates were chemically etched and annealed to ensure TiO_2 surface termination. The substrates were first immersed in buffered hydrofluoric acid for 60 seconds before being annealed at 900°C for 6 hours in an O_2-rich environment. After annealing, the substrates were etched again in buffered hydrofluoric acid

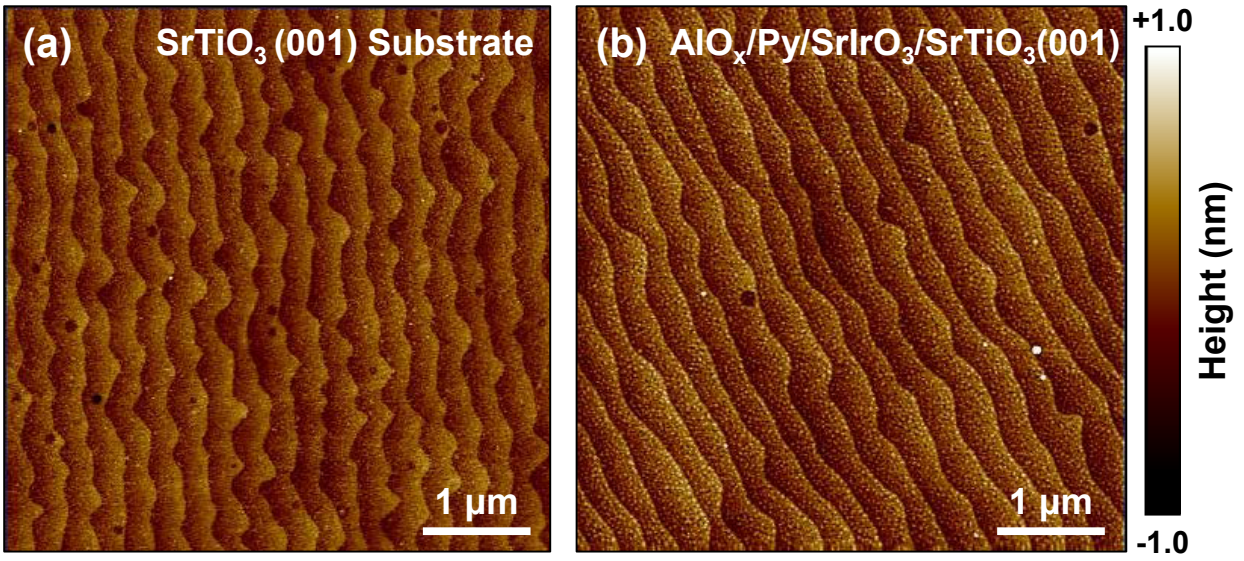


Figure 5.5: (a) Atomic force microscopy images of a treated (001) $SrTiO_3$ substrate (b) subsequently deposited heterostructure of AlO_x(1 nm)/Py(3 nm)/$SrIrO_3$(8 nm) showing near preservation of the atomically smooth $SrTiO_3$ substrate surface.

to remove any leftover SrO on the surface. The PLD growth recipe was discussed in Chapter 2. After the $SrIrO_3$ growth, the sample was cooled down in an oxygen rich atmosphere. The chamber was then re-evacuated at room temperature and $Ni_{0.81}Fe_{0.19}$ (Py) was sputter deposited at an Ar pressure of 3 mTorr with a background pressure of less than 5×10^{-8} Torr, followed by deposition of a 1 nm Al passivation layer, which presumably oxidized to form AlO_x. This *in situ* synthesis preserves the interface transparency that is critical for the spin-current transmission and the efficiency of spin-orbit torque generation[163,164]. The Py film was found to be polycrystalline by the observation of RHEED diffraction rings after deposition. Atomic force microscopy images of the 1 nm AlO_x/3.5nm Py/8 nm (20 uc) $SrIrO_3$ surface in Figure 5.5 reveals an atomically-smooth surface preserving the substrate step-terrace morphology. In Figure 5.6, we show the cross-sectional filtered STEM-HAADF image of an 8 nm $SrIrO_3$ film on (001) $SrTiO_3$ capped with 2.5 nm Py. Here, the contrast of the image is approximately proportional to the atomic number Z where brighter colors represent heavier elements (heaviest atom in our case being Ir). From the image, we determine that our $SrIrO_3$ shares the same pseudocubic epitaxial arrangement as the $SrTiO_3$ substrate, with sharp interfaces between both the $SrIrO_3$/STO interface and the $SrIrO_3$/Py interface. We confirmed by x-ray diffraction that the $SrIrO_3$ film grows $[110]_o$ out-of-plane, with

$[1\bar{1}0]_o$ and $[001]_o$ in-plane along $[100]_c$ and $[010]_c$ of $SrTiO_3$, respectively, as described in Chapter 2.

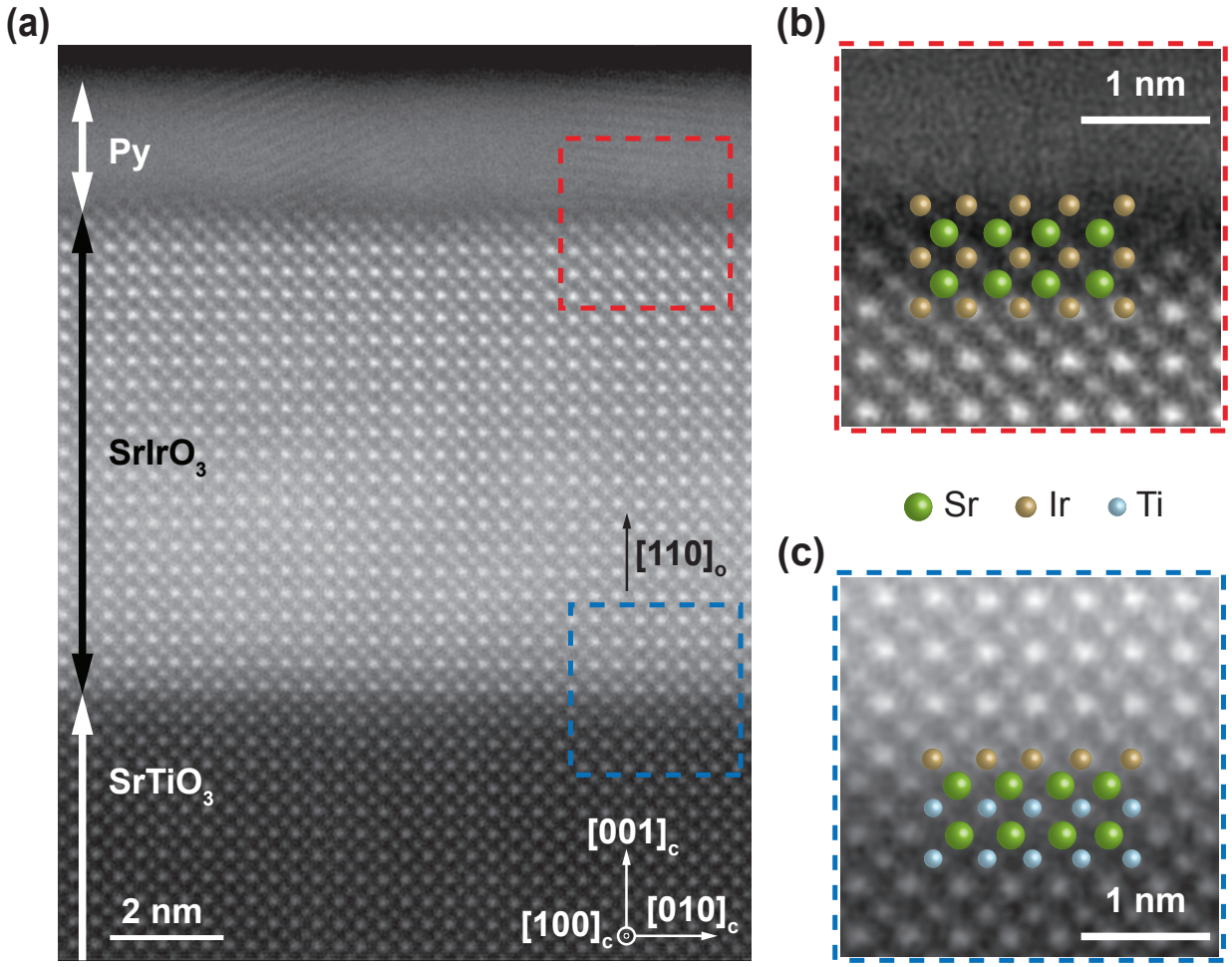


Figure 5.6: (a) Scanning transmission electron microscope image of Py/$SrIrO_3$ heterostructure on (001) $SrIrO_3$ substrate. The image contrast is approximately proportional to the atomic number Z, where brighter colors represent heavier elements. Subscripts c and o denote the cubic and orthorhombic notation, respectively. (a, (c), Expanded image of the top Py/$SrIrO_3$ interface [shown in (b)], and the bottom $SrIrO_3$/$SrTiO_3$ interface [shown in (c)], showing the high quality $SrIrO_3$ film with atomically-sharp interfaces. The stacking of the atomic constituents are highlighted in the blown-up images by the superimposed filled dots of different colors (Sr in green, Ir in yellow and Ti in blue).

5.3.2 ST-FMR results of spin-orbit torque in Py/$SrIrO_3$

The spin Hall effect in $SrIrO_3$ was probed by measuring the spin-orbit torque in the adjacent Py layer by using the spin-torque ferromagnetic resonance (ST-FMR) technique [156,164,165], as illustrated

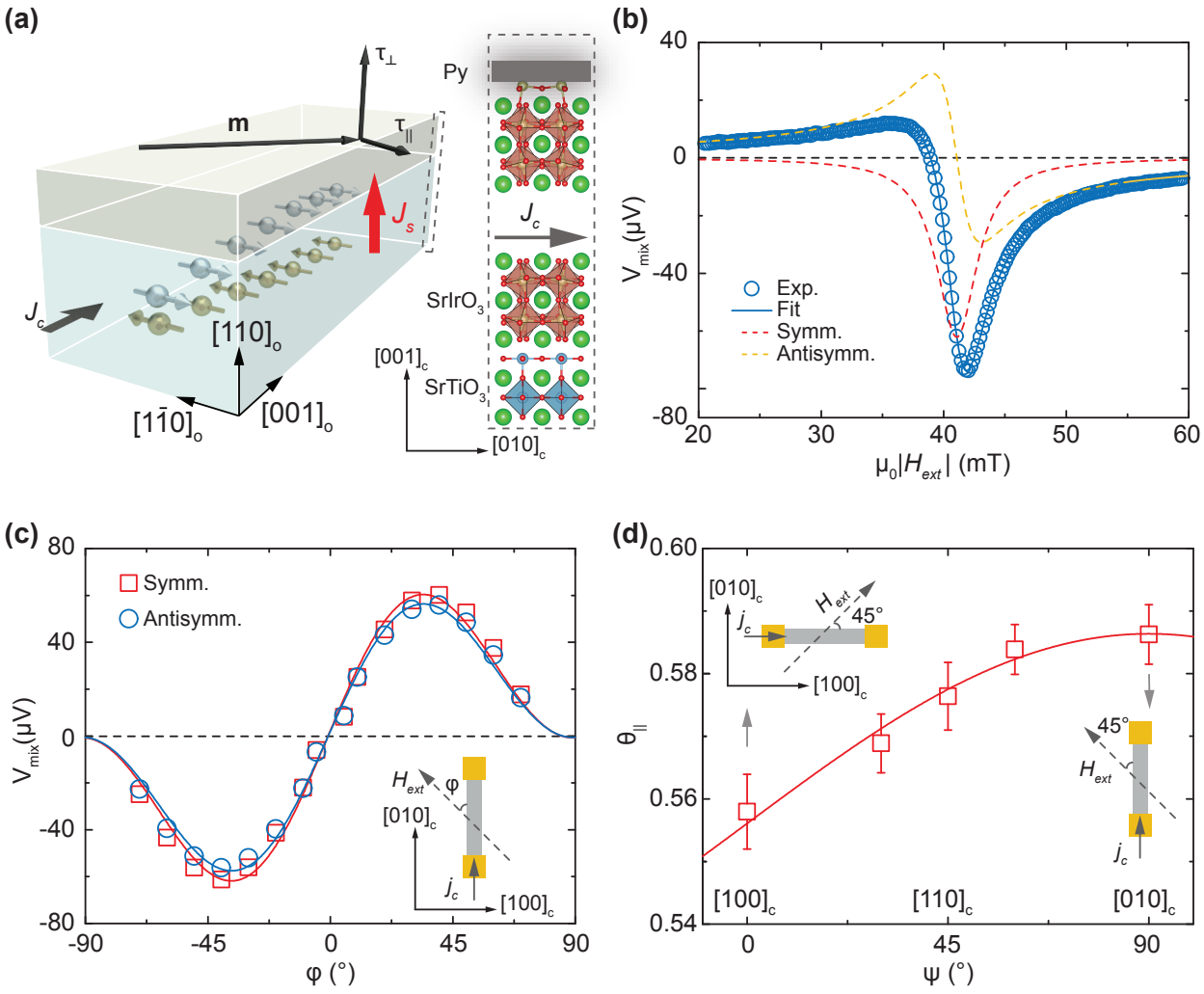


Figure 5.7: (a) Schematic of the Py/$SrIrO_3$ bilayer on $SrTiO_3$(001) and the current-induced torque geometries. Incoming charge current (J_c) generates a spin current (J_s) along the out-of-plane $[110]_o$ direction of the $SrIrO_3$ film ($[001]_c$ of the $SrTiO_3$ substrate) (b) ST-FMR spectrum (fitted to a Lorentzian function, solid line) for a 3.5 nm Py/8 nm (20 uc) $SrIrO_3$ sample with microwave current applied along the $[010]_c$ axis. The dashed lines represent the fits of the symmetric and antisymmetric components. The external magnetic field is oriented at an angle $\phi = -45°$ with respect to the current axis. The applied microwave frequency and power are 5.5 GHz and 12 dBm. The V_{mix} across the device bar is acquired by a dc voltage meter (c) Symmetric and antisymmetric resonance components as a function of the external magnetic field angle ϕ, which are fitted to $\sin(2\phi)cos\phi$ (d) In-plane crystallographic orientation (current applied along from $[100]_c$ to $[010]_c$) dependence of the measured spin-torque ratio. The external magnetic field angle is fixed at $\phi = 45°$. The solid line shows the fit to $\sin(\psi + \psi_0)$.

in the schematic of the Py/$SrIrO_3$ bilayer system [Figure 5.7(a)]. When an alternating charge current flows in $SrIrO_3$, spin accumulates at the interfaces due to the spin Hall effect and induces a spin current that flows into Py. This spin current exerts torque on the Py and excites the magnetic moment into precession, generating an alternating change of the resistance due to the anisotropic magnetoresistance (AMR) in Py. We measure a dc voltage signal V_{mix} across the device bar that arises from the mixing between the alternating current and changes in the device resistance. The resonance spectrum is obtained at a fixed microwave frequency, and with an in-plane external magnetic field swept through the ferromagnetic resonance condition in Py.

Figure 5.7(b) shows a typical ST-FMR spectrum for a 3.5 nm Py/8 nm (20 uc) $SrIrO_3$ sample (device size of 20 μm $\times$ 40 μm) with a microwave current applied along the substrate $[010]_c$ axis (subscript c for cubic notation). The in-plane magnetic field is swept at an angle $\phi = -45^\circ$ with respect to the current axis. The resonance line shape is well fitted to a sum of symmetric and antisymmetric Lorentzian components (red and yellow dashed curves), where the anti-damping (in-plane, $\tau_\parallel$) and field torque (out-of-plane, $\tau_\perp$) components are proportional to the amplitudes of the symmetric and antisymmetric line shape, respectively (see Appendix C). As shown in Figure 5.7(c), the symmetric and antisymmetric components both depend on ϕ according to the form $\sin(2\phi)\cos\phi$, which can be interpreted as the product of the contributions from AMR in Py [$dR/d\phi \propto \sin(2\phi)$] and the current-induced torque ($\tau \propto \cos\phi$)[156,165]. From the symmetric and antisymmetric amplitudes, (see Appendix C, Figure C.2 for the line shape analysis and the calibration of microwave currents), we find the in-plane $\sigma_\parallel$ and out-of-plane torque conductivity $\sigma_\perp$ (torque per unit electric field) to be $(1.4\pm0.2)\times10^5\ \hbar/2e\,\Omega^{-1}m^{-1}$ and $(2.9\pm0.5)\times10^4\ \hbar/2e\,\Omega^{-1}m^{-1}$, respectively, by averaging different measurement frequencies (4.5 to 7 GHz, see Appendix C, Figure C.3). The sign for $\sigma_\parallel$ is consistent with our first-principle calculations for bulk $SrIrO_3$ and that of the heavy metal Pt. The magnitude of $\sigma_\parallel$ is comparable to that of Pt which has a much larger charge conductivity σ than $SrIrO_3$ (the charge conductivities are summarized in Appendix C). This indicates a large value for the spin-torque ratio $\theta_\parallel$ $\left(=2e/\hbar\dfrac{\sigma_\parallel}{\sigma}\right)$, figure of merit (generation of anti-damping torque per unit charge current density), for $SrIrO_3$ of 0.55 ± 0.08, which is about one order of magnitude higher than that reported for Pt thin films[151] (see Appendix C, Figure C.5 for Pt/Py control sample)

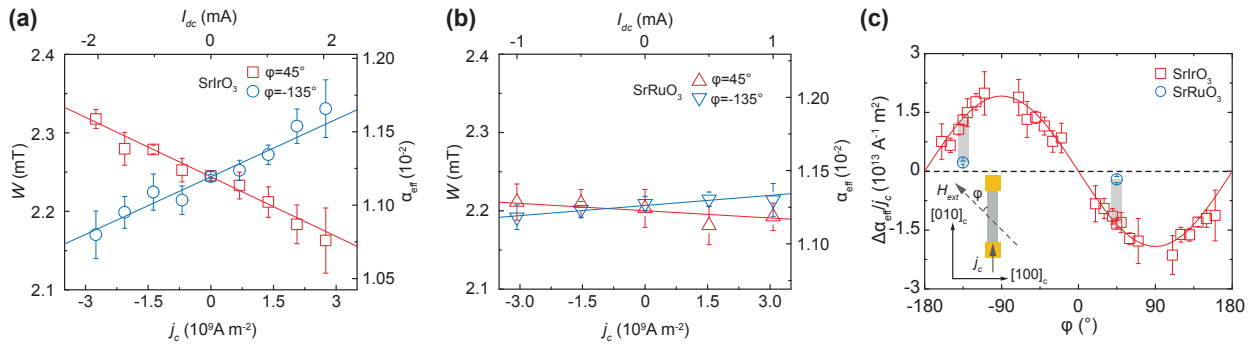


Figure 5.8: (a), (b) Resonance linewidth and effective magnetic damping as a function of dc current density in $SrIrO_3$ for Py/$SrIrO_3$ [shown in (a)] and for Py/$SrRuO_3$ [shown in (b)] with both positive and negative external magnetic field. The solid lines represent linear fitting (c) Current-induced modulation of Py effective damping as a function of external magnetic field angle for the Py/$SrIrO_3$ sample. The solid line shows the fit to $\sin\phi$. The Py/$SrRuO_3$ data points are taken at $\phi = 45°$ and $-135°$.

and slightly larger than the efficiency reported for $beta$-phase W[155]. From the sign of $\sigma_\perp$, the out-of-plane field-like torque is oriented in the same direction as the torque from the Oersted field that comes from the current in $SrIrO_3$. But the value for $\sigma_\perp$ is larger than the expected Oersted field $\sigma_{Oe} = 1.3 \times 10^4\ \hbar/2e\ \Omega^{-1}\ m^{-1}$ estimated by Amperes law. Besides the strong spin Hall effect from $SrIrO_3$, the Rashba-Edelsein effect[24,166] at the Py/$SrIrO_3$ interface could also contribute to the observed field-like torque.

We also investigated the crystal orientation dependence of the spin-torque ratio as shown in Figure 5.7(d) motivated by the likely epitaxial relationship between the orthorhombic $SrIrO_3$ thin film and the cubic $SrTiO_3$ substrate (discussed further below). We performed the ST-FMR measurements on devices patterned along various in-plane crystal orientations from the $[100]_c$ axis or $[\text{-}110]_o$ (subscript o for orthorhombic notation) to $[010]_c$ or $[001]_o$ while fixing the magnetic field angle at $\phi = 45°$. The crystal orientation dependent $\Delta\theta_\parallel$ can be fitted to $sin(\psi - \psi_0)$, where ψ is the angle between the $[010]_c$ and the current axis, and ψ_0) accounts for the misalignment between the device pattern and the crystal orientation. We note that the higher $\theta_\parallel$ axis along the $[010]_c$ coincides with the lower resistivity axis of the $SrIrO_3$ thin film (see Appendix C, Figure C.6 for the anisotropic resistivity of $SrIrO_3$).

We further confirmed the large spin-torque ratio in $SrIrO_3$ by measuring the dc current-induced

transformation of the ST-FMR resonance[156,165]. The injection of the dc current exerts an additional dc spin-torque on the adjacent Py. The dc in-plane torque component modifies the relaxation of the Py magnetization precession, modulating its resonance linewidth, as this torque component is parallel or antiparallel to the Gilbert damping torque depending on the relative orientation between the current and magnetic field[143]. We performed ST-FMR measurements on the Py/$SrIrO_3$ bilayer device patterned along $[010]_c$ axis (20 μm $\times$ 40 μm) with applied dc current by using a lock-in amplifier. A quantitative analysis of the $\theta_{\|}$ is shown in Figure 5.8(a), where resonance linewidth W scales linearly with the applied dc current. The magnitude of the in-plane torque is proportional to the change of the effective Gilbert damping α_{eff} over the current density j_c in $SrIrO_3$ (Appendix C). We find that the sign and magnitude of $\theta_{\|} = 0.52 \pm 0.07$, averaged by different frequencies and devices) measured by the dc biased ST-FMR (see Appendix C for the frequency dependent $\theta_{\|}$) is in good agreement with the ST-FMR line shape analysis. To investigate the importance of SOC on the spin-orbit torque, we also performed a control experiment on a 3.5 nm Py/7 nm $SrRuO_3$ bilayer. While $SrRuO_3$ assumes a similar crystal structure as $SrIrO_3$, the Ru atom hosts 4*d* electrons with relatively weak spin-orbit coupling compared to the Ir in $SrIrO_3$. We see that the ruthenate control sample yields a much smaller current-induced change in α_{eff}, which corresponds to a $\theta_{\|}$ of 0.09 ± 0.05 [Figure 5.8(b)]. Figure 5.8(c) shows the in-plane magnetic field angle ϕ-dependent current-induced change in the effective damping $\Delta\alpha_{eff}/j_c$ [slope of the linear fit in Figure 5.8(a) and 5.8(b)], which can be well-fitted to $\sin\phi$. This is consistent with the symmetry of the current-induced torque, again suggesting that the large spin-torque ratio in$SrIrO_3$ is free from any spurious microwave rectification or thermoelectric effects.

5.3.3 Tuning of spin-torque by crystal structure of $SrIrO_3$ films

Having established a large spin-torque efficiency in our 20 uc $SrIrO_3$ films, we next investigated the effect of structural variation on the spin-torque efficiency. Our motivation for this work was the previously reported structural transition with increasing thickness from tetragonal to orthorhombic in the chemically similar $SrRuO_3$[162]. To see if a similar transition in $SrIrO_3$ existed that could influence the spin-torque, we performed a study on a series of $SrIrO_3$/Py bilayers where the $SrIrO_3$

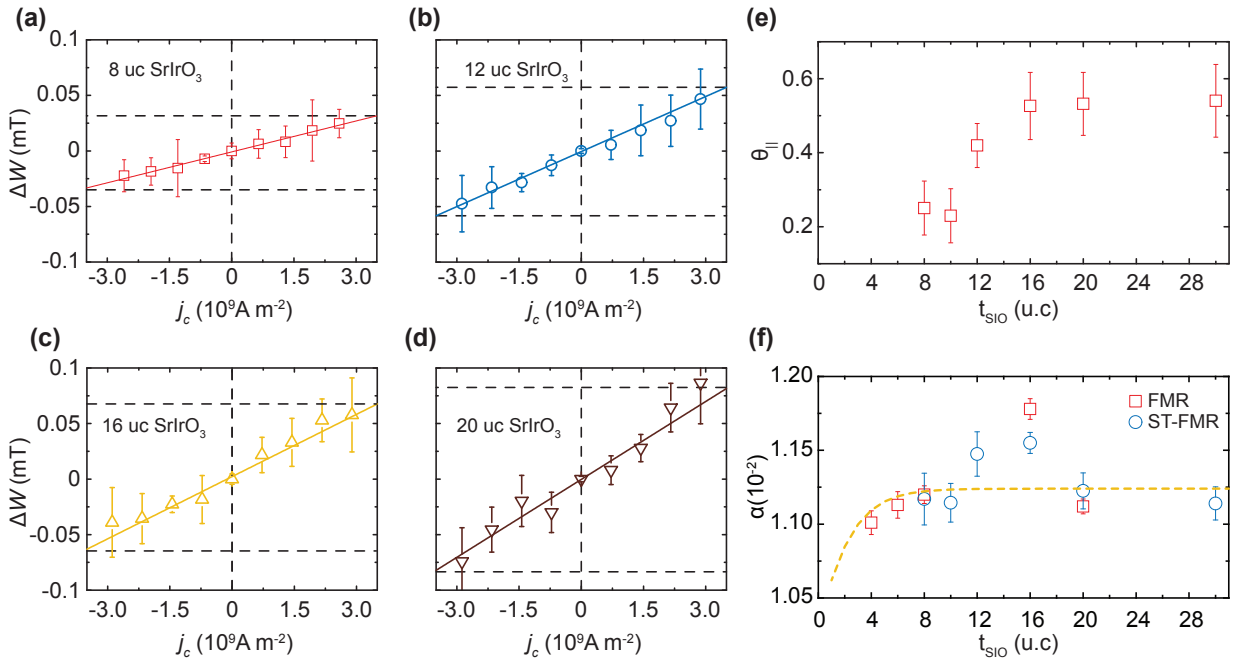


Figure 5.9: (a), (b), (c), (d) The change of resonance linewidth as the functions of applied current and the corresponding current density in $SrIrO_3$ for the 3.5 nm Py/$SrIrO_3$ with the $SrIrO_3$ thicknesses of 8 uc (a), 12 uc (b), 16 uc (c), and 20 uc (d). The solid lines represent linear fitting. All measurements were taken with the external magnetic field applied at $\phi = -135°$. The microwave power is 12 dBm and the frequency is 5.5 GHz. (e) $SrIrO_3$ thickness dependent of spin orbit ratio $\theta_{\|}$ determined by the dc biased ST-FMR measurements. (f) $SrIrO_3$ thickness dependent of Gilbert damping parameter α determined by ST-FMR and broadband FMR measurements. The dashed curve represents the fit to the diffusive spin-pumping model.

thickness was varied from 8 uc to 20 uc (with the Py thickness fixed) using the dc-biased ST-FMR The dc current was restricted to below 2 mA to acquire a good fit curve and minimize Joule heating. The current density in $SrIrO_3$ film is estimated by using a parallel resistance model (See Appendix C). Figure 5.9(a)-(d) shows the change of resonance linewidth as the functions of current density in $SrIrO_3$ for the Py/$SrIrO_3$ bilayer, in which the Py thickness is fixed at 3.5 nm and the $SrIrO_3$ thickness varies from 8 uc to 20 uc (at $\phi = -135°$ only). As shown in Figure 5.9(a), the resulting $\sigma_{\|}$ linewidth is much smaller in the 8 uc $SrIrO_3$ than in the thicker three starting at t_{SIO} of 16 uc [Figure 5.9(b)-(d)]. It can clearly be seen from Figure 5.9(e) that $\theta_{\|}$) also sharply increases in this interval. This abrupt change cannot be explained simply by standard spin-diffusion theory[167], as the $SrIrO_3$ shows a short spin-diffusion length of about 1.5 nm determined from its resonance linewidth broadening [Figure 5.9(f)], which agrees with a recent report on $SrRuO_3$[168].

To investigate the structure of the $SrIrO_3$ thickness series, we performed synchrotron x-ray diffraction experiments to determine their tilt and symmetry. As discussed in Chapter 2, it is known[20] that orthorhombic perovskites like $SrIrO_3$ with *Pbnm* space group symmetry orient themselves on cubic substrates like $SrTiO_3$ with $[110]_o$ out of plane along $[001]_c$ with $[1\bar{1}0]_o$ and $[001]_o$ in-plane along $[100]_c$ and $[010]_c$, respectively, as shown in Figure 5.10(a). Such epitaxial arrangement produces a distortion of the orthorhombic unit cell due to the compressive/tensile strain along $[\bar{1}10]_o$, which causes the orthorhombic film to assume a slightly distorted monoclinic structure with $\alpha = \beta = 90^\circ \neq \gamma$. By examining the $\{103\}_{pc}$ reflection at 90° increments, it is possible to determine the pseudocubic tilt of the orthorhombic films by comparing the peak position in L at each ϕ angle, as their film peak positions will show deviations in the surface-normal component of Q_z, the surface normal component of the x-ray scattering vector. This will shift the peak position in L along two of the ϕ-angle peaks, whereas the other two alignments will have identical peak positions in L. The L-shifts will exist along the $[103]_{pc}$ and $[-103]_{pc}$ directions since the in-plane direction of the strain that creates the distorted tilt lies along $[100]_c$ as shown in Figure 5.10(a). Therefore, the $[013]_{pc}$ and $[0\text{-}13]_{pc}$ (see Appendix C for the relationship between pseudocubic and orthorhombic coordinates used here) reflections should exhibit the same film peak position in L since no tilt exists along this direction. As can be seen in Figure 5.10(b), the splitting from [103] and [-103] is pronounced at 20 uc, but is slowly suppressed as the film thickness decreases. At 8 uc, the entire $\{103\}_{pc}$ family shows no deviation in L, indicating that relatively no tilt from the strain exists, which means that a global tetragonal symmetry is established. From the position of these L peaks, geometrical analysis was performed to calculate the a/b ratio[20] that is presented in Figure 5.11 below.

However, while such scans are effective for determining the tilt from epitaxial strain, they ignore tilting of the octahedral from small orthorhombic tilt that remains. Since lower symmetry perovskites like orthorhombic $SrIrO_3$ show tilts and rotation patterns in their octahedra along different pseudocubic directions[18], they will exhibit extra x-ray reflections[92] between pseudocubic peaks that arise from doubling the unit cell along particular crystallographic directions. Therefore, based on the bulk tilt pattern of $SrIrO_3$, scans to look for the $(221)_o$ reflection were performed to

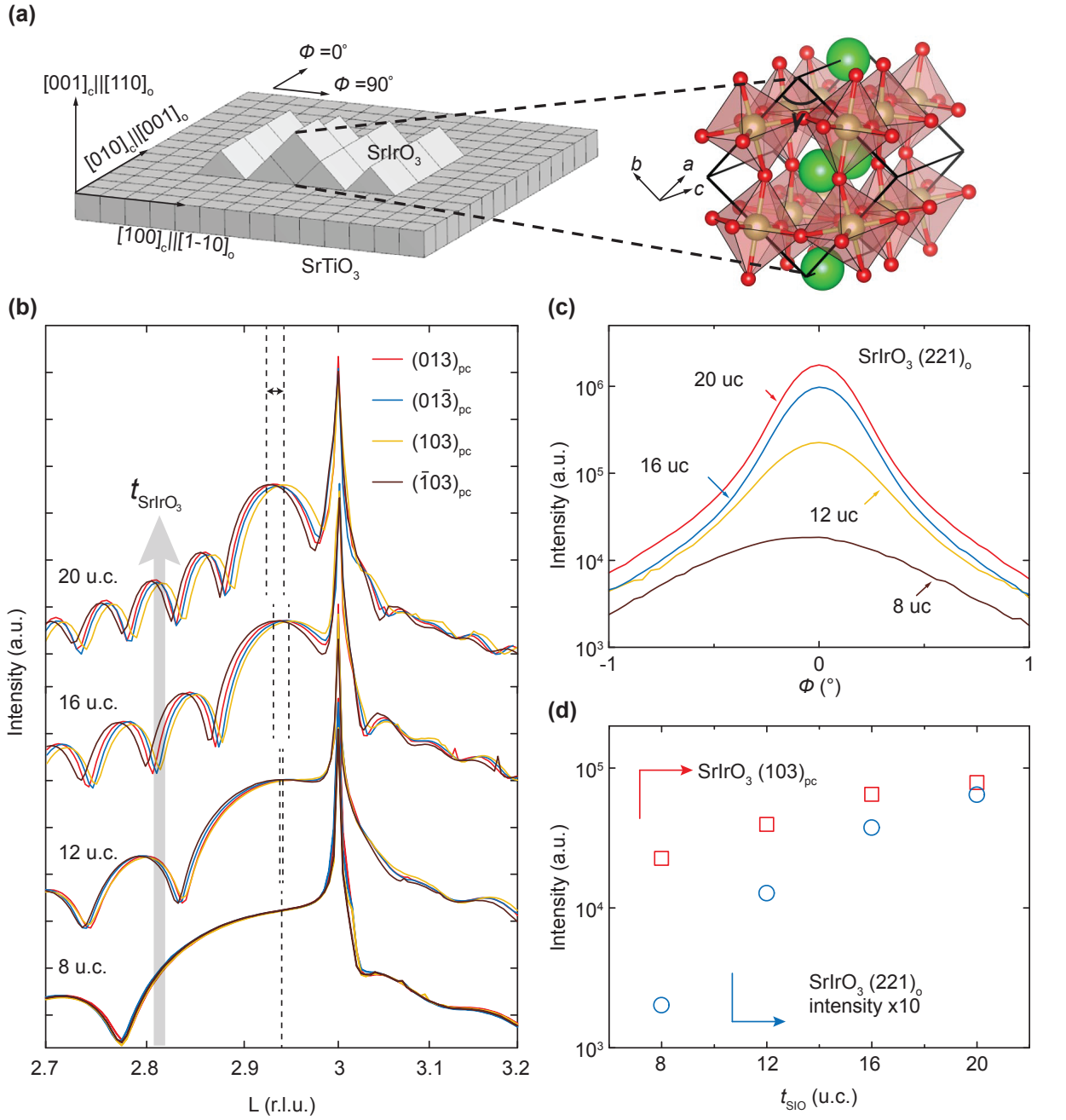


Figure 5.10: (a) Epitaxial arrangement of orthorhombic $SrIrO_3$ on cubic $SrTiO_3$ (b) Integrated reciprocal space mappings around the {103} $SrTiO_3$ substrate reflection of 8, 12, 16, and 20 uc $SrIrO_3$ films on $SrIrO_3$(001) substrates. The separation of the $(103)_{pc}$ and $(-103)_{pc}$ film peak positions, which indicate an out-of-plane tilt of the $SrIrO_3$ film relative to the substrate due to the coherent epitaxial strain, is shown to decrease to zero from 20 uc to 8 uc, indicating a partial suppression of the IrO_6 orthorhombic tilt to a near tetragonal-like structure (c) Intensity of orthorhombic $(221)_o$ $SrIrO_3$ peak, which decreases from 20 to 8 uc (d) Intensity comparison of the $SrIrO_3$ $(103)_{pc}$ and $(221)_o$ peak intensities as a function of film thickness.

check if the IrO_6 tilting in the films was completely suppressed. This reflection corresponds to a half-order pseudocubic $\{\frac{1}{2}02\}$ family of reflections that do not exist in non-tilted system. Thus, any measured intensity from the $(221)_o$ peak would indicate the orthorhombic tilting in the films. In Figure 5.10(c) we see that intensity from the measured $(221)_o$ reflection in our $SrIrO_3$ films persists even in the 8 uc film that showed no tilt from the $\{103\}_{pc}$ work. It should be noted however, that although the $(221)_o$ peak is still observable in the thin 8 uc film, the intensity of this peak drops much more quickly with decreasing thickness than the primary $(103)_{pc}$ peak from 20 to 8 uc. If this $(221)_o$ intensity change were solely due to the progressively thinner $SrIrO_3$ films, the $(103)_{pc}$ should decrease at the same rate, which is not the case, as shown in Figure 5.10(d). Thus, this signifies a partial suppression of the IrO_6. Thus, while the 8 uc film retains small orthorhombic tilts [this was also verified from RHEED experiments along the (1,0) and (0,1) in-plane substrate directions], these titles are greatly suppressed as the global structure clearly tends towards the tetragonal symmetry from 20 to 8 uc. It was also confirmed both from x-ray and RHEED that mixed orthorhombic domains in the $SrIrO_3$ existed, as discussed in Chapter 2.

Thus, the suppression of $\sigma_{\parallel}$ [plotted again in Figure 5.11(b)] can be closely related to the global $SrIrO_3$ lattice symmetry transition (from orthorhombic to tetragonal) with the decreasing t_{SIO} as shown in Figure 5.11(a), where the orthorhombicity a/b is the ratio between the $SrIrO_3$ orthorhombic lattice parameters whose components line along the in-plane $[100]_c$ and out-of-plane $[001]_c$ substrate directions. As just stated such orthorhombic distortions (a/b > 1) originate from the IrO_6 octahedral tilt, which is partially suppressed below a critical thickness of 12 uc likely due to the structural imprint of the underlying cubic $SrIrO_3$ substrate that does not exhibit TiO_6 tilt. This yields a strained tetragonal $SrIrO_3$ structure [Figure 5.11(c)]. Since the degree of rotation and distortion of the octahedra in perovskites can dramatically change the band structure of the material, we expect that this structural transition explains our observation of suppressed spin-torque efficiency. This strong dependency of $\sigma_{\parallel}$ on lattice symmetry points out a direct connection between the $SrIrO_3$ crystal structure and its spin-torque efficiency. By tuning the crystal structure of epitaxial $SrIrO_3$ through strain, we demonstrate that the $SrIrO_3$ SHC produces characteristic signatures of an intrinsic spin Hall effect.

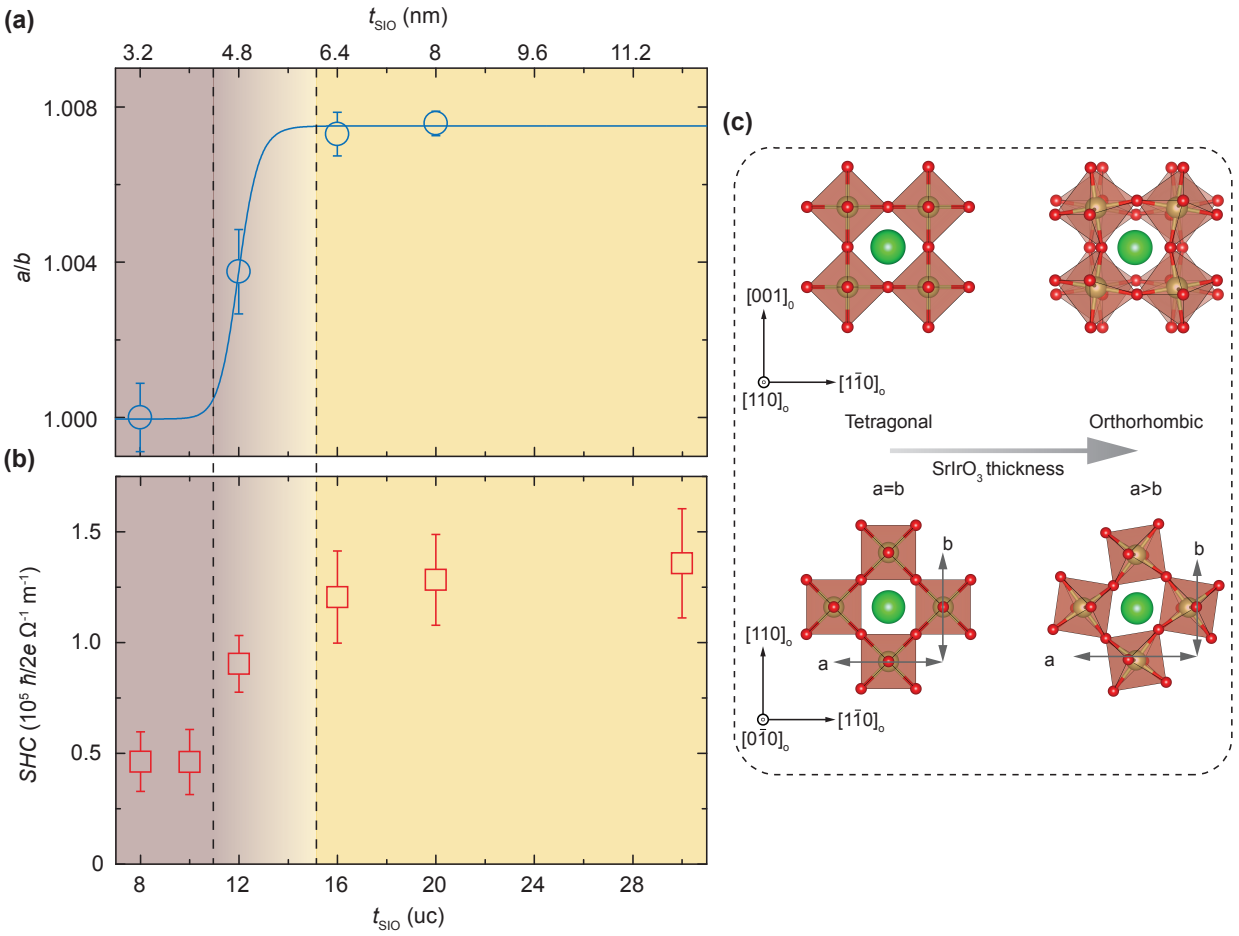


Figure 5.11: (a) Thickness dependent orthorhombicity factor, defined as a/b, of $SrIrO_3$. The dashed line represents a trend for the $SrIrO_3$ crystalline symmetry transition (b) SHC $\sigma_{||}$ of Py/$SrIrO_3$ bilayer (with Py thickness fixed at 3.5 nm) as a function of $SrIrO_3$ thickness (c) Schematic illustrations of the $SrIrO_3$ lattice symmetry change originating from the IrO_6 octahedral distortion that is partially suppressed up to 12 unit cells when grown on $SrTiO_3$.

5.3.4 Experimental configuration SHC for bulk and thin film slab

To get an insight about the intrinsic origin of the observed spin Hall effect, we further theoretically investigated the SHC based on the Berry curvature mechanism[151,152]. It is important to re-emphasize that the intrinsic effects encoded in the electron bands are generated by the interplay of spin-orbit coupling and tilted oxygen octahedra. For the electron band structure of $SrIrO_3$, we employed an effective tight-binding model constructed for the bulk orthorhombic perovskite structure[35,36] [see Figure 5.4(a)-(c)]. The model incorporates various spin-dependent hopping channels for Ir electrons generated by oxygen octahedron tilting in the bulk structure. Using the Kubo for-

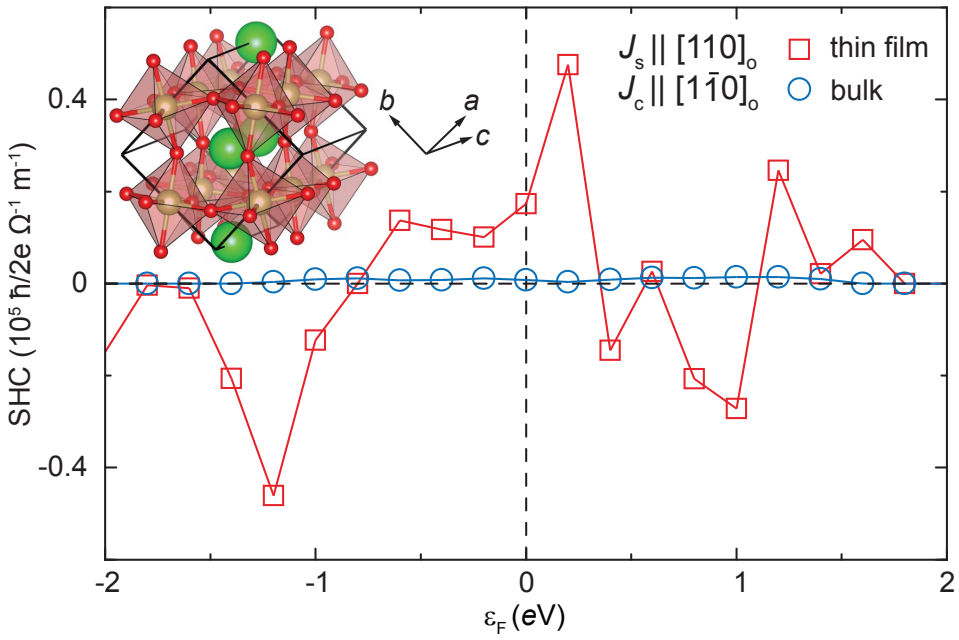


Figure 5.12: Calculated SHC in $SrIrO_3$ film slab (red) and the bulk (blue) for the experimental configuration (where the spin current is along the $[110]_o$ direction). In the film slab system, significant enhancement of SHC is observed compared to the bulk system.

mula for the intrinsic spin Hall effect (see Appendix D), we calculate the SHC. We found that the bulk system exhibits the largest SHC when spin current (J_s) is along the $[001]_o$ direction [Figure 5.4(a)], while the magnitude of the SHC depends strongly on the orientation of the charge and spin currents (see Appendix D, Figure D.2). The origin of the large SHC is revealed by investigating momentum resolved SHC $\Omega(\boldsymbol{k})$. High intensities of $\Omega(\boldsymbol{k})$ appear around the $\boldsymbol{k}$ points where the Fermi level crosses the nearly degenerate bands in Figure 5.4(b) and 5.4(c) (See Appendix D, Figure D.1). Remarkably, the high intensity points occur with the same sign in the form of loops extended over zone boundaries. These patterns contrast $SrIrO_3$ with Pt where the SHC is dominated by a few high symmetry points[152].

In order to make more direct contact with the experiment, we further computed SHC on the bulk $SrIrO_3$ crystal structure in a slab geometry with boundary conditions that corresponded to our experimental configuration (J_s parallel to $[110]_o$). Qualitatively consistent with our experimental results, a large intrinsic SHC is found around $\epsilon_F = 0$ as shown in Figure 5.12 (red). This is one order of magnitude larger compared to the bulk SHC for the same configuration [blue in Figure

5.12]. Such enhancement of SHC in the film system compared to the bulk implies the importance of the change in the lattice symmetry and boundary surfaces in our $SrIrO_3$ films (the bulk lattice symmetries that are broken in the $[110]_o$ slab geometry are shown in Appendix D, Table D.1 and Figure D.3). These two factors may substantially affect the electronic structure due to the extended nature of the $SrIrO_3$ 5*d* orbitals, which are sensitive to the change in lattice symmetry. Our results illustrate the eventual need for more refined calculations based on the true film band structure that arises from the observed $SrIrO_3$ film crystal structure (orthorhombic bulk vs. monoclinic thin film distortion of the bulk). Nonetheless, from this theoretical investigation, we find an unusually large SHC for the bulk system that is qualitatively consistent with our experimental results and also illustrates the intrinsic origin of the large spin Hall effect in $SrIrO_3$.

5.4 Conclusions

In conclusion, we have discovered a new material candidate for spin-orbit torque applications in a transition metal perovskite with spin-orbit coupled 5*d* electrons in which SOC and the crystal structure combine to produce the largest spin-torque efficiency in a bulk system to date. From the application point of view, less current is shunted through the adjacent metallic ferromagnets (due to the semimetallic nature of $SrIrO_3$) compared to the surface driven mechanisms which show a comparable efficiency. This material also acts as an ideal building block for oxide spintronics, since a broad range of ferromagnetic perovskites can be easily integrated in an epitaxial heterostructure with atomically sharp interfaces for efficient spin current transmission. Furthermore, the extended nature of 5*d* orbitals allows sensitive response of the electronic band structure to an externally manipulated lattice structure. This is, for example, manifested in the strong dependency of the SHC on the octahedral tilting and rotation. Such intricate coupling between the electronic and lattice degrees of freedom can thus open up a new avenue to engineer spin-orbit torque by tailoring the lattice symmetry. With this approach, an even stronger spin Hall effect could be theoretically designed and stabilized in a geometrically constrained heterostructure. Therefore, we anticipate that the use of 5*d* transition metal perovskites will lead to substantial advances in spintronics.

The research presented in this chapter used resources of the Advanced Photon Source, a U.S. Department of Energy (DOE) Office of Science User Facility operated for the DOE Office of Science by Argonne National Laboratory under Contract No. DE-AC02-06CH11357.

Chapter 6

Conclusions and outlook

6.1 Novelty of $SrIrO_3$ thin films

In this work, I have presented a coordinated effort of synthesis, characterization, and computational theory work to design, grow, and ultimately better understand, a metastable polymorph: perovksite $SrIrO_3$. This work demonstrates $SrIrO_3$ as a candidate for understanding fundamental materials science of interfaces and also opening up new frontiers in material discovery for advanced technologies. In Chapter 1, the vast flexibility of perovskite oxides and their related compounds was introduced, along with their complex electronic structure that arises from the strongly correlated *d*-electrons in the B-site. The inclusion to this electronic structure of strong-spin orbit coupling in materials like $SrIrO_3$ adds new or enhanced functionality to these materials. However, since perovskite $SrIrO_3$ is an unstable polymorph material that is relatively new in the community, the true nature of its intrinsic band structure remains largely unsettled, leaving room for significant advances in the fundamental understanding of the relationship between the material structure and its physical properties.

6.2 Structure of $SrIrO_3$ thin films on $(001)_{pc}$ perovskites

In Chapter 2, the PLD synthesis and subsequent structure of $SrIrO_3$ on (001) The x-ray work on $SrTiO_3$ revealed multi-domain films where $[001]_o$ oriented along both $[100]_c$ and [010]. While

increasing the miscut may yet yield single-domain $SrIrO_3$ thin films, such studies to date suggest this does not result in single-domain films[93]. The other common cubic perovskite substrate, $(LaAlO_3)_{0.3}$-$(Sr_2AlTaO_6)_{0.7}$[] (LSAT) also produced multi-domain films[42]. Thus, it may be that single-domain $SrTiO_3$ on cubic substrates may prove challenging or impossible. While our preliminary results on orthorhombic scandate substrates suggest single-domain $SrIrO_3$, which verifies a very recent report[91], scandates exhibit magnetism[169], and so careful study should be undertaken to determine if this influences the various spin-related phenomena that motivate $SrIrO_3$ research. Ideally, given their close elemental relationship and identical charge layering, single-domain $SrIrO_3$ on $SrTiO_3$ is preferable. More work may investigate the possibility of inducing immediate step-flow growth of PLD-grown $SrIrO_3$, as this may create the desired single-domain structure on cubic substrates.

As mentioned many times in this thesis, the bulk perovskite $SrIrO_3$ phase currently only exists as in polycrystalline material. To truly probe the intrinsic bulk properties, a single-crystal bulk sample should be produced. If synthesizing bulk material by solid state methods cannot achieve this, perhaps growing the metastable perovskite $SrIrO_3$ as film and then subsequently removing it from the underlying substrate may succeed in producing a single-crystal. Etching the substrate has been shown as a way to create $SrRuO_3$ membranes[170] and it has been demonstrated that that nanomembrane $SrTiO_3/La_{2/3}Sr_{1/3}MnO_3$ superlattices can be grown on a water-soluble $Sr_3Al_2O_6$ sacrifical layer epitaxially stabilized on a $SrTiO_3$ substrate[171]. Thus, $SrIrO_3$ nanomembrane fabrication is at least conceivable. Whether or not a metastable perovskite like $SrIrO_3$ could survive without the structural inprint of the perovskite substrate, however, is another matter to consider. But if such challenges could be overcome, the prospect exists for the creation of a bulk single crystal perovskite $SrIrO_3$ sample. While synthesizing a membrane of $SrIrO_3$ would allow both the stabilization of a single-crystal and eliminate the complication of strain on the $SrIrO_3$ band structure, the converse of this would be the allowed study of extreme elastic stretching or membrane, which, like epitaxial strain, would be expected to allow tuning of the band structure. Thus, nanomembrane fabrication of $SrIrO_3$, while challenging, could be a key component of future research on this system.

6.3 Polar (111) $SrIrO_3$ interfaces

In Chapter 3, the growth of polar (111) $SrTiO_3$/$SrIrO_3$ was demonstrated. While thick films on (111) $SrTiO_3$ produce monoclinic-phase $SrIrO_3$, we successfully synthesized the desired perovskite phase by growing ultra-thin $SrIrO_3$ on (111) $SrTiO_3$ and then capping it with $SrTiO_3$ to impose perovskite boundary conditions on both (111) interfaces in the heterostructure. This work is the first reported synthesis of perovskite $SrIrO_3$ along the (11) direction, which is the critical first step to allow probing of the possible existence of the topological states predicted by theory in this system.

In Chapter 4, work on the B-site interfacial configuration in polar (111) and non-polar (001) $SrTiO_3$/SIO heterostructures was presented. By designing polar/polar and non-polar/non-polar interfaces with identical A-site cations, we were able to study the B-site interfacial structure in perovskites without the added complications of A-site intermixing and polar discontinuities. It was found from COBRA-resolved electron planar densities of the heterostructures that the B-site strongly favors intermixing at the polar (111) interface compared to the non-polar (001) case. COBRA studies on the treated (111) and (001) $SrTiO_3$ substrates revealed depleted planar layerings about 4 bilayers into (111) $SrTiO_3$ substrate surface compared to the (001) substrate, which was close to nominal charge apart from the observed double TiO_2 layer on the surface. The intermixing of the (111) interface was concluded to be a result of this initial substrate surface.

This work illustrates an important geometric consideration that must be heeded during the design of artificial materials and interfaces with properties that manifest themselves on the (111) perovskite surface, particularly in ultra-thin honeycomb layerings. Since the B-site cation hosts the various strongly-correlated d-band electrons that usually determine the electronic structure in this class of materials, the findings presented here are relevant for the design of material properties that require particular interfacial structures, e.g. the (111) surface. Furthermore, if such observed atomic intermixing can be precisely controlled, interfacially-doped (111) interfaces could be geometrically designed to create desirable interfacial B-site alloy properties.

It is now proposed that electron correlations play a larger role than originally expected in 5*d*

oxides, and these interactions may suppress the topological states that were originally proposed by theory in the (111) geometry. This has been experimentally observed in (111) superlattices of $NdNiO_3$ and $LaAlO_3$, local orbital distortions at the honeycomb nodes create an anti-ferromagnetic insulating state[119]. From a theory point of view, it has been suggested that an anti-ferromagnetic insulating state for (111) $SrIrO_3$ is expected[56], although it is also proposed that the correct degree of strain could force the $SrIrO_3$ back to a topological state. An magnetic insulating state was found in superlattices of $Sr_{0.5}Ca_{0.5}O_3$ sandwiched between $SrTiO_3$[105], but the characteristic electronic behavior of pure-phase $SrIrO_3$ (111) remains unreported. Since it can only be synthesized in thin layers, as we have demonstrated, this characterization may be quite challenging. Angle-resolved photoemission spectroscopy on the ultra-thin (111) $SrIrO_3$ would be a worthwhile study to see if the strain from the $SrTiO_3$ substrate indeed pushes $SrIrO_3$ back into the TI state.

6.4 Large intrinsic spin-orbit torque in $Ni_{0.81}Fe_{0.19}/SrIrO_3$ heterostructures

Perhaps the most promising result of this thesis regarding the specific application of next-generation spintronics is the finding of large spin torques generated on ferromagnetic $Ni_{0.81}Fe_{0.19}$ (Py) by the strong spin Hall effect in $SrIrO_3$, which was discussed in Chapter 5. In this chapter, it was first found that the large spin-torques in the Py showed both a large magnitude due to the strong spin-orbit coupling in the $SrIrO_3$ band structure. Next, the directionaliy of the spin-torques was demonstrated, as the torques showed change along different directions in the orthorhombic crystal. Finally, by inducing a global structural transition from tetragonal to othorhombic in the $SrIrO_3$, the magnitude of the spin-torque was enhanced. The spin Hall effect observed in the thin films qualitatively agreed with our theory calculation for a film slab configuration that exceeded the predicted value from the bulk configuration by an order of magnitude, confirming the novelty of the thin film as a means to achieve the strong spin-torques. These results demonstrate the intrinsic nature of the spin Hall effect in $SrIrO_3$, which arises as a result of the strong spin-orbit coupling and suppression/enhancement of the octahedral tilting that strongly influence the band structure.

Future work will involve a careful study of the effect of strain on the spin Hall effect in $SrIrO_3$.

Our preliminary results on scandates show that the spin-torque can be tuned based on epitaxial strain. As mentioned in Chapter 2, there are at least 5 different substrates on which $SrIrO_3$ can be stabilized, so this initial finding opens up a huge avenue to systematically study the effect of strain on the spin Hall effect.

From a theory standpoint, it is evident from the discrepancy in our experimental results compared to the bulk theory prediction that the band structure of $SrIrO_3$ thin films is quite different from that of its bulk. This is likely due to subtle changes to the structure that particularly manifests in the tilting and rotations of the IrO_6 octahedra. This work has recently been systematically reported for $SrIrO_3$ films on $SrTiO_3$, $DyScO_3$, $GdScO_3$, and $NdScO_3$ [91], which means first principles theory calculations of the film band structure could be undertaken at this time. Due to the variety of the reported $SrIrO_3$ structures, careful verification of the film structure may be necessary before the optimal $SrIrO_3$ crystal structure can be definitively identified. While our film slab configuration qualitatively agrees with the experimental results, more refined calculations with the film band structure calculated from first principles could help directly match theory and experiment.

6.5 Final Thoughts

The huge discrepancy in the reported $SrIrO_3$ transport behavior and band structure is an obvious indication of sample variation, likely due to sensitive changes in film stoichiometry that almost certainly result from the complicated synthesis. At the very least, it can be said that the electronic properties of $SrIrO_3$ are quite sensitive to defects and also the strain state imposed on the films by the underlying substrates. It has also been demonstrated that PLD-grown $SrIrO_3$ films can be very sensitive to lithography [84], which complicates the fabrication of measurement devices needed to obtain accurate transport. These findings are unsurprising, as $SrIrO_3$ is relatively new material. And as is true with any relatively new material, synthesizing a clean sample is the difficult first step before any progress is achieved. The past decade has brought significant advancement in the design and synthesis of these iridates, particularly by molecular beam epitaxy and PLD.

While the difficulty of maintaining property film structure and stoichiometry of $SrIrO_3$ in PLD films has been mentioned several times in this thesis, the method also comes with some benefits.

Two examples of by the reported possibilities to selectively engineer different $Sr_{n+1}Ir_nO_{3n+1}$ phases from a single-phase target by exploiting thermodynamic growth behavior[172] and also the laser plume[173].

Most recently, sputtering of epitaxial $SrIrO_3$ have been demonstrated. Growth of $SrIrO_3$ by sputtering is a potential game-changer, as it significantly decreases the cost and also increases the scalability, which is paramount for any real-world application of these materials. The development of sputtering with *in situ* RHEED analysis[174] could allow real-time analysis of sputtered $SrIrO_3$ films that are traditionally only viable in more expensive growth techniques such as MBE and PLD. As more techniques are developed or improved[175] that widen the stoichiometric growth window, our understanding of this complicated material will also become clearer.

Appendix A: Experimental supplement for Chapter 2

A.1 AFM of $SrIrO_3$ Grown on Perovskite Substrates

The AFM images of $SrIrO_3$ films presented back in Figure 2.13 are presented here in Figure A.1. The film on $NdGaO_3$, which was expected from the x-ray data to be of poorer quality than films on the other substrates, is shown in Figure A.1(a). Here, preservation of the global $NdGaO_3$ terraced surface structure is preserved, but with roughing from uc-height islands. The films on (001) $(LaAlO_3)_{0.3}$-$(Sr_2AlTaO_6)_{0.7}$(LSAT) and $SrIrO_3$ [Figure 2.13(c)] shows the previously-mentioned "wedding cake" morphology, where the islands are more or less atomically smooth and of 1 uc height. These islands appear slightly more smooth on the $SrTiO_3$ The two films on (110)-oriented $DyScO_3$ and $GdScO_3$ are shown in Figure A.1(d) and A.1(e), respectively. These films show the overall smoothest films surfaces in this substrate study, as close to atomically smooth surface with uc-thick islands as shown in the figure are observed for both. This is unsurprising, as these substrates impose the least amount of epitaxial strain on the metastable $SrIrO_3$. The inevitable particles depicted in these images resulted from the PLD "particle-splashing" is common in PLD, and it is usually due to high-energy laser fluence knocking out defective regions in the ceramic target. However, the lowering the laser fluence could not eliminate these surface particles without affecting the stoichiometry of the films, which as stated, was achieved between 1.0-1.5 J/cm^2. Thus, particle size was reduced with laser fluence to a certain point, but could not be eliminated. Several films on (001)-oriented $DyScO_3$ and $GdScO_3$ were also grown to test the spin-torque work discussed in

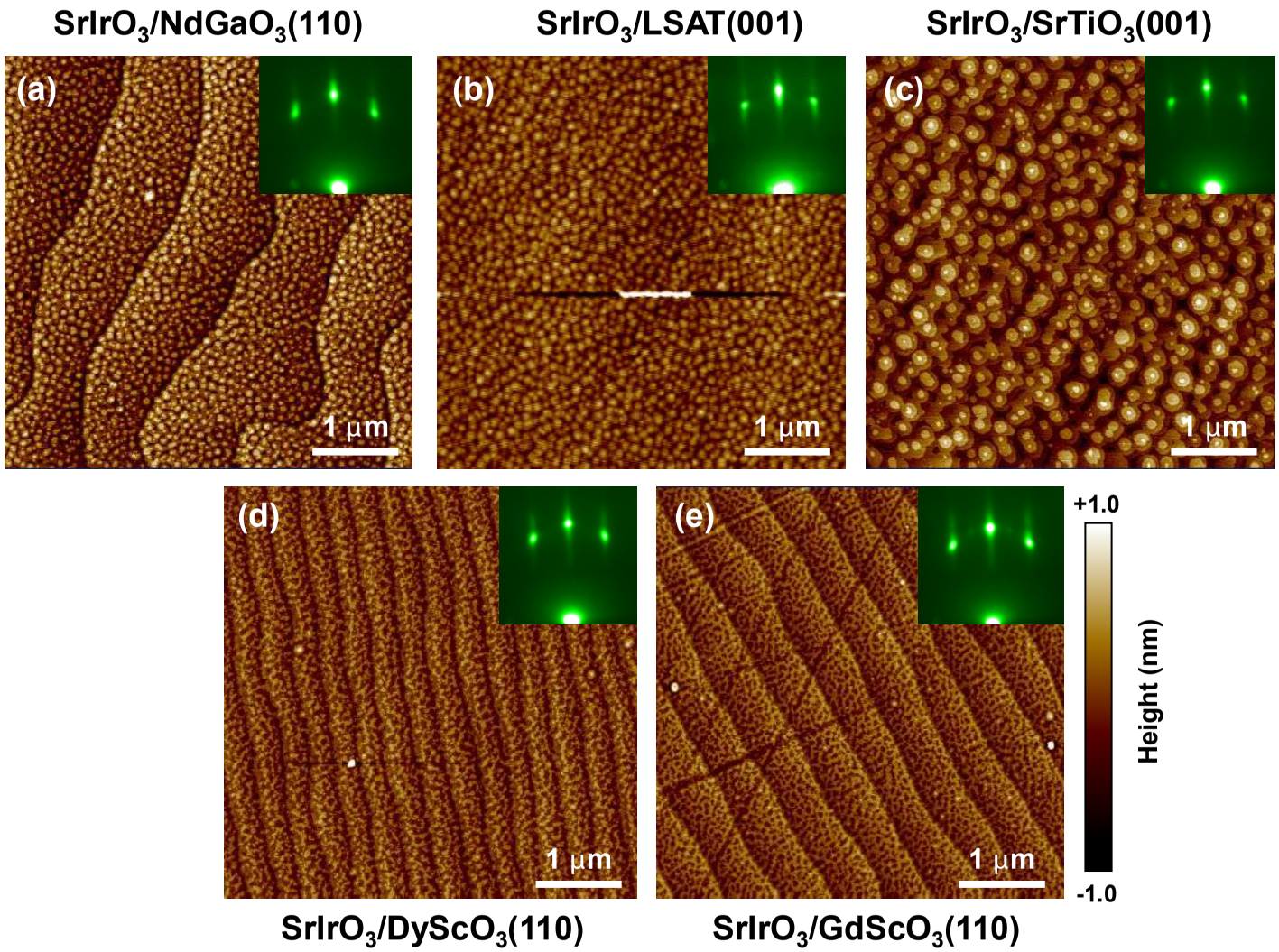


Figure A.1: AFM images of $SrIrO_3$ films grown on (a) $NdGaO_3$ (b) $(LaAlO_3)_{0.3}$-$(Sr_2AlTaO_6)_{0.7}$ (LSAT) (c) $SrTiO_3$ (d) $DyScO_3$ and (e) $GdScO_3$. The RHEED pattern taken at the end of the growth (at growth temperature and pressure) of each film is shown in the insets.

Chapter 4. These films yielded similar surfaces to their counterparts grown on (110)-oriented $DyScO_3$ and $GdScO_3$ substrates.

A.2 RHEED studies of $SrIrO_3$ on ABO_3 substrates

RHEED studies were undertaken on $SrIrO_3$ films on (001) $SrTiO_3$ in which the $SrIrO_3$ thickness was varied from 4, 8, 20, and 40 uc. Since structural analysis from RHEED requires diffraction patterns from at least 2 directions, RHEED images around the (1,0) and (0,1) reflections were taken. In all cases, the RHEED patterns at the growth temperature was compared to that at room temperature. In Figure A.2, data for 4, 8, and 40 uc $SrIrO_3$ films on (001) $SrTiO_3$ are presented. In all cases of $SrIrO_3$, the diffraction pattern preserves the symmetry of the underlying substrate, indicating that the $SrIrO_3$ films are cubic at the growth temperature. This has been observed in $SrRuO_3$ thin films as well. Upon cooling, however, the film undergoes a structural change to its preferred orthorhombic, as evidenced by superstructure peaks between the primary diffraction spots. These spots are distinguished by the arrows in Figure A.2(b) and A.2(a), which are observed along both in-plane (1,0) and (0,1) directions. As was mentioned in Chapter 2, $SrIrO_3$ exhibits mixed $[001]_o$ along both in-plane $[100]_c$ and $[010]_c$ directions, and this RHEED data is further proof of this. However, in Figure A.2(a), no such superstructure spots are observed, indicating that the 4 uc $SrIrO_3$ thin film remains cubic in-plane, which means a tetragonal structure with no octahedral tilt in the plane is established. This supports our findings in Chapter 4, where it was found that $SrIrO_3$ films show structural tendencies towards a tetragonal structure with decreasing thickness.

Additionally, analogous RHEED measurements on 20 uc films grown on (110)-oriented $DyScO_3$, $GdScO_3$, and $NdScO_3$ were taken. This data is summarized in Figure A.3 along with a 20 uc film on $SrTiO_3$ for direct comparison. As can be seen in Figure A.3(a) again shows the mixed-domain structure shown in the previous figure. However, comparison of the films grown on scandates, in Figure A.3(b), A.3(c), and A.3(b) show that the RHEED pattern of the substrates is preserved at room temperature, which provides evidence that the films have single-domain orientation.

Future work on this front will be to verify this domain structure with x-ray techniques pre-

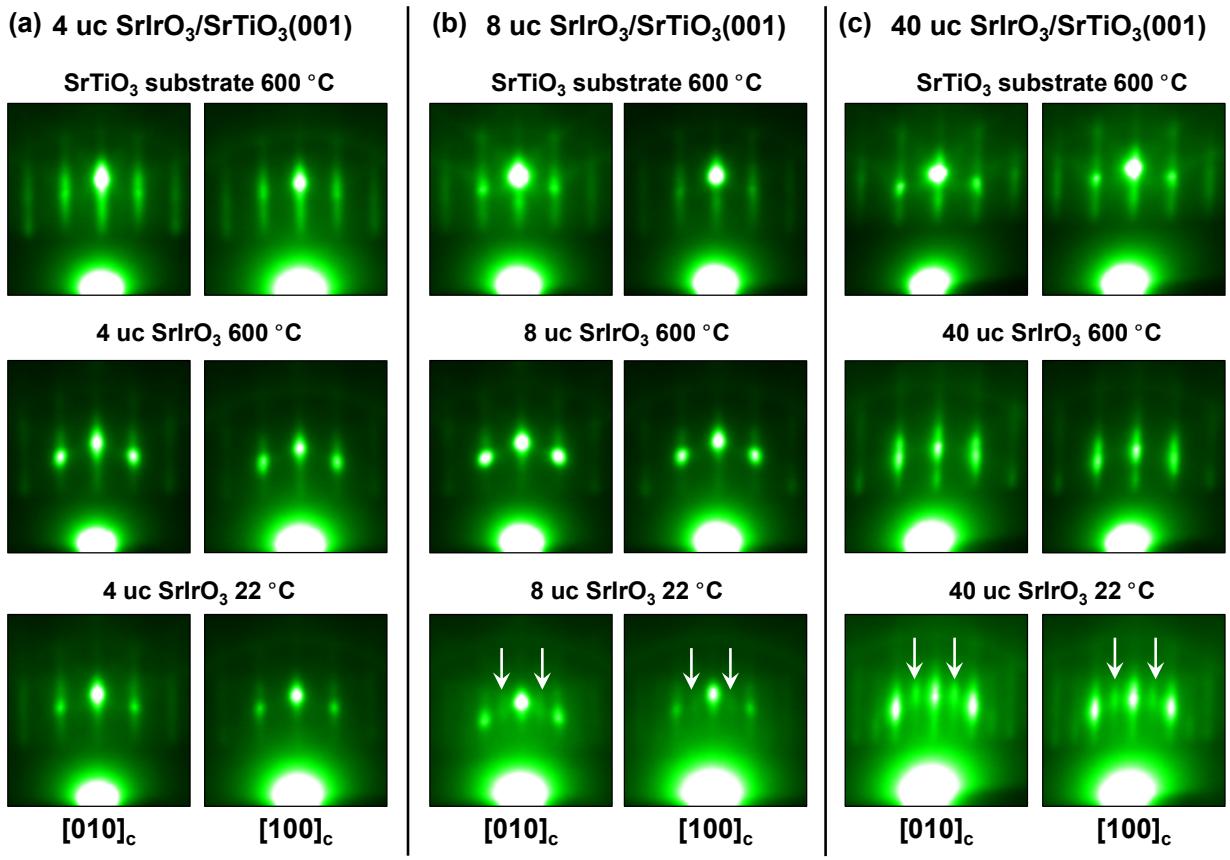


Figure A.2: (a), (b), (c) RHEED patterns of $SrIrO_3$ films on $SrTiO_3$(001) substrates as a function of thickness for 4, 8, and 40 uc, respectively. The substrate and $SrIrO_3$ patterns for each thickness are shown at the growth temperature and partial O_2 pressure in the first 2 rows, and the $SrIrO_3$ films at room temperature and partial O_2 pressure are shown in the bottom row. As can be seen, the $SrIrO_3$ films are cubic at the growth temperature, but the 8 and 40 uc samples show extra peaks in between the pseudocubic diffraction peaks, indicating orthorhombic [001] domains along that direction. The 4 uc $SrIrO_3$ film is cubic in-plane, indicating a purely tetragonal symmetry is established at this thickness.

sented in Chapter 2, along with temperature-dependent RHEED and x-ray studies to determine the structural transition temperature point of the growth-environment $SrIrO_3$ structure to its room-temperature distorted orthorhombic structure.

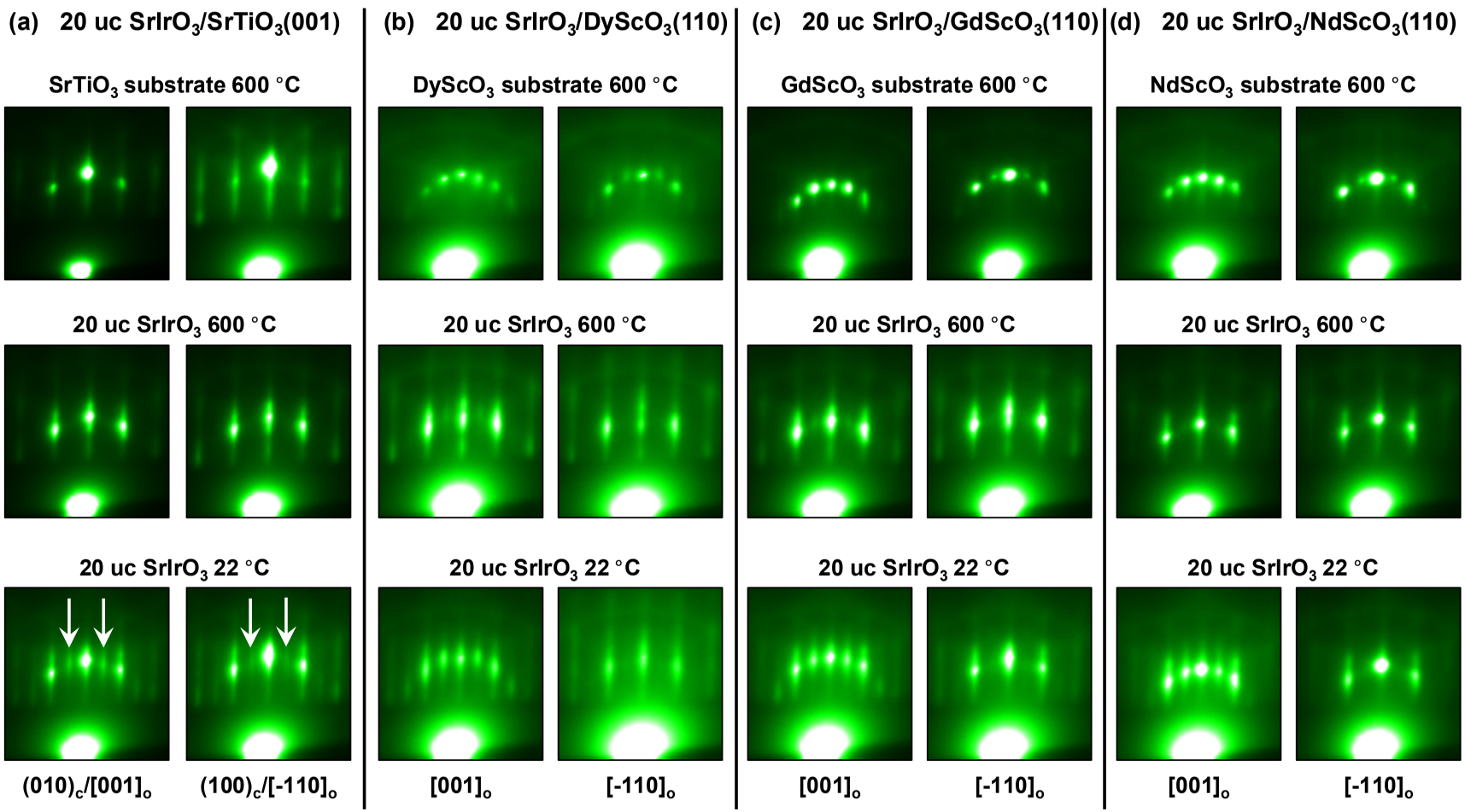


Figure A.3: RHEED patterns of 20 uc $SrIrO_3$ films on (a) $SrTiO_3$(001) (b) $DyScO_3$(110) (c) $GdScO_3$(110) (d) $NdScO_3$(110) substrates. The substrate and $SrIrO_3$ patterns for each substrate are shown at the growth temperature and partial O_2 pressure in the first 2 rows, and the $SrIrO_3$ films at room temperature and partial O_2 pressure are shown in the bottom row. As can be seen in (a), the $SrIrO_3$ films show orthorhombic [001] domains along both in-plane directions (white arrows). Inspection of the $SrIrO_3$ RHEED patterns on the 3 scandates in (b), (c), (d) suggests the symmetry of the underlying orthorhombic substrates is preserved at room temperature.

Appendix B: Experimental supplement for Chapters 3 and 4

B.1 Supplement to Chapter 3

B.1.1 Transmission electron microscopy

Scanning transmission electron microscopy (STEM) was used to examine the epitaxial microstructure of the honeycomb $SrTiO_3/SrIrO_3$ heterostructures. $SrTiO_3/SrIrO_3$ heterostructures were prepared and imaged by Dr. Lin Xie at the University of Michigan, the University of California-Irvine, and Nanjing University.

B.1.2 Synchrotron XRD and COBRA methods

Crystal truncation rods (CTRs) of the various $SrIrO_3$ heterostructures were measured at Argonne National Laboratory at the 33-ID-D beamline of the Advanced Photon Source by and with Dr. Hua Zhou. These measurements were used to study the symmetry of the films when lab-source diffractometer intensity was insufficient.

B.2 Supplement to Chapter 4

B.2.1 Transmission electron microscopy

Scanning transmission electron microscopy (STEM) was used to examine the epitaxial microstructure and interfacial sharpness of the (111) and (001) $SrTiO_3/SrIrO_3$ heterostructures. $SrTiO_3/SrIrO_3$

heterostructures were prepared, imaged, and analyzed by Dr. Lin Xie at the University of Michigan, the University of California-Irvine, and Nanjing University under the support and guidance of Prof. Xiaoqing Pan.

In Figure B.1(a) and B.1(b), the integrated and averaged HAADF-STEM Sr stacking column intensity across the (001) and (111) $SrTiO_3$/$SrIrO_3$ heterostructures is shown. Here, we see little deviation in Sr occupancy except in the top $SrTiO_3$ film and near the surface of the $SrTiO_3$ substrate. The former is attributed to incomplete layering in the $SrTiO_3$ capping film (recall that the $SrTiO_3$ capping films in chapter 3 and 4 were deposited at the $SrIrO_3$ growth condition to avoid damaging the $SrIrO_3$ film). The latter depletion is consistent with the intensities of both the Sr columns shown in Figure B.1(a) and the SrO_3^{-4} columns shown in Figure 4.6(a). Recall that these partially-depleted layers are a result of the substrate surface treatments prior to growth.

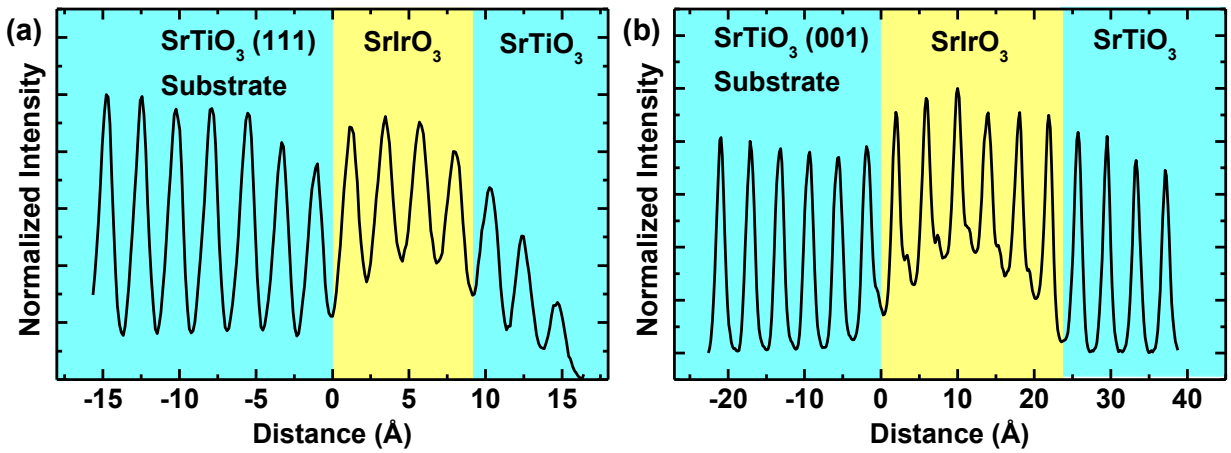


Figure B.1: (a), (b) Integrated HAADF-STEM Sr column intensities for the (111) and (001) $SrIrO_3$/$SrTiO_3$heterostructures, respectively. The decrease in Sr intensity in the surface layers of the (111) $SrTiO_3$ is consistent with the COBRA resolved SrO_3^{-4} planar configuration shown in Figures 4.5 and 4.6. The increase of the background intensity in the SrIrO3 films in (a) and (b) is likely due to $SrIrO_3$ film degradation from the TEM prep. The decrease in electron number of the top $SrTiO_3$ layers in the (111) sample is due to incomplete coverage in these layers.

B.2.2 Synchrotron XRD and COBRA methods

Crystal truncation rod (CTR) measurements on the (111) and (001) $SrIrO_3$/$SrTiO_3$ heterostructures and $SrTiO_3$ substrates were measured at Argonne National Laboratory at the 33-ID-D beamline of the Advanced Photon Source with Drs. Hua Zhou, Jacob Podkaminer, and Sangwoo Ryu. The

samples were mounted on a Kappa 4 + 2 circle diffractometer along with a Pilatus 100K 2D pixel area detector. The $SrTiO_3$ substrates were mounted on a temperature stage in a vacuum chamber that allowed the flow of O_2 flow to study the substrate surface structure under typical growth conditions. The studies presented in Chapter 4 utilized the Coherent Bragg Rod Analysis [121] method, which allowed extraction of the electron densities at the atomic planar level from each CTR. This analysis was undertaken/supervised by Dr. Hua Zhou. Jacob Patzner and I performed portions of the COBRA analysis at UW-Madison.

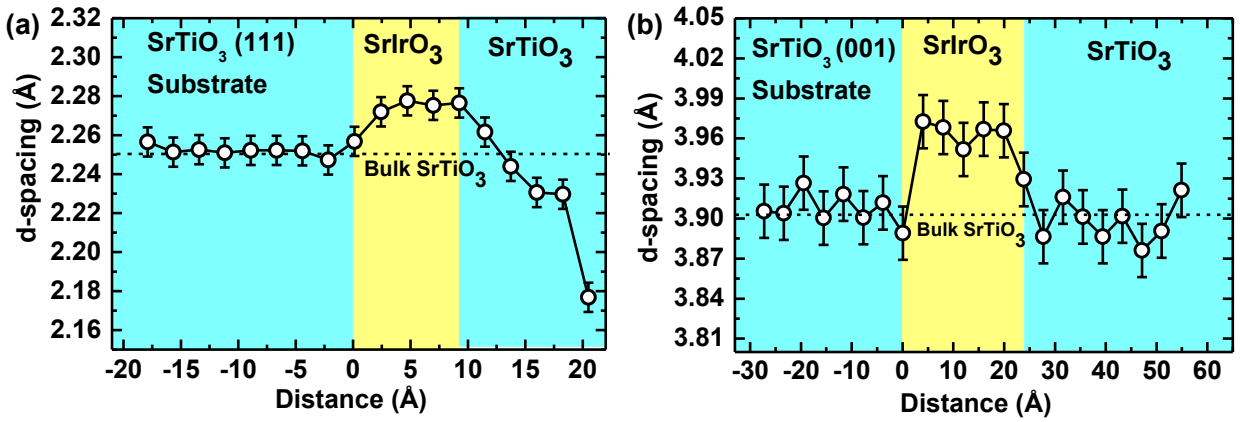


Figure B.2: (a), (b) d-spacing as a function of distance normal to the surface of the (111) and (001) $SrTiO_3/SrIrO_3/SrTiO_3$ heterostructures, respectively. The origin on the x-axis denotes the position of the $SrIrO_3$ film/$SrTiO_3$ substrate interface.

In Figure B.2(a) and B.2(b), the COBRA-extracted surface-normal bilayer/uc d-spacings of both heterostructures are shown. The d-spacing of the (111) $SrTiO_3$ is close to the bulk bilayer spacing of 2.252 Å, and the coherent $SrIrO_3$ film shows a elongated d-spacing of approximately 2.28 Å. The (001) $SrTiO_3$, like the (111), is also close to the bulk uc spacing, whereas the $SrIrO_3$ shows a strained lattice parameter of about 3.97 Å. The (001) $SrIrO_3$ films show more lattice elongation normal to the surface than the (111) films.

In Figure B.3 the raw CTRs and COBRA fit of the (111) and (001) $SrTiO_3$ substrates at conditions close to the growth (550 °C and 10^{-3} mbar O_2 partial pressure) are shown. Here, we see good agreement between the measured CTR intensities and the COBRA fittings. Both figures show clear features in the midzone regions that are indicative of the surface characteristics on the substrates presented in chapter 4. It should be noted that the midzone region between the (111) Bragg peaks

was at or below the measurement noise level, and was therefore omitted.

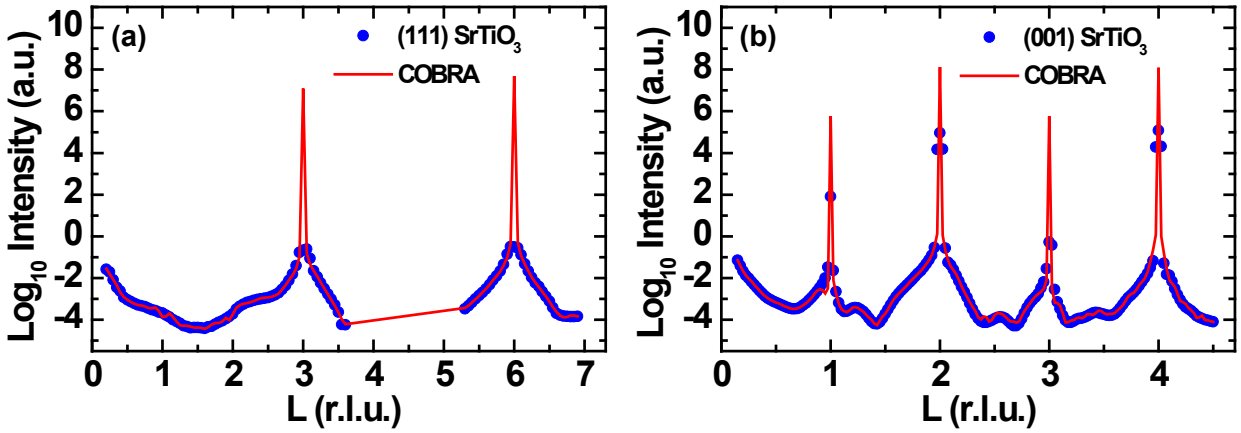


Figure B.3: (a), (b) Specular crystal truncation rod scans of the (111) and (001) $SrTiO_3$ substrates at 550 °C and 10^{-3} mbar, respectively, showing discernable midzone features and good agreement with the COBRA calculated CTRs.

Appendix C: Experimental supplement for chapter 5

C.1 Lab source x-ray diffraction

In Figure C.1, the lab-source x-ray diffraction data of a 1nm AlO_x/$Ni_{0.81}Fe_{0.19}$(Py) (3.5 nm)/$SrIrO_3$(12 nm)/ $SrTiO_3$(001) heterostructure is presented. For the purposes of the x-ray discussion in this appendix and in Chapter 5, we define pseudocubic (pc) lattice parameters for $SrIrO_3$, where $[100]_{pc}$, $[010]_{pc}$, and $[001]_{pc}$ lie along the $SrIrO_3$ orthorhombic (o) $[1\text{-}10]_o$, $[001]_o$, and $[110]_o$ directions, respectively. The $2\theta - \omega$ out-of-plan scan aligned to the (002) $SrTiO_3$ peak in C.1(a) shows an epitaxial $SrIrO_3$ film without the presence of additional peaks that would indicate that different phases of $SrIrO_3$ exist. The $SrIrO_3$ films show distinct Kiessig fringes around the main (001) and (002) pseudocubic reflections, which indicates a smooth film surface and interfacial structure. The azimuthal ϕ-scan around the $(101)_{pc}$ reflection in C.1(b) shows that the $SrIrO_3$ film shares the same pseudocubic arrangement with the underlying $SrTiO_3$ substrate, which agrees with the TEM result presented in Figure 5.6. From the reciprocal space mapping around the (103) $SrTiO_3$ peak shown in C.1(c), we show that our $SrIrO_3$ films are fully coherent with the underlying $SrTiO_3$ substrate.

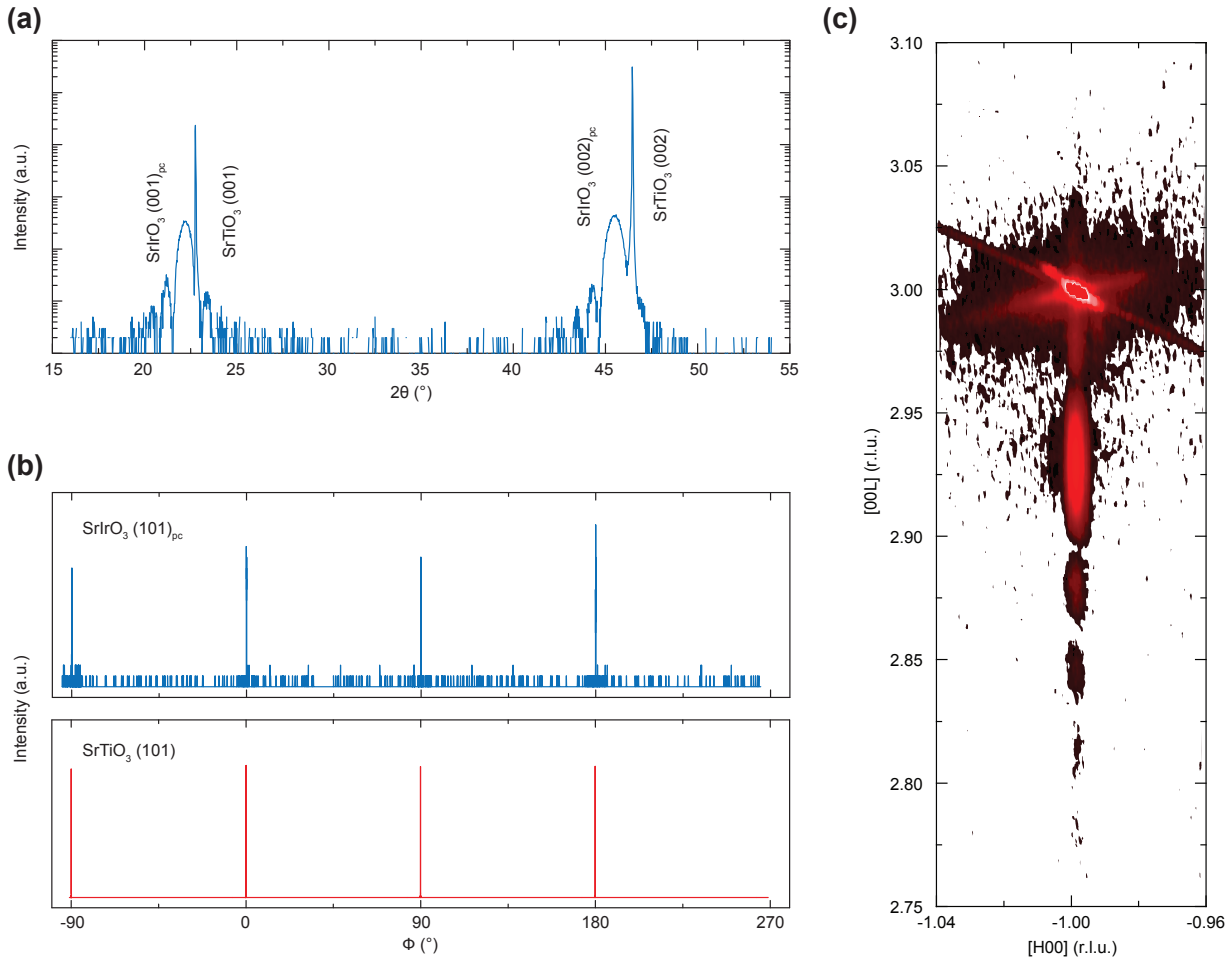


Figure C.1: Epitaxial structure and coherence of $SrIrO_3$ thin films from x-ray diffraction. a, $2\theta - \omega$ x-ray scan of 30 uc (12 nm) $SrIrO_3$ thin film on $SrTiO_3$(001) substrate showing single-phase $SrIrO_3$ with thickness oscillations indicating a smooth surface and sharp interface with the substrate. (b) ϕ-scan of the $SrIrO_3$ film showing its equivalent pseudocubic epitaxial arrangement with the underlying $SrTiO_3$ substrate. (c) reciprocal space mapping around the $(\bar{1}03)$ $SrTiO_3$ substrate peak confirming the fully coherent in-plane lattice of the $SrIrO_3$ film on the $SrTiO_3$ substrate.

C.2 Transmission electron microscopy

Py/$SrIrO_3$ films were examined using TEM by Dr. Si-Young Choi and Gi-Yeop Kim at The Korea Institute for Advanced Study. TEM specimens were prepared by a focused ion multi-beam system (JIB-4610F, JEOL, Japan). To protect the Py/$SrIrO_3$ films, an amorphous carbon layer was deposited on the top surface before the ion beam milling. A Ga^+ ion beam with an acceleration voltage of 30 kV was used to fabricate the thin TEM lamella. To minimize the surface damage

induced by the Ga+ ion beam milling, the sample was further milled by an Ar+ ion beam (PIPS II, Gatan, USA) with an acceleration voltage of 100 meV for 4 min. HAADF-STEM images were taken by using a scanning transmission electron microscope (JEM-2100F, JEOL, Japan) at 200 kV with a spherical aberration corrector (CEOS GmbH, Germany). The optimum size of the electron probe was 0.9 Å. The collection semi-angles of the HAADF detector were adjusted from 70 to 200 mrad in order to collect large-angle elastic scattering electrons for clear Z-sensitive images. The obtained raw images were processed with a band-pass Wiener filter with a local window to reduce a background noise (HREM research Inc., Japan).

C.3 Synchrotron x-ray thin film diffraction

Synchrotron X-ray diffraction measurements were carried out by Dr. Hua Zhou and Yongqi Dong at Argonne National Laboratory to precisely characterize the structural and lattice symmetry evolution as a function of thickness of $SrIrO_3$ thin films epitaxially grown on a (001) $SrTiO_3$ substrate. The thin film diffraction measurements were performed on a five-circle diffractometer with χ-circle geometry, using an X-ray energy of 20 keV (wavelength λ = 0.6197 Å) at sector 12-ID-D of the Advanced Photon Source, Argonne National Laboratory. The X-ray beam at the beamline 12-ID-D has a total flux of 4.0×10^{12} photons/s and was vertically focused by beryllium compound refractive lenses down to a beam profile of about 50 μm. The L-scans along respective truncation rods $\{10L\}$ were obtained by subtracting the diffuse background contributions using the two-dimensional images acquired with a pixel 2D array area detector (Dectris PILATUS-1mm Si 100K). The separation of respective 103 film peak position in reciprocal space can be used to extract the out-of-plane tilt angle of the $SrIrO_3$ film with respect to a cubic perovskite lattice, so that we can obtain the degree of orthorhombic distortion (a/b > 1) for each $SrIrO_3$ thin film as a function of thickness.

C.4 Setup for ST-FMR measurements

The spin-torque ferromagnetic resonance (ST-FMR)[176] spectra for the Py/$SrIrO_3$ heterostructures presented in chapter 5 were measured by Dr. Tianxiang Nan at UW-Madison. To verify the mea-

surements performed at UW-Madison, similar measurements were taken by X.J. Wang at Northeastern University and by Jonathan Gibbons at Cornell University.

The photolithography, ST-FMR measurements and subsequent analysis was done by Dr. Tianxiang Nan. First, the Py/$SrIrO_3$ sample was patterned using photolithography followed by ion beam milling. Then 200 nm Pt/5 nm Ti electrodes were sputter deposited and defined by a lift-off procedure. Devices for ST-FMR were patterned into microstrips (20-50 μm wide and 40-100 μm long) with ground-signal-ground electrodes. Devices for electrical transport measurements were patterned into 100 μm wide and 500 μm long Hall bars.

During ST-FMR measurements, a microwave current at a fixed frequency (4.5 to 7 GHz) is applied to the ac port of a bias-T and a RF ground-signal-ground probe tip. The microwave power output (8 to 14 dBm) is also fixed. For our applied powers, the line shape of the ST-FMR spectrum is within the linear region of small-angle precession. The in-plane magnetic fields ($\pm$0.12 T) are generated by a rotary electromagnet. For the line shape analysis, the rectified mixing voltage is detected by using a dc voltage meter through the dc port of the bias-T. For the dc-tuned analysis, we modulate the rf current amplitude and measure the mixing voltage signal by using a lock-in amplifier. The j_c is carefully calibrated by measuring the 4-point-resistance for each layer with a parallel resistor model. For the crystalline orientation dependent measurement, devices were patterned on the same sample to minimize the possible variations on sample fabrication. And the in-plane magnetic field angle is fixed at $\phi = 45^\circ$, the microwave frequency and power is 5.5 GHz and 12 dBm.

C.4.1 ST-FMR line shape analysis and frequency dependent spin torque ratio

The ST-FMR signal with the current-induced in-plane and out-of-plane torque components can be described by the Landau-Lifshitz-Gilbert-Slonczewski equation[134].

$$\frac{d\vec{M}}{dt} = -\gamma\vec{m} \times \mu_0\vec{H}_{\text{eff}} + \alpha\vec{m} \times \frac{d\vec{m}}{dt} + \tau_\perp\vec{\sigma} \times \vec{m} + \tau_\parallel\vec{m} \times (\vec{\sigma} \times \vec{m}) \tag{C.1}$$

Here γ is the gyromagnetic ratio, μ_0 is the permeability in vacuum, $\vec{H}_{\text{eff}}$ is the effective magnetic

field including the external magnetic field H-ext and the demagnetization field, α is the Gilbert damping coefficient, $\tau_\perp$ and $\tau_\parallel$ are the out-of-plane and in-plane torque components shown in Figure 5.7. The ST-FMR mixing voltage can be then written in the form of:

$$V_{mix} = S\frac{W^2}{(\mu_0 H_{ext} - \mu_0 H_{FMR})^2 + W^2} + A\frac{W(\mu_0 H_{ext} - \mu_0 H_{FMR})}{(\mu_0 H_{ext} - \mu_0 H_{FMR})^2 + W^2} \tag{C.2}$$

Here, W is the half-width-at-half-maximum resonance linewidth, H_{FMR} is the resonance field. S and A are the symmetric and antisymmetric amplitude of the Lorentzian, and can be expressed by the following equations:

$$S = -\frac{I_{RF}}{2}\left(\frac{dR}{d\phi}\right)\frac{1}{\alpha\left(2\mu_0 H_{FMR} + \mu_0 M_{eff}\right)}\tau_\parallel \tag{C.3}$$

$$A = -\frac{I_{RF}}{2}\left(\frac{dR}{d\phi}\right)\frac{\sqrt{1 + M_{eff}/H_{FMR}}}{\alpha\left(2\mu_0 H_{FMR} + \mu_0 M_{eff}\right)}\tau_\perp \tag{C.4}$$

where I_{RF} is the microwave current, $R(\phi)$ is the device resistance as a function of in-plane magnetic field angle ϕ due to the anisotropic magnetoresistance of Py, and $\mu_0 M_{eff}$ is the effective magnetization. The S and A amplitudes are proportional to the microwave power [Figure C.2(a)], which indicates that the measurement is within the linear regime to the driving field. In this study, we directly measured the V_{mix} by a dc voltmeter without any amplitude modulation of the microwave power. To calibrate $dR/d\phi$, we measure the device resistance as a function of magnetic field angle by rotating an in-plane magnetic field of 0.1 T produced by a rotary electromagnet [Figure C.2(b)]. By fitting the ΔR to $cos(2\phi)$, we can calculate $dR/d\phi$ at certain ϕ angle. The microwave current I_{RF} is calibrated by measuring the device resistance change due to the Joule heating effect[177,178]. This same amount of heating can be obtained with an injection of dc current I_{dc} by comparing the change of the device resistance. Therefore, the rf current can be determined as $I_{RF} = \sqrt{2} I_{dc}$, since the Joule heating from ac and dc current are $\frac{1}{2} I^2 R$ and $I^2 R$. Figure C.2(c) shows a typical device resistance change curve due to dc (blue) and rf (red, 5.5 GHz) currents, in which they are fitted to a quadratic and a linear function respectively. We estimated the rf current for different rf frequencies and powers.

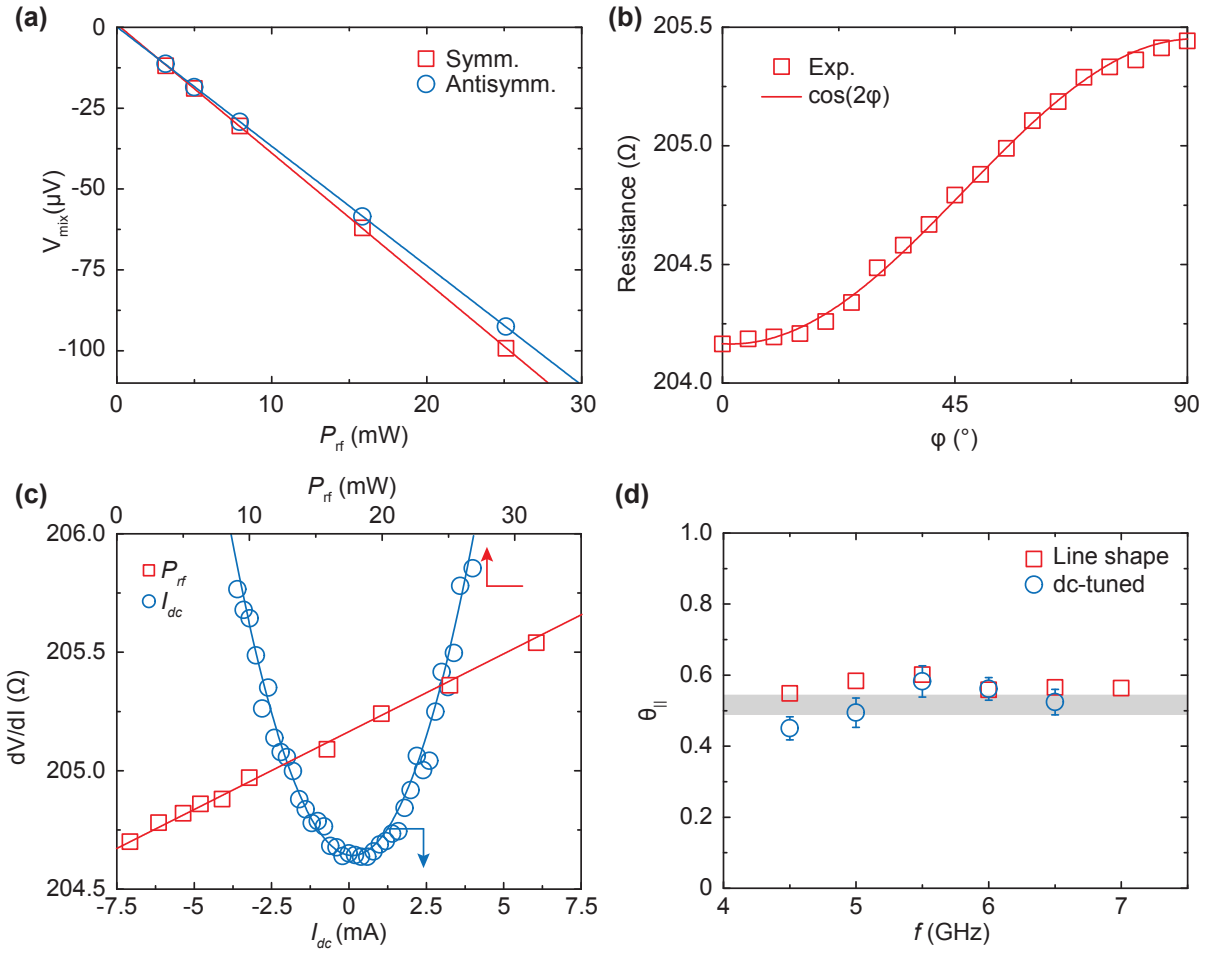


Figure C.2: Calculation of spin-Hall angle with ST-FMR lineshape and the calibration of microwave current. (a) Microwave power dependence of the symmetric and antisymmetric components of the mixed voltage V_{mix} for a 3.5 nm Py/ 20 uc $SrIrO_3$ bilayer sample (20 μm 40 μm) at f = 5.5 GHz and $\phi = -135°$ (b) Resistance R of the same device as a function of the external magnetic field angle ϕ. ΔR is fitted to $cos(2\phi)$ for extracting $dR/d\phi$. (c) Applied microwave power (red) and dc current (blue) induced device resistance change due to the Joule heating effect (d) Frequency dependent spin torque ratio of a 20 uc $SrIrO_3$ sample determined from ST-FMR line shape (red) and dc-tuned (blue) analysis.

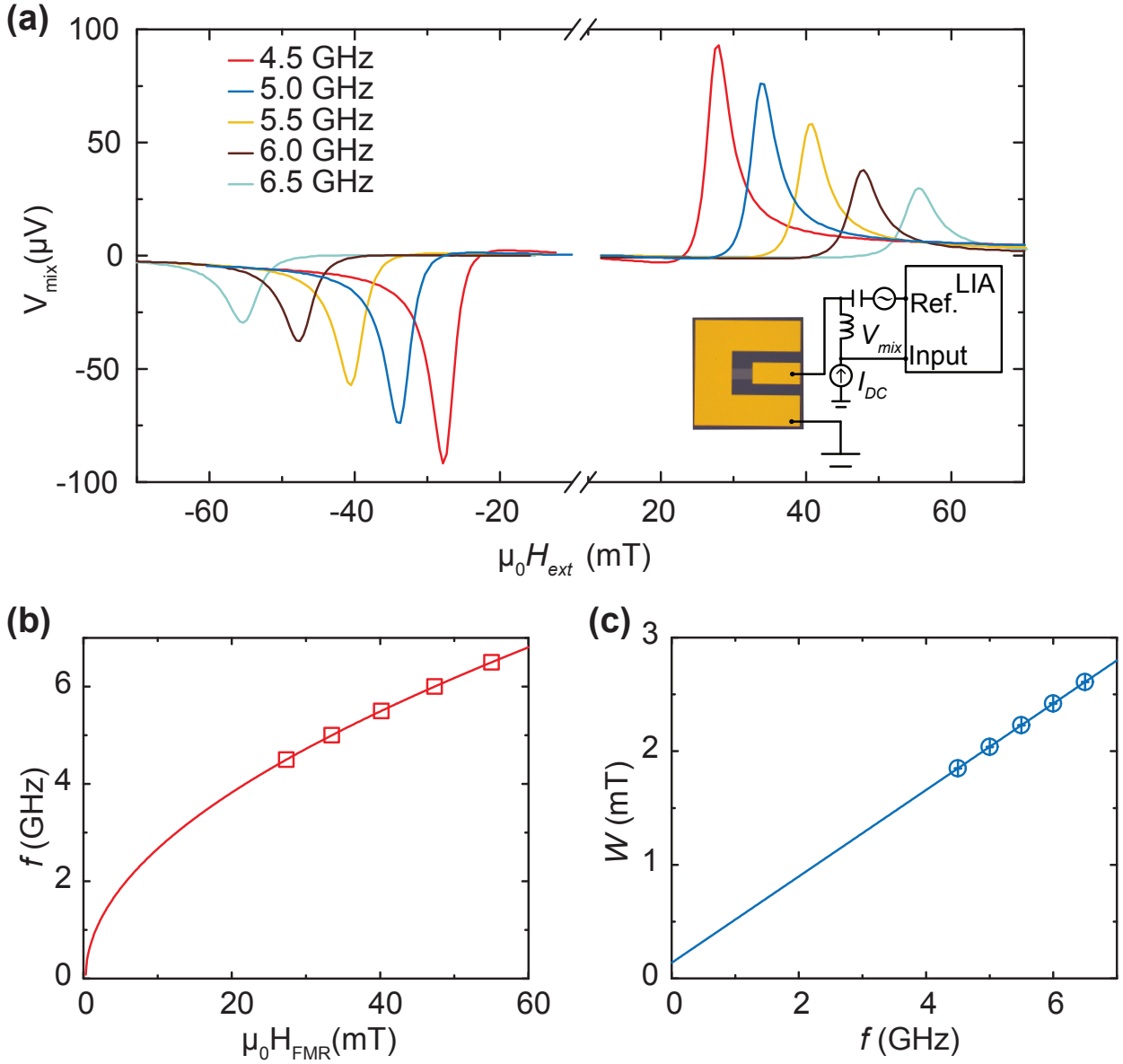


Figure C.3: Spin-torque ferromagnetic resonance (ST-FMR) in 3.5 nm Py/ 20 uc $SrIrO_3$ bilayer at different frequency f. (a) ST-FMR spectral for Py/$SrIrO_3$ sample at various f (4.5-6.5 GHz) and with the external magnetic field H_{ext} angle of $45°$ and $-135°$. Inset shows an optical image of the device layout and ST-FMR measurement circuit. b, Dependence of the frequency f on the resonance magnetic field HFMR. The data is fitted to the Kittel equation, which gives an effective magnetization of 0.85 T. (c) Frequency f dependence of the resonance linewidth W. The solid curve shows the fit to a linear function, which gives a Gilbert damping coefficient of 0.011.

Then, the magnitude of torque components can be determined by extracting the symmetric and antisymmetric amplitude from Equation C.3 and Equation C.4. The two torque ratios can be calculated as $\theta_{\parallel/\perp} = \tau_{\parallel/\perp} M_s t \frac{I_{RF} R}{l cos(\phi)} \left(\frac{2e}{\hbar}\right) \rho$, where M_s and t are the saturation magnetization and the thickness of Py; l is the length of the device bar, $\hbar$ is the reduced Plancks constant, e is the electron charge. The saturation magnetization M_s is measured by vibration sample magnetometry. The effective magnetization Meff is obtained by measuring the frequency dependent H_{FMR} with a fit to Kittel equation, given by

$$2\pi f = \gamma \sqrt{\mu_0 H_{FMR}(\mu_0 H_{FMR} + \mu_0 H_K)(\mu_0 H_{FMR} + \mu_0 H_K + \mu_0 M_{eff})} \tag{C.5}$$

Here, $\mu_0 H_K$ is the in-plane magnetic anisotropy field [Figure C.3]. We find $M_{eff} \approx M_s$ for all samples with 4.5 nm Py, indicating negligible perpendicular magnetic anisotropy. Figure C.3(a) shows the frequency dependent ST-FMR spectra for a 3.5 nm Py/20 uc $SrIrO_3$ bilayer sample, in which we determined the Py effective magnetization M_{eff} [Figure C.3(b)] and Gilbert damping parameter [Figure C.3(c)]. We then calculated the spin torque ratio $\theta_{\parallel}$ of a 20 uc $SrIrO_3$ sample at various frequencies (4.5-7 GHz), since the spin torque ration is expected to be independent of frequency[164]. Figure C.2(d) shows the frequency dependent spin torque ratio determined from both ST-FMR line shape (red) and dc-tuned analysis (blue). Both methods give a small frequency variation.

C.4.2 ST-FMR dc-tuned analysis and thickness dependent spin torque ratio

Alternatively, we obtain the spin torque ratio by inserting a dc I_{dc} current superimposed with the microwave current which induces a subtle change in the ST-FMR line shape[155,165,179,180]. In particular, we quantify the $\theta_{\parallel}$ by a linear fitting of the current dependent resonance linewidth or α_{eff} as given by:

$$|\theta_{\parallel}| = \frac{2|e|}{\hbar} \frac{(H_{FMR} + M_{eff}/2)\mu_0 M_s t}{|\sin\phi|} \left| \frac{\Delta\alpha_{eff}}{\Delta j_c} \right| \tag{C.6}$$

Here, α_{eff} is the effective magnetic damping of Py and can be related to W as $\alpha_{eff} = \frac{\gamma}{2\pi f}(W -$

W_0). To extract resonance linewidth with smaller deviation, we modulate the rf current amplitude and measure the mixing voltage signal by using a lock-in amplifier.

The current density in $SrIrO_3$ layer is estimated by using a parallel resistance model. The Py resistivity is first measured in a AlO_x/Py/$SrTiO_3$ control sample. Then in a AlO_x/Py/$SrIrO_3$/$SrTiO_3$ sample, the resistivity and current fraction of $SrIrO_3$ can be determined by assuming that the Py has the same resistivity as the control sample. The estimated current fraction as a function of $SrIrO_3$ can be found in Figure C.6(b).

C.4.3 Transmission of spin current in Py/$SrIrO_3$

To estimate the spin diffusion length in our $SrIrO_3$ thin film, we characterize the Gilbert damping parameter α of Py in Py/$SrIrO_3$ bilayer with various $SrIrO_3$ thicknesses by using both ST-FMR (on patterned samples) and a broadband FMR (on 5 mm by 5 mm samples). The Gilbert damping parameter is obtained from the frequency dependent measurement (4.5-6.5 GHz for ST-FMR, and 5-12 GHz for FMR) of the resonance linewidth W. We observed the enhancement of with the increasing $SrIrO_3$ thickness due to the spin pumping effect as shown in Figure 5.9(f). The data can be fitted to diffusive spin transport model, which is given by:

$$\alpha = \alpha_0 + \frac{g_{op}\mu_B\hbar}{2e^2 M_s t_{SrIrO_3}} \left[\frac{1}{G_{\uparrow\downarrow}} + 2\rho\lambda_s \coth\left(\frac{t_{SrIrO_3}}{\lambda_s}\right)\right]^{-1} \tag{C.7}$$

Here, g_{op} is Landau g factor, α_0 is the Gilbert damping with zero $SrIrO_3$ thickness, $G_{\uparrow\downarrow}$ is the interfacial spin mixing conductance per unit area, λ_s is the spin diffusion length in $SrIrO_3$. We use a constant $SrIrO_3$ resistivity ρ in the fit, which gives the spin mixing conductance $G_{\uparrow\downarrow}$ of $1.8 \times 10^{14}\Omega^{-1}m^{-2}$ and the spin diffusion length of 1.4 nm. This is consistent with that reported of the $La_{2/3}Sr_{1/3}MnO_3$/$SrRuO_3$ system[168]. The large spin mixing conductance of $SrIrO_3$ enables efficient spin transport at the Py/$SrIrO_3$ interface. While the spin diffusion length in $SrIrO_3$ suggests that the spin accumulation in $SrIrO_3$ can take place in a very short thickness length scale. The measured changes in the $SrIrO_3$ SHC occur at a thickness scale well above the $SrIrO_3$ spin diffusion length, allowing us to conclude that the suppression of the SHC at the thin $SrIrO_3$ sample is due to the change of lattice symmetry rather than due to spin diffusion.

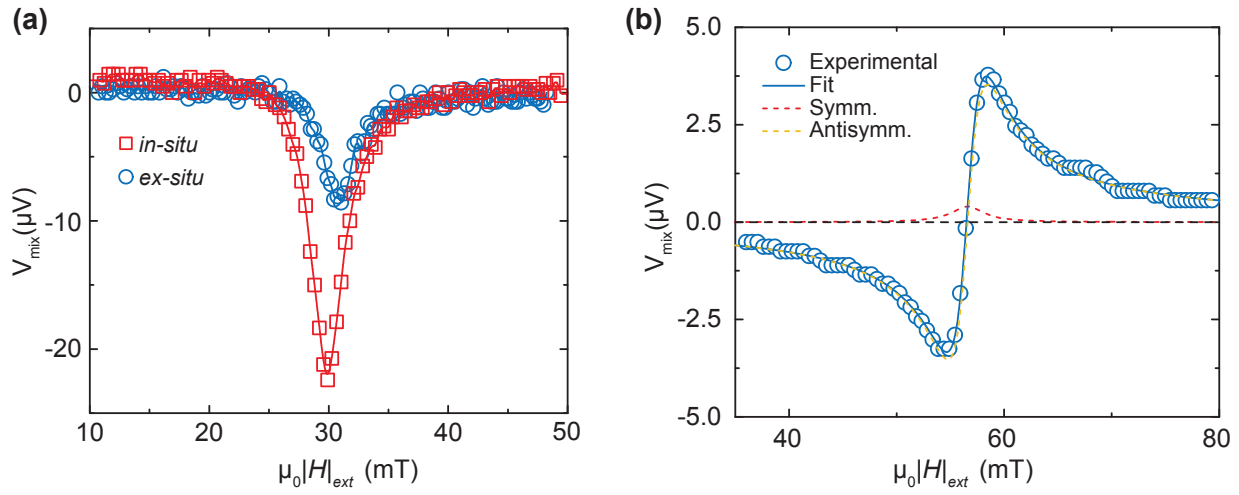


Figure C.4: ST-FMR measurements on an *ex-situ* Py deposition and a bare Py control sample (a) ST-FMR spectral for an in-situ (red) and an *ex-situ* (blue) deposited sample. The microwave power is fixed at 12 dBm at a frequency of f = 6 GHz. The external magnetic field Hext is oriented at an angle $\phi = 45°$ with respect to the current axis (b) ST-FMR spectrum of a bare 10 nm Py control sample taken at $\phi = 45°$ and f = 5.5 GHz. The microwave power is fixed at 12 dBm.

C.4.4 Measurements on *ex-situ* Py/$SrIrO_3$, Py, and Pt/Py controls samples

As discussed in Chapter 5, we also performed ST-FMR measurements on an ex-situ grown Py/$SrIrO_3$ sample since the Py/$SrIrO_3$ interfacial transparency plays an important role in the spin current transmission and the spin torque generation[163,164,181,182]. Figure C.4(a) shows the ST-FMR spectra for the ex-situ and in-situ grown Py/$SrIrO_3$ sample. For the ex-situ sample, Py was deposited after breaking the chamber vacuum for 2 minute. Two samples have the same layered structure (3.5 nm Py/20 uc $SrIrO_3$) and similar $SrIrO_3$ film quality characterized with XRD and AFM. At the same ST-FMR measurement condition (12 dBm, 6 GHz), the in-situ sample shows a much higher S and A amplitudes. Assuming both samples have the same microwave current flow during the measurements, the in-situ sample would exhibit much higher spin torque ratio. This suggests that the non-idea Py/$SrIrO_3$ interface decreases the spin mixing conductance.

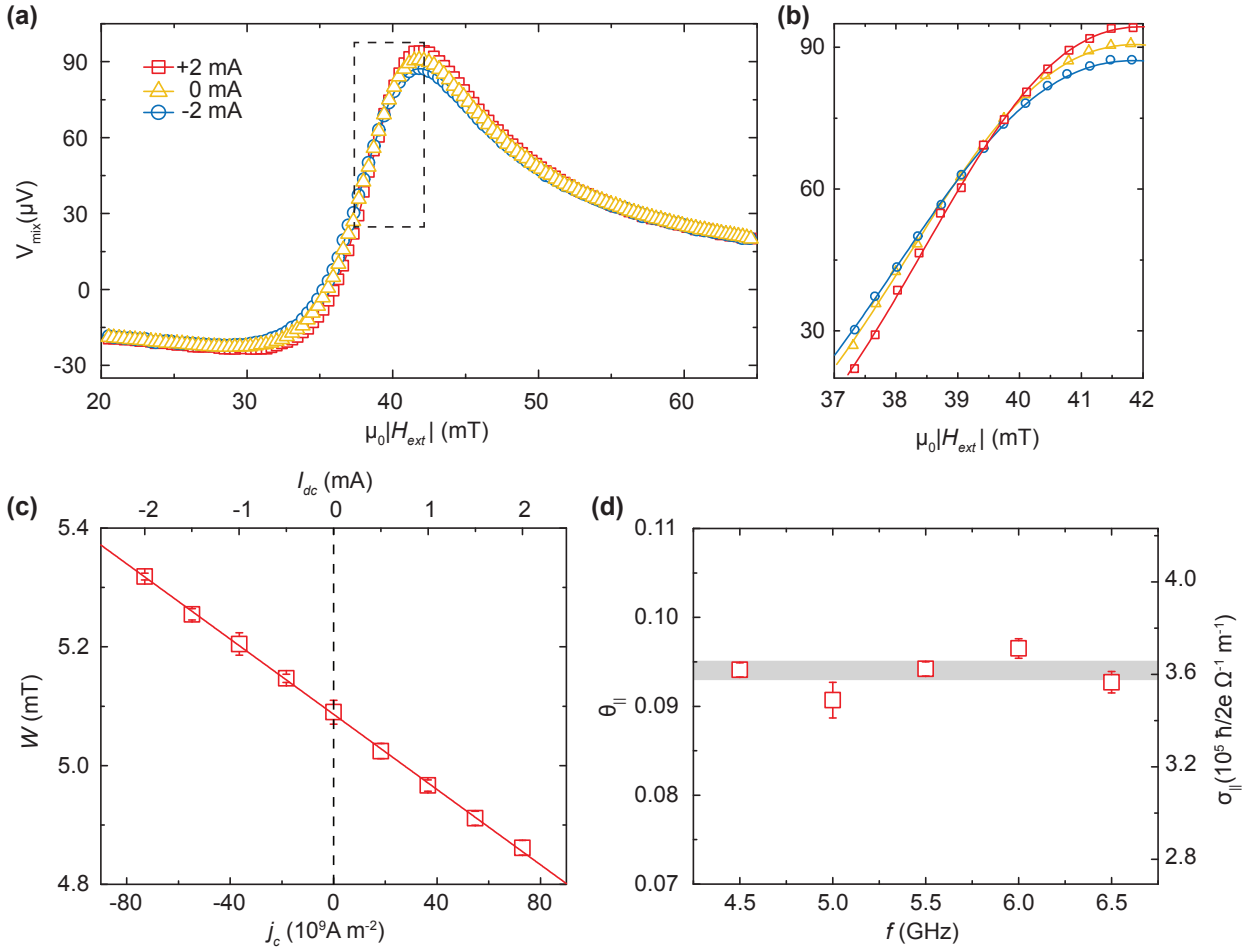


Figure C.5: ST-FMR measurements on a Pt/Py control sample. (a) ST-FMR spectral for the 4 nm Pt/ 4 nm Py/$SrTiO_3$ sample with different applied I_{dc} at $\phi = -135°$. The microwave power is fixed at 12 dBm and the frequency at 5.5 GHz. (b) The zoom-in view of the resonance peak shown in (a) (c) Resonance linewidth and effective magnetic damping as the functions of applied current and the corresponding current density in Pt for the Pt/Py. The solid lines represent linear fitting. (d) Spin torque ratio and the spin Hall conductivity of the Pt/Py bilayer measured at various microwave frequencies.

To check for any spurious effect from the non-uniform current distribution at microwave frequency, we performed ST-FMR measurements on the single layer Py sample. Figure C.4(b) shows the ST-FMR spectrum of a 10 nm Py/LSAT sample. The symmetric component of the Py sample is negligible small and opposite to that of Py/$SrIrO_3$ samples. The observed small antisymmetric component can be attributed to the FMR rectification or non-uniform current distribution in Py[156,165]. We also performed ST-FMR measurement and dc-tuned analysis on a 4 nm Pt/ 4 nm

Py/$SrTiO_3$ sample as shown in Figure C.5. The resistivity of Pt is 26 $\mu\Omega$-cm, and its current fraction is 0.73. In a 5 μm wide, 10 μm long device, we injected 2 mA dc current, which modifies the ST-FMR spectrum [Figure C.5(a)]. By fitting the change of the resonance linewidth as a function of current density in $SrIrO_3$ to a linear function [Figure C.5(c)], we calculated the spin torque ratio based on Equation C.6. Averaging over various frequencies [Figure C.5(d)], we find the Pt spin torque ratio $\theta_{\|} = 0.093 \pm 0.002$ and SHC $\sigma = 3.57 \times 10^5\ \hbar/2e\ \Omega^{-1}m^{-1}$, which is in a good agreement with the previously reported values[151].

C.5 $SrIrO_3$ and AlO_x/Py/$SrIrO_3$ Transport Properties

The bare $SrIrO_3$ thin film transport property was measured by using the van der Pauw technique in 5 mm $\times$ 5 mm $SrIrO_3$/$SrTiO_3$ samples by Neil Campbell at UW-Madison. The $SrIrO_3$ room temperature resistivity shows a slight sample-to-sample variation. To determine the anisotropy of the transport property of $SrIrO_3$, the sheet resistance of the $SrIrO_3$ thin film was measured by using a 4-point resistance technique on Hall bars patterned along the substrate $[100]_c$ and $[010]_c$ axes. Typical $SrIrO_3$ resistivity versus temperature curves are shown in Figure C.6(a) exhibiting metallic transport characteristics in both crystalline orientations.

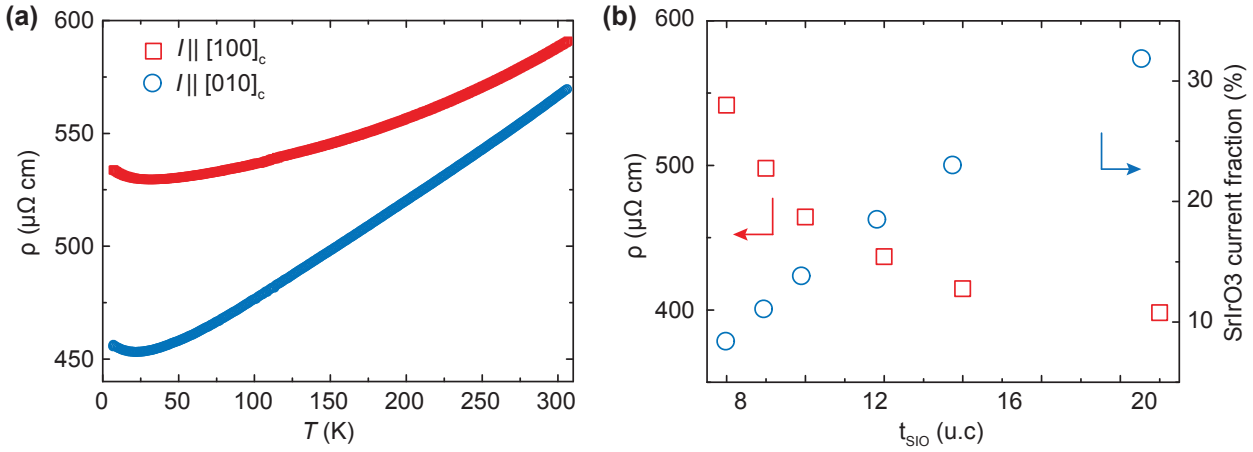


Figure C.6: Transport and dc current faction of $SrIrO_3$ thin films. (a) Temperature dependence of the resistivity of the 20 uc $SrIrO_3$/$SrTiO_3$ sample with the current applied along both $SrTiO_3$ $[100]_c$ and $[010]_c$ directions. (b) $SrIrO_3$ room temperature resistivity and the current fraction of the 3.5 nm Py/$SrIrO_3$/$SrTiO_3$ with various $SrIrO_3$ thicknesses.

The Py resistivity was measured by using the van der Pauw technique in AlO_x/Py/$SrTiO_3$ refer-

ence samples. The resistivity for the 3.5 nm Py in our work is 62 $\mu\Omega$-cm. To determine the current fraction of $SrIrO_3$ in each Py/$SrIrO_3$ bilayer samples, we treated the Py and $SrIrO_3$ layers as parallel resistors. The $SrIrO_3$ resistivity and its current fraction are estimated by assuming that the Py resistivity is constant among different samples. C.6(b) shows the estimated $SrIrO_3$ resistivity and its current fraction as a function of $SrIrO_3$ thickness t_{SIO} in 3.5 nm Py/$SrIrO_3$/$SrTiO_3$ samples.

Appendix D: Theoretical supplement for chapter 5

D.1 Bulk spin Hall conductivity in $SrIrO_3$

Theory calculations were undertaken by Dr. Kyusung Hwang at the University of Toronto to calculate the bulk spin Hall conductivity of $SrIrO_3$.

D.1.1 Tight-binding model

For the spin Hall conductivity calculation shown in Figure 5.4, we employed a $j_{\text{eff}} = 1/2$ tight-binding model constructed for the orthorhombic perovskite bulk structure.[35,36] The model incorporates various spin-dependent hopping channels for Ir electrons generated by oxygen octahedron tilting in the bulk structure. The model Hamiltonian H consists of four doubly degenerate electron bands on account of the four Ir sites in each unit cell.

$$H = \sum_{\mathbf{k}} \psi^{\dagger}_{\mathbf{k}} H_{\mathbf{k}} \psi_{\mathbf{k}} \tag{D.1}$$

Here, $\psi = (\psi_{1\uparrow}, \psi_{2\uparrow}, \psi_{3\uparrow}, \psi_{4\uparrow}, \psi_{1\downarrow}, \psi_{2\downarrow}, \psi_{3\downarrow}, \psi_{4\downarrow})^T$ are electron operators with the subscripts meaing the sublattice (1,2,3,4) and $j_{\text{eff}} = 1/2$ pseudo-spin $(\uparrow, \downarrow)$. The explicit form of $H_{\mathbf{k}}$ can be found elsewhere[35,36]. The SHC tensor $\sigma^{\rho}_{\mu\nu}$ (where charge current applied along the μ direction generates a spin current along the ν direction with the spin polarization along ρ_s) is calculated by the Kubo formula[151,152]:

$$\sigma^{\rho}_{\mu\nu} = \sum_{\boldsymbol{k}} \Omega^{\rho}_{\mu\nu}(\boldsymbol{k}) \tag{D.2}$$

where

$$B^{\rho}_{\mu\nu}(\mathbf{k}) = \frac{2e\hbar}{V} \sum_{\epsilon_{n\mathbf{k}}<\epsilon_F<\epsilon_{m\mathbf{k}}} \mathrm{Im}\left[\frac{\langle m\mathbf{k}|\mathcal{J}^{\rho}_{\mu}|n\mathbf{k}\rangle\langle n\mathbf{k}|J_{\nu}|m\mathbf{k}\rangle}{(\epsilon_{m\mathbf{k}}-\epsilon_{n\mathbf{k}})^2}\right]. \tag{D.3}$$

Here, J_ν $(= \sum_{\mathbf{k}} \psi^{\dagger}_{\mathbf{k}} \frac{\partial H_{\mathbf{k}}}{\partial k_\nu} \psi_{\mathbf{k}})$ is charge current, and $\mathcal{J}^{\rho}_{\mu}$ $(= \frac{1}{4}\{\sigma^{\rho}, J_\mu\})$ is spin current with the $j_{\text{eff}} = 1/2$ spin represented by the Pauli matrix σ^{ρ}.

In the above expression, V is the volume of the system, ϵ_F means fermi level, and $|m\mathbf{k}\rangle$ represents a Bloch state of H with energy $\epsilon_{m\mathbf{k}}$. The momentum-resolved SHC represented by $\Omega^{\rho}_{\mu\nu}(\boldsymbol{k})$ enables us to trace the electron states responsible for the large spin Hall effect. The bulk SHC in Figure 5.4(a) corresponds to the tensor component σ^{a}_{cb} where a, b, c represent the orthorhombic axes, and the right inset of the figure shows $\sigma^{a}_{cb}(\boldsymbol{k})$ in the Brillouin zone for the case ϵ_F = 0. In the Brillouin zone, = (0,0,π), Y = (π,0,0), = (0,π,0), S = (π,π,0), R = (π,π,π), U = (0,π,π) in the coordinate of (k_a,k_b,k_c) [= (***k***· ***a***, ***k***· ***b***, ***k***· ***c***)] where ***a***, ***b***, and ***c*** are the orthorhombic lattice vectors.

The film SHC calculation in Figure 5.12 was performed for a slab with a finite thickness (8 unit cells or 16 Ir-layers) along the $[110]_{\text{o}}$ direction. Assuming the bulk Hamiltonian H in the slab geometry, we computed the SHC tensor component $-\sigma^{x}_{zy}$ which corresponds to the experimental configuration. Instead of the orthorhombic axes {***a***,***b***,***c***}, here we have used the pseudo-cubic axes {***x***,***y***,***z***} where the ***x*** and ***y*** axes correspond to the $[1\bar{1}0]_{\text{o}}$ and $[110]_{\text{o}}$ directions, respectively [***x*** = (***a***-***b***)/$\sqrt{2}$, ***y*** = (***a***+***b***)/$\sqrt{2}$, ***z*** = ***c***/2][35,36]. In this slab calculation, the Hamiltonian (H) and current operators (J_ν,J^{ρ}_{μ}) are expressed in real space for the $[110]_{\text{o}}$ direction due to the lack of translation symmetry in that direction.

D.1.2 Origin of the large $SrIrO_3$ bulk SHC and its directional dependence

The large bulk spin Hall conductivity (σ^{a}_{cb}) presented in Figure 5.4 has major contribution from the nearly degenerate energy bands at the XURS plane of the Brillouin zone. This can be seen clearly by resolving the SHC in momentum space as shown in Fig D.1. By comparing the momentum

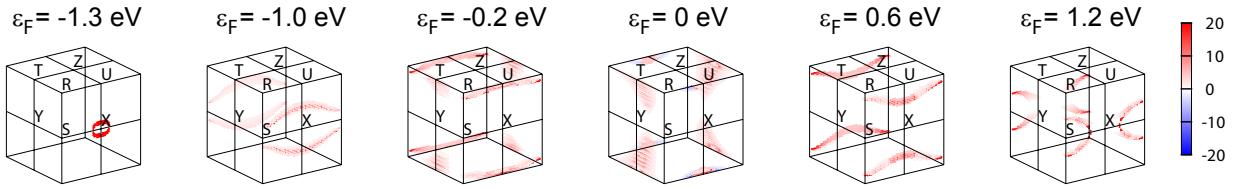


Figure D.1: Momentum-resolved spin Hall conductivity $\Omega^a_{cb}(\mathbf{k})$ of the bulk system. As Fermi level arises, the distribution of $\Omega^a_{cb}(\mathbf{k})$ changes in accordance with the shape of fermi surface on the XURS plane of the Brillouin zone.

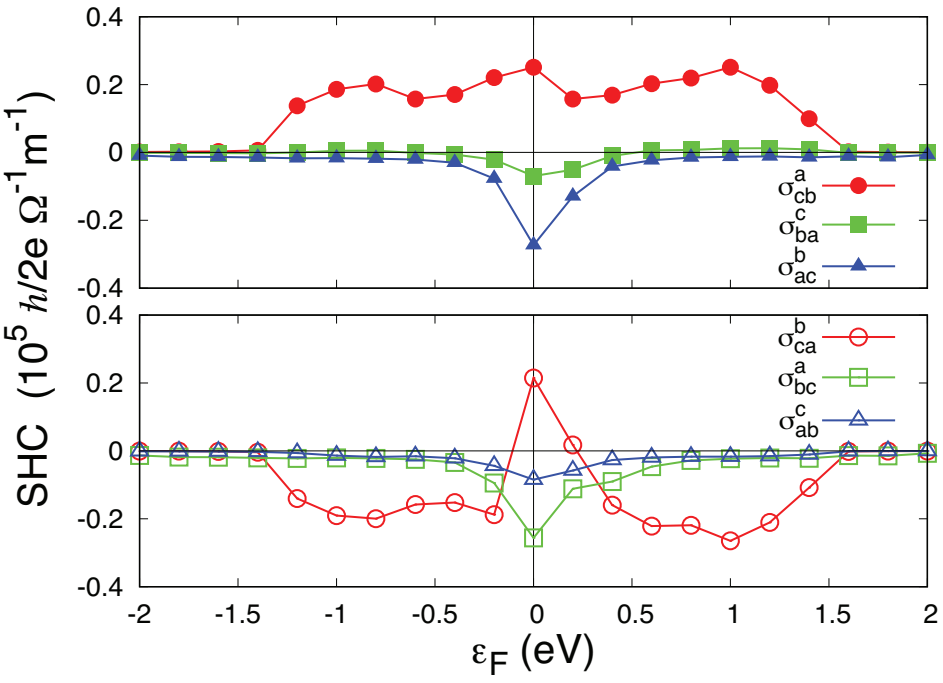


Figure D.2: Directional dependence of the bulk spin Hall conductivity $\sigma^{\rho}_{\mu\nu}$. Depending on the configuration represented by ρ (spin polarization axis), μ (spin current direction), ν (charge current direction), the system shows a different pattern of spin Hall response.

Table D.1: Non-symmorphic symmetries in bulk $SrIrO_3$. (*) denotes symmetries broken in the $[110]_o$ film slab.

Symmetry Axis	Coordinate Transformation
b-glide*	$\left(-l+\frac{1}{2}, m+\frac{1}{2}, n\right)$
n-glide*	$\left(l+\frac{1}{2}, -m+\frac{1}{2}, n+\frac{1}{2}\right)$
Mirror	$\left(l, m, -n+\frac{1}{2}\right)$
Inversion	$(-l, -m, -n)$
a-screw*	$\left(l+\frac{1}{2}, -m+\frac{1}{2}, -n\right)$
b-screw*	$\left(-l+\frac{1}{2}, -m+\frac{1}{2}, -n+\frac{1}{2}\right)$
c-screw	$\left(-l, -m, -n+\frac{1}{2}\right)$

resolved SHC $[\Omega^a_{cb}(\mathbf{k})]$ with the band structure in Figure 5.4(b), one can see that high intensity peaks of $\Omega^a_{cb}(\mathbf{k})$ occur around the k points where Fermi level crosses the nearly degenerate bands (i.e., the Fermi surface cross section cut by the XURS plane). When the Fermi energy is close to zero, the bulk SHC has additional contributions from interior regions of the Brillouin zone (see the case ϵ_F = 0 in Figure D.1).

D.1.3 Lattice symmetry in the $[110]_o$ slab geometry

The bulk and film $SrIrO_3$ systems exhibit a quite different pattern of spin Hall effect as shown in Figure 5.12. Since the spin Hall conductivity is determined by the electron wave functions of the occupied energy levels, lattice symmetry is an important factor influencing the spin Hall effect. The orthorhombic perovskite bulk $SrIrO_3$ possesses the *pbnm* (No. 62) space group symmetry. As shown in Table D.1, the space group is generated by various different nonsymmorphic symmetries

(glide and screw-axis) as well as inversion and mirror symmetries. In the $[110]_o$ slab geometry representing our film $SrIrO_3$, most of the nonsymmorphic symmetries are broken due to the lack of translation symmetry along the *a* and *b* axes. For example, the n-glide is the combination of the translation by (*a*+*c*)/2 and reflection about a plane perpendicular to the *b* axis. Under the n-glide, the $[110]_o$ slab transforms to a $[1\text{-}10]_o$ slab. Broken bulk lattice symmetries in the $[110]_o$ slab are marked by (*) in Table D.1. Figure D.3 shows the n-glide plane and translation vector $\frac{a+c}{2}$ for a $[110]_o$ slab.

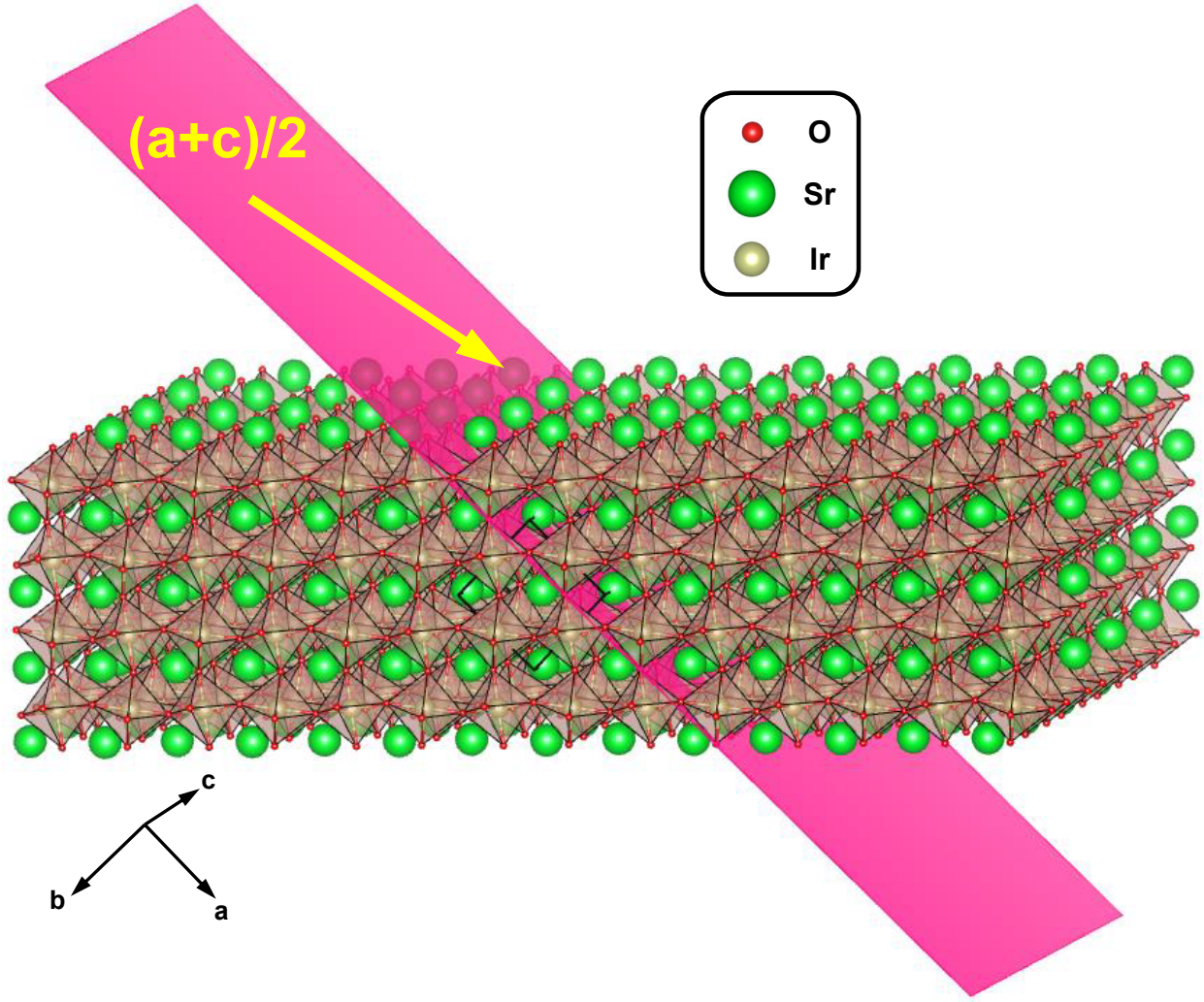


Figure D.3: n-glide and a $[110]_o$ slab of $SrIrO_3$. The yellow arrow and pink plane represent the translation vector $\frac{a+c}{2}$ and reflection plane (perpendicular to the b axis) composing the n-glide.

Bibliography

[1] Editorial. The interface is still the device. *Nature Materials*, 11(2):91–91, 2012.

[2] Koichi Momma and Fujio Izumi. VESTA 3 for three-dimensional visualization of crystal, volumetric and morphology data. *Journal of Applied Crystallography*, 44(6):1272–1276, 2011.

[3] D.G. Schlom, L.Q. Chen, X.Q. Pan, A. Schmehl, and M.A. Zurbuchen. A thin film approach to engineering functionality into oxides. *Journal of the American Ceramic Society*, 91(8):2429–2454, 2008.

[4] H. Y. Hwang, Y. Iwasa, M. Kawasaki, B. Keimer, N. Nagaosa, and Y. Tokura. Emergent phenomena at oxide interfaces. *Nature Materials*, 11(2):103–113, 2012.

[5] Jak Chakhalian, John W. Freeland, Andrew J. Millis, Christos Panagopoulos, and James M. Rondinelli. Colloquium : Emergent properties in plane view: Strong correlations at oxide interfaces. *Reviews of Modern Physics*, 86(4):1189–1202, 2014.

[6] M Imada, A Fujimori, and Y Tokura. Metal-insulator transitions. *Reviews of Modern Physics*, 70(4):1039–1263, 1998.

[7] V. M. Goldschmidt. Die Gesetze der Krystallochemie. *Die Naturwissenschaften*, 14(21):477, 1926.

[8] H. D. Megaw. Crystal Structure of Barium Titanate. *Nature*, 155(3938):484–485, 1945.

[9] G.H. Jonker and J.H. Van Santen. Ferromagnetic compounds of manganese with perovskite structure. *Physica*, 16(3):337–349, 1950.

[10] C. W. Searle and S. T. Wang. Studies of the ionic ferromagnet (LaPb)MnO3 III. Ferromagnetic resonance studies. *Canadian Journal of Physics*, 47(23):2703–2708, 1969.

[11] J. G. Bednorz and K. A. Müller. Possible High Tc Superconductivity in the Ba La Cu O System. *Zeitschrift fuer Physik B*, 193:267–271, 1986.

[12] A. Shilling, M. Contoni, J. D. Guo, and H. R. Ott. Superconductivity above 130 K in the Hg-Ba-Ca-Cu-O System. *Nature*, 363:56–58, 1993.

[13] A. Ohtomo and H. Y. Hwang. A high-mobility electron gas at the LaAlO3/SrTiO3 heterointerface. *Nature*, 427(6973):423–426, 2004.

[14] J. Wang, J. B. Neaton, H. Zheng, V. Nagarajan, S. B. Ogale, B. Liu, D. Viehland, V. Vaithyanathan, D. G. Schlom, U. V. Waghmare, N. A. Spaldin, K. M. Rabe, M. Wuttig, and R. Ramesh. Epitaxial BiFeO3 multiferroic thin film heterostructures. *Science*, 299(5613):1719–1722, 2003.

[15] H. J. Xiang. Origin of polar distortion in LiNbO3-type "ferroelectric" metals: Role of A-site instability and short-range interactions. *Physical Review B*, 90(9):094108, 2014.

[16] Danilo Puggioni and James M. Rondinelli. Designing a robustly metallic noncenstrosymmetric ruthenate oxide with large thermopower anisotropy. *Nature Communications*, 5:3432, 2014.

[17] T. H. Kim, D. Puggioni, Y. Yuan, L. Xie, H. Zhou, N. Campbell, P. J. Ryan, Y. Choi, J.-W. Kim, J. R. Patzner, S. Ryu, J. P. Podkaminer, J. Irwin, Y. Ma, C. J. Fennie, M. S. Rzchowski, X. Q. Pan, V. Gopalan, J. M. Rondinelli, and C. B. Eom. Polar metals by geometric design. *Nature*, 533(7601):68–72, 2016.

[18] A. M. Glazer. The classification of tilted octahedra in perovskites. *Acta Crystallographica Section B Structural Crystallography and Crystal Chemistry*, 28(11):3384–3392, 1972.

[19] James M. Rondinelli and Nicola A. Spaldin. Structure and Properties of Functional Oxide Thin Films: Insights From Electronic-Structure Calculations. *Advanced Materials*, 23(30):3363–3381, 2011.

[20] A. Vailionis, H. Boschker, W. Siemons, E. P. Houwman, D. H . A. Blank, G. Rijnders, and G. Koster. Misfit strain accommodation in epitaxial ABO3 perovskites: Lattice rotations and lattice modulations. *Physical Review B*, 83(6):064101, 2011.

[21] Bum Ki Moon and Hiroshi Ishiwara. Roles of Buffer Layers in Epitaxial Growth of SrTiO3 Films on Silicon Substrates. *Japanese Journal of Applied Physics*, 33(3A):1472–1477, 1994.

[22] S. H. Baek, J. Park, D. M. Kim, V. A. Aksyuk, R. R. Das, S. D. Bu, D. A. Felker, J. Lettieri, V. Vaithyanathan, S. S. N. Bharadwaja, N. Bassiri-Gharb, Y. B. Chen, H. P. Sun, C. M. Folkman, H. W. Jang, D. J. Kreft, S. K. Streiffer, R. Ramesh, X. Q. Pan, S. Trolier-McKinstry, D. G. Schlom, M. S. Rzchowski, R. H. Blick, and C. B. Eom. Giant Piezoelectricity on Si for Hyperactive MEMS. *Science*, 334(6058):958–961, 2011.

[23] Y. Tokura and N. Nagaosa. Orbital Physics in Transition-Metal Oxides. *Science*, 288(5465):462–468, 2000.

[24] A Manchon, H C Koo, J Nitta, S M Frolov, and R A Duine. New perspectives for Rashba spin-orbit coupling. *Nat Mater*, 14(9):871–882, 2015.

[25] Anjan Soumyanarayanan, Nicolas Reyren, Albert Fert, and Christos Panagopoulos. Emergent phenomena induced by spin-orbit coupling at surfaces and interfaces. *Nature*, 539(7630):509–517, 2016.

[26] Igor Zutic, Jaroslav Fabian, and S. Das Sarma. Spintronics: Fundamentals and applications. *Reviews of Modern Physics*, 76(2):323–410, 2004.

[27] William Witczak-Krempa, Gang Chen, Yong Baek Kim, and Leon Balents. Correlated

Quantum Phenomena in the Strong Spin-Orbit Regime. *Annual Review of Condensed Matter Physics*, 5(1):57–82, 2014.

[28] S J Moon, H Jin, K W Kim, W S Choi, Y S Lee, J Yu, G Cao, A Sumi, H Funakubo, C Bernhard, and T W Noh. Dimensionality-Controlled Insulator-Metal Transition and Correlated Metallic State in 5d Transition Metal Oxides Sr(n+1)Ir(n)O(3n+1) (n=1, 2, and infinity). *Physical Review Letters*, 101(22):226402, nov 2008.

[29] B J Kim, H Ohsumi, T Komesu, S Sakai, T Morita, H Takagi, and T Arima. Phase-sensitive observation of a spin-orbital Mott state in Sr2IrO4. *Science (New York, N.Y.)*, 323(5919):1329–1332, 2009.

[30] Fa Wang and T Senthil. Twisted Hubbard Model for Sr2IrO4: Magnetism and Possible High Temperature Superconductivity. *Physical Review Letters*, 106(13):136402, 2011.

[31] Fa Wang and Ying Ran. Nearly flat band with Chern number C = 2 on the dice lattice. *Physical Review B*, 84(24):241103, 2011.

[32] Jason K. Kawasaki, Masaki Uchida, Hanjong Paik, Darrell G. Schlom, and Kyle M. Shen. Evolution of electronic correlations across the rutile, perovskite, and Ruddelsden-Popper iridates with octahedral connectivity. *Physical Review B*, 94(12):121104, 2016.

[33] A. Yamasaki, H. Fujiwara, S. Tachibana, D. Iwasaki, Y. Higashino, C. Yoshimi, K. Nakagawa, Y. Nakatani, K. Yamagami, H. Aratani, O. Kirilmaz, M. Sing, R. Claessen, H. Watanabe, T. Shirakawa, S. Yunoki, A. Naitoh, K. Takase, J. Matsuno, H. Takagi, A. Sekiyama, and Y. Saitoh. Three-dimensional electronic structures and the metal-insulator transition in Ruddlesden-Popper iridates. *Physical Review B*, 94(11):115103, 2016.

[34] Di Xiao, Wenguang Zhu, Ying Ran, Naoto Nagaosa, and Satoshi Okamoto. Interface engineering of quantum Hall effects in digital transition metal oxide heterostructures. *Nature Communications*, 2:596, 2011.

[35] Jean-Michel Carter, Vijay V. Shankar, M. Ahsan Zeb, and Hae-Young Kee. Semimetal and Topological Insulator in Perovskite Iridates. *Physical Review B*, 85(11):115105, 2012.

[36] Yige Chen, Yuan-Ming Lu, and Hae-Young Kee. Topological crystalline metal in orthorhombic perovskite iridates. *Nature Communications*, 6:6593, 2015.

[37] Linsey C. Seitz, Colin F. Dickens, Kazunori Nishio, Yasuyuki Hikita, Joseph Montoya, Andrew Doyle, Charlotte Kirk, Aleksandra Vojvodic, Harold Y. Hwang, Jens K. Norskov, and Thomas F. Jaramillo. A highly active and stable IrOx/SrIrO3 catalyst for the oxygen evolution reaction. *Science*, 353(6303):1011–1014, 2016.

[38] I Pallecchi, M T Buscaglia, V Buscaglia, E Gilioli, G Lamura, F Telesio, M R Cimberle, and D Marré. Thermoelectric behavior of RuddlesdenPopper series iridates. *Journal of Physics: Condensed Matter*, 28(6):065601, 2016.

[39] J.M. Longo, J.A. Kafalas, and R.J. Arnott. Structure and properties of the high and low pressure forms of SrIrO3. *Journal of Solid State Chemistry*, 3(2):174–179, 1971.

[40] Yong Kwan Kim, Akihiro Sumi, Kenji Takahashi, Shintaro Yokoyama, Shinichi Ito, Takayuki Watanabe, Kensuke Akiyama, Satoru Kaneko, Keisuke Saito, and Hiroshi Funakubo. Metalorganic Chemical Vapor Deposition of Epitaxial Perovskite SrIrO3 Films on (100)SrTiO3 Substrates. *Japanese Journal of Applied Physics*, 45(1):L36–L38, 2006.

[41] Jian Liu, J. H. Chu, C Rayan Serrao, D. Yi, J Koralek, C. Nelson, C. Frontera, D. Kriegner, L. Horák, E Arenholz, J Orenstein, A Vishwanath, X. Marti, and R Ramesh. Tuning the electronic properties of J eff=1/2 correlated semimetal in epitaxial perovskite SrIrO3. *arXiv:1305.1732 [cond-Mat]*, 2013.

[42] Y. F. Nie, P. D. C. King, C. H. Kim, M. Uchida, H. I. Wei, B. D. Faeth, J. P. Ruf, J. P. C. Ruff, L. Xie, X. Pan, C. J. Fennie, D. G. Schlom, and K. M. Shen. Interplay of Spin-Orbit Interactions, Dimensionality, and Octahedral Rotations in Semimetallic SrIrO3. *Physical Review Letters*, 114(1):016401, 2015.

[43] Z Z Li, O Schneegans, and L Fruchter. Synthesis of Perovskite SrIrO3 Thin Films by Sputtering Technique. *arXiv:1610.03722v1 [condmat]*, 2016.

[44] J. Matsuno, K. Ihara, S. Yamamura, H. Wadati, K. Ishii, V.V. Shankar, Hae-Young Kee, and H. Takagi. Engineering a Spin-Orbital Magnetic Insulator by Tailoring Superlattices. *Physical Review Letters*, 114(24):247209, 2015.

[45] J. G. Zhao, L. X. Yang, Y. Yu, F. Y. Li, R. C. Yu, Z. Fang, L. C. Chen, and C. Q. Jin. High-pressure synthesis of orthorhombic SrIrO3 perovskite and its positive magnetoresistance. *Journal of Applied Physics*, 103(10):103706, 2008.

[46] Peter E.R. Blanchard, Emily Reynolds, Brendan J. Kennedy, Justin A. Kimpton, Maxim Avdeev, and Alexei A. Belik. Anomalous thermal expansion in orthorhombic perovskite SrIrO3: Interplay between spin-orbit coupling and the crystal lattice. *Physical Review B*, 89(21):214106, 2014.

[47] J. Fujioka, T. Okawa, A. Yamamoto, and Y. Tokura. Correlated Dirac semimetallic state with unusual positive magnetoresistance in strain-free perovskite SrIrO3. *Physical Review B*, 95(12):121102(R), 2017.

[48] Fei-Xiang Wu, Jian Zhou, L. Y. Zhang, Yan-feng B. Chen, Shan-tao Zhang, Zheng-Bin Gu, Shu-Hua Yao, and Yan-feng B. Chen. Metal-insulator transition in SrIrO3 with strong spin-orbit interaction. *Journal of physics. Condensed matter : an Institute of Physics journal*, 25(12):125604, 2013.

[49] Abhijit Biswas, Ki-Seok Kim, and Yoon Hee Jeong. Metal insulator transitions in perovskite SrIrO3 thin films. *Journal of Applied Physics*, 116(21):213704, 2014.

[50] John H Gruenewald, John Nichols, Jasminka Terzic, Gang Cao, Joseph W. Brill, and Sung S.Ambrose Seo. Compressive strain-induced metalinsulator transition in orthorhombic SrIrO3 thin films. *Journal of Materials Research*, 29(21):2491–2496, 2014.

[51] Lunyong Zhang, Qifeng Liang, Ye Xiong, Binbin Zhang, Lei Gao, Handong Li, Yan B. Chen, Jian Zhou, Shan-Tao Zhang, Zheng-Bin Gu, Shu-hua Yao, Zhiming Wang, Yuan Lin, and Yan-Feng Chen. Tunable semimetallic state in compressive-strained SrIrO3 films revealed by transport behavior. *Physical Review B*, 91(3):035110, 2015.

[52] Z. T. Liu, M. Y. Li, Q. F. Li, J. S. Liu, W. Li, H. F. Yang, Q. Yao, C. C. Fan, X. G. Wan, Z. Wang, and D. W. Shen. Direct observation of the Dirac nodes lifting in semimetallic perovskite SrIrO3 thin films. *Scientific Reports*, 6:30309, 2016.

[53] Jian Liu, D. Kriegner, L. Horak, D. Puggioni, C. Rayan Serrao, R. Chen, D. Yi, C. Frontera, V. Holy, a. Vishwanath, J. M. Rondinelli, X. Marti, and R. Ramesh. Strain-induced nonsymmorphic symmetry breaking and removal of Dirac semimetallic nodal line in an orthoperovskite iridate. *Physical Review B*, 93(8):085118, 2016.

[54] M. Ahsan Zeb and Hae-Young Kee. Interplay between spin-orbit coupling and Hubbard interaction in SrIrO3 and related Pbnm perovskite oxides. *Physical Review B*, 86(8):085149, 2012.

[55] Jean-Michel Carter, Vijay Shankar V., and Hae-Young Kee. Theory of metal-insulator transition in the family of perovskite iridium oxides. *Physical Review B*, 88(3):035111, 2013.

[56] Satoshi Okamoto, Wenguang Zhu, Yusuke Nomura, Ryotaro Arita, Di Xiao, and Naoto Nagaosa. Correlation effects in (111) bilayers of perovskite transition-metal oxides. *Physical Review B*, 89(19):195121, 2014.

[57] So Yeun Kim, Choong H. Kim, L. J. Sandilands, C. H. Sohn, J. Matsuno, H. Takagi, K. W. Kim, Y. S. Lee, S. J. Moon, and T. W. Noh. Manipulation of electronic structure via alteration of local orbital environment in [(SrIrO3)m,(SrTiO3)](m = 1,2, and infinity) superlattices. *Physical Review B*, 94(24):245113, 2016.

[58] Di Yi, Jian Liu, Shang-Lin Hsu, Lipeng Zhang, Yongseong Choi, Jong-Woo Kim, Zuhuang Chen, James D. Clarkson, Claudy R. Serrao, Elke Arenholz, Philip J. Ryan, Haixuan

Xu, Robert J. Birgeneau, and Ramamoorthy Ramesh. Atomic-scale control of magnetic anisotropy via novel spinorbit coupling effect in La2/3Sr1/3MnO3/SrIrO3 superlattices. *Proceedings of the National Academy of Sciences*, 113(23):6397–6402, 2016.

[59] John Nichols, Xiang Gao, Shinbuhm Lee, Tricia L. Meyer, John W. Freeland, Valeria Lauter, Di Yi, Jian Liu, Daniel Haskel, Jonathan R. Petrie, Er-Jia Guo, Andreas Herklotz, Dongkyu Lee, Thomas Z. Ward, Gyula Eres, Michael R. Fitzsimmons, and Ho Nyung Lee. Emerging magnetism and anomalous Hall effect in iridatemanganite heterostructures. *Nature Communications*, 7:12721, 2016.

[60] Satoshi Okamoto, John Nichols, Changhee Sohn, So Yeun Kim, Tae Won Noh, and Ho Nyung Lee. Charge Transfer in Iridate-Manganite Superlattices. *Nano Letters*, 17(4):2126–2130, 2017.

[61] Jobu Matsuno, Naoki Ogawa, Kenji Yasuda, Fumitaka Kagawa, Wataru Koshibae, Naoto Nagaosa, Y. Tokura, and M. Kawasaki. Interface-driven topological Hall effect in SrRuO3-SrIrO3 bilayer. *Science Advances*, 2(7):e1600304, 2016.

[62] H.G. Liddel and R. Scott. *A Greek-English Lexicon*. Oxford University Press, 9th edition, 1940.

[63] Milton Ohring. *The Materials Science of Thin Films*. Academic Press, 1992.

[64] Gertjan Koster and Guus Rijnders, editors. *In situ characterization of thin film growth*. Woodhead Publishing Limited, 2011.

[65] J. Choi, C. B. Eom, G. Rijnders, H. Rogalla, and D. H. A. Blank. Growth mode transition from layer by layer to step flow during the growth of heteroepitaxial SrRuO3 on (001) SrTiO3. *Applied Physics Letters*, 79(10):1447–1449, 2001.

[66] R. Bachelet, F. Sanchez, J. Santiso, C. Munuera, C. Ocal, and J. Fontcuberta. Self-Assembly of SrTiO3 (001) Chemical-Terminations: A Route for Oxide-Nanostructure Fabrication by Selective Growth. *Chemistry of Materials*, 21(12):2494–2498, 2009.

[67] R. Bachelet, C. Ocal, L. Garzón, J. Fontcuberta, and F. Sánchez. Conducted growth of SrRuO3 nanodot arrays on self-ordered La0.18Sr0.82Al0.59Ta0.41O3 (001) surfaces. *Applied Physics Letters*, 99(5):051914, 2011.

[68] M Kawasaki, K Takahashi, T Maeda, R Tsuchiya, M Shinohara, I Osamu, T Yonezawa, M Yoshimoto, and H Koinuma. Atomic Control of the SrTiO3 Crystal Surface. 266(5190):1540–1542, 1994.

[69] M. Kawasaki, A. Ohtomo, T. Arakane, K. Takahashi, M. Yoshimoto, and H. Koinuma. Atomic control of SrTiO3 surface for perfect epitaxy of perovskite oxides. *Applied Surface Science*, 107:102–106, 1996.

[70] Gertjan Koster, Boike L. Kropman, Guus J H M Rijnders, Dave H A Blank, and Horst Rogalla. Quasi-ideal strontium titanate crystal surfaces through formation of strontium hydroxide. *Applied Physics Letters*, 73(20):2920–2922, 1998.

[71] Tsuyoshi Ohnishi, Kazuhiro Takahashi, Masashi Nakamura, Masashi Kawasaki, Mamoru Yoshimoto, and Hideomi Koinuma. A-site layer terminated perovskite substrate: NdGaO3. *Applied Physics Letters*, 74(17):2531–2533, 1999.

[72] Jaewan Chang, Yoon-Seok Park, and Sang-Koog Kim. Atomically flat single-terminated SrTiO3 (111) surface. *Applied Physics Letters*, 92(15):152910, 2008.

[73] Joseph H. Ngai, Todd C. Schwendemann, Anna E. Walker, Yaron Segal, Fred J. Walker, Eric I. Altman, and Charles H. Ahn. Achieving A-Site Termination on La0.18Sr0.82Al0.59Ta0.41O3 Substrates. *Advanced Materials*, 22(26-27):2945–2948, 2010.

[74] Josée E. Kleibeuker, Gertjan Koster, Wolter Siemons, David Dubbink, Bouwe Kuiper, Jeroen L. Blok, Chan Ho Yang, Jayakanth Ravichandran, Ramamoorthy Ramesh, Johan E. Ten Elshof, Dave H. A. Blank, and Guus Rijnders. Atomically defined rare-earth scandate crystal surfaces. *Advanced Functional Materials*, 20(20):3490–3496, 2010.

[75] H M Christen and G Eres. Recent advances in pulsed-laser deposition of complex oxides. *Journal of Physics: Condensed Matter*, 20(26):264005, 2008.

[76] E. Langenberg, E. Ferreiro-Vila, V. Leboran, A. O. Fumega, V. Pardo, and F. Rivadulla. Analysis of the temperature dependence of the thermal conductivity of insulating single crystal oxides. *APL Materials*, 4(10):104815, 2016.

[77] S Nishikawa and S Kikuchi. The Diffraction of Cathode Rays by Calcite. *Proceedings of the Imperial Academy*, (4):475–477, 1928.

[78] W. Braun. *Applied RHEED: Reflection High Energy Electron Diffraction During Crystal Growth*. Springer-Verlag, 1999.

[79] Guus J. H. M. Rijnders, Gertjan Koster, Dave H. A. Blank, and Horst Rogalla. In situ monitoring during pulsed laser deposition of complex oxides using reflection high energy electron diffraction under high oxygen pressure. *Applied Physics Letters*, 70(14):1888–1890, 1997.

[80] M. C. Sullivan, M. J. Ward, Araceli Gutierrez-Llorente, Eli R. Adler, H. Joress, A. Woll, and J. D. Brock. Complex oxide growth using simultaneous in situ reflection high-energy electron diffraction and x-ray reflectivity: When is one layer complete? *Applied Physics Letters*, 106(3):031604, 2015.

[81] Olivier Guillon, Jesus Gonzalez-Julian, Benjamin Dargatz, Tobias Kessel, Gabi Schierning, Jan Raethel, and Mathias Herrmann. Field-assisted sintering technology/spark plasma sintering: Mechanisms, materials, and technology developments. *Advanced Engineering Materials*, 16(7):830–849, 2014.

[82] Yongshang Tian, Yansheng Gong, Zhaoying Li, Feng Jiang, and Hongyun Jin. Synthetic process and spark plasma sintering of SrIrO3 composite oxide. *Journal of Advanced Ceramics*, 2(4):347–352, 2013.

[83] Seung Yup Jang, Soon Jae Moon, Byung Chul Jeon, and Jin-Seok Chung. PLD Growth Behavior of Epitaxially Stabilized 5d Perovskite SrIrO3 Thin Films. *Journal of the Korean Physical Society*, 56(6):1814, 2010.

[84] D. J. Groenendijk, N. Manca, G. Mattoni, L. Kootstra, S. Gariglio, Y. Huang, E. van Heumen, and a. D. Caviglia. Epitaxial growth and thermodynamic stability of SrIrO3 /SrTiO3 heterostructures. *Applied Physics Letters*, 109(4):041906, 2016.

[85] Daisuke Kan and Yuichi Shimakawa. films with laser fluence Controlled cation stoichiometry in pulsed laser deposition-grown BaTiO3 epitaxial thin films with laser fluence. *Applied Physics Letters*, 081907(8):2011–2014, 2011.

[86] E. Breckenfeld, N. Bronn, J. Karthik, A. R. Damodaran, S. Lee, N. Mason, and L. W. Martin. Effect of Growth Induced (Non)Stoichiometry on Interfacial Conductance in LaAlO3/SrTiO3. *Physical Review Letters*, 110(19):196804, 2013.

[87] C. Xu, S. Wicklein, a. Sambri, S. Amoruso, M. Moors, and R. Dittmann. Impact of the interplay between nonstoichiometry and kinetic energy of the plume species on the growth mode of SrTiO3 thin films. *Journal of Physics D: Applied Physics*, 47(3):034009, 2014.

[88] Shishir Pandya, Anoop R. Damodaran, Ruijuan Xu, Shang-Lin Hsu, Joshua C. Agar, and Lane W. Martin. Strain-induced growth instability and nanoscale surface patterning in perovskite thin films. *Scientific Reports*, 6(1):26075, 2016.

[89] B.E. Warren. *X-Ray Diffraction*. Addison-Wesley, 1969.

[90] Jens Als-Nielsen and Des McMorrow. *Elements of Modern X-ray Physics*. John Wiley & Sons, Ltd, 2nd edition, 2011.

[91] Lukas Horak, Dominik Kriegner, Jian Liu, Carlos Frontera, Xavier Marti, and Vaclav Holy. Structure of epitaxial SrIrO3 perovskite studied by interference between X-ray waves diffracted by the substrate and the thin film. *Journal of Applied Crystallography*, 50(2):385–398, 2017.

[92] A. M. Glazer. Simple ways of determining perovskite structures. *Acta Crystallographica Section A*, 31(6):756–762, 1975.

[93] Lunyong Zhang, Hong-Yan Wu, Jian Zhou, Fei-Xiang Wu, Y.B. Chen, Shu-Hua Yao, Shan-Tao Zhang, and Yan-Feng Chen. TEM study of SrIrO3 thin films with various thicknesses grown on (001) SrTiO3 substrates synthesized by pulsed laser deposition. *Applied Surface Science*, 280:282–286, 2013.

[94] Q. Gan, R. A. Rao, and C. B. Eom. Control of the growth and domain structure of epitaxial SrRuO3 thin films by vicinal (001) SrTiO3 substrates. *Applied Physics Letters*, 70(15):1962–1964, 1997.

[95] J. C. Jiang, W. Tian, X. Q. Pan, Q. Gan, and C. B. Eom. Domain structure of epitaxial SrRuO3 thin films on miscut (001) SrTiO3 substrates. *Applied Physics Letters*, 72(23):2963–2965, 1998.

[96] C. M. Folkman, R. R. Das, C. B. Eom, Y. B. Chen, and X. Q. Pan. Single domain strain relaxed PrScO3 template on miscut substrates. *Applied Physics Letters*, 89(22):219–221, 2006.

[97] Y. B. Chen, M. B. Katz, X. Q. Pan, R. R. Das, D. M. Kim, S. H. Baek, and C. B. Eom. Ferroelectric domain structures of epitaxial (001) BiFeO3 thin films. *Applied Physics Letters*, 90(7):072907, 2007.

[98] L. Vasylechko, L. Akselrud, W. Morgenroth, U. Bismayer, A. Matkovskii, and D. Savytskii. Crystal structure of NdGaO3 at 100 K and 293 K based on synchrotron data. *Journal of Alloys and Compounds*, 297(1-2):46–52, 2000.

[99] B. C. Chakoumakos, D. G. Schlom, M. Urbanik, and J. Luine. Thermal expansion of LaAlO3 and (La,Sr)(Al,Ta)O3, substrate materials for superconducting thin-film device applications. *Journal of Applied Physics*, 83(4):1979–1982, 1998.

[100] Farrel W. Lytle. X-ray diffractometry of low-temperature phase transformations in strontium titanate. *Journal of Applied Physics*, 35(7):2212–2215, 1964.

[101] J. Schubert, O. Trithaveesak, A. Petraru, C. L. Jia, R. Uecker, P. Reiche, and D. G. Schlom. Structural and optical properties of epitaxial BaTiO3 thin films grown on GdScO3(110). *Applied Physics Letters*, 82(20):3460–3462, 2003.

[102] B. J. Kim, Hosub Jin, S J Moon, J.-Y. Kim, B.-G. Park, C. S. Leem, Jaejun Yu, T. W. Noh, C Kim, S.-J. Oh, J.-H. Park, V. Durairaj, G. Cao, and E. Rotenberg. Novel J eff = 1/2 Mott State Induced by Relativistic Spin-Orbit Coupling in Sr2IrO4. *Physical Review Letters*, 101(7):076402, 2008.

[103] Dmytro Pesin and Leon Balents. Mott physics and band topology in materials with strong spinorbit interaction. *Nature Physics*, 6(5):376–381, 2010.

[104] A. Sumi, Y.K. Kim, N. Oshima, K. Akiyama, K. Saito, and H. Funakubo. MOCVD growth of epitaxial SrIrO3 films on (111)SrTiO3 substrates. *Thin Solid Films*, 486(1-2):182–185, 2005.

[105] Daigorou Hirai, Jobu Matsuno, and Hidenori Takagi. Fabrication of (111)-oriented Ca0.5Sr0.5IrO3/SrTiO3 superlatticesA designed playground for honeycomb physics. *APL Materials*, 3(4):041508, 2015.

[106] T. J. Anderson, S. Ryu, H. Zhou, L. Xie, J. P. Podkaminer, Y. Ma, J. Irwin, X. Q. Pan, M. S. Rzchowski, and C. B. Eom. Metastable honeycomb SrTiO3/SrIrO3 heterostructures. *Applied Physics Letters*, 108(15):151604, 2016.

[107] Andreas Ruegg and Gregory A. Fiete. Topological insulators from complex orbital order in transition-metal oxides heterostructures. *Physical Review B*, 84(20):201103, 2011.

[108] Satoshi Okamoto. Doped Mott Insulators in (111) Bilayers of Perovskite Transition-Metal Oxides with a Strong Spin-Orbit Coupling. *Physical Review Letters*, 110(6):066403, 2013.

[109] David Doennig, Warren E. Pickett, and Rossitza Pentcheva. Massive symmetry breaking in LaAlO3/SrTiO3(111) quantum wells: A three-orbital strongly correlated generalization of graphene. *Physical Review Letters*, 111(12):126804, 2013.

[110] D. Rubi, A.H.G. Vlooswijk, and B. Noheda. Growth of flat SrRuO3 (111) thin films suitable as bottom electrodes in heterostructures. *Thin Solid Films*, 517(6):1904–1907, 2009.

[111] Jaewan Chang, Jong Woo Lee, and Sang Koog Kim. Layer-by-layer growth of SrFeO3-gamma thin films on atomically flat single-terminated SrRuO3/SrTiO3 (111) surfaces. *Journal of Crystal Growth*, 312(4):621–623, 2010.

[112] J. L. Blok, X. Wan, G. Koster, D. H A Blank, and G. Rijnders. Epitaxial oxide growth on polar (111) surfaces. *Applied Physics Letters*, 99(15):151917, 2011.

[113] G. Herranz, F. Sánchez, N. Dix, M. Scigaj, and J. Fontcuberta. High mobility conduction at (110) and (111) LaAlO3/SrTiO3 interfaces. *Scientific Reports*, 2(110):758, 2012.

[114] I. Hallsteinsen, J. E. Boschker, M. Nord, S. Lee, M. Rzchowski, P. E. Vullum, J. K. Grepstad, R. Holmestad, C. B. Eom, and T. Tybell. Surface stability of epitaxial La0.7Sr0.3MnO3 thin films on (111)-oriented SrTiO3. *Journal of Applied Physics*, 113(18):183512, 2013.

[115] Ingrid Hallsteinsen, Magnus Nord, Torsatein Bolstad, Per-erik Vullum, Jos Emiel Boschker, Paolo Longo, Ryota Takahashi, Randi Holmestad, Mikk Lippmaa, and Thomas Tybell. The effect of polar (111)-oriented SrTiO3 on initial perovskite growth. *Crystal Growth and Design*, 16(111):2357, 2016.

[116] Marta Gibert, Pavlo Zubko, Raoul Scherwitzl, Jorge Íñiguez, and Jean-Marc Triscone. Exchange bias in LaNiO3LaMnO3 superlattices. *Nature Materials*, 11(3):195–198, 2012.

[117] S. Middey, D. Meyers, M. Kareev, E. J. Moon, B. A. Gray, X. Liu, J. W. Freeland, and J. Chakhalian. Epitaxial growth of (111)-oriented LaAlO3/LaNiO3 ultra-thin superlattices. *Applied Physics Letters*, 101(26):261602, 2012.

[118] Yue Jia, Rajesh V. Chopdekar, Elke Arenholz, Zhiqi Liu, Michael D. Biegalski, Zachary D. Porter, Apurva Mehta, and Yayoi Takamura. Thickness dependence of exchange coupling in (111)-oriented perovskite oxide superlattices. *Physical Review B*, 93(10):104403, 2016.

[119] S. Middey, D. Meyers, D. Doennig, M. Kareev, X. Liu, Y. Cao, Zhenzhong Yang, Jinan Shi, Lin Gu, P. J. Ryan, R. Pentcheva, J. W. Freeland, and J. Chakhalian. Mott Electrons in an Artificial Graphenelike Crystal of Rare-Earth Nickelate. *Physical Review Letters*, 116(5):056801, 2016.

[120] S. Middey, P. Rivero, D. Meyers, M. Kareev, X. Liu, Y. Cao, J.W. Freeland, S. Barraza-Lopez, and J. Chakhalian. Polarity compensation in ultra-thin films of complex oxides: The case of a perovskite nickelate. *Scientific Reports*, 4(1):6819, 2015.

[121] Yizhak Yacoby, Mukhles Sowwan, Edward Stern, Julie O. Cross, Dale Brewe, Ron Pindak, John Pitney, Eric M. Dufresne, and Roy Clarke. Direct determination of epitaxial interface structure in Gd2O3 passivation of GaAs. *Nature Materials*, 1(2):99–101, 2002.

[122] R D Shannon. Revised Effective Ionic Radii and Systematic Studies of Interatomic Distances in Halides and Chaleogenides. *Acta Crystallographica*, A32:751, 1976.

[123] R. Herger, P. R. Willmott, O. Bunk, C. M. Schlepuetz, B. D. Patterson, B. Delley, V. L. Shneerson, P. F. Lyman, and D. K. Saldin. Surface structure of SrTiO3(001). *Physical Review B*, 76(19):195435, 2007.

[124] Ryota Shimizu, Katsuya Iwaya, Takeo Ohsawa, Susumu Shiraki, Tetsuya Hasegawa, Tomihiro Hashizume, and Taro Hitosugi. Atomic-Scale Visualization of Initial Growth of Homoepitaxial SrTiO3 Thin Film on an Atomically Ordered Substrate. *ACS Nano*, 5(10):7967–7971, 2011.

[125] L. D. Marks, A. N. Chiaramonti, S. U. Rahman, and M. R. Castell. Transition from Order to Configurational Disorder for Surface Reconstructions on SrTiO3(111). *Physical Review Letters*, 114(22):226101, 2015.

[126] Ke Zou, Subhasish Mandal, Stephen D. Albright, Rui Peng, Yujia Pu, Divine Kumah, Claudia Lau, Georg H. Simon, Omur E. Dagdeviren, Xi He, Ivan Božović, Udo D. Schwarz, Eric I. Altman, Donglai Feng, Fred J. Walker, Sohrab Ismail-Beigi, and Charles H. Ahn. Role of double TO2 layers at the interface of FeSe/SrTiO3 superconductors. *Physical Review B*, 93(18):180506(R), 2016.

[127] Mark Johnson and R. H. Silsbee. Interfacial charge-spin coupling: Injection and detection of spin magnetization in metals. *Physical Review Letters*, 55(17):1790–1793, 1985.

[128] M. N. Baibich, J. M. Broto, A. Fert, F. Nguyen Van Dau, F. Petroff, P. Etienne, G. Creuzet, A. Friederich, and J. Chazelas. Giant Magnetoresistance of (001)Fe/(001)Cr Magnetic Superlattices. *Physical Review Letters*, 61(21):2472–2475, 1988.

[129] G. Binasch, P. Gruenberg, F. Saurenbach, and W. Zinn. Enhanced magnetoresistance in layered magnetic structures with antiferromagnetic interlayer exchange. *Physical Review B*, 39(7):4828–4830, 1989.

[130] W.J. Gallagher and S.S.P. Parkin. Development of the magnetic tunnel junction MRAM at IBM : From first junctions to a 16-Mb MRAM demonstrator chip. *IBM Journal of Research and Development*, 50(1):5–24, 2006.

[131] J. Akerman. Toward a Universal Memory. *Science*, 308(5721):508–510, 2005.

[132] Arne Brataas, Andrew D. Kent, and Hideo Ohno. Current-induced torques in magnetic materials. *Nature Materials*, 11(5):372–381, 2012.

[133] D.C. Ralph and M.D. Stiles. Spin transfer torques. *Journal of Magnetism and Magnetic Materials*, 320(7):1190–1216, 2008.

[134] J.C. Slonczewski. Current-driven excitation of magnetic multilayers. *Journal of Magnetism and Magnetic Materials*, 159(1-2):L1–L7, 1996.

[135] M.I. Dyakonov and V. I. Perel. Possibility of orienting electron spins with current. *Sov. Phys. JETP Lett.*, 13(11):467, 1971.

[136] A.A. Bakun, P. Zakharchenya, A.A. Rogachev, M.N. Tkachuk, and V.G. Fleisher. Observation of a surface photocurrent caused by optical orientation of electrons in a semiconductor, 1984.

[137] J. E. Hirsch. Spin Hall Effect. *Physical Review Letters*, 83(9):1834–1837, 1999.

[138] Shuichi Murakami, Naoto Nagaosa, and Shou-Cheng Zhang. Dissipationless Quantum Spin Current at Room Temperature. *Science*, 301(5638):1348–1351, 2003.

[139] Jairo Sinova, Dimitrie Culcer, Q. Niu, N. A. Sinitsyn, T. Jungwirth, and A. H. MacDonald. Universal intrinsic spin Hall effect. *Physical Review Letters*, 92(12):126603–1, 2004.

[140] Y. K. Kato, R.C. Myers, A.C. Gossard, and D.D. Awschalom. Observation of the Spin Hall Effect in Semiconductors. *Science*, 306(5703):1910–1913, 2004.

[141] Sergio O. Valenzuela and M. Tinkham. Direct electronic measurement of the spin Hall effect. *Nature*, 442(7099):176–179, 2006.

[142] T. Kimura, Y. Otani, T. Sato, S. Takahashi, and S. Maekawa. Room-temperature reversible spin hall effect. *Physical Review Letters*, 98(15):156601, 2007.

[143] K. Ando, S. Takahashi, K. Harii, K. Sasage, J. Ieda, S. Maekawa, and E. Saitoh. Electric Manipulation of Spin Relaxation Using the Spin Hall Effect. *Physical Review Letters*, 101(3):036601, 2008.

[144] Ioan Mihai Miron, Kevin Garello, Gilles Gaudin, Pierre-Jean Zermatten, Marius V. Costache, Stéphane Auffret, Sébastien Bandiera, Bernard Rodmacq, Alain Schuhl, and Pietro Gambardella. Perpendicular switching of a single ferromagnetic layer induced by in-plane current injection. *Nature*, 476(7359):189–193, 2011.

[145] L. Liu, C.-F. Pai, Y. Li, H. W. Tseng, D. C. Ralph, and R. A. Buhrman. Spin-Torque Switching with the Giant Spin Hall Effect of Tantalum. *Science*, 336(6081):555–558, 2012.

[146] Vladislav E. Demidov, Sergei Urazhdin, Henning Ulrichs, Vasyl Tiberkevich, Andrei Slavin, Dietmar Baither, Guido Schmitz, and Sergej O. Demokritov. Magnetic nano-oscillator driven by pure spincurrent. *Nature Materials*, 11(12):1028–1031, 2012.

[147] Luqiao Liu, Chi Feng Pai, D. C. Ralph, and R. A. Buhrman. Magnetic oscillations driven by the spin hall effect in 3-terminal magnetic tunnel junction devices. *Physical Review Letters*, 109(18):186602, 2012.

[148] P. P. J. Haazen, E. Murè, J. H. Franken, R. Lavrijsen, H. J. M. Swagten, and B. Koopmans. Domain wall depinning governed by the spinHalleffect. *Nature Materials*, 12(4):299–303, 2013.

[149] Satoru Emori, Uwe Bauer, Sung-Min Ahn, Eduardo Martinez, and Geoffrey S. D. Beach. Current-driven dynamics of chiral ferromagnetic domain walls. *Nature Materials*, 12(7):611–616, 2013.

[150] M. I. Dyakonov. Magnetoresistance due to edge spin accumulation. *Physical Review Letters*, 99(12):6–9, 2007.

[151] J. Sinova, S. O. Valenzuela, J. Wunderlich, C. H. Back, and T. Jungwirth. Spin Hall effects. *Reviews of Modern Physics*, 87(4):1213–1260, 2015.

[152] G. Y. Guo, S. Murakami, T. W. Chen, and N. Nagaosa. Intrinsic spin hall effect in platinum: First-principles calculations. *Physical Review Letters*, 100(9):3–7, 2008.

[153] Andrew D Kent and Daniel C Worledge. A new spin on magnetic memories. *Nature Nanotechnology*, 10(3):187–191, 2015.

[154] T. Tanaka, H. Kontani, M. Naito, T. Naito, D. S. Hirashima, K. Yamada, and J. Inoue. Intrinsic spin Hall effect and orbital Hall effect in 4d and 5d transition metals. *Physical Review B*, 77(16):165117, 2008.

[155] Kai-Uwe Demasius, Timothy Phung, Weifeng Zhang, Brian P. Hughes, See-Hun Yang, Andrew Kellock, Wei Han, Aakash Pushp, and Stuart S. P. Parkin. Enhanced spinorbit torques by oxygen incorporation in tungsten films. *Nature Communications*, 7:10644, feb 2016.

[156] A. R. Mellnik, J. S. Lee, A. Richardella, J. L. Grab, P. J. Mintun, M. H. Fischer, A. Vaezi, A. Manchon, E.-A. Kim, N. Samarth, and D. C. Ralph. Spin-transfer torque generated by a topological insulator. *Nature*, 511(7510):449–451, 2014.

[157] Yabin Fan, Pramey Upadhyaya, Xufeng Kou, Murong Lang, So Takei, Zhenxing Wang, Jianshi Tang, Liang He, Li-Te Chang, Mohammad Montazeri, Guoqiang Yu, Wanjun Jiang, Tianxiao Nie, Robert N. Schwartz, Yaroslav Tserkovnyak, and Kang L. Wang. Magnetization switching through giant spinorbit torque in a magnetically doped topological insulator heterostructure. *Nature Materials*, 13(7):699–704, 2014.

[158] Kohei Fujiwara, Yasuhiro Fukuma, Jobu Matsuno, Hiroshi Idzuchi, Yasuhiro Niimi, YoshiChika Otani, and Hidenori Takagi. 5d iridium oxide as a material for spin-current detection. *Nature Communications*, 4:1–6, 2013.

[159] E. Lesne, Yu Fu, S. Oyarzun, J. C. Rojas-Sánchez, D. C. Vaz, H. Naganuma, G. Sicoli, J.-P. Attané, M. Jamet, E. Jacquet, J.-M. George, A. Barthélémy, H. Jaffrès, A. Fert, M. Bibes, and L. Vila. Highly efficient and tunable spin-to-charge conversion through Rashba coupling at oxide interfaces. *Nature Materials*, 15(12):1261–1266, 2016.

[160] Qi Song, Hongrui Zhang, Tang Su, Wei Yuan, Yangyang Chen, Wenyu Xing, Jing Shi, Jirong Sun, and Wei Han. Observation of inverse Edelstein effect in Rashba-split 2DEG between SrTiO 3 and LaAlO 3 at room temperature. *Science Advances*, 3(3):e1602312, 2017.

[161] Ryo Ohshima, Yuichiro Ando, Kosuke Matsuzaki, Tomofumi Susaki, Mathias Weiler, Stefan Klingler, Hans Huebl, Eiji Shikoh, Teruya Shinjo, Sebastian T. B. Goennenwein, and Masashi Shiraishi. Strong evidence for d-electron spin transport at room temperature at a LaAlO3/SrTiO3 interface. *Nature Materials*, 16(6):609–614, 2017.

[162] Seo Hyoung Chang, Young Jun Chang, S. Y. Jang, D. W. Jeong, C. U. Jung, Y. J. Kim, J. S. Chung, and T. W. Noh. Thickness-dependent structural phase transition of strained SrRuO3 ultrathin films: The role of octahedral tilt. *Physical Review B*, 84(10):104101, 2011.

[163] Weifeng Zhang, Wei Han, Xin Jiang, See-Hun Yang, and Stuart S. P. Parkin. Role of transparency of platinumferromagnet interfaces in determining the intrinsic magnitude of the spin Hall effect. *Nature Physics*, 11(6):496–502, 2015.

[164] Tianxiang Nan, Satoru Emori, Carl T. Boone, Xinjun Wang, Trevor M. Oxholm, John G. Jones, Brandon M. Howe, Gail J. Brown, and Nian X. Sun. Comparison of spin-orbit torques and spin pumping across NiFe/Pt and NiFe/Cu/Pt interfaces. *Physical Review B - Condensed Matter and Materials Physics*, 91(21):214416, 2015.

[165] Luqiao Liu, Takahiro Moriyama, D. C. Ralph, and R. A. Buhrman. Spin-Torque Ferromagnetic Resonance Induced by the Spin Hall Effect. *Physical Review Letters*, 106(3):036601, 2011.

[166] E.I. Rashba. Properties of semiconductors with an extremum loop .1. Cyclotron and combinational resonance in a magnetic field perpendicular to the plane of the loop. *Sov. Phys. Solid State*, 2:1224–1238, 1960.

[167] Yaroslav Tserkovnyak, Arne Brataas, Gerrit E W Bauer, and Bertrand I Halperin. Nonlocal Magnetization Dynamics in Ferromagnetic Hybrid Nanostructures. *Reviews of Modern Physics*, 77(6):1375–1421, 2005.

[168] Satoru Emori, Urusa S. Alaan, Matthew T. Gray, Volker Sluka, Yizhang Chen, Andrew D. Kent, and Yuri Suzuki. Spin transport and dynamics in all-oxide perovskite La2/3Sr1/3MnO3/SrRuO3 bilayers probed by ferromagnetic resonance. *Physical Review B*, 94(22):224423, 2016.

[169] X. Ke, C. Adamo, D. G. Schlom, M. Bernhagen, R. Uecker, and P. Schiffer. Low temperature magnetism in the perovskite substrate DyScO3. *Applied Physics Letters*, 94(15):152503, 2009.

[170] Deborah M. Paskiewicz, Rebecca Sichel-Tissot, Evguenia Karapetrova, Liliana Stan, and Dillon D. Fong. Single-Crystalline SrRuO3 Nanomembranes: A Platform for Flexible Oxide Electronics. *Nano Letters*, 16(1):534–542, 2016.

[171] Di Lu, David J. Baek, Seung Sae Hong, Lena F. Kourkoutis, Yasuyuki Hikita, and HaroldY. Hwang. Synthesis of freestanding single-crystal perovskite films and heterostructures by etching of sacrificial water-solublelayers. *Nature Materials*, 15(12):1255–1260, 2016.

[172] Kazunori Nishio, Harold Y Hwang, and Yasuyuki Hikita. Thermodynamic guiding principles in selective synthesis of strontium iridate Ruddlesden-Popper epitaxial films. *APL Materials*, 4(3):036102, 2016.

[173] S. S A Seo, J. Nichols, J. Hwang, J. Terzic, J. H. Gruenewald, M. Souri, J. Thompson, J. G. Connell, and G. Cao. Selective growth of epitaxial Sr2IrO4 by controlling plume dimensions in pulsed laser deposition. *Applied Physics Letters*, 109(20):201901, 2016.

[174] J. P. Podkaminer, J. J. Patzner, B. a. Davidson, and C. B. Eom. Real-time and in situ monitoring of sputter deposition with RHEED for atomic layer controlled growth. *APL Materials*, 4(8):086111, 2016.

[175] Bharat Jalan, Pouya Moetakef, and Susanne Stemmer. Molecular beam epitaxy of SrTiO3 with a growth window. *Applied Physics Letters*, 95(3):032906, 2009.

[176] Jack C. Sankey, Yong-Tao Cui, Jonathan Z. Sun, John C. Slonczewski, Robert A. Buhrman, and Daniel C. Ralph. Measurement of the spin-transfer-torque vector in magnetic tunnel junctions. *Nature Physics*, 4(1):67–71, 2007.

[177] V. Tshitoyan, C. Ciccarelli, A. P. Mihai, M. Ali, A. C. Irvine, T. A. Moore, T. Jungwirth, and A. J. Ferguson. Electrical manipulation of ferromagnetic NiFe by antiferromagnetic IrMn. *Physical Review B*, 92(21):214406, 2015.

[178] Wei Zhang, Matthias B. Jungfleisch, Frank Freimuth, Wanjun Jiang, Joseph Sklenar, John E. Pearson, John B. Ketterson, Yuriy Mokrousov, and Axel Hoffmann. All-electrical manip-

ulation of magnetization dynamics in a ferromagnet by antiferromagnets with anisotropic spin Hall effects. *Physical Review B*, 92(14):144405, 2015.

[179] Shinya Kasai, Kouta Kondou, Hiroaki Sukegawa, Seiji Mitani, Kazuhito Tsukagoshi, and Yoshichika Otani. Modulation of effective damping constant using spin Hall effect. *Applied Physics Letters*, 104(9):092408, 2014.

[180] A. Ganguly, K. Kondou, H. Sukegawa, S. Mitani, S. Kasai, Y. Niimi, Y. Otani, and A. Barman. Thickness dependence of spin torque ferromagnetic resonance in Co75Fe25/Pt bilayer films. *Applied Physics Letters*, 104(7):072405, 2014.

[181] Yongxi Ou, Chi-Feng Pai, Shengjie Shi, D. C. Ralph, and R. A. Buhrman. Origin of fieldlike spin-orbit torques in heavy metal/ferromagnet/oxide thin film heterostructures. *Physical Review B*, 94(14):140414, 2016.

[182] Chi-Feng Pai, Yongxi Ou, Luis Henrique Vilela-Leão, D. C. Ralph, and R. A. Buhrman. Dependence of the efficiency of spin Hall torque on the transparency of Pt/ferromagnetic layer interfaces. *Physical Review B*, 92(6):064426, 2015.